This is to certify that the
dissertation entitled

Investigating Feedback and Relaxation in Clusters of Galaxies with the Chandra X-ray Observatory

presented by

Kenneth W. Cavagnolo

has been accepted towards fulfillment
of the requirements for the

Ph.D. degree in Astronomy & Astrophysics

Major Professor's Signature

Date

MSU is an affirmative action, equal-opportunity employer

INVESTIGATING FEEDBACK AND RELAXATION IN CLUSTERS OF GALAXIES WITH THE CHANDRA X-RAY OBSERVATORY

By

Kenneth W. Cavagnolo

AN ABSTRACT OF A DISSERTATION

Submitted to
Michigan State University
in partial fulfillment of the requirements
for the degree of

DOCTOR OF PHILOSOPHY

Department of Astronomy and Astrophysics

2008

Dr. Megan Donahue

ABSTRACT

INVESTIGATING FEEDBACK AND RELAXATION IN CLUSTERS OF GALAXIES WITH THE CHANDRA X-RAY OBSERVATORY

By

Kenneth W. Cavagnolo

Presented in this dissertation is an analysis of the X-ray emission from the intracluster medium (ICM) in clusters of galaxies observed with the *Chandra* X-ray Observatory. The cluster dynamic state is investigated via ICM temperature inhomogeneity, and ICM entropy is used to evaluate the thermodynamics of cluster cores.

If the hot ICM is nearly isothermal in the projected region of interest, the X-ray temperature inferred from a broadband (0.7-7.0 keV) spectrum should be identical to the X-ray temperature inferred from a hard-band (2.0-7.0 keV) spectrum. However, if unresolved cool lumps of gas are contributing soft X-ray emission, the temperature of a best-fit single-component thermal model will be cooler for the broadband spectrum than for the hard-band spectrum. Using this difference as a diagnostic, the ratio of best-fitting hard-band and broadband temperatures may indicate the presence of cooler gas even when the X-ray spectrum itself may not have sufficient signal-to-noise ratio (S/N) to resolve multiple temperature components.

In Chapter 2 we explore this band dependence of the inferred X-ray temperature of the ICM for 192 well-observed galaxy clusters selected from the *Chandra* X-ray Observatory's Data Archive. We extract X-ray spectra from core-excised annular regions for each cluster in the archival sample. We compare the X-ray temperatures inferred from single-temperature fits when the energy range of the fit is 0.7-7.0 keV (broad) and when the energy range is $2.0/(1+z)$-7.0 keV (hard). We find that the hard-band

temperature is significantly higher, on average, than the broadband temperature. On further exploration, we find this temperature ratio is enhanced preferentially for clusters which are known merging systems. In addition, cool-core clusters tend to have best-fit hard-band temperatures that are in closer agreement with their best-fit broadband temperatures.

ICM entropy is of great interest because it dictates ICM global properties and records the thermal history of a cluster. Entropy is therefore a useful quantity for studying the effects of feedback on the cluster environment and investigating the breakdown of cluster self-similarity. Radial entropy profiles of the ICM for a collection of 239 clusters taken from the *Chandra* X-ray Observatory's Data Archive are presented in Chapter 3. We find that most ICM entropy profiles are well-fit by a model which is a power-law at large radii and approaches a constant value at small radii: $K(r) = K_0 + K_{100}(r/100\mathrm{kpc})^{\alpha}$, where K_0 quantifies the typical excess of core entropy above the best fitting power-law found at larger radii. We also show that the K_0 distributions of both the full archival sample and the primary *HIFLUGCS* sample of Reiprich (2001) are bimodal with a distinct gap centered at $K_0 \approx 40\mathrm{keV\ cm}^2$ and population peaks at $K_0 \sim 15\mathrm{keV\ cm}^2$ and $K_0 \sim 150\mathrm{keV\ cm}^2$.

Utilizing the results of the the *Chandra* X-ray Observatory archival study of intracluster entropy presented in Chapter 3, we show in Chapter 4 that Hα and radio emission from the brightest cluster galaxy are much more pronounced when the cluster's core gas entropy is $\lesssim 30\mathrm{keV\ cm}^2$. The prevalence of H$\alpha$ emission below this threshold indicates that it marks a dichotomy between clusters that can harbor multiphase gas and star formation in their cores and those that cannot. The fact that strong central radio emission also appears below this boundary suggests that feedback from an active galactic nucleus (AGN) turns on when the ICM starts to condense, strengthening the case for AGN feedback as the mechanism that limits star formation in the Universe's most luminous galaxies.

INVESTIGATING FEEDBACK AND RELAXATION IN CLUSTERS OF GALAXIES WITH THE CHANDRA X-RAY OBSERVATORY

By

Kenneth W. Cavagnolo

A DISSERTATION

Submitted to
Michigan State University
in partial fulfillment of the requirements
for the degree of

DOCTOR OF PHILOSOPHY

Department of Astronomy and Astrophysics

2008

ABSTRACT

INVESTIGATING FEEDBACK AND RELAXATION IN CLUSTERS OF GALAXIES WITH THE CHANDRA X-RAY OBSERVATORY

By

Kenneth W. Cavagnolo

Presented in this dissertation is an analysis of the X-ray emission from the intracluster medium (ICM) in clusters of galaxies observed with the *Chandra* X-ray Observatory. The cluster dynamic state is investigated via ICM temperature inhomogeneity, and ICM entropy is used to evaluate the thermodynamics of cluster cores.

If the hot ICM is nearly isothermal in the projected region of interest, the X-ray temperature inferred from a broadband (0.7-7.0 keV) spectrum should be identical to the X-ray temperature inferred from a hard-band (2.0-7.0 keV) spectrum. However, if unresolved cool lumps of gas are contributing soft X-ray emission, the temperature of a best-fit single-component thermal model will be cooler for the broadband spectrum than for the hard-band spectrum. Using this difference as a diagnostic, the ratio of best-fitting hard-band and broadband temperatures may indicate the presence of cooler gas even when the X-ray spectrum itself may not have sufficient signal-to-noise ratio (S/N) to resolve multiple temperature components.

In Chapter 2 we explore this band dependence of the inferred X-ray temperature of the ICM for 192 well-observed galaxy clusters selected from the *Chandra* X-ray Observatory's Data Archive. We extract X-ray spectra from core-excised annular regions for each cluster in the archival sample. We compare the X-ray temperatures inferred from single-temperature fits when the energy range of the fit is 0.7-7.0 keV (broad) and when the energy range is $2.0/(1+z)$-7.0 keV (hard). We find that the hard-band temperature is significantly higher, on average, than the broadband temperature.

On further exploration, we find this temperature ratio is enhanced preferentially for clusters which are known merging systems. In addition, cool-core clusters tend to have best-fit hard-band temperatures that are in closer agreement with their best-fit broadband temperatures.

ICM entropy is of great interest because it dictates ICM global properties and records the thermal history of a cluster. Entropy is therefore a useful quantity for studying the effects of feedback on the cluster environment and investigating the breakdown of cluster self-similarity. Radial entropy profiles of the ICM for a collection of 239 clusters taken from the *Chandra* X-ray Observatory's Data Archive are presented in Chapter 3. We find that most ICM entropy profiles are well-fit by a model which is a power-law at large radii and approaches a constant value at small radii: $K(r) = K_0 + K_{100}(r/100\text{kpc})^{\alpha}$, where K_0 quantifies the typical excess of core entropy above the best fitting power-law found at larger radii. We also show that the K_0 distributions of both the full archival sample and the primary *HIFLUGCS* sample of Reiprich (2001) are bimodal with a distinct gap centered at $K_0 \approx 40\text{keV cm}^2$ and population peaks at $K_0 \sim 15\text{keV cm}^2$ and $K_0 \sim 150\text{keV cm}^2$.

Utilizing the results of the the *Chandra* X-ray Observatory archival study of intracluster entropy presented in Chapter 3, we show in Chapter 4 that Hα and radio emission from the brightest cluster galaxy are much more pronounced when the cluster's core gas entropy is $\lesssim 30\text{keV cm}^2$. The prevalence of H$\alpha$ emission below this threshold indicates that it marks a dichotomy between clusters that can harbor multiphase gas and star formation in their cores and those that cannot. The fact that strong central radio emission also appears below this boundary suggests that feedback from an active galactic nucleus (AGN) turns on when the ICM starts to condense, strengthening the case for AGN feedback as the mechanism that limits star formation in the Universe's most luminous galaxies.

Dedicated to my mother: Miss Lorna Lorraine Cox.

ACKNOWLEDGMENTS

Thanks to Christopher Waters for the LaTeX class used to format this thesis. My dissertation would not have been possible without the multitude of grants from NASA and the Chandra X-ray Center. I also thank the MSU College of Natural Science for awarding me the Dissertation Completion Fellowship which helped fund my final year at MSU.

My deepest thanks to Megan Donahue and Mark Voit for their guidance, wisdom, patience, and without whom I would be in quantum computing. I can only say, "Thank you, Megan," for allowing me the time and space to find my bearings after my mother's passing, words are insufficient to express my gratitude. Many thanks to my friend Ming Sun who always listened, always had time for a question, and was never wrong. Thanks also to Jack Baldwin who nutured my painfully slow development as a research assistant – a more soothing voice there has never been. On behalf of everyone that has never said so, "We love you, Shawna Prater. MSU Astronomy and Astrophysics could function without you." And of course, Debbie Simmons, without whom I would have been dropped from all courses and locked out of the building.

Every time I feel the warmth of the Sun on my skin, it is an invigorating experience. Bathed in photons millions of years old from an inconceivably large nuclear power plant over a hundred million kilometers away, I feel connected to the Universe in a way that is surreal. To feel purposely cared for by the feckless Sun, whose existence and operation are arguably devoid of purpose, is quite profound. For that I say, "Thank you, Sun!"

To my wife, Lisa: Our vows were foretelling, I will indeed require the course of an entire life to express my appreciation for the tenderness, care, love, and humor you gave during completion of this dissertation. You are, and always will be, my beloved.

PREFACE

Our universe is predominantly an untold story. Within a larger, nested framework of complex mechanisms, humans evolved with minimal impact on the systems which support and nurture our existance. Yet, during the short epoch of global industrialization, we have compromised the effectiveness and function of the systems which formed the biodiversity which makes our planet such a wonderful place. As an acknowledgment of our species' appreciation for the Earth, and as a show of our understanding that humanity's presence on Earth is fleeting, let us strive to utilize the pursuit of knowledge, through application of reason and logic, such that our actions benefit "all the children, of all species, for all of time" (McDonough & Braungart, 2002). Let us all exert effort such that the Earth and the Universe will be enriched by humanity, and that our actions – local, global, and possibly interplanetary – will leave the places we inhabit and visit nourished from our presence.

TABLE OF CONTENTS

LIST OF TABLES

LIST OF FIGURES

Images in this dissertation are presented in color.

LIST OF SYMBOLS

Mpc Megaparsec: A unit of length representing one million parsecs. The parsec (pc) is a historical unit for measuring parallax and equals 3.0857×10^{13} km. 1

z Dimensionless redshift: As is common in most of astronomy, I adopt the definition of redshift using a dimensionless ratio of wavelengths, $z = (\lambda_{\rm observed}/\lambda_{\rm rest}) - 1$, where the wavelength shift occurs because of cosmic expansion. 1

H_0 Hubble constant: The current ratio of recessional velocity arising from expansion of the Universe to an object's distance from the observer, $v = H_0 D$. H_0 is assumed here to be $\sim$ 70km s^{-1} Mpc^{-1} . Inverted, the Hubble constant yields the present age of the Universe, $H_0^{-1} \approx$ 13.7 billion years. $H(z)$ denotes the Hubble constant at a particular redshift, z. 1

ρ_c Critical density: The density necessary for a universe which has spatially flat geometry and in which the expansion rate of spacetime balances gravitational attraction and prevents recollapse. In terms of relevant quantities $\rho_c = 3H(z)^2/8\pi G$, with units g cm^{-3}. 1

Ω_Λ Cosmological constant energy density of the Universe: The ratio of energy density due to a cosmological constant to the critical density. Ω_Λ is assumed here to be ~ 0.7. 1

Ω_M Matter density of the Universe: The ratio of total matter density to the critical density. $\Omega_{\rm M}$ is currently measured to be ~ 0.3. 1

$M_\odot$ Mass of the Sun: One solar mass equals 1.9891×10^{30}kg 3

$Z_\odot$ Metal abundance of the Sun: Individual elemental abundances can be found in Anders & Grevesse (1989). 9

N_H Neutral hydrogen column density: The Galaxy is rich with metals such as C, N, O, S, and Si which absorb incoming extragalactic soft X-ray radiation. The density of neutral hydrogen is assumed to be a surrogate for the density of metals. Photoelectric absorption models are used to quantify the attenuation of soft X-rays, and typically take as input the column density (cm^{-2}) of neutral hydrogen in a particular direction. $N_{\rm H}$ is related to the number density, n_H (cm^{-3}), along the line of sight, dl, as $N_{\rm H} = \int n_H dl$. 11

Λ Cooling function: A function describing plasma emissivity for a given temperature and metal composition, and typically given in units of $\mathrm{erg cm^3 s^{-1}}$. 13

D_C Comoving distance: The distance which would be measured between two objects today if those two points were moving away from each other with the expansion of the Universe. 17

D_A Angular diameter distance: The ratio of an object's true transverse size to its angular size. For a nearly flat universe, D_A is a good approximation of the comoving distance, $D_A \approx D_C/(1+z)$. 17

Ω_S Solid angle: For a sphere of a given radius, for example the distance to an object D_C, the area of that object, A, on the sphere subtends an angle equal to $\Omega_S = A/D_C^2$. This is the solid angle. 17

Ω_k Curvature of the Universe: For a spatially flat universe, such as our own, $\Omega_k \approx 0$. 17

V_C Comoving volume: The volume in which the number density of slowly evolving objects locked into the local Hubble flow, like galaxy clusters, is constant with redshift. The comoving volume element for redshift element dz and solid angle element $d\Omega_S$ element is $dV_C = D_C[D_A(1+z)]^2[\Omega_{\mathrm{M}}(1+z)^3 + \Omega_k(1+z)^2 + \Omega_\Lambda]^{-1/2}\ d\Omega_S\ dz$. 17

Chapter 1: Introduction

1.1 Clusters of Galaxies

Of the luminous matter in the Universe, stars and galaxies are often the most familiar to a sky gazer. Aside from the Moon and the occasional bright planet, stars are the most abundantly obvious patrons of the night sky. Viewed from a sufficiently dark location, the stars form a band of light interspersed with dust and gaseous clouds which define the Milky Way, our home galaxy. The Milky Way is only one of more than 30 galaxies in a gravitationally bound group of galaxies, named the Local Group, which includes the well-known, nearby galaxy Andromeda. But in cosmological terms, the Local Group is very small in comparison to immense structures containing thousands of galaxies. In a turn of wit, these structures are appropriately named clusters of galaxies, and are the focus of this dissertation.

Galaxy clusters are the most massive gravitationally bound structures to have yet formed in the Universe. As where galaxy groups have roughly 10-50 galaxies, galaxy clusters have hundreds to thousands of galaxies. When viewed through a telescope, a galaxy cluster appears as a tight distribution of mostly elliptical and S0 spiral galaxies within a radius of $\sim 1 - 5$ Mpc[1] of each other. Rich galaxy clusters are truly spectacular objects, as can be seen in Figure 1.1 which shows the *Hubble* Space Telescope's close-up of the strong lensing cluster Abell 1689.

[1]Throughout this dissertation, a flat A ΛCDM cosmology with $H_0 = 70$ km s^{-1} Mpc^{-1}, $\Omega_{\rm M} = 0.27$, and $\Omega_\Lambda = 0.73$ is adopted cosmology of $H_0 = 70$km s^{-1} Mpc^{-1}, $\Omega_\Lambda = 0.7$, and $\Omega_{\rm M} = 0.3$ is assumed. These values are taken from Spergel et al. (2007).

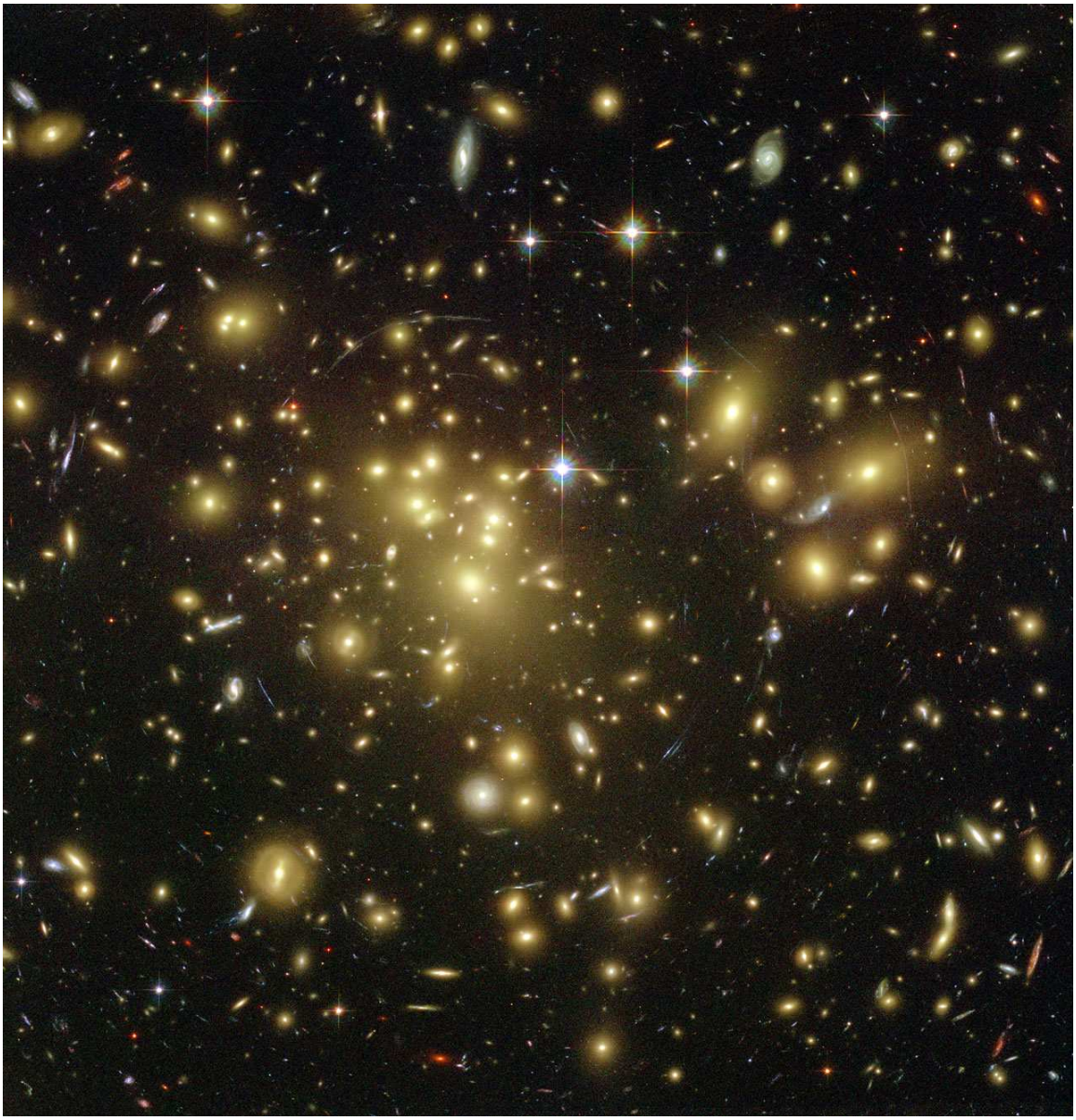

Figure 1.1 Optical image of the galaxy cluster Abell 1689 as observed with the ACS instrument on-board the *Hubble* Space Telescope. The fuzzy yellowish spheres are giant elliptical (gE) galaxies in the cluster, with the gE nearest the center of the image being the brightest cluster galaxy – ostensibly, the cluster "center". Image taken from NASA's Hubblesite.org. Image Credits: NASA, N. Benitez (JHU), T. Broadhurst (The Hebrew University), H. Ford (JHU), M. Clampin(STScI), G. Hartig (STScI), G. Illingworth (UCO/Lick Observatory), the ACS Science Team and ESA.

Galaxy clusters are deceptively named. As with most objects in the Universe, one of the most revealing characteristics of an object is its mass, and the mass of clusters of galaxies is not dominated by galaxies. A cluster of galaxies mass is dominated ($\gtrsim 85\%$) by dark matter with most ($\gtrsim 80\%$) of the baryonic mass[2] in the form of a hot ($kT \approx 2 - 15$ keV; 10-100 million degrees K), luminous (10^{43-46}erg s^{-1}), diffuse ($10^{-1} - 10^{-4}$cm^{-3}) intracluster medium (ICM) which is co-spatial with the galaxies but dwarfs them in mass (Blumenthal et al., 1984; David et al., 1990). For comparison, the ICM in the core region of a galaxy cluster is, on average, 10^{20} times less dense than typical Earth air, 10^5 times denser than the mean cosmic density, more than 2000 times hotter than the surface of the Sun, and shines as bright as 10^{35} 100 watt light bulbs.

Because of the ICM's extreme temperature, the gas is mostly ionized, making it a plasma. For the temperature range of clusters, the ICM is most luminous at X-ray wavelengths of the electromagnetic spectrum. This makes observing galaxy clusters with X-ray telescopes, like NASA's *Chandra* X-ray Observatory, a natural choice. Clusters have masses ranging over 10^{14-15} M$_\odot$ with velocity dispersions of $500 - 1500$km s^{-1}. The ICM has also been enriched with metals[3] to an average value of ~ 0.3 solar abundance. Shown in Figure 1.2 is an optical, X-ray, and gravitational lensing composite image of the galaxy cluster 1E0657-56. This cluster is undergoing an especially spectacular and rare merger in the plane of the sky which allows for the separate dominant components of a cluster – dark matter, the ICM, and galaxies – to be "seen" distinctly.

As knowing the characteristics of galaxy clusters is a small part of the discovery process, we must also wonder, why study clusters of galaxies? Galaxy clusters have two very important roles in the current research paradigm:

[2]Baryonic is a convenient term used to describe ordinary matter like atoms or molecules, while non-baryonic matter is more exotic like free electrons or dark matter particles.

[3]It is common practice in astronomy to classify "metals" as any element with more than two protons.

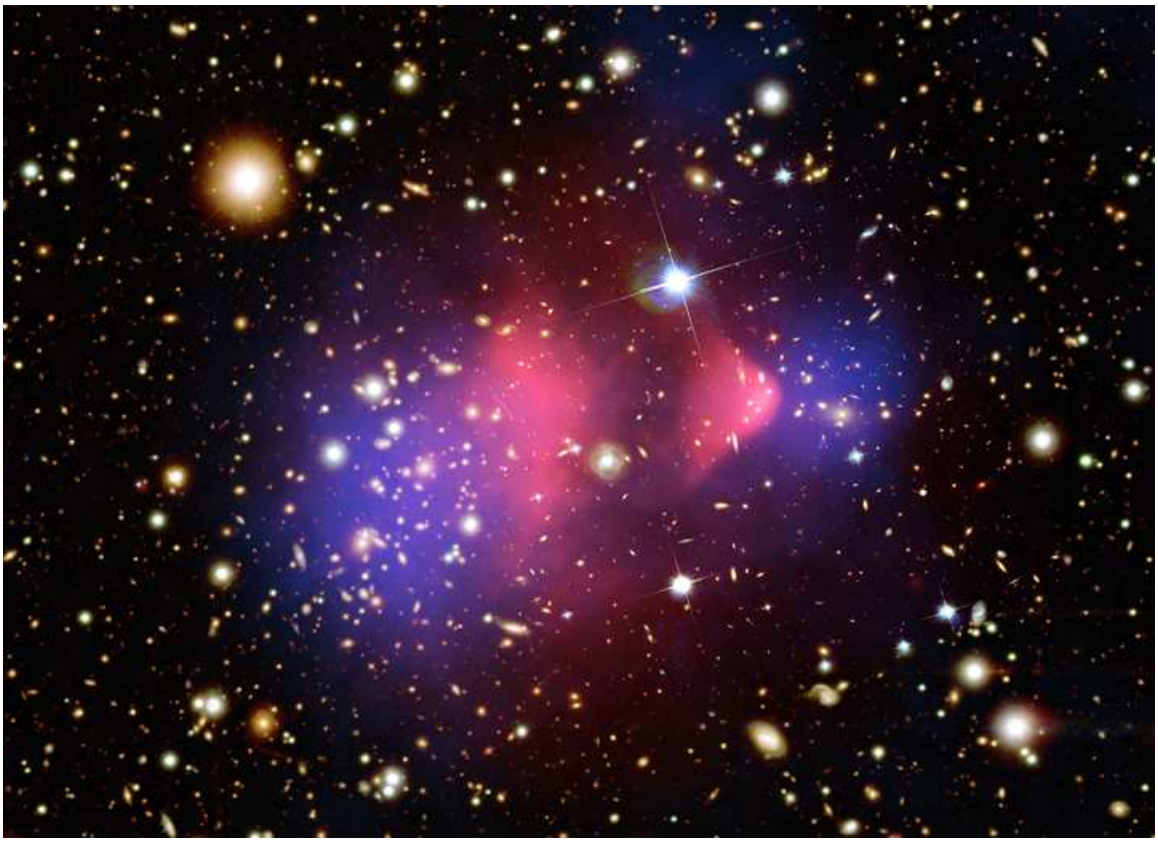

Figure 1.2 The galaxy cluster 1E0657-56, a.k.a. the Bullet Cluster. All of the primary components of a galaxy cluster can be seen in this image: the X-ray ICM (pink), dark matter (blue), and galaxies. The brilliant white object with diffraction spikes is a star. This cluster has become very famous as the merger dynamics provide direct evidence for the existence of dark matter (Clowe et al., 2006). Image taken from NASA Press Release 06-297. Image credits: NASA/CXC/CfA/Markevitch et al. (2002) (X-ray); NASA/STScI/Magellan/U.Arizona/Clowe et al. (2006) (Optical); NASA/STScI/ESO WFI/Magellan/U.Arizona/Clowe et al. (2006) (Lensing).

1. Galaxy clusters represent a unique source of information about the Universe's underlying cosmological parameters, including the nature of dark matter and the dark energy equation of state. Large-scale structure growth is exponentially sensitive to some of these parameters, and by counting the number of clusters found in a comoving volume of space, specifically above a given mass threshold, clusters may be very useful in cosmological studies (Voit, 2005).

2. The cluster gravitational potential well is deep enough to retain all the matter which has fallen in over the age of the Universe. This slowly evolving "sealed box" therefore contains a comprehensive history of all the physical processes involved in galaxy formation and evolution, such as: stellar evolution, supernovae feedback, black hole activity in the form of active galactic nuclei, galaxy mergers, ram pressure stripping of in-falling galaxies and groups, *et cetera*. The time required for the ICM in the outskirts of a cluster to radiate away its thermal energy is longer than the age of the Universe, hence the ICM acts as a record-keeper of all the aforementioned activity. Therefore, by studying the ICM's physical properties, the thermal history of the cluster can be partially recovered and utilized in developing a better understanding of cluster formation and evolution.

In this dissertation I touch upon both these points by studying the emergent X-ray emission of the ICM as observed with the *Chandra* X-ray Observatory.

While clusters have their specific uses in particular areas of astrophysics research, they also are interesting objects in their own right. A rich suite of physics is brought to bear when studying galaxy clusters. A full-blown, theoretical construction of a galaxy cluster requires, to name just a few: gravitation, fluid mechanics, thermodynamics, hydrodynamics, magnetohydrodynamics, and high-energy/particle/nuclear physics. Multiwavelength observations of galaxy clusters provide excellent datasets for testing the theoretical predictions from other areas of physics, and clusters are also a unique

laboratory for empirically establishing how different areas of physics interconnect. Just this aspect of clusters puts them in a special place among the objects in our Universe worth intense, time-consuming, (and sometimes expensive) scrutiny. At a minimum, galaxy clusters are most definitely worthy of being the focus of a humble dissertation from a fledgling astrophysicist.

As this is a dissertation focused around observational work, in Section §1.2 I provide a brief primer on the X-ray observable properties of clusters which are important to understanding this dissertation. Section §1.2.2 provides discussion of gas entropy, a physical property of the ICM which may be unfamiliar to many readers and is utilized heavily in Chapters 3 and 4. In Section §1.3, I more thoroughly discuss reasons for studying clusters of galaxies which are specific to this dissertation. Presented in Section §1.3.1 is a discussion of why clusters of different masses are not simply scaled versions of one another, and in Section §1.3.2 the unresolved "cooling flow problem" is briefly summarized. The current chapter concludes with a brief description of the *Chandra* X-ray Observatory (CXO) and its instruments in Section §1.4. *Chandra* is the space-based telescope with which all of the data presented in this dissertation was collected.

1.2 The Intracluster Medium

In Section §1.1, the ICM was presented as a mostly ionized, hot, diffuse plasma which dominates the baryonic mass content of clusters. But where did it come from and what is the composition of this pervasive ICM? What are the mechanisms that result in the ICM's X-ray luminescence? How do observations of the ICM get converted into physical properties of a cluster? In this section I briefly cover the answers to these questions in order to give the reader a better understanding of the ICM.

Galaxy clusters are built-up during the process of hierarchical merger of dark matter halos and the baryons gravitationally coupled to those halos (White & Rees,

1978). Owing to the inefficiency of galaxy formation and the processes of galactic mass ejection and ram pressure stripping, many of the baryons in these dark matter halos are in the form of diffuse gas and not locked up in galaxies. During the merger of dark matter halos, gravitational potential energy is converted to thermal energy and the diffuse gas is heated to the virial temperature of the cluster potential through processes like adiabatic compression and accretion shocks. The cluster virial temperature is calculated by equating the average kinetic energy of a gas particle to its thermal energy,

$$\frac{1}{2}\mu m\langle\sigma^2\rangle = \frac{3}{2}kT_{\rm virial} \tag{1.1}$$

$$T_{\rm virial} = \frac{\mu m\langle\sigma^2\rangle}{3k} \tag{1.2}$$

where μ is the mean molecular weight, k is the Boltzmann constant, $T_{\rm virial}$ is the virial temperature, m is the mass of a test particle, and $\langle\sigma\rangle$ is the average velocity of the test particle. In this equation, $\langle\sigma\rangle$ can be replaced with the line-of-sight galaxy velocity dispersion (a cluster observable) because all objects within the cluster potential (stars, galaxies, protons, *etc.*) are subject to the same dynamics and hence have comparable thermal and kinetic energies.

Galaxy clusters are the most massive objects presently in the Universe. The enormous mass means deep gravitational potential wells and hence very high virial temperatures. Most cluster virial temperatures are in the range $kT_{\rm virial} = 1 - 15$keV. At these energy scales, gases are collisionally ionized plasmas and will emit X-rays via thermal bremsstrahlung (discussed in Section §1.2.1). The ICM is not a pure ionized hydrogen gas, as a result, atomic line emission from heavy elements with bound electrons will also occur. The ICM is also optically thin at X-ray wavelengths, *e.g.* the ICM optical depth to X-rays is much smaller than unity, $\tau_\lambda \ll 1$, and hence the X-rays emitted from clusters stream freely into the Universe. In the next section I

briefly cover the processes which give rise to ICM X-ray emission and the observables which result. For a magnificently detailed treatise of this topic, see Sarazin (1986)[4] and references therein.

1.2.1 X-ray Emission

Detailed study of clusters proceeds mainly through spatial and spectral analysis of the ICM. By directly measuring the X-ray emission of the ICM, quantities such as temperature, density, and luminosity per unit volume can be inferred. Having this knowledge about the ICM provides an observational tool for indirectly measuring ICM dynamics, composition, and mass. In this way a complete picture of a cluster can be built up and other processes, such as brightest cluster galaxy (BCG) star formation, AGN feedback activity, or using ICM temperature inhomogeneity to probe cluster dynamic state, can be investigated. In this section, I briefly cover how X-ray emission is produced in the ICM and how basic physical properties are then measured.

The main mode of interaction in a fully ionized plasma is the scattering of free electrons off heavy ions. During this process, charged particles are accelerated and thus emit radiation. The mechanism is known as 'free-free' emission (ff), or by the tongue-twisting thermal bremsstrahlung (German for "braking radiation"). It is also called bremsstrahlung cooling since the X-ray emission carries away large amounts of energy. The timescale for protons, ions, and electrons to reach equipartition is typically shorter than the age of a cluster (Sarazin, 2003), thus the gas particles populating the emitting plasma can be approximated as being at a uniform temperature with a Maxwell-Boltzmann velocity distribution,

$$f(\vec{v}) = 4\pi \left(\frac{m}{2\pi kT}\right)^{3/2} \vec{v}^2 \exp\left[\frac{-m\vec{v}^2}{2kT}\right] \tag{1.3}$$

where m is mass, T is temperature, k is the Boltzmann constant, and velocity, $\vec{v}$, is

[4]Also available at http://nedwww.ipac.caltech.edu/level5/March02/Sarazin/TOC.html

defined as $\vec{v} = \sqrt{v_x^2 + v_y^2 + v_z^2}$. The power emitted per cubic centimeter per second (erg $\mathrm{s}^{-1}\mathrm{cm}^{-3}$) from this plasma can be written in the compact form

$$\epsilon^{ff} \equiv 1.4 \times 10^{-27} T^{1/2} n_e n_i Z^2 \bar{g}_B \tag{1.4}$$

where 1.4×10^{-27} is in cgs and is the condensed form of the physical constants and geometric factors associated with integrating over the power per unit area per unit frequency, n_e and n_i are the electron and ion densities, Z is the number of protons of the bending charge, $\bar{g}_B$ is the frequency averaged Gaunt factor (of order unity), and T is the global temperature determined from the spectral cut-off frequency (Rybicki & Lightman, 1986). Above the cut-off frequency, $\nu_c = kT/\hbar$, few photons are created because the energy supplied by charge acceleration is less than the minimum energy required for creation of a photon. Worth noting is that free-free emission is a two-body process and hence the emission goes as the gas density squared while having a weak dependence on the thermal energy, $\epsilon \propto \rho^2 T^{1/2}$ for $T \gtrsim 10^7$ K when the gas has solar abundances.

Superimposed on the thermal emission of the plasma are emission lines of heavy element contaminants such as C, Fe, Mg, N, Ne, O, S, and Si. The widths and relative strengths of these spectral lines are used to constrain the metallicity of the ICM, which is typically quantified using units relative to solar abundance, $Z_\odot$. On average, the ICM has a metallicity of $\sim 0.3\ Z_\odot$, which is mostly stellar detritus (Mushotzky & Loewenstein, 1997; Allen & Fabian, 1998b; Fukazawa et al., 1998). In collisionally ionized plasmas with temperatures and metallicities comparable to the ICM, the dominant ion species is that of the 'closed-shell' helium-like ground state (K and L-shells) (Peterson & Fabian, 2006). The K and L shell transitions are extremely sensitive to temperature and electron densities, therefore providing an excellent diagnostic for constraining both of these quantities. The strongest K-shell transition of the ICM can be seen from iron at $kT \sim 6.7$ keV. If signal-to-noise of the

spectrum is of high enough quality, measuring a shift in the energy of this spectral line can be used to confirm or deduce the approximate redshift, and hence distance, of a cluster. The rich series of iron L-shell transitions occur between $0.2 \lesssim T \lesssim 2.0$ keV and are the best diagnostic for measuring metallicity. For the present generation of X-ray instruments, the L-shell lines are seen as a blend with a peak around ~ 1 keV.

Shown in Figs. 1.3 and 1.4 are the unredshifted synthetic spectral models generated with XSPEC (Arnaud, 1996) of a 2 keV and 8 keV gas. Both spectral models have a component added to mimic absorption by gas in the Milky Way, which is seen as attenuation of flux at $E \lesssim 0.4$ keV. For both spectral models the metal abundance is 0.3 $Z_{\odot}$. These two spectral models differ by only a factor of four in temperature but note the extreme sensitivity of both the thermal bremsstrahlung exponential cut-off and emission line strengths to temperature.

Equation 1.4 says that observations of ICM X-ray emission will yield two quantities: temperature and density. The gas density can be inferred from the *emission integral*,

$$EI = \int n_e n_p \, dV \tag{1.5}$$

where n_e is the electron density, n_p is the density of hydrogen-like ions, and dV is the gas volume within a differential element. The emission integral is essentially the sum of the square of gas density for all the gas parcels in a defined region. Thus, the gas density within a projected volume can be obtained from the spectral analysis, but it can also be obtained from spatial analysis of the cluster emission, for example from cluster surface brightness.

The number of photons detected per unit area (projected on the plane of the sky) per second is given the name *surface brightness*. Assuming spherical symmetry, 2-dimensional surface brightness can be converted to 3-dimensional emission density. By dividing a cluster observation into concentric annuli originating from the cluster

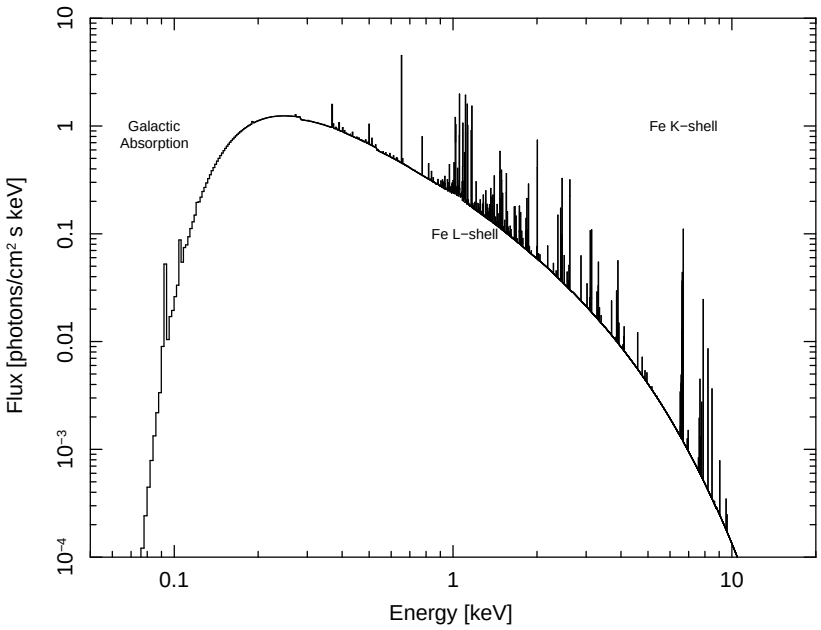

Figure 1.3 Synthetic absorbed thermal spectral model of a $N_H = 10^{20}\mathrm{cm}^{-2}$, $kT_X = 2.0$ keV, $Z/Z_\odot = 0.3$, and zero redshift gas. Notice that the strength of the iron L-shell emission lines is much greater than the iron K-shell lines for this model.

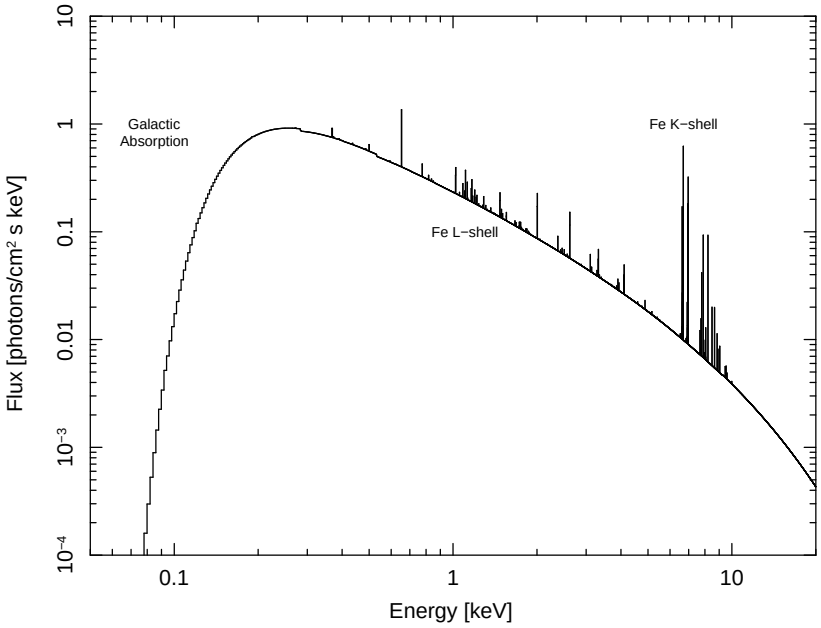

Figure 1.4 Same as Fig. 1.3 except for a $kT_X = 8.0$ keV gas. Notice that for this spectral model the iron L-shell emission lines are much weaker and the iron K-shell lines are much stronger than in the $kT_X = 2.0$ keV model. Also note that the exponential cut-off of this model occurs at a higher energy ($E > 10$ keV) than in the model shown in Figure 1.3.

center and subtracting off cluster emission at larger radii from emission at smaller radii, the amount of emission from a spherical shell can be reconstructed from the emission in an annular ring. For the spherical shell defined by radii r_i and r_{i+1}, Kriss et al. (1983) shows the relation between the emission density, $C_{i,i+1}$, to the observed surface brightness, $S_{m,m+1}$, of the ring with radii r_m and r_{m+1}, is

$$S_{m,m+1} = \frac{b}{A_{m,m+1}} \sum_{i-1}^{m} C_{i,i+1} \; [(V_{i,m+1} - V_{i+1,m+1}) - (V_{i,m} - V_{i+1,m})]. \qquad (1.6)$$

where b is the solid angle subtended on the sky by the object, $A_{m,m+1}$ is the area of the ring, and the V terms are the volumes of various shells. This method of reconstructing the cluster emission is called *deprojection*. While assuming spherical symmetry is clearly imperfect, it is not baseless. The purpose of such an assumption is to attain angular averages of the volume density at various radii from an azimuthally averaged surface density. Systematic uncertainties associated with deprojection are discussed in Section §3.3.2.

In this dissertation the spectral model MeKaL (Mewe et al., 1985, 1986; Liedahl et al., 1995) is used for all of the spectral analysis. The MeKaL model normalization, η, is defined as

$$\eta = \frac{10^{-14}}{4\pi D_A^2 (1+z)^2} \; EI \qquad (1.7)$$

where z is cluster redshift, D_A is the angular diameter distance, and EI is the emission integral from eqn. 1.5. Recognizing that the count rate, $f(r)$, per volume is equivalent to the emission density, $C_{i,i+1} = f(r)/\int dV$, where dV can be a shell (deprojected) or the sheath of a round column seen edge-on (projected), combining eqns. 1.6 and 3.1 yields an expression for the electron gas density which is a function of direct observables,

$$n_{\rm e}(r) = \sqrt{\frac{1.2 C(r) \eta(r) 4\pi [D_A(1+z)]^2}{f(r) 10^{-14}}} \qquad (1.8)$$

where the factor of 1.2 comes from the ionization ratio $n_{\rm e}$=1.2$n_{\rm p}$, $C(r)$ is the radial emission density derived from eqn. 1.6, η is the spectral normalization from eqn. 3.1, D_A is the angular diameter distance, z is the cluster redshift, and $f(r)$ is the spectroscopic count rate.

Simply by measuring surface brightness and analyzing spectra, the cluster temperature, metallicity, and density can be inferred. These quantities can then be used to derive pressure, $P = nkT$, where $n \approx 2n_{\rm e}$. The total gas mass can be inferred using gas density as $M_{gas} = \int (4/3)\pi r^3 n_{\rm e} dr$. By further assuming the ICM is in hydrostatic equilibrium, the total cluster mass within radius r is

$$M(r) = \frac{kT(r)r}{\mu m_H G}\left[\frac{d(log\ n_{\rm e}(r))}{d(log\ r)} + \frac{d(log\ T(r))}{d(log\ r)}\right] \tag{1.9}$$

where all variables have their typical definitions. The rate at which the ICM is cooling can also be expressed in simple terms of density and temperature. Given a cooling function, Λ , which is sensitive to temperature and metal abundance (for the ICM $\Lambda(T, Z) \sim 10^{-23}{\rm ergcm^3 s^{-1}}$), the cooling rate is given by $r_{cool} = n^2\Lambda(T, Z)$. For some volume, V, the cooling time is then simply the time required for a gas parcel to radiate away its thermal energy,

$$t_{cool} V r_{cool} = \gamma NkT \tag{1.10}$$

$$t_{cool} = \frac{\gamma nkT}{n^2\Lambda(T, Z)} \tag{1.11}$$

where γ is a constant specific to the type of cooling process (*e.g.* 3/2 for isochoric and 5/2 for isobaric). The cooling time of the ICM can be anywhere between 10^{7-10} yrs. Cooling time is a very important descriptor of the ICM because processes such as the formation of stars and line-emitting nebulae are sensitive to cooling time.

By "simply" pointing a high-resolution X-ray telescope, like *Chandra*, at a cluster and exposing long enough to attain good signal-to-noise, it is possible to derive a roster

of fundamental cluster properties: temperature, density, pressure, mass, cooling time, and even entropy. Entropy is a very interesting quantity which can be calculated using gas temperature and density and is most likely fundamentally connected to processes like AGN feedback and star formation (discussed in Chapters 3 and 4). In the following section I discuss how gas entropy is derived, why it is a useful quantity for understanding clusters, and how it will be utilized later in this dissertation.

1.2.2 Entropy

Entropy has both a macroscopic definition (the measure of available energy) and microscopic definition (the measure of randomness), with each being useful in many areas of science. Study of the ICM is a macro-scale endeavor, so the definition of entropy pertinent to discussion of the ICM is as a measure of the thermodynamic processes involving heat transfer. But the conventional macroscopic definition of entropy, $dS = dQ/T$, is not the quantity which is most useful in the context of studying astrophysical objects. Thus we must resort to a simpler, measurable surrogate for entropy, like the adiabat. The adiabatic equation of state for an ideal monatomic gas is $P = K\rho^{\gamma}$ where K is the adiabatic constant and γ is the ratio of specific heat capacities and has the value of 5/3 for a monatomic gas. Setting $P = \rho kT/\mu m_H$ and solving for K one finds

$$K = \frac{kT}{\mu m_H \rho^{2/3}}. \tag{1.12}$$

where μ is the mean molecular weight of the gas and m_H is the mass of the Hydrogen atom. The true thermodynamic specific entropy using this formulation is $s = k \ln K^{3/2} + s_0$, so neglecting constants and scaling K shall be called entropy in this dissertation. A further simplification can be made to recast eqn. 1.12 using the

observables electron density, $n_{\rm e}$, and X-ray temperature, T_X (in keV):

$$K = \frac{T_X}{n_{\rm e}^{2/3}}. \tag{1.13}$$

Equation 1.13 is the definition of entropy used throughout this dissertation. With a simple functional form, "entropy" can be derived directly from X-ray observations. But why study the ICM in terms of entropy?

ICM temperature and density alone primarily reflect the shape and depth of the cluster dark matter potential (Voit et al., 2002). But it is the specific entropy of a gas parcel, $s = c_v \ln(T/\rho^{\gamma-1})$, which governs the density at a given pressure. In addition, the ICM is convectively stable when $ds/dr \geq 0$, thus, without perturbation, the ICM will convect until the lowest entropy gas is near the core and high entropy gas has buoyantly risen to large radii. ICM entropy can also only be changed by addition or subtraction of heat, thus the entropy of the ICM reflects most of the cluster thermal history. Therefore, properties of the ICM can be viewed as a manifestation of the dark matter potential and cluster thermal history - which is encoded in the entropy structure. It is for these reasons that the study of ICM entropy has been the focus of both theoretical and observational study (David et al., 1996; Bower, 1997; Ponman et al., 1999; Lloyd-Davies et al., 2000; Tozzi & Norman, 2001; Voit et al., 2002; Ponman et al., 2003; Piffaretti et al., 2005; Pratt et al., 2006; Donahue et al., 2005, 2006; Morandi & Ettori, 2007; McCarthy et al., 2008).

Hierarchical accretion of the ICM should produce an entropy distribution which is a power-law across most radii with the only departure occurring at radii smaller than 10% of the virial radius (Voit et al., 2005). Hence deviations away from a power-law entropy profile are indicative of prior heating and cooling and can be exploited to reveal the nature of, for example, AGN feedback. The implication of the intimate connection between entropy and non-gravitational processes being that *both* the breaking of self-similarity and the cooling flow problem (both discussed in

Section §1.3) can be studied with ICM entropy.

In Chapter 3 and Chapter 4 I present the results of an exhaustive study of galaxy cluster entropy profiles for a sample of over 230 galaxy clusters taken from the *Chandra* Data Archive. Analysis of these profiles has yielded important results which can be used to constrain models of cluster feedback, understand truncation of the high-mass end of the galaxy luminosity function, and what effect these processes have on the global properties of clusters. The size and scope of the entropy profile library presented in this dissertation is unprecedented in the current scientific literature, and we hope our library, while having provided immediate results, will have a long-lasting and broad utility for the research community. To this end, we have made all data and results available to the public via a project web site[5].

1.3 The Incomplete Picture of Clusters

The literature on galaxy clusters is extensive. There has been a great deal already written about clusters (with much more eloquence), and I strongly suggest reading Mushotzky (1984); Kaiser (1986); Evrard (1990); Kaiser (1991); Sarazin (1986); Fabian (1994); Voit (2005); Peterson & Fabian (2006); Markevitch & Vikhlinin (2007); McNamara & Nulsen (2007), and references therein for a comprehensive review of the concepts and topics to be covered in this dissertation. The discussion of Sections §1.3.1 and §1.3.2 focuses on a few unresolved mysteries involving galaxy clusters: the breaking of self-similarity in relation to using clusters in cosmological studies and the cooling flow problem as it relates to galaxy formation.

1.3.1 Breaking of Self-Similarity

We now know the evolution of, and structure within, the Universe are a direct result of the influence from dark energy and dark matter. An all pervading repulsive

[5]http://www.pa.msu.edu/astro/MC2/accept/

dark energy has been posited to be responsible for the accelerating expansion of the Universe (Riess et al., 1998; Perlmutter et al., 1999; Riess et al., 2007). Dark matter is an unknown form of matter which interacts with itself and ordinary matter (both baryonic and non-baryonic) through gravitational forces. Up until the last ~ 5 billion years (Riess et al., 1998; Perlmutter et al., 1999; Riess et al., 2007), the influence of dark matter on the Universe has been greater than that of dark energy. The early dominance of dark matter is evident from the existence of large-scale structure like galaxy clusters.

An end result of the gravitational attraction between amalgamations of dark matter particles, called dark matter halos, is the merger of small halos into ever larger halos. Since dark matter far outweighs baryonic matter in the Universe, the baryons are coupled to the dark matter halos via gravity, and hence are dragged along during the halo merger process. Like raindrops falling in a pond that drains into a river which flows into the ocean, the process of smaller units merging to create larger units is found *ad infinitum* in the Universe and is given the name hierarchical structure formation. A useful visualization of the hierarchical structure formation process is shown in Fig. 1.5. Hierarchical formation begins with small objects like the first stars, continues on to galaxies, and culminates in the largest present objects, clusters of galaxies.

In an oversimplified summary, one can say dark energy is attempting to push space apart while dark matter is attempting to pull matter together within that space. Were the balance and evolution of dark energy and dark matter weighted heavily toward one or the other it becomes clear that the amount of structure and its distribution will be different. Thus, the nature of dark matter and dark energy ultimately influence the number of clusters found at any given redshift (*e.g.* White et al., 1993) and hence cluster number counts are immensely powerful in determining cosmological parameters (*e.g.* Borgani et al., 2001).

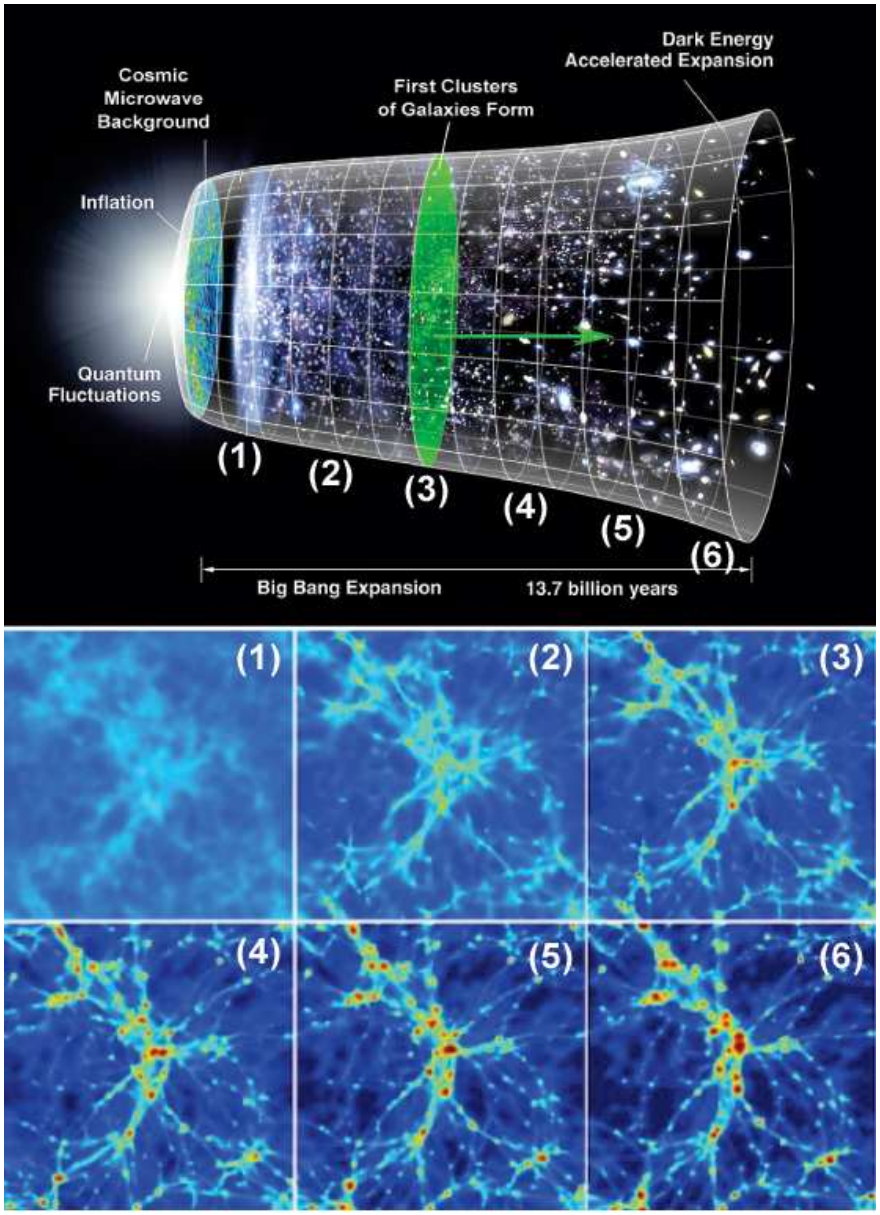

Figure 1.5 *Top panel:* Illustration of hierarchical structure formation. *Bottom panel:* Snapshots from the simulation of a galaxy cluster forming. Each pane is 10 Mpc on a side. Color coding represents gas density along the line of sight (deep red is highest, dark blue is lowest). Each snapshot is numbered on the illustration at the approximate epoch each stage of cluster collapse occurs. Notice that, at first (1-2), very small objects like the first stars and protogalaxies collapse and then these smaller objects slowly merge into much larger halos (3-5). The hierarchical merging process ultimately results in a massive galaxy cluster (6) which continues to grow as sub-clusters near the box edge creep toward the cluster main body. Illustration taken from NASA/WMAP Science Team and modified by author. Simulation snapshots taken from images distributed to the public by the Virgo Consortium on behalf of Dr. Craig Booth: http://www.virgo.dur.ac.uk

Individual clusters do not yield the information necessary to study the underlying cosmogony. However, the number density of clusters above a given mass threshold within a comoving volume element, *i.e.* the cluster mass function, is a useful quantity (Voit, 2005). But the cluster mass function is a powerful cosmological tool only if cluster masses can be accurately measured. With no direct method of measuring cluster mass, easily observable properties of clusters must be used as proxies to infer mass.

Reliable mass proxies, such as cluster temperature and luminosity, arise naturally from the theory that clusters are scaled versions of each other. This property is commonly referred to as self-similarity of mass-observables. More precisely, self-similarity presumes that when cluster-scale gravitational potential wells are scaled by the cluster-specific virial radius, the full cluster population has potential wells which are simply scaled versions of one another (Navarro et al., 1995, 1997). Self-similarity is also expected to yield low-scatter scaling relations between cluster properties such as luminosity and temperature (Kaiser, 1986, 1991; Evrard & Henry, 1991; Navarro et al., 1995, 1997; Eke et al., 1998; Frenk et al., 1999). Consequently, mass-observable relations, such as mass-temperature and mass-luminosity, derive from the fact that most clusters are virialized, meaning the cluster's energy is shared such that the virial theorem, $-2\langle T\rangle = \langle V\rangle$ where $\langle T\rangle$ is average kinetic energy and $\langle V\rangle$ is average potential energy, is a valid approximation. Both theoretical (Evrard et al., 1996; Bryan & Norman, 1998; Mohr et al., 1999; Bialek et al., 2001; Borgani et al., 2002) and observational (Mushotzky, 1984; Edge & Stewart, 1991; White et al., 1997; Allen & Fabian, 1998a; Markevitch et al., 1998; Arnaud & Evrard, 1999; Finoguenov et al., 2001) studies have shown cluster mass correlates well with X-ray temperature and luminosity, but that there is much larger ($\approx 20 - 30\%$) scatter and different slopes for these relations than expected. The breaking of self-similarity is attributed to non-gravitational processes such as ongoing mergers (eg Randall et al., 2002), heating via

feedback (eg Cavaliere et al., 1999; Bower et al., 2001), or radiative cooling in the cluster core (eg Voit & Bryan, 2001; Voit et al., 2002).

To reduce the scatter in mass scaling-relations and to increase their utility for weighing clusters, how secondary processes alter temperature and luminosity must first be quantified. It was predicted that clusters with a high degree of spatial uniformity and symmetry (*e.g.* clusters with the least substructure in their dark matter and gas distributions) would be the most relaxed and have the smallest deviations from mean mass-observable relations. The utility of substructure in quantifying relaxation is prevalent in many natural systems, such as a placid lake or spherical gas cloud of uniform density and temperature. Structural analysis of cluster simulations, take for example the recent work of Jeltema et al. (2008) or Ventimiglia et al. (2008), have shown measures of substructure correlate well with cluster dynamical state. But spatial analysis is at the mercy of perspective. If equally robust aspect-independent measures of dynamical state could be found, then quantifying deviation from mean mass-scaling relations would be improved and the uncertainty of inferred cluster masses could be further reduced. Scatter reduction ultimately would lead to a more accurate cluster mass function, and by extension, the constraints on theories explaining dark matter and dark energy could grow tighter.

In Chapter 2, I present work investigating ICM temperature inhomogeneity, a feature of the ICM which has been proposed as a method for better understanding the dynamical state of a cluster (**?**). Temperature inhomogeneity has the advantage of being a spectroscopic quantity and therefore falls into the class of aspect-independent metrics which may be useful for reducing scatter in mass-observable relations. In a much larger context, this dissertation may contribute to the improvement of our understanding of the Universe's make-up and evolution.

1.3.2 The Cooling Flow Problem

For $50\% - 66\%$ of galaxy clusters, the densest and coolest ($kT_X \lesssim T_{\rm virial}/2$) ICM gas is found in the central $\sim 10\%$ of the cluster gravitational potential well (Stewart et al., 1984; Edge et al., 1992; White et al., 1997; Peres et al., 1998; Bauer et al., 2005). For the temperature regime of the ICM, radiative cooling time, t_{cool} (see eqn. 3.7), is more strongly dependent on density than temperature, $t_{cool} \propto T_g^{1/2}\rho^2$, where T_g is gas temperature and ρ is gas density. The energy lost via radiative cooling is seen as diffuse thermal X-ray emission from the ICM (Gursky et al., 1971; Mitchell et al., 1976; Serlemitsos et al., 1977). When thermal energy is radiated away from the ICM, the gas density must increase while gas temperature and internal pressure respond by decreasing. The cluster core gas densities ultimately reached through the cooling process are large enough such that the cooling time required for the gas to radiate away its thermal energy is much shorter than both the age of the Universe, *e.g.* $t_{cool} \ll H_0^{-1}$, and the age of the cluster (Cowie & Binney, 1977; Fabian & Nulsen, 1977). Without compensatory heating, it thus follows that the ICM in some cluster cores should cool and condense.

Gas within the cooling radius, $r_{\rm cool}$, (defined as the radius at which $t_{cool} = H_0^{-1}$) is underpressured and cannot provide sufficient pressure support to prevent overlying gas layers from forming a subsonic flow of gas toward the bottom of the cluster gravitational potential. However, if when the flowing gas enters the central galaxy it has cooled to the point where the gas temperature equals the central galaxy virial temperature, then adiabatic compression[6] from the galaxy's gravitational potential well can balance heat losses from radiative cooling. But, if the central galaxy's gravitational potential is flat, then the gas energy gained via gravitational effects can also be radiated away and catastrophic cooling can proceed.

The sequence of events described above was given the name "cooling flow" (Fabian

[6]As the name indicates, no heat is exchanged during adiabatic compression; but gas temperature rises because the internal gas energy increases due to external work being done on the system.

& Nulsen, 1977; Cowie & Binney, 1977; Mathews & Bregman, 1978) and is the most simplistic explanation of what happens to the ICM when it is continuously cooling, spherically symmetric, and homogeneous (see Fabian, 1994; Peterson & Fabian, 2006; Donahue & Voit, 2004, for reviews of cool gas in cluster cores). The theoretical existence of cooling flows comes directly from X-ray observations, yet the strongest observational evidence for the existence of cooling flows will be seen when the gas cools below X-ray emitting temperatures and forms stars, molecular clouds, and emission line nebulae. Unfortunately, cooling flow models were first presented at a time when no direct, complementary observational evidence for cooling flows existed, highlighting the difficulty of confronting the models. Undeterred, the X-ray astrophysics community began referring to all clusters which had cores meeting the criterion $t_{cool} < H_0^{-1}$ as "cooling flow clusters," a tragic twist of nomenclature fate which has plagued many scientific talks.

A mass deposition rate, $\dot{M}$, can be inferred for cooling flows based on X-ray observations: $\dot{M} \propto L_X(r < r_{\rm cool})(kT_X)^{-1}$, where $L_X(r < r_{\rm cool})$ is the X-ray luminosity within the cooling region, kT_X is the X-ray gas temperature, and $\dot{M}$ typically has units of $\mathrm{M_\odot yr^{-1}}$. The quantity $\dot{M}$ is useful in getting a handle on how much gas mass is expected to be flowing into a cluster core. Mass deposition rates have been estimated for many clusters and found to be in the range $100 - 1000 \mathrm{M_\odot yr^{-1}}$ (Fabian et al., 1984; White et al., 1997; Peres et al., 1998). Mass deposition rates can also be estimated using emission from individual spectral lines: $\dot{M} \propto L_X(r < r_{\rm cool})\epsilon_f(T)$, where $L_X(r < r_{\rm cool})$ is the X-ray luminosity within the cooling region and $\epsilon_f(T)$ is the emissivity fraction attributable to a particular emission line. The ICM soft X-ray emission lines of Fe XVII, O VIII, and Ne X at $E < 1.5$ keV for example, are especially useful in evaluating the properties of cooling flows. Early low-resolution spectroscopy found mass deposition rates consistent with those from X-ray observations (*e.g.* Canizares et al., 1982).

Not surprisingly, the largest, brightest, and most massive galaxy in a cluster, the BCG, typically resides at the bottom of the cluster potential, right at the center of where a cooling flow would terminate. Real cooling flows were not expected to be symmetric, continuous, or in thermodynamic equilibrium with the ambient medium. Under these conditions, gas parcels at lower temperatures and pressures experience thermal instability and are expected to rapidly develop and collapse to form gaseous molecular clouds and stars. The stellar and gaseous components of some BCGs clearly indicate some amount of cooling and mass deposition has occurred. But are the properties of the BCG population consistent with cooling flow model predictions? For example, BCGs should be supremely luminous and continually replenished with young, blue stellar populations since the epoch of a BCG's formation. One should then expect the cores of clusters suspected of hosting a cooling flow to have very bright, blue BCGs bathed in clouds of emission line nebulae. However, observations of cooling flow clusters reveal the true nature of the core to not match these expectations of extremely high star formation rates, at least not at the rate of $> 100 \mathrm{M}_{\odot} \mathrm{yr}^{-1}$.

The optical properties of massive galaxies and BCGs are well known and neither population are as blue or bright as would be expected from the extended periods of growth via cooling flows (Madau et al., 1996; Shaver et al., 1996; Cowie et al., 1996; Crawford et al., 1999). While attempts were made in the past to selectively channel the unobserved cool gas into optically dark objects, such as in low-mass, distributed star formation (*e.g.* Prestwich & Joy, 1991), methodical searches in the optical, infrared, UV, radio, and soft X-ray wavelengths ($kT_X \lesssim 2.0$ keV) have revealed that the total mass of cooler gas associated with cooling flows is much less than expected (Hu et al., 1985; Heckman et al., 1989; McNamara et al., 1990; O'Dea et al., 1994b,a; Antonucci & Barvainis, 1994; McNamara & Jaffe, 1994; Voit & Donahue, 1995; Jaffe & Bremer, 1997; Falcke et al., 1998; Donahue et al., 2000; Edge & Frayer, 2003).

Confirming the suspicion that cooling flows are not cooling as advertised, high-

resolution *XMM-Newton* RGS X-ray spectroscopy of clusters expected to host very massive cooling flows definitively proved that the ICM was not cooling to temperatures less than 1/3 of the cluster virial temperature (Peterson et al., 2001; Tamura et al., 2001; Peterson et al., 2003). A cooling X-ray medium which has emission discontinuities at soft energies is not predicted by the simplest single-phase cooling flow models, and a troubling amount of fine-tuning (*e.g.* minimum temperatures, hidden soft emission) must be added to agree with observations. Modifications such as preferential absorption of soft X-rays in the core region (*e.g.* Allen et al., 1993) or turbulent mixing of a multi-phase cooling flow (*e.g.* Fabian et al., 2002) have been successful in matching observations, but these models lack the universality needed to explain why *all* cooling flows are not as massive as expected.

All of the observational evidence has resulted in a two-component "cooling flow problem": (1) spectroscopy of soft X-ray emission from cooling flow clusters is inconsistent with theoretical predictions, and (2) multiwavelength observations reveal a lack of cooled gas mass or stars to account for the enormous theoretical mass deposition rates implied by simple cooling flow models. So why and how is the cooling of gas below $T_{\rm virial}/3$ suppressed? As is the case with most questions, the best answer thus far is simple: the cooling flow rates were wrong, with many researchers suggesting the ICM has been intermittently heated. But what feedback mechanisms are responsible for hindering cooling in cluster cores? How do these mechanisms operate? What observational constraints can we find to determine which combination of feedback mechanism hypotheses are correct? The answers to these questions have implications for both cluster evolution and massive galaxy formation.

The cores of clusters are active places, so finding heating mechanisms is not too difficult. The prime suspect, and best proposed solution to the cooling flow problem thus far, invokes some combination of supernovae and outbursts from the active galactic nucleus (AGN) in the BCG (Binney & Tabor, 1995; Bower, 1997; Loewenstein,

2000; Voit & Bryan, 2001; Churazov et al., 2002; Brüggen & Kaiser, 2002; Brüggen et al., 2002; Nath & Roychowdhury, 2002; Ruszkowski & Begelman, 2002; Alexander, 2002; Omma et al., 2004; McCarthy et al., 2004; Roychowdhury et al., 2004; Hoeft & Brüggen, 2004; Dalla Vecchia et al., 2004; Soker & Pizzolato, 2005; Pizzolato & Soker, 2005; Voit & Donahue, 2005; Brighenti & Mathews, 2006; Mathews et al., 2006). However, there are some big problems: (1) AGN tend to deposit their energy along preferred axes, while cooling in clusters proceeds in a nearly spherically symmetric distribution in the core; (2) depositing AGN outburst energy at radii nearest the AGN is difficult and how this mechanism works is not understood; (3) there is a serious scale mismatch in heating and cooling processes which has hampered the development of a self-regulating feedback loop involving AGN. Radiative cooling proceeds as the square of gas density, whereas heating is proportional to volume. Hence, modeling feedback with a small source object, $r \sim 1$pc, that is capable of compensating for radiative cooling losses over an $\approx 10^6$kpc^3 volume, where the radial density can change by four orders of magnitude, is quite difficult. Dr. Donahue once framed this problem as, "trying to heat the whole of Europe with something the size of a button."

The basic model of how AGN feedback works is that first gas accretes onto a supermassive black hole at the center of the BCG, resulting in the acceleration and ejection of very high energy particles back into the cluster environment. The energy released in an AGN outburst is of order 10^{58-61}erg. Under the right conditions, and via poorly understood mechanisms, energy output by the AGN is transferred to the ICM and thermalized, thereby heating the gas. The details of how this process operates is beyond the scope of this dissertation (see McNamara & Nulsen, 2007, for a recent review). However, in this dissertation I do investigate some observable properties of clusters which are directly impacted by feedback mechanisms.

Utilizing the quantity ICM entropy, I present results in Chapter 3 which show

that radial ICM entropy distributions for a large sample of clusters have been altered in ways which are consistent with AGN feedback models. Entropy and its connection to AGN feedback is discussed in Subsection 1.2.2 of this chapter. In Chapter 4 I also present observational results which support the hypothesis of Voit et al. (2008) that electron thermal conduction may be an important mechanism in distributing AGN feedback energy. Hence, this dissertation, in small part, seeks to add to the understanding of how feedback functions in clusters, and thus how to resolve the cooling flow problem – the resolution of which will lead to better models of galaxy formation and cluster evolution.

1.4 Chandra X-Ray Observatory

In this section I briefly describe what makes the *Chandra* X-ray Observatory (*Chandra* or CXO for short) a ground-breaking and unique telescope ideally suited for the work carried out in this dissertation. In depth details of the telescope, instruments, and spacecraft can be found at the CXO web sites[7,8] or in Weisskopf et al. (2000). Much of what is discussed in the following sections can also be found with more detail in "The Chandra Proposers' Observatory Guide."[9] All figures cited in this section are presented at the end of the corresponding subsection.

1.4.1 Telescope and Instruments

The mean free path of an X-ray photon in a gas with the density of the Earth's atmosphere is very short. Oxygen and nitrogen in the atmosphere photoelectrically absorb X-ray photons resulting in 100% attenuation and make X-ray astronomy impossible from the Earth's surface. Many long-standing theories in astrophysics predict a wide variety of astronomical objects as X-ray emitters. Therefore, astronomers and engi-

[7] http://chandra.harvard.edu/
[8] http://cxc.harvard.edu/
[9] http://cxc.harvard.edu/proposer/POG/

neers have been sending X-ray telescopes into the upper atmosphere and space for over 30 years now.

The most recent American X-ray mission to fly is the *Chandra* X-ray Observatory. It is one of NASA's Great Observatories along with *Compton* (γ-rays), *Hubble* (primarily optical), and *Spitzer* (infrared). *Chandra* was built by Northrop-Grumman and is operated by the National Aeronautics and Space Agency. *Chandra* was launched in July 1999 and resides in a highly elliptical orbit with an apogee of $\sim 140,000$ km and a perigee of $\sim 16,000$ km. One orbit takes ≈ 64 hours to complete. The telescope has four nested iridium-coated paraboloid-hyperboloid mirrors with a focal length of ~ 10 m. An illustration of the *Chandra* spacecraft is shown in Figure 1.6.

All data presented in this dissertation was collected with the Advanced CCD Imaging Spectrometer (ACIS) instrument[10]. ACIS is quite an amazing and unique instrument in that it is an imager and medium-resolution spectrometer at the same time. When an observation is taken with ACIS, the data collected contains spatial and spectral information since the location and energy of incoming photons are recorded. The dual nature of ACIS allows the data to be analyzed by spatially dividing up a cluster image and then extracting spectra for these subregions of the image, a technique which is used heavily in this dissertation.

The observing elements of ACIS are 10 1024×1024 CCDs: six linearly arranged CCDs (ACIS-S array) and four CCDs arranged in a 2×2 mosaic (ACIS-I array). The ACIS focal plane is currently kept at a temperature of $\sim -120°$C. During an observation, the ACIS instrument is dithered along a Lissajous curve so parts of the sky which fall in the chip gaps are also observed. Dithering also ensures pixel variations of the CCD response are removed.

The high spatial and energy resolution of *Chandra* and its instruments are ideal for

[10]http://acis.mit.edu/acis

studying clusters of galaxies. The telescope on-board *Chandra* achieves on-axis spatial resolutions of $\lesssim 0.5''$/pixel but it is the pixel size of the ACIS instrument ($\sim 0.492''$) which sets the resolution limit for observations. ACIS also has an extraordinary energy resolution of $\Delta E/E \sim 100$. Below energies of ~ 0.3 keV and above energies of ~ 10 keV the ACIS effective area is ostensibly zero. The ACIS effective area also peaks in the energy range $E \sim 0.7 - 2.0$ keV. As shown in Figs. 1.3 and 1.4, a sizeable portion of galaxy cluster emission occurs in the same energy range where the ACIS effective area peaks. The energy resolution of ACIS also allows individual emission line blends to be resolved in cluster spectra. These aspects make *Chandra* a perfect choice for studying clusters and the ICM in detail. Shown in Fig. 1.7 are raw observations of Abell 1795 with the aim-points on ACIS-I (top panel) and ACIS-S (bottom panel). In Fig. 1.8 is a spectrum for the entire cluster extracted from the ACIS-I observation.

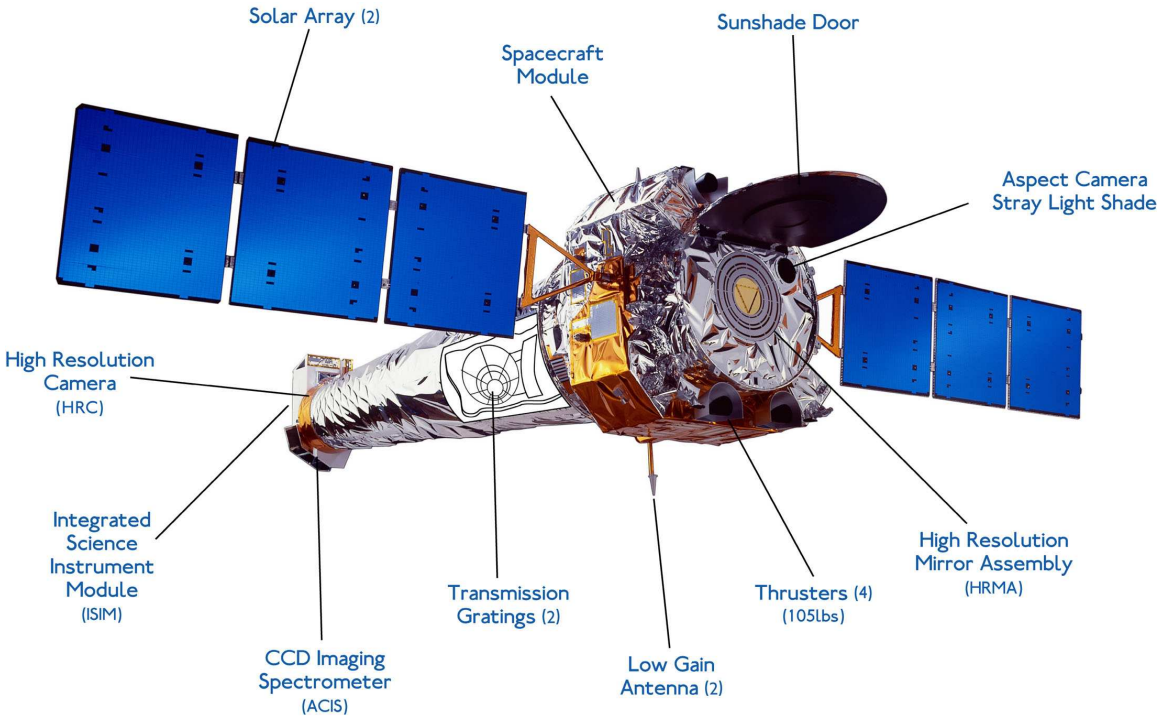

Figure 1.6 An artist's rendition of the *Chandra* spacecraft. *Chandra* is the largest ($\sim$ 17 m long; $\sim$ 4 m wide) and most massive ($\sim$ 23K kg) payload ever taken into space by NASA's Space Shuttle Program. The planned lifetime of the mission was 5 years, and the 10 year anniversary party is already planned. Illustration taken from Chandra X-ray Center.

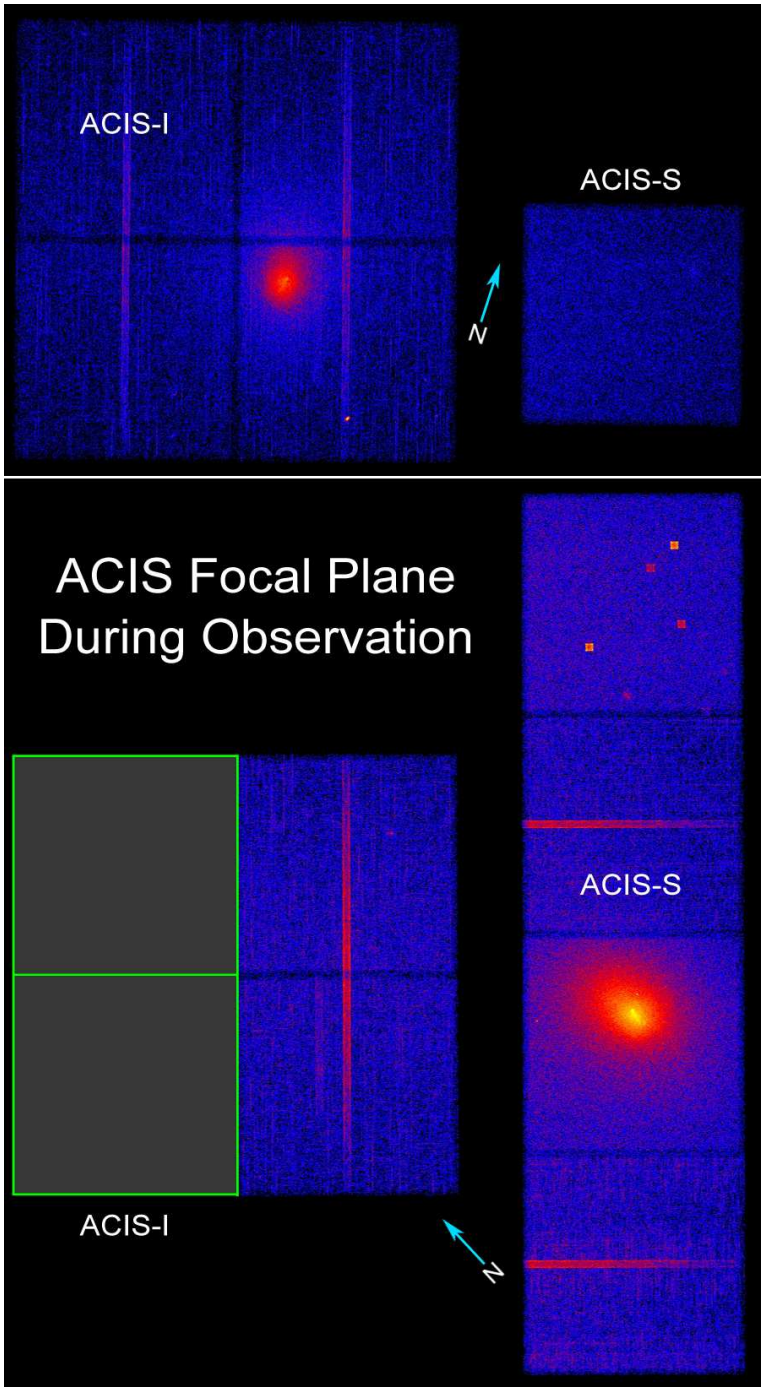

Figure 1.7 In both panels celestial North is indicated by the blue arrow. *Top panel:* ACIS-I aimed observation of Abell 1795. The image has been binned by a factor of four so the whole field could be shown. *Bottom panel:* ACIS-S aimed observation of Abell 1795. Again, the image is binned by a factor of four to show the whole field. For reference, the green boxes mark the ACIS-I chips which were off during this observation.

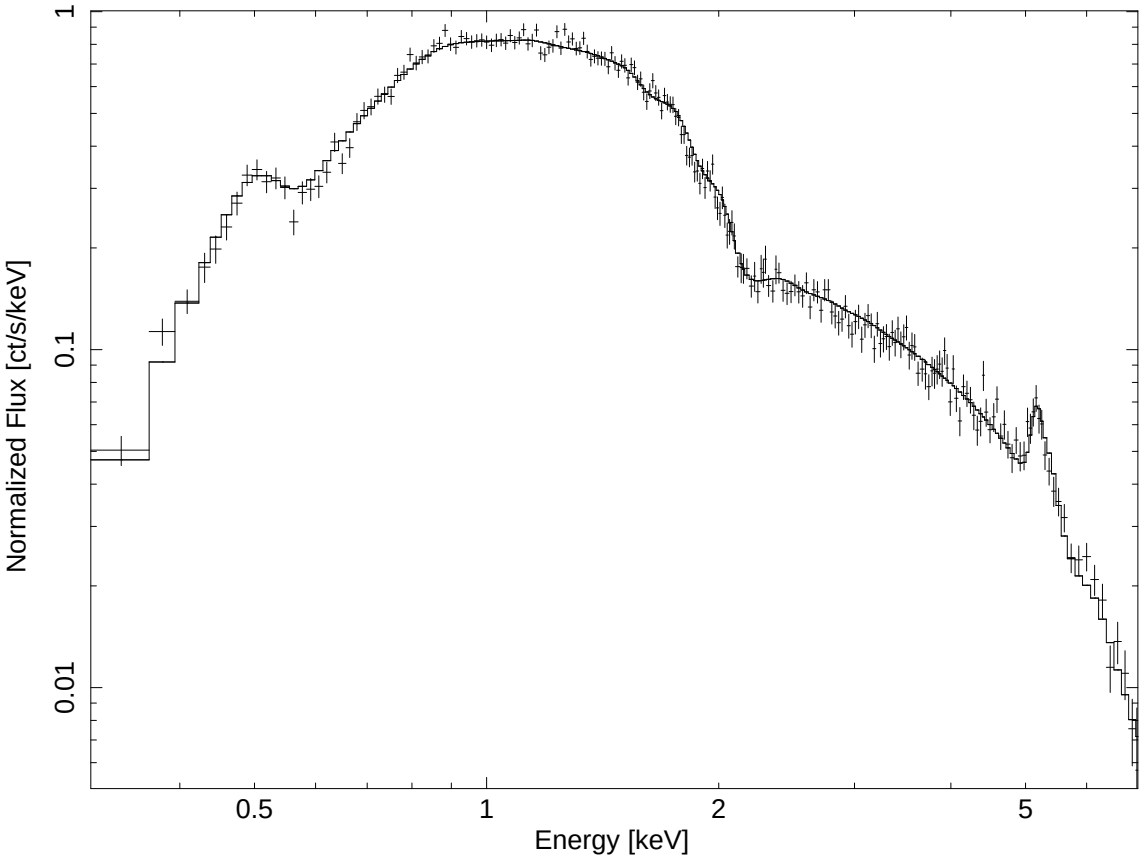

Figure 1.8 Global spectrum of the cluster Abell 1795 with the best-fit single-component absorbed thermal spectral model overplotted (solid line). Comparing this spectrum with those of Figs. 1.3 and 1.4, the effects of finite energy resolution and convolving the spectral model with instrument responses are apparent. Individual spectral lines are now blends, and the spectral shape for $E < 1.0$ keV has changed because of diminishing effective area.

1.4.2 X-ray Background and Calibration

Chandra is a magnificent piece of engineering, but it is not perfect: observations are contaminated by background, the instruments do not operate at full capacity, and the observatory has a finite lifetime. In this section I briefly discuss these areas and how they might affect past, current, and future scientific study with *Chandra*.

Cosmic X-ray Background (CXB)

Chandra is in a very high Earth orbit and is constantly bathed in high-energy, charged particles originating from the cosmos which interact with the CCDs (the eyes) and the materials housing the instruments (the skull). The CXB is composed of a soft ($E < 2$ keV) component attributable to extragalactic emission, local discrete sources, and spatially varying diffuse Galactic emission. There are also small contributions from the the "local bubble" (Snowden, 2004) and charge exchange within the solar system (Wargelin et al., 2004). The possibility of emission from unresolved point sources and other unknown CXB components also exists. In most parts of the sky the soft CXB is not a large contributor to the total background and can be modeled using a combination of power-law and thermal spectral models and then subtracted out of the data.

The CXB also has a hard ($E > 2$ keV) component which arises from mostly extragalactic sources such as quasars and is well modeled as a power-law. The spectral shape of the hard particle background has been quite stable (up until mid-2005) and thus subtracting off the emission by normalizing between observed and expected count rates in a carefully chosen energy band makes removal of the hard component straightforward.

Occasionally there are also very strong X-ray flares. These flares are quite easy to detect in observations because, for a judiciously chosen energy band/time bin combination, the count rate as a function of observation time exhibits a dramatic

spike during flaring. The time intervals containing flare episodes can be excluded from the analysis rendering them harmless. Harmless that is provided the flare was not too long and some of the observing time allotment is usable.

Instrumental Effects and Sources of Uncertainty

There are a number of instrumental effects which must be considered when analyzing data taken with *Chandra*. The geometric area of the telescope's mirrors does not represent the "usable" area of the mirrors. The true *effective area* of *Chandra* has been defined by the Chandra X-ray Center (CXC) as the product of mirror geometric area, reflectivity, off-axis vignetting, quantum efficiency of the detectors, energy resolution of the detectors, and grating efficiency (gratings were not in use during any of the observations used in this dissertation). To varying degrees, all of these components depend on energy and a few of them also have a spatial dependence. Discussion of the effective area is a lengthy and involved topic. A more concise understanding of the effective area can be attained from visualization, hence the effective area as a function of energy is shown in Figure 1.9.

The ACIS instrument is also subject to dead/bad pixels, damage done by interaction with very high-energy cosmic rays, imperfect read-out as a function of CCD location, and a hydrocarbon contaminate which has been building up since launch (Marshall et al., 2004).

Observations are also at the mercy of uncertainty sources. The data reduction software provided by the CXC (CIAO) and our own reduction pipeline (CORP, discussed in Appendix C) takes into consideration:

1. Instrumental effects and calibration
2. $\approx 3\%$ error in absolute ACIS flux calibration
3. Statistical errors in the sky and background count rates

4. Errors due to uncertainty in the background normalization

5. Error due to the $\approx 2\%$ systematic uncertainty in the background spectral shape

6. Cosmic variance of X-ray background sources

7. Unresolved source intensity

8. Scattering of source flux

The list provided above is not comprehensive, but highlights the largest sources of uncertainty: counting statistics, instrument calibration, and background. In each section of this dissertation where data analysis is discussed, the uncertainty and error analysis is discussed in the context of the science objectives.

The *Chandra* mission was scheduled for a minimum five year mission with the expectation that it would go longer. Nearing the ten year anniversary of launch, it is therefore useful to wonder how *Chandra* might be operating in years to come and what the future holds for collecting data with *Chandra* five and even ten years from now. The "life expectancy" of *Chandra* can be broken down into the categories: spacecraft health, orbit stability, instrument performance, and observation constraint evolution. Given the continued progress of understanding *Chandra*'s calibration, the relative stability of the X-ray background, and the overall health of the telescope as of last review, it has been suggested that *Chandra* will survive at least a 15 year mission, *e.g.* a decommissioning $\sim$ 2014 (Bucher, 2007, 2008).

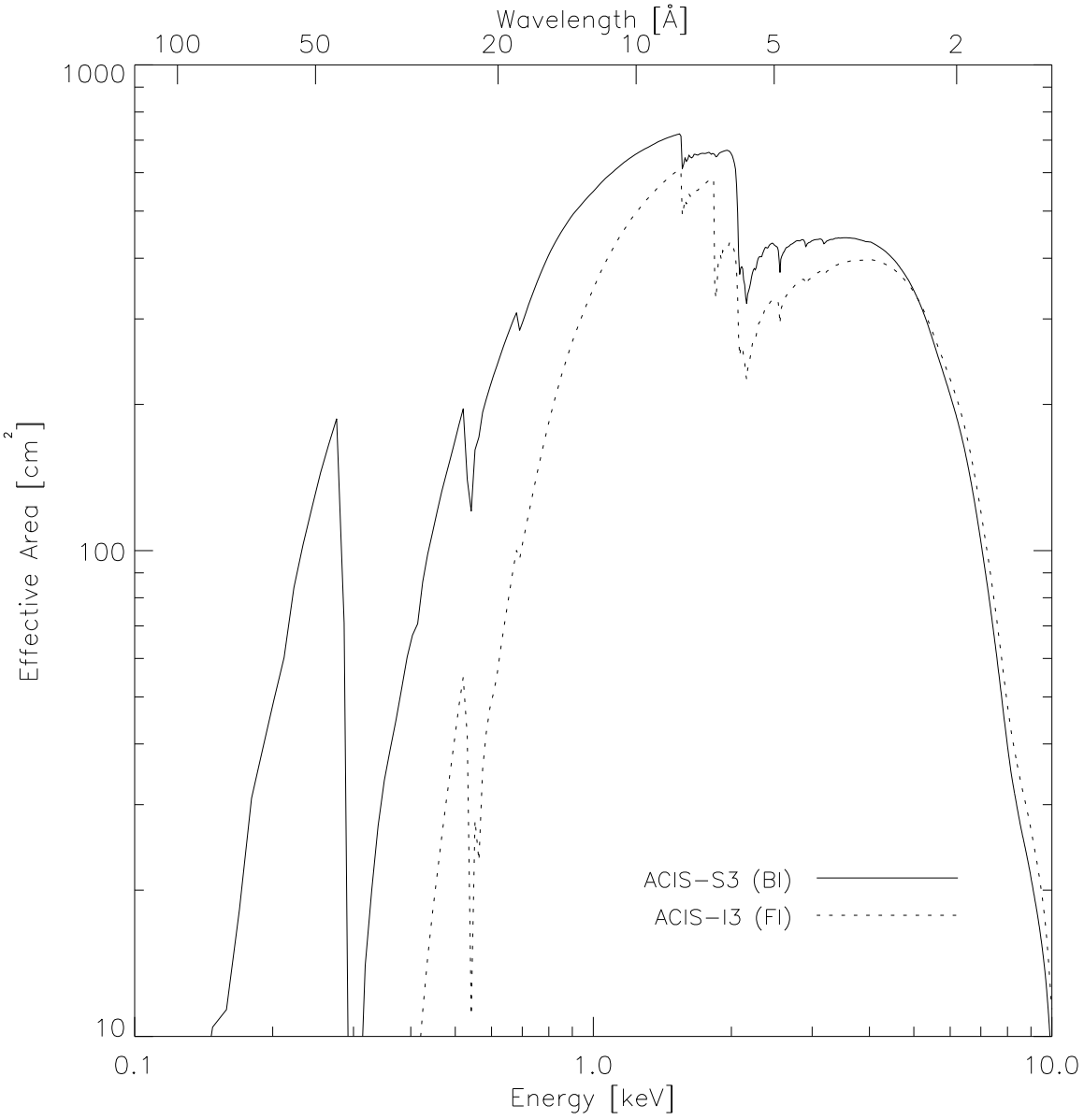

Figure 1.9 *Chandra* effective area as a function of energy. The effective area results from the product of mirror geometric area, reflectivity, off-axis vignetting, quantum efficiency of the detectors, energy resolution of the detectors, and grating efficiency. Note the ACIS peak sensitivity is in the energy range where the majority of the ICM emission occurs, $E = 0.1 - 2.0$ keV. Figure taken from the CXC.

Chapter Two

Cavagnolo, Kenneth W., Donahue, Megan, Voit, G. Mark, Sun, Ming (2008). Bandpass Dependence of X-ray Temperatures in Galaxy Clusters. The Astrophysical Journal. 682:821-830.

Chapter 2: Bandpass Dependence of X-ray Temperatures in Galaxy Clusters

2.1 Introduction

The normalization, shape, and evolution of the cluster mass function are useful for measuring cosmological parameters (*e.g.* Evrard, 1989; Wang & Steinhardt, 1998; Haiman et al., 2001; Wang et al., 2004b). In particular, the evolution of large scale structure formation provides a complementary and distinct constraint on cosmological parameters to those tests which constrain them geometrically, such as supernovae (Riess et al., 1998, 2007) and baryon acoustic oscillations (Eisenstein et al., 2005). However, clusters are a useful cosmological tool only if we can infer cluster masses from observable properties such as X-ray luminosity, X-ray temperature, lensing shear, optical luminosity, or galaxy velocity dispersion. Empirically, the correlation of mass to these observable properties is well-established (see Voit, 2005, for a review). But, there is non-negligible scatter in mass-observable scaling relations which must be accounted for if clusters are to serve as high-precision mass proxies necessary for using clusters to study cosmological parameters such as the dark energy equation of state. However, if we could identify a "second parameter" – possibly reflecting the degree of relaxation in the cluster – we could improve the utility of clusters as cosmological probes by parameterizing and reducing the scatter in mass-observable

scaling relations.

Toward this end, we desire to quantify the dynamical state of a cluster beyond simply identifying which clusters appear relaxed and those which do not. Most clusters are likely to have a dynamical state which is somewhere in between (O'Hara et al., 2006; Kravtsov et al., 2006; Ventimiglia et al., 2008). The degree to which a cluster is virialized must first be quantified within simulations that correctly predict the observable properties of the cluster. Then, predictions for quantifying cluster virialization may be tested, and possibly calibrated, with observations of an unbiased sample of clusters (*e.g.*REXCESS sample of Böhringer et al., 2007).

One study that examined how relaxation might affect the observable properties of clusters was conducted by (**?**, hereafter ME01) using the ensemble of simulations by Mohr & Evrard (1997). ME01 found that most clusters which had experienced a recent merger were cooler than the cluster mass-observable scaling relations predicted. They attributed this to the presence of cool, spectroscopically unresolved accreting subclusters which introduce energy into the ICM and have a long timescale for dissipation. The consequence was an under-prediction of cluster binding masses of $15 - 30\%$ (**?**). It is important to note that the simulations of Mohr & Evrard (1997) included only gravitational processes. The intervening years have proven that radiative cooling is tremendously important in shaping the global properties of clusters (*e.g.* McCarthy et al., 2004; Poole et al., 2006; Nagai et al., 2007). Therefore, the magnitude of the effect seen by ME01 could be somewhat different if radiative processes are included.

One empirical observational method of quantifying the degree of cluster relaxation involves using ICM substructure and employs the power in ratios of X-ray surface brightness moments (Buote & Tsai, 1995, 1996; Jeltema et al., 2005). Although an excellent tool, power ratios suffer from being aspect-dependent (Jeltema et al., 2008; Ventimiglia et al., 2008). The work of ME01 suggested a complementary measure

of substructure which does not depend on projected perspective. In their analysis, they found hard-band (2.0-9.0 keV) temperatures were $\sim 20\%$ hotter than broadband (0.5-9.0 keV) temperatures. Their interpretation was that the cooler broadband temperature is the result of unresolved accreting cool subclusters which are contributing significant amounts of line emission to the soft band ($E < 2$ keV). This effect has been studied and confirmed by Mazzotta et al. (2004) and Vikhlinin (2006) using simulated *Chandra* and *XMM-Newton* spectra.

ME01 suggested that this temperature skewing, and consequently the fingerprint of mergers, could be detected utilizing the energy resolution and soft-band sensitivity of *Chandra*. They proposed selecting a large sample of clusters covering a broad dynamical range, fitting a single-component temperature to the hard-band and broadband, and then checking for a net skew above unity in the hard-band to broadband temperature ratio. In this chapter we present the findings of just such a temperature-ratio test using *Chandra* archival data. We find the hard-band temperature exceeds the broadband temperature, on average, by $\sim 16\%$ in multiple flux-limited samples of X-ray clusters from the *Chandra* archive. This mean excess is weaker than the 20% predicted by ME01, but is significant at the 12σ level nonetheless. Hereafter, we refer to the hard-band to broadband temperature ratio as T_{HBR}. We also find that non-cool core systems and mergers tend to have higher values of T_{HBR}. Our findings suggest that T_{HBR} is an indicator of a cluster's temporal proximity to the most recent merger event.

This chapter proceeds in the following manner: In §2.2 we outline sample-selection criteria and *Chandra* observations selected under these criteria. Data reduction and handling of the X-ray background is discussed in §2.3. Spectral extraction is discussed in §2.4, while fitting and simulated spectra are discussed in §2.5. Results and discussion of our analysis are presented in §2.6. A summary of our work is presented in §2.7. For this work we have assumed a flat ΛCDM Universe with cosmology $\Omega_M = 0.3$,

$\Omega_\Lambda = 0.7$, and $H_0 = 70$ km s^{-1} Mpc^{-1}. All quoted uncertainties are at the 1.6σ level (90% confidence).

2.2 Sample Selection

Our sample was selected from observations publicly available in the *Chandra* X-ray Telescope's Data Archive (CDA). Our initial selection pass came from the *ROSAT* Brightest Cluster Sample (Ebeling et al., 1998), RBC Extended Sample (Ebeling et al., 2000), and *ROSAT* Brightest 55 Sample (Edge et al., 1990; Peres et al., 1998). The portion of our sample at $z \gtrsim 0.4$ can also be found in a combination of the *Einstein* Extended Medium Sensitivity Survey (Gioia et al., 1990), North Ecliptic Pole Survey (Henry et al., 2006), *ROSAT* Deep Cluster Survey (Rosati et al., 1995), *ROSAT* Serendipitous Survey (Vikhlinin et al., 1998), and Massive Cluster Survey (Ebeling et al., 2001). We later extended our sample to include clusters found in the REFLEX Survey (Böhringer et al., 2004). Once we had a master list of possible targets, we cross-referenced this list with the CDA and gathered observations where a minimum of R_{5000} (defined below) is fully within the CCD field of view.

R_{Δ_c} is defined as the radius at which the average cluster density is Δ_c times the critical density of the Universe, $\rho_c = 3H(z)^2/8\pi G$. For our calculations of R_{Δ_c} we adopt the relation from Arnaud et al. (2002):

$$\begin{aligned} R_{\Delta_c} &= 2.71 \text{ Mpc } \beta_T^{1/2} \Delta_z^{-1/2} (1+z)^{-3/2} \left(\frac{kT_X}{10 \text{ keV}} \right)^{1/2} \\ \Delta_z &= \frac{\Delta_c \Omega_M}{18\pi^2 \Omega_z} \\ \Omega_z &= \frac{\Omega_M (1+z)^3}{[\Omega_M (1+z)^3] + [(1-\Omega_M - \Omega_\Lambda)(1+z)^2] + \Omega_\Lambda} \end{aligned} \tag{2.1}$$

where R_{Δ_c} is in units of h_{70}^{-1}, Δ_c is the assumed density contrast of the cluster at R_{Δ_c}, and β_T is a numerically determined, cosmology-independent ($\lesssim \pm 20\%$) normalization

for the virial relation $GM/2R = \beta_T kT_{virial}$. We use $\beta_T = 1.05$ taken from Evrard et al. (1996).

The result of our CDA search was a total of 374 observations of which we used 244 for 202 clusters. The clusters making up our sample cover a redshift range of $z = 0.045 - 1.24$, a temperature range of $T_X = 2.6 - 19.2$ keV, and bolometric luminosities of $L_{bol} = 0.12 - 100.4 \times 10^{44}$ ergs s^{-1}. The bolometric ($E = 0.1 - 100$ keV) luminosities for our sample clusters plotted as a function of redshift are shown in Figure 2.1. These L_{bol} values are calculated from our best-fit spectral models and are limited to the region of the spectral extraction (from $R = 70$ kpc to $R = R_{2500}$, or R_{5000} in the cases in which no R_{2500} fit was possible). Basic properties of our sample are listed in Table A.1.

For the sole purpose of defining extraction regions based on fixed overdensities as discussed in §2.4, fiducial temperatures (measured with *ASCA*) and redshifts were taken from Horner (2001) (all redshifts confirmed with NED[1]). We show below that the *ASCA* temperatures are sufficiently close to the *Chandra* temperatures such that R_{Δ_c} is reliably estimated to within 20%. Note that R_{Δ_c} is proportional to $T^{1/2}$, so that a 20% error in the temperature leads to only a 10% error in R_{Δ_c}, which in turn has no detectable effect on our final results. For clusters not listed in Horner (2001) , we used a literature search to find previously measured temperatures. If no published value could be located, we measured the global temperature by recursively extracting a spectrum in the region $0.1 < r < 0.2R_{500}$ fitting a temperature and recalculating R_{500}. This process was repeated until three consecutive iterations produced R_{500} values which differed by $\leq 1\sigma$. This method of temperature determination has been employed in other studies, see Sanderson et al. (2006) and Henry et al. (2006) as examples.

[1]http://nedwww.ipac.caltech.edu/

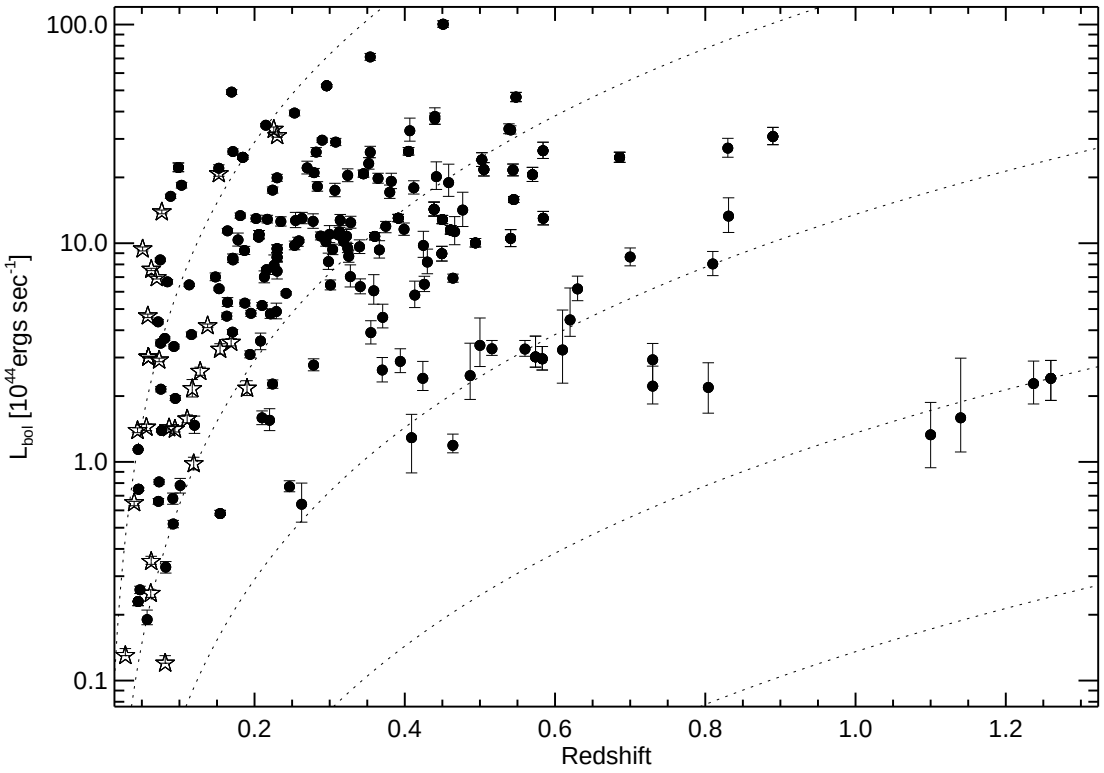

Figure 2.1 Bolometric luminosity ($E = 0.1 - 100$ keV) plotted as a function of redshift for the 202 clusters which make up the initial sample. L_{bol} values are limited to the region of spectral extraction, $R = R_{2500-\mathrm{CORE}}$. For clusters without $R_{2500-\mathrm{CORE}}$ fits, $R = R_{5000-\mathrm{CORE}}$ fits were used and are denoted in the figure by empty stars. Dotted lines represent constant fluxes of 3.0×10^{-15}, 10^{-14}, 10^{-13}, and 10^{-12}erg s^{-1} cm^{-2}.

2.3 *Chandra* Data

2.3.1 Reprocessing and Reduction

All data sets were reduced using the *Chandra*} Interactive Analysis of Observations package (CIAO) and accompanying Calibration Database (CalDB). Using CIAO 3.3.0.1 and CalDB 3.2.2, standard data analysis was followed for each observation to apply the most up-to-date time-dependent gain correction and when appropriate, charge transfer inefficiency correction (Townsley et al., 2000).

Point sources were identified in an exposure-corrected events file using the adaptive wavelet tool wavdetect (Freeman et al., 2002). A 2σ region surrounding each point source was automatically output by wavdetect to define an exclusion mask. All point sources were then visually confirmed and we added regions for point sources which were missed by wavdetect and deleted regions for spuriously detected "sources." Spurious sources are typically faint CCD features (chip gaps and chip edges) not fully removed after dividing by the exposure map. This process resulted in an events file (at "level 2") that has been cleaned of point sources.

To check for contamination from background flares or periods of excessively high background, light curve analysis was performed using Maxim Markevitch's contributed CIAO script lc_clean.sl[2]. Periods with count rates $\geq 3\sigma$ and/or a factor ≥ 1.2 of the mean background level of the observation were removed from the good time interval file. As prescribed by Markevitch's cookbook[3], ACIS front-illuminated (FI) chips were analyzed in the $0.3 - 12.0$ keV range, and the $2.5 - 7.0$ keV energy range for the ACIS back-illuminated (BI) chips.

When a FI and BI chip were both active during an observation, we compared light curves from both chips to detect long duration, soft-flares which can go undetected on the FI chips but show up on the BI chips. While rare, this class of flare must

[2]http://cxc.harvard.edu/contrib/maxim/acisbg/
[3]http://cxc.harvard.edu/contrib/maxim/acisbg/COOKBOOK

be filtered out of the data, as it introduces a spectral component which artificially increases the best-fit temperature via a high energy tail. We find evidence for a long duration soft flare in the observations of Abell 1758 (David & Kempner, 2004), CL J2302.8+0844, and IRAS 09104+4109. These flares were handled by removing the time period of the flare from the GTI file.

Defining the cluster "center" is essential for the later purpose of excluding cool cores from our spectral analysis (see §2.4). To determine the cluster center, we calculated the centroid of the flare cleaned, point-source free level-2 events file filtered to include only photons in the $0.7 - 7.0$ keV range. Before centroiding, the events file was exposure-corrected and "holes" created by excluding point sources were filled using interpolated values taken from a narrow annular region just outside the hole (holes are not filled during spectral extraction discussed in §2.4). Prior to centroiding, we defined the emission peak by heavily binning the image, finding the peak value within a circular region extending from the peak to the chip edge (defined by the radius R_{max}), reducing R_{max} by 5%, reducing the binning by a factor of 2, and finding the peak again. This process was repeated until the image was unbinned (binning factor of 1). We then returned to an unbinned image with an aperture centered on the emission peak with a radius R_{max} and found the centroid using CIAO's DMSTAT. The centroid, (x_c, y_c), for a distribution of N good pixels with coordinates (x_i, y_j) and values f(x_i,y_j) is defined as:

$$\begin{aligned} Q &= \sum_{i,j=1}^{N} f(x_i, y_i) \\ x_c &= \frac{\sum_{i,j=1}^{N} x_i \cdot f(x_i, y_i)}{Q} \\ y_c &= \frac{\sum_{i,j=1}^{N} y_i \cdot f(x_i, y_i)}{Q}. \end{aligned} \tag{2.2}$$

If the centroid was within 70 kpc of the emission peak, the emission peak was

selected as the center, otherwise the centroid was used as the center. This selection was made to ensure all "peaky" cool cores coincided with the cluster center, thus maximizing their exclusion later in our analysis. All cluster centers were additionally verified by eye.

2.3.2 X-ray Background

Because we measured a global cluster temperature, specifically looking for a temperature ratio shift in energy bands which can be contaminated by the high-energy particle background or the soft local background, it was important to carefully analyze the background and subtract it from our source spectra. Below we outline three steps taken in handling the background: customization of blank-sky backgrounds, re-normalization of these backgrounds for variation of hard-particle count rates, and fitting of soft background residuals.

We used the blank-sky observations of the X-ray background from Markevitch et al. (2001) and supplied within the CXC CalDB. First, we compared the flux from the diffuse soft X-ray background of the *ROSAT* All-Sky Survey (*RASS*) combined bands $R12$, $R45$, and $R67$ to the 0.7-2.0 keV flux in each extraction aperture for each observation. *RASS* combined bands give fluxes for energy ranges of 0.12-0.28, 0.47-1.21, and 0.76-2.04 keV respectively corresponding to $R12$, $R45$, and $R67$. For the purpose of simplifying subsequent analysis, we discarded observations with an $R45$ flux $\geq 10\%$ of the total cluster X-ray flux.

The appropriate blank-sky dataset for each observation was selected from the CalDB, reprocessed exactly as the observation was, and then reprojected using the aspect solutions provided with each observation. For observations on the ACIS-I array, we reprojected blank-sky backgrounds for chips I0-I3 plus chips S2 and/or S3. For ACIS-S observations, we created blank-sky backgrounds for the target chip, plus chips I2 and/or I3. The additional off aim-point chips were included only if they were

active during the observation and had available blank-sky data sets for the observation time period. Off aim-point chips were cleaned for point sources and diffuse sources using the method outlined in §2.3.1.

The additional off aim-point chips were included in data reduction since they contain data which is farther from the cluster center and are therefore more useful in analyzing the observation background. For observations which did not have a matching off aim-point blank-sky background, a source-free region of the active chips is located and used for background normalization. To normalize the hard particle component we measured fluxes for identical regions in the blank-sky field and target field in the 9.5-12.0 keV range. The effective area of the ACIS arrays above 9.5 keV is approximately zero, and thus the collected photons there are exclusively from the particle background.

A histogram of the ratios of the 9.5-12.0 keV count rate from an observation's off aim-point chip to that of the observation specific blank-sky background are presented in Figure 2.2. The majority of the observations are in agreement to $\lesssim 20\%$ of the blank-sky background rate, which is small enough to not affect our analysis. Even so, we re-normalized all blank-sky backgrounds to match the observed background.

Normalization brings the observation background and blank-sky background into agreement for $E > 2$ keV, but even after normalization, typically, there may exist a soft excess/deficit associated with the spatially varying soft Galactic background. Following the technique detailed in Vikhlinin et al. (2005), we constructed and fit soft residuals for this component. For each observation we subtracted a spectrum of the blank-sky field from a spectrum of the off aim-point field to create a soft residual. The residual was fit with a solar abundance, zero-redshift MeKaL model (Mewe et al., 1985, 1986; Liedahl et al., 1995) in which the normalization was allowed to be negative. The resulting best-fit temperatures for all of the soft residuals identified here were between 0.2-1.0 keV, which is in agreement with results of Vikhlinin et al.

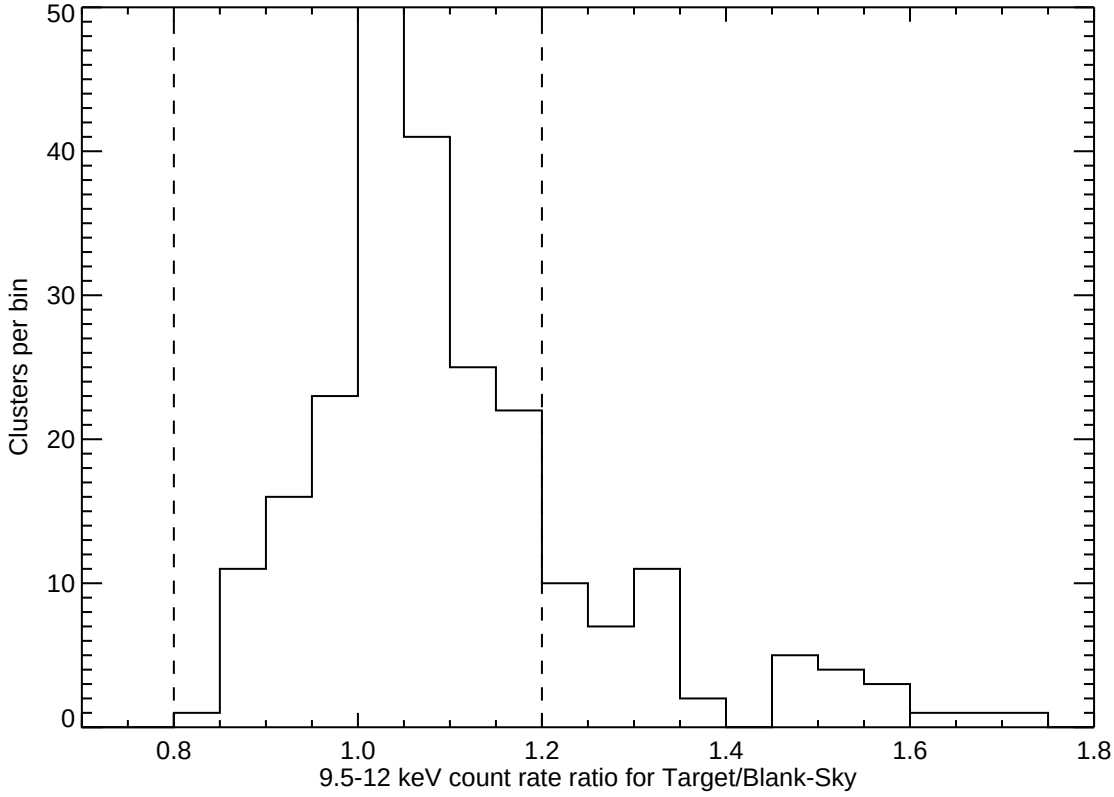

Figure 2.2 Ratio of target field and blank-sky field count rates in the 9.5-12.0 keV band for all 244 observations in our initial sample. Vertical dashed lines represent $\pm 20\%$ of unity. Despite the good agreement between the blank-sky background and observation count rates for most observations, all backgrounds are normalized.

(2005). The model normalization of this background component was then scaled to the cluster sky area. The re-scaled component was included as a fixed background component during fitting of a cluster's spectra.

2.4 Spectral Extraction

The simulated spectra calculated by ME01 were analyzed in a broad energy band of $0.5 - 9.0$ keV and a hard energy band of $2.0_{\rm rest} - 9.0$ keV, but to make a reliable comparison with *Chandra* data we used narrower energy ranges of 0.7-7.0 keV for the broad energy band and $2.0_{\rm rest} - 7.0$ keV for the hard energy band. We excluded data below 0.7 keV to avoid the effective area and quantum efficiency variations of the ACIS detectors, and excluded energies above 7.0 keV in which diffuse source emission is dominated by the background and where *Chandra*'s effective area is small. We also accounted for cosmic redshift by shifting the lower energy boundary of the hard-band from 2.0 keV to $2.0/(1+z)$ keV (henceforth, the 2.0 keV cut is in the rest frame).

ME01 calculated the relation between $T_{0.5-9.0}$ and $T_{2.0-9.0}$ using apertures of R_{200} and R_{500} in size. While it is trivial to calculate a temperature out to R_{200} or R_{500} for a simulation, such a measurement at these scales is extremely difficult with *Chandra* observations (see Vikhlinin et al. (2005) for a detailed example). Thus, we chose to extract spectra from regions with radius R_{5000}, and R_{2500} when possible. Clusters analyzed only within R_{5000} are denoted in Table A.1 by a double dagger (‡).

The cores of some clusters are dominated by gas at $\lesssim T_{virial}/2$ which can greatly affect the global best-fit temperature; therefore, we excised the central 70 kpc of each aperture. These excised apertures are denoted by "-CORE" in the text. Recent work by Maughan (2007) has shown excising 0.15 R_{500} rather than a static 70 kpc reduces scatter in mass-observable scaling relations. However, our smaller excised region seems sufficient for this investigation because for cool core clusters the average radial temperature at $r > 70$ kpc is approximately isothermal (Vikhlinin et al., 2005).

Indeed, we find that cool core clusters have smaller than average T_{HBR} when the 70 kpc region has been excised (§2.6.3).

Although some clusters are not circular in projection, but rather are elliptical or asymmetric, we found that assuming spherical symmetry and extracting spectra from a circular annulus did not significantly change the best-fit values. For another such example see Bauer et al. (2005).

After defining annular apertures, we extracted source spectra from the target cluster and background spectra from the corresponding normalized blank-sky dataset. By standard CIAO means we created weighted effective area functions (WARFs) and redistribution matrices (WRMFs) for each cluster using a flux-weighted map (WMAP) across the entire extraction region. The WMAP was calculated over the energy range 0.3-2.0 keV to weight calibrations that vary as a function of position on the chip. The CCD characteristics which affect the analysis of extended sources, such as energy dependent vignetting, are contained within these files. Each spectrum was then binned to contain a minimum of 25 counts per channel.

2.5 Spectral Analysis

2.5.1 Fitting

Spectra were fit with XSPEC 11.3.2ag (Arnaud, 1996) using a single-temperature MeKaL model in combination with the photoelectric absorption model WABS (Morrison & McCammon, 1983) to account for Galactic absorption. Galactic absorption values, N_H, are taken from Dickey & Lockman (1990). The potentially free parameters of the absorbed thermal model are N_H, X-ray temperature (T_X), metal abundance normalized to solar (elemental ratios taken from Anders & Grevesse, 1989), and a normalization proportional to the integrated emission measure of the cluster. Results from the fitting are presented in Tables A.3 and A.4. No systematic error

is added during fitting, and thus all quoted errors are statistical only. The statistic used during fitting was χ^2 (XSPEC statistics package CHI). Every cluster analyzed was found to have greater than 1500 background-subtracted source counts in the spectrum.

For some clusters, more than one observation was available in the archive. We utilized the power of the combined exposure time by first extracting independent spectra, WARFs, WRMFs, normalized background spectra, and soft residuals for each observation. Then, these independent spectra were read into XSPEC simultaneously and fit with one spectral model which had all parameters, except normalization, tied among the spectra. The simultaneous fit is what is reported for these clusters, denoted by a star ($\star$), in Tables A.3 and A.4.

Additional statistical error was introduced into the fits because of uncertainty associated with the soft local background component discussed in §2.3.2. To estimate the sensitivity of our best-fit temperatures to this uncertainty, we used the differences between T_X for a model using the best-fit soft background normalization and T_X for models using $\pm 1\sigma$ of the soft background normalization. The statistical uncertainty of the original fit and the additional uncertainty inferred from the range of normalizations to the soft X-ray background component were then added in quadrature to produce a final error. In all cases this additional background error on the temperature was less than 10% of the total statistical error, and therefore represents a minor inflation of the error budget.

When comparing fits with fixed Galactic column density with those where it was a free parameter, we found that neither the goodness of fit per free parameter nor the best-fit T_X were significantly different. Thus, N_H was fixed at the Galactic value with the exception of three cases: Abell 399 (Sakelliou & Ponman, 2004), Abell 520, and Hercules A. For these three clusters N_H is a free parameter. In all fits, the metal abundance was a free parameter.

After fitting we rejected several data sets as their best-fit $T_{2.0-7.0}$ had no upper bound in the 90% confidence interval and thus were insufficient for our analysis. All fits for the clusters Abell 781, Abell 1682, CL J1213+0253, CL J1641+4001, IRAS 09104+4109, Lynx E, MACS J1824.3+4309, MS 0302.7+1658, and RX J1053+5735 were rejected. We also removed Abell 2550 from our sample after finding it to be an anomalously cool ($T_X \sim 2$ keV) "cluster". In fact, Abell 2550 is a line-of-sight set of groups, as discussed by Martini et al. (2004). After these rejections, we are left with a final sample of 192 clusters which have $R_{2500-\mathrm{CORE}}$ fits and 166 clusters which have $R_{5000-\mathrm{CORE}}$ fits.

2.5.2 Simulated Spectra

To quantify the effect a second, cooler gas component would have on the fit of a single-component spectral model, we created an ensemble of simulated spectra for each real spectrum in our entire sample using XSPEC. With these simulated spectra we sought to answer the question: Given the count level in each observation of our sample, how bright must a second temperature component be for it to affect the observed temperature ratio? Put another way, we asked at what flux ratio a second gas phase produces a temperature ratio, T_{HBR}, of greater than unity with 90% confidence.

We began by adding the observation-specific background to a convolved, absorbed thermal model with two temperature components observed for a time period equal to the actual observation's exposure time and adding Poisson noise. For each realization of an observation's simulated spectrum, we defined the primary component to have the best-fit temperature and metallicity of the $R_{2500-\mathrm{CORE}}$ 0.7-7.0 keV fit, or $R_{5000-\mathrm{CORE}}$ if no $R_{2500-\mathrm{CORE}}$ fit was performed. We then incremented the secondary component temperature over the values 0.5, 0.75, 1.0, 2.0, and 3.0 keV. The metallicity of the secondary component was fixed and set equal to the metallicity of

the primary component.

We adjusted the normalization of the simulated two-component spectra to achieve equivalent count rates to those in the real spectra. The sum of normalizations can be expressed as $N = N_1 + \xi N_2$. We set the secondary component normalization to $N_2 = \xi N_{bf}$, where N_{bf} is the best-fit normalization of the appropriate 0.7-7.0 keV fit and ξ is a preset factor taking the values 0.4, 0.3, 0.2, 0.15, 0.1, and 0.05. The primary component normalization, N_1, was determined through an iterative process to make real and simulated spectral count rates match. The parameter ξ therefore represents the fractional contribution of the cooler component to the overall count rate.

There are many systematics at work in the full ensemble of observation specific simulated spectra, such as redshift, column density, and metal abundance. Thus as a further check of spectral sensitivity to the presence of a second gas phase, we simulated additional spectra for the case of an idealized observation. We followed a similar procedure to that outlined above, but in this instance we used a finer temperature and ξ grid of $T_2 = 0.5 \rightarrow 3.0$ in steps of 0.25 keV, and $\xi = 0.02 \rightarrow 0.4$ in steps of 0.02. The input spectral model was $N_H = 3.0 \times 10^{20}$ cm^{-2}, $T_1 = 5$ keV, $Z/Z_\odot = 0.3$ and $z = 0.1$. We also varied the exposure times such that the total number of counts in the 0.7-7.0 keV band was 15K, 30K, 60K, or 120K. For these spectra we used the on-axis sample response files provided to Cycle 10 proposers[4]. Poisson noise is added, but no background is considered.

We also simulated a control sample of single-temperature models. The control sample is simply a simulated version of the best-fit model. This control provides us with a statistical test of how often the actual hard-component temperature might differ from a broadband temperature fit if calibration effects are under control. Fits for the control sample are shown in the far right panels of Figure 2.3.

[4]http://cxc.harvard.edu/caldb/prop_plan/imaging/index.html

For each observation, we have 65 total simulated spectra: 35 single-temperature control spectra and 30 two-component simulated spectra (5 secondary temperatures, each with six different ξ). Our resulting ensemble of simulated spectra contains 12,765 spectra. After generating all the spectra we followed the same fitting routine detailed in §2.5.1.

With the ensemble of simulated spectra we then asked the question: for each T_2 and ΔT_X (defined as the difference between the primary and secondary temperature components) what is the minimum value of ξ, called ξ_{min}, that produces $T_{HBR} \geq 1.1$ at 90% confidence? From our analysis of these simulated spectra we have found these important results:

1. In the control sample, a single-temperature model rarely ($\sim$ 2% of the time) gives a significantly different $T_{0.7-7.0}$ and $T_{2.0-7.0}$. The weighted average (Fig. 2.3, right panels) for the control sample is 1.002 ± 0.001 and the standard deviation is ± 0.044. The T_{HBR} distribution for the control sample appears to have an intrinsic width which is likely associated with statistical noise of fitting in XSPEC (Dupke, private communication). This result indicates that our remaining set of observations is statistically sound, *e.g.* our finding that T_{HBR} significantly differs from 1.0 cannot result from statistical fluctuations alone.

2. Shown in Table 2.1 are the contributions a second cooler component must make in the case of the idealized spectra in order to produce $T_{HBR} \geq 1.1$ at 90% confidence. In general, the contribution of cooler gas must be $> 10\%$ for $T_2 < 2$ keV to produce T_{HBR} as large as 1.1. The increase in percentages at $T_2 <$ 1.0 keV is owing to the energy band we consider (0.7-7.0 keV) as gas cooler than 0.7 keV must be brighter than at 1.0 keV in order to make an equivalent contribution to the soft end of the spectrum at 0.7 keV.

3. In the full ensemble of observation-specific simulated spectra, we find a great

deal of statistical scatter in ξ_{min} at any given ΔT_X. This was expected as the full ensemble is a superposition of spectra with a broad range of total counts, N_H, redshifts, abundance, and backgrounds. But using the idealized simulated spectra as a guide, we find for those spectra with $N_{\rm counts} \gtrsim 15000$, producing $T_{HBR} \geq 1.1$ at 90% confidence again requires the cooler gas to be contributing $> 10\%$ of the emission. These results are also summarized in Table 2.1. The good agreement between the idealized and observation-specific simulated spectra indicates that while many more factors are in play for the observation-specific spectra, they do not degrade our ability to reliably measure $T_{HBR} > 1.1$. The trend here of a common soft component sufficient to change the temperature measurement in a single-temperature model is statistical, a result that comes from an aggregate view of the sample rather than any individual fit.

4. As redshift increases, gas cooler than 1.0 keV is slowly redshifted out of the observable X-ray band. As expected, we find from our simulated spectra that for $z \geq 0.6$, T_{HBR} is no longer statistically distinguishable from unity. In addition, the $T_{2.0-7.0}$ lower boundary nears convergence with the $T_{0.7-7.0}$ lower boundary as z increases, and for $z = 0.6$, the hard-band lower limit is 1.25 keV, while at the highest redshift considered, $z = 1.2$, the hard-band lower limit is only 0.91 keV. For the 14 clusters with $z \geq 0.6$ in our real sample we are most likely underestimating the actual amount of temperature inhomogeneity. We have tested the effect of excluding these clusters on our results, and find a negligible change in the overall skew of T_{HBR} to greater than unity.

Table 2.1: Summary of two-component simulations

Idealized Spectra		Observation-Specific Spectra	
T_2 keV	ξ_{min}	T_2 keV	ξ_{min}
0.50	$\geq 12\% \pm 4\%$	0.50	$\geq 14.5\% \pm 0.1\%$
0.75	$\geq 12\% \pm 4\%$	0.75	$\geq 11.7\% \pm 0.1\%$
1.00	$\geq 8\% \pm 3\%$	1.00	$\geq 11.6\% \pm 0.1\%$
1.25	$\geq 17\% \pm 3\%$	-	-
1.50	$\geq 23\% \pm 5\%$	-	-
1.75	$\geq 28\% \pm 4\%$	-	-
2.00	none	2.00	$\geq 25.5\% \pm 0.1\%$
3.00	none	3.00	$\geq 28.9\% \pm 0.1\%$

Table 2.1 summarizes the results of the two temperature component spectra simulations for the ideal and observation-specific cases (see §2.5.2 for details). The parameter ξ_{min} represents the minimum fractional contribution of the cooler component, T_2, to the overall count rate in order to produce $T_{HBR} \geq 1.1$ at 90% confidence. The results for the observation-specific spectra are for spectra with $N_{\rm counts} > 15,000$.

2.6 Results and Discussion

2.6.1 Temperature Ratios

For each cluster we have measured a ratio of the hard-band to broadband temperature defined as $T_{HBR} = T_{2.0-7.0}/T_{0.7-7.0}$. We find that the mean T_{HBR} for our entire sample is greater than unity at more than 12σ significance. The weighted mean values for our sample are shown in Table 2.2. Quoted errors in Table 2.2 are standard deviation of the mean calculated using an unbiased estimator for weighted samples. Simulated sample has been culled to include only T_2=0.75 keV. Presented in Figure 2.3 are the binned weighted means and raw T_{HBR} values for $R_{2500-\rm CORE}$, $R_{5000-\rm CORE}$, and the simulated control sample. The peculiar points with $T_{HBR} <$ 1 are all statistically consistent with unity. The presence of clusters with $T_{HBR} =$

1 suggests that systematic calibration uncertainties are not the sole reason for deviations of T_{HBR} from 1. We also find that the temperature ratio does not depend on the best-fit broadband temperature, and that the observed dispersion of T_{HBR} is greater than the predicted dispersion arising from systematic uncertainties.

The uncertainty associated with each value of T_{HBR} is dominated by the larger error in $T_{2.0-7.0}$, and on average, $\Delta T_{2.0-7.0} \approx 2.3\Delta T_{0.7-7.0}$. This error interval discrepancy naturally results from excluding the bulk of a cluster's emission which occurs below 2 keV. While choosing a temperature-sensitive cut-off energy for the hard-band (other than 2.0 keV) might maintain a more consistent error budget across our sample, we do not find any systematic trend in T_{HBR} or the associated errors with cluster temperature.

Table 2.2: Weighted averages for various apertures

	..... Without Core			..... With Core		
	[0.7-7.0]	[2.0-7.0]	T_{HBR}	[0.7-7.0]	[2.0-7.0]	T_{HBR}
Aperture	keV	keV		keV	keV	
R_{2500}	4.93±0.03	6.24±0.07	1.16±0.01	4.47±0.02	5.45±0.05	1.13±0.01
R_{5000}	4.75±0.02	5.97±0.07	1.14±0.01	4.27±0.02	5.29±0.05	1.14±0.01
Simulated	3.853±0.004	4.457±0.009	1.131±0.002	-	-	-
Control	4.208±0.003	4.468±0.006	1.002±0.001	-	-	-

2.6.2 Systematics

In this study we have found the average value of T_{HBR} is significantly greater than one and that $\sigma_{HBR} > \sigma_{\rm control}$, with the latter result being robust against systematic uncertainties. As predicted by ME01, both of these results are expected to arise naturally from the hierarchical formation of clusters. But systematic uncertainty related to *Chandra* instrumentation or other sources could shift the average value of T_{HBR} one would get from "perfect" data. In this section we consider some additional sources of uncertainty. 5A First, the disagreement between *XMM-Newton*

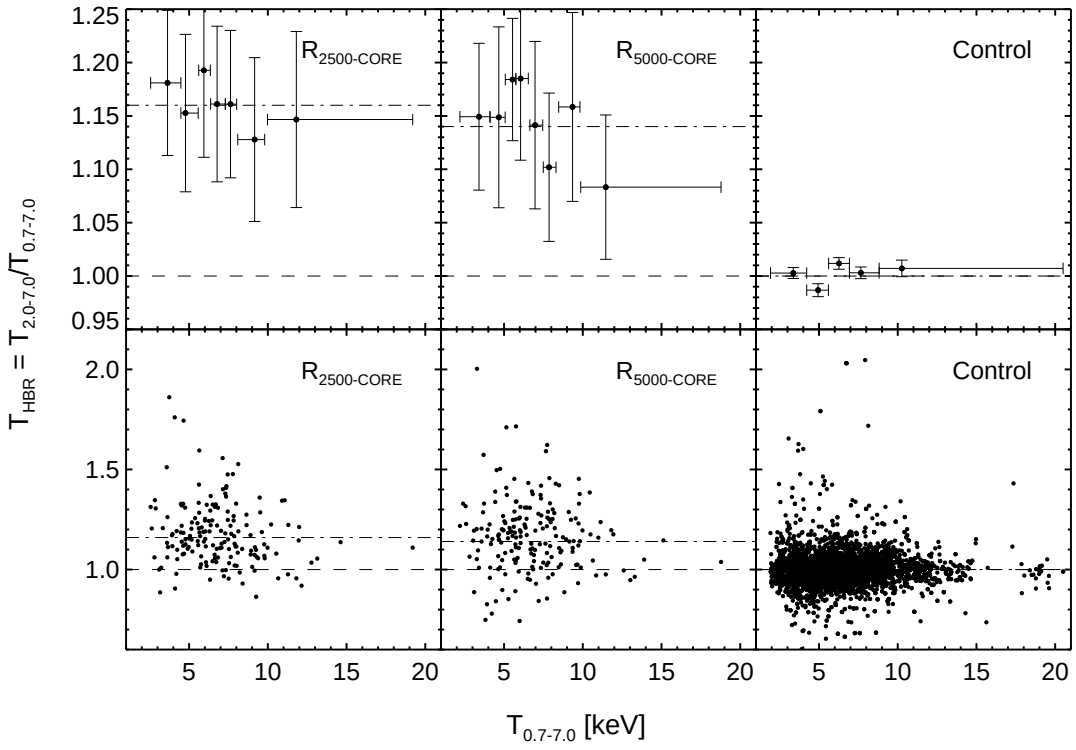

Figure 2.3 Best-fit temperatures for the hard-band, $T_{2.0-7.0}$, divided by the broad-band, $T_{0.7-7.0}$, and plotted against the broadband temperature. For binned data, each bin contains 25 clusters, with the exception of the highest temperature bins which contain 16 and 17 for $R_{2500-\mathrm{CORE}}$ and $R_{5000-\mathrm{CORE}}$, respectively. The simulated data bins contain 1000 clusters with the last bin having 780 clusters. The line of equality is shown as a dashed line and the weighted mean for the full sample is shown as a dashed-dotted line. Error bars are omitted in the unbinned data for clarity. Note the net skewing of T_{HBR} to greater than unity for both apertures with no such trend existing in the simulated data. The dispersion of T_{HBR} for the real data is also much larger than the dispersion of the simulated data.

and *Chandra* cluster temperatures has been noted in several independent studies, i.e. Vikhlinin et al. (2005) and Snowden et al. (2008). But the source of this discrepancy is not well understood and efforts to perform cross-calibration between *XMM-Newton* and *Chandra* have thus far not been conclusive. One possible explanation is poor calibration of *Chandra* at soft X-ray energies which may arise from a hydrocarbon contaminant on the High Resolution Mirror Assembly (HRMA) similar in nature to the contaminant on the ACIS detectors (Marshall et al., 2004). We have assessed this possibility by looking for systematic trends in T_{HBR} with time or temperature, as such a contaminant would most likely have a temperature and/or time dependence.

As noted in §2.6.1 and seen in Figure 2.3, we find no systematic trend with temperature either for the full sample or for a sub-sample of single-observation clusters with $> 75\%$ of the observed flux attributable to the source (higher S/N observations will be more affected by calibration uncertainty). Plotted in the lower-left pane of Figures 2.4 and 2.5 is T_{HBR} versus time for single observation clusters (clusters with multiple observations are fit simultaneously and any time effect would be washed out) where the spectral flux is $> 75\%$ from the source. We find no significant systematic trend in T_{HBR} with time, which suggests that if T_{HBR} is affected by any contamination of *Chandra*'s HRMA, then the contaminant is most likely not changing with time. Our conclusion on this matter is that the soft calibration uncertainty is not playing a dominant role in our results.

Aside from instrumental and calibration effects, some other possible sources of systematic error are S/N, redshift selection, Galactic absorption, and metallicity. Also presented in Figures 2.4 and 2.5 are three of these parameters versus T_{HBR} for $R_{2500-\mathrm{CORE}}$ and $R_{5000-\mathrm{CORE}}$, respectively. The trend in T_{HBR} with redshift is expected as the $2.0/(1+z)$ keV hard-band lower boundary nears convergence with the 0.7 keV broadband lower boundary at $z \approx 1.85$. We find no systematic trends of T_{HBR} with S/N or Galactic absorption, which might occur if the skew in T_{HBR}

were a consequence of poor count statistics, inaccurate Galactic absorption, or very poor calibration. In addition, the ratio of T_{HBR} for $R_{2500-\mathrm{CORE}}$ to $R_{5000-\mathrm{CORE}}$ for every cluster in our sample does not significantly deviate from unity. Our results are robust to changes in aperture size.

Also shown in Figures 2.4 and 2.5 are the ratios of *ASCA* temperatures taken from Horner (2001) to *Chandra* temperatures derived in this work. The spurious point below 0.5 with very large error bars is MS 2053.7-0449, which has a poorly constrained *ASCA* temperature of $10.03^{+8.73}_{-3.52}$. Our value of ~ 3.5 keV for this cluster is in agreement with the recent work of Maughan et al. (2008). Not all our sample clusters have an *ASCA* temperature, but a sufficient number (53) are available to make this comparison reliable. Apertures used in the extraction of *ASCA* spectra had no core region removed and were substantially larger than R_{2500}. *ASCA* spectra were also fit over a broader energy range (0.6-10 keV) than we use here. Nonetheless, our temperatures are in good agreement with those from *ASCA*, but we do note a trend of comparatively hotter *Chandra* temperatures for $T_{Chandra} > 10$ keV. For both apertures, the clusters with $T_{Chandra} > 10$ keV are Abell 1758, Abell 2163, Abell 2255, and RX J1347.5-1145. Based on this trend, we test excluding the hottest clusters ($T_{Chandra} > 10$ keV where *ASCA* and *Chandra* disagree) from our sample. The mean temperature ratio for $R_{2500-\mathrm{CORE}}$ remains 1.16 and the error of the mean increases from ± 0.014 to ± 0.015, while for $R_{5000-\mathrm{CORE}}$ T_{HBR} increases by a negligible 0.9% to 1.15 ± 0.014. Our results are not being influenced by the inclusion of hot clusters.

The temperature range of the clusters we have analyzed ($T_X \sim 3 - 20$ keV) is broad enough that the effect of metal abundance on the inferred spectral temperature is clearly not negligible. In Figure 2.6 we have plotted T_{HBR} versus abundance in solar units. Despite covering a factor of seven in temperature and metal abundances ranging from $Z/Z_{\odot} \approx 0$ to solar, we find no trend in T_{HBR} with metallicity. The

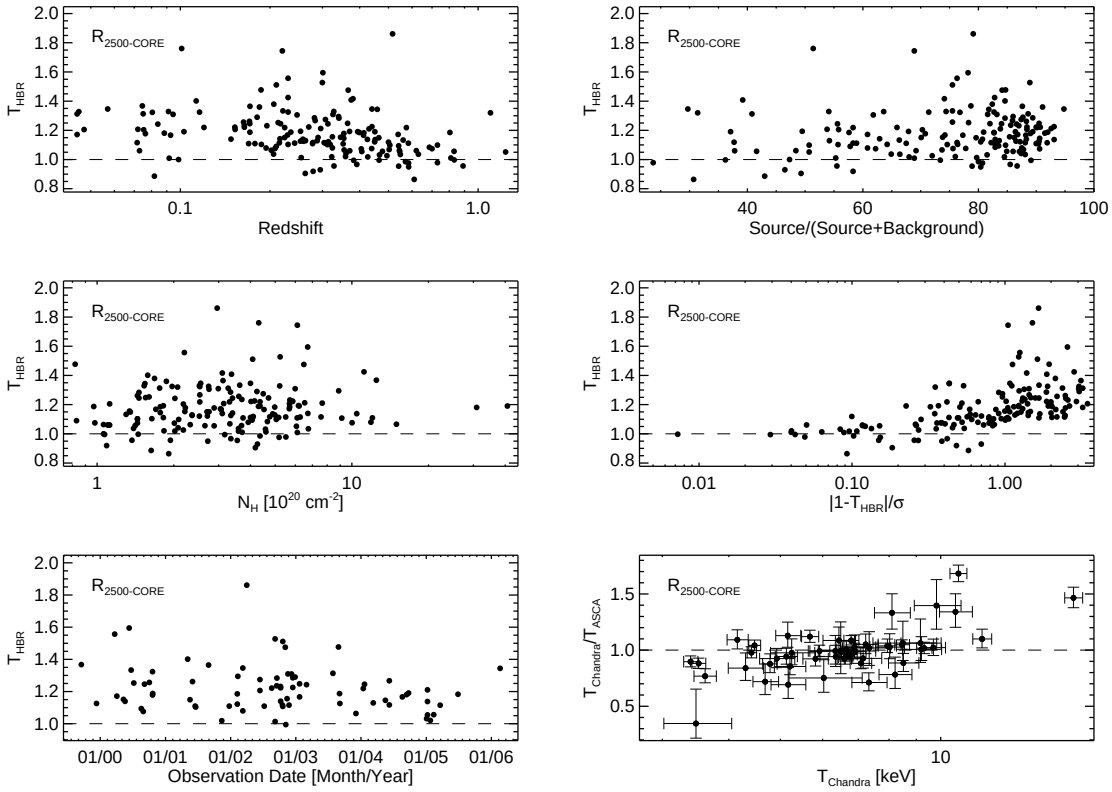

Figure 2.4 A few possible sources of systematic uncertainty vs. T_{HBR} calculated for the $R_{2500-\mathrm{CORE}}$ apertures (192 clusters). Error bars have been omitted in several plots for clarity. The line of equality is shown as a dashed line in all panels. *(Top left:)* T_{HBR} vs. redshift for the entire sample. The trend in T_{HBR} with redshift is expected as the $T_{2.0-7.0}$ lower boundary nears convergence with the $T_{0.7-7.0}$ lower boundary at $z \approx 1.85$. Weighted values of T_{HBR} are consistent with unity starting at $z \sim 0.6$. *(Top right:)* T_{HBR} vs. percentage of spectrum flux which is attributed to the source. We find no trend with signal-to-noise which suggests calibration uncertainty not is playing a major role in our results. *(Middle left:)* T_{HBR} vs. Galactic column density. We find no trend in absorption which would result if N_H values are inaccurate or if we had improperly accounted for local soft contamination. *(Middle right:)* T_{HBR} vs. the deviation from unity in units of measurement uncertainty. Recall that we have used 90% confidence (1.6σ) for our analysis. *(Bottom left:)* T_{HBR} plotted vs. observation start date. The plotted points are culled from the full sample and represent only clusters which have a single observation and where the spectral flux is $> 75\%$ from the source. We note no systematic trend with time. *(Bottom right:)* Ratio of *Chandra* temperatures derived in this work to *ASCA* temperatures taken from Horner (2001). We note a trend of comparatively hotter *Chandra* temperatures for clusters > 10 keV, otherwise our derived temperatures are in good agreement with those of *ASCA*.

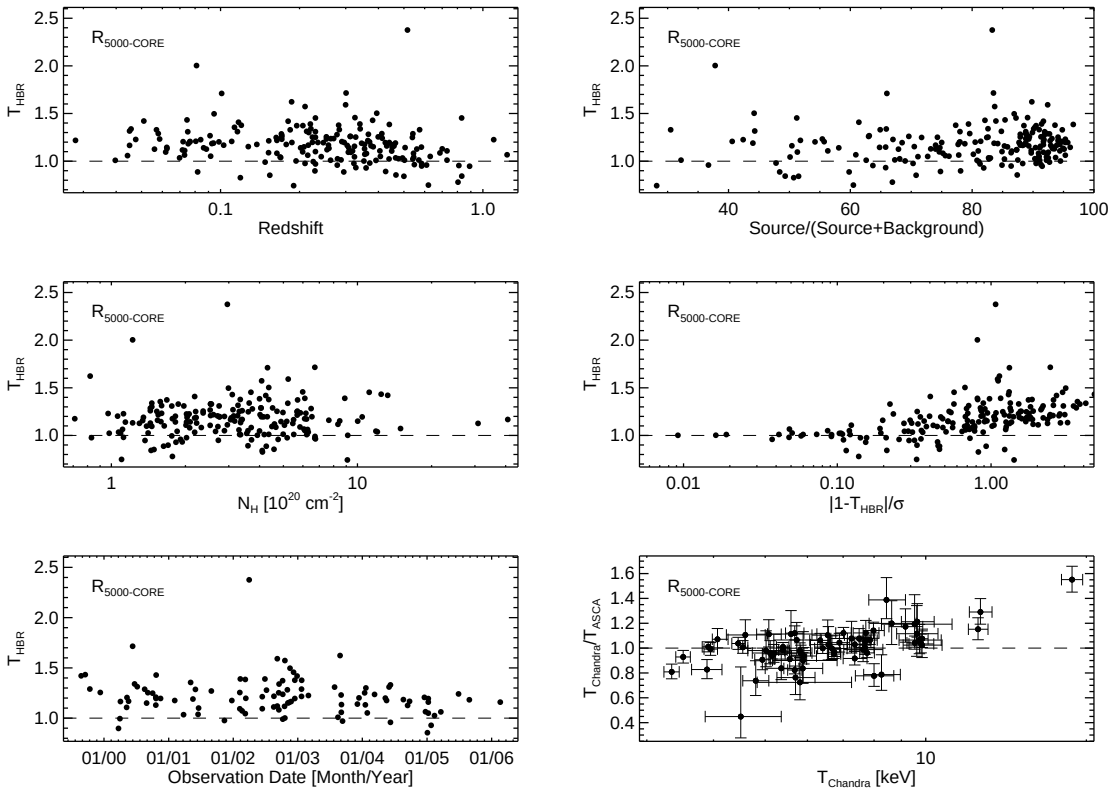

Figure 2.5 Same as Fig. 2.4 except using the $R_{5000-\mathrm{CORE}}$ apertures (166 clusters).

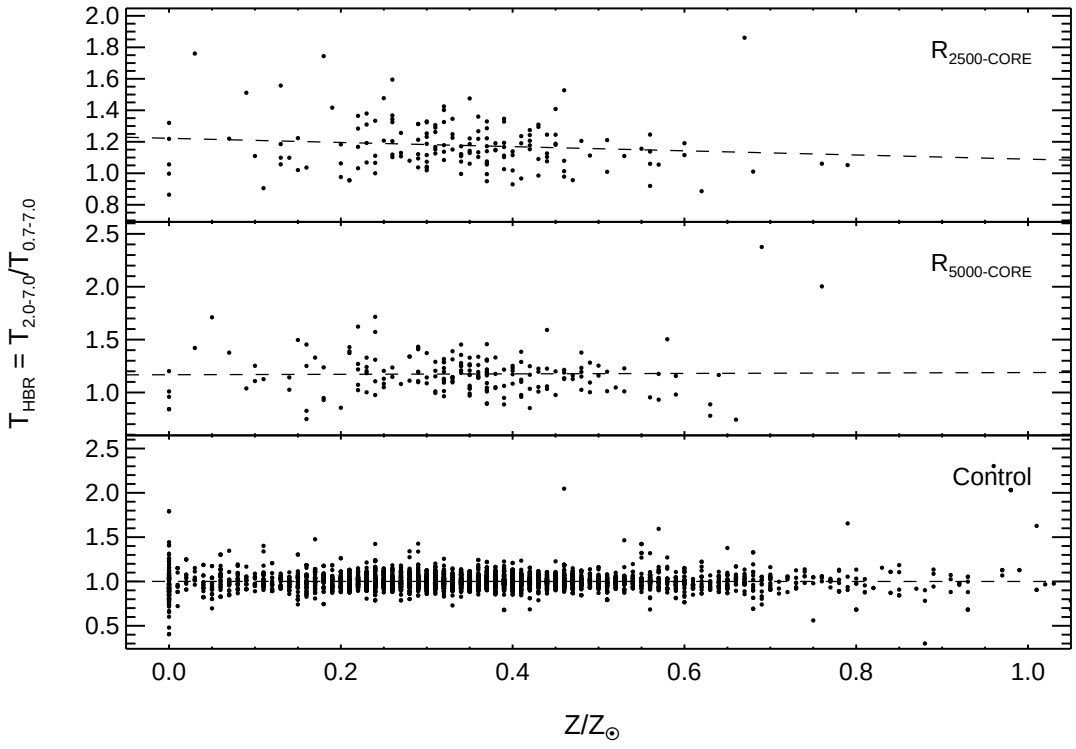

Figure 2.6 T_{HBR} as a function of metal abundance for $R_{2500-\mathrm{CORE}}$, $R_{5000-\mathrm{CORE}}$, and the control sample (see discussion of control sample in §2.5.2). Error bars are omitted for clarity. The dashed-line represents the linear best-fit using the bivariate correlated error and intrinsic scatter (BCES) method of **?** which takes into consideration errors on both T_{HBR} and abundance when performing the fit. We note no trend in T_{HBR} with metallicity (the apparent trend in the top panel is not significant) and also note the low dispersion in the control sample relative to the observations. The striation of abundance arises from our use of two decimal places in recording the best-fit values from XSPEC.

slight trend in the $R_{2500-\mathrm{CORE}}$ aperture (Fig. 2.6, top) is insignificant, while there is no trend at all in the control sample or $R_{5000-\mathrm{CORE}}$ aperture.

2.6.3 Using T_{HBR} as a Test of Relaxation

Cool Core Versus Non-Cool Core

As discussed in 2.1, ME01 gives us reason to believe the observed skewing of T_{HBR} to greater than unity is related to the dynamical state of a cluster. It has also been suggested that the process of cluster formation and relaxation may robustly result in the formation of a cool core (Ota et al., 2006; Burns et al., 2008). Depending on classification criteria, completeness, and possible selection biases, studies of flux-limited surveys have placed the prevalence of cool cores at $34\% - 60\%$ (White et al., 1997; Peres et al., 1998; Bauer et al., 2005; Chen et al., 2007). It has thus become rather common to divide up the cluster population into two distinct classes, cool core (CC) and non-cool core (NCC), for the purpose of discussing their different formation or merger histories. We thus sought to identify which clusters in our sample have cool cores, which do not, and if the presence or absence of a cool core is correlated with T_{HBR}. It is very important to recall that we excluded the core during spectral extraction and analysis.

To classify the core of each cluster, we extracted a spectrum for the 50 kpc region surrounding the cluster center and then defined a temperature decrement,

$$T_{\mathrm{dec}} = T_{50}/T_{\mathrm{cluster}} \tag{2.3}$$

where T_{50} is the temperature of the inner 50 kpc and T_{cluster} is either the $R_{2500-\mathrm{CORE}}$ or $R_{5000-\mathrm{CORE}}$ temperature. If T_{dec} was 2σ less than unity, we defined the cluster as having a CC, otherwise the cluster was defined as NCC. We find CCs in 35% of our sample and when we lessen the significance needed for CC classification from 2σ

to 1σ, we find 46% of our sample clusters have CCs. It is important to note that the frequency of CCs in our study is consistent with other more detailed studies of CC/NCC populations.

When fitting for T_{50}, we altered the method outlined in §2.5.1 to use the XSPEC modified Cash statistic (Cash, 1979), CSTAT, on ungrouped spectra. This choice was made because the distribution of counts per bin in low count spectra is not Gaussian but instead Poisson. As a result, the best-fit temperature using χ^2 is typically cooler (Nousek & Shue, 1989; Balestra et al., 2007). We have explored this systematic in ***all*** of our fits and found it to be significant only in the lowest count spectra of the inner 50 kpc apertures discussed here. But, for consistency, we fit all inner 50 kpc spectra using the modified Cash statistic.

With each cluster core classified, we then took cuts in T_{HBR} and asked how many CC and NCC clusters were above these cuts. Figure 2.7 shows the normalized number of CC and NCC clusters as a function of cuts in T_{HBR}. If T_{HBR} were insensitive to the state of the cluster core, we expect, for normally distributed T_{HBR} values, to see the number of CC and NCC clusters decreasing in the same way. However, the number of CC clusters falls off more rapidly than the number of NCC clusters. If the presence of a CC is indicative of a cluster's advancement towards complete virialization, then the significantly steeper decline in the percent of CC clusters versus NCC as a function of increasing T_{HBR} indicates higher values of T_{HBR} are associated with a less relaxed state. This result is insensitive to our choice of significance level in the core classification, i.e. the result is the same whether using 1σ or 2σ significance when considering $T_{\rm dec}$.

Because of the CC/NCC definition we selected, our identification of CCs and NCCs was only as robust as the errors on T_{50} allowed. One can thus ask the question, did our definition bias us towards finding more NCCs than CCs? To explore this question we simulated 20 spectra for each observation following the method outlined

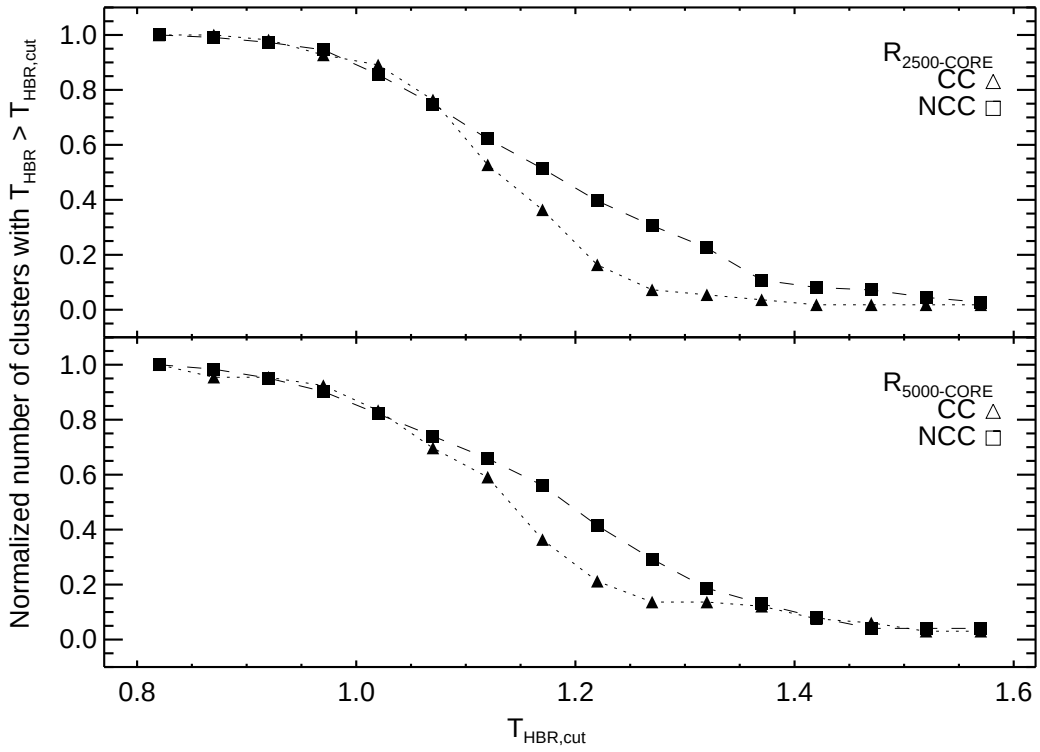

Figure 2.7 Normalized number of CC and NCC clusters as a function of cuts in T_{HBR}. There are 192 clusters plotted in the top panel and 166 in the bottom panel. We have defined a cluster as having a CC when the temperature for the 50 kpc region around the cluster center divided by the temperature for $R_{2500-\mathrm{CORE}}$, or $R_{5000-\mathrm{CORE}}$, was less than one at the 2σ level. We then take cuts in T_{HBR} at the 1σ level and ask how many CC and NCC clusters are above these cuts. The number of CC clusters falls off more rapidly than NCC clusters in this classification scheme suggesting higher values of T_{HBR} prefer less relaxed systems which do not have cool cores. This result is insensitive to our choice of significance level in both the core classification and T_{HBR} cuts.

in §2.5.2 for the control sample but using the inner 50 kpc spectral best-fit values as input. For each simulated spectrum, we calculated a temperature decrement (eq. 2.3) and re-classified the cluster as having a CC or NCC. Using the new set of mock classifications we assigned a reliability factor, ψ, to each real classification, which is simply the fraction of mock classifications which agree with the real classification. A value of $\psi = 1.0$ indicates complete agreement, with $\psi = 0.0$ indicating no agreement. When we removed clusters with $\psi < 0.9$ and repeated the analysis above, we found no significant change in the trend of a steeper decrease in the relative number of CC versus NCC clusters as a function of T_{HBR}.

Recall that the coolest ICM gas is being redshifted out of the observable band as z increases and becomes a significant effect at $z \geq 0.6$ (§2.5.2). Thus, we are likely not detecting "weak" CCs in the highest redshift clusters of our sample and consequently these cores are classified as NCCs and are artificially increasing the NCC population. When we excluded the 14 clusters at $z \geq 0.6$ from this portion of our analysis and repeated the calculations, we found no significant change in the results.

Mergers Versus Nonmergers

Looking for a correlation between cluster relaxation and a skewing in T_{HBR} was the primary catalyst of this work. The result that increasing values of T_{HBR} are more likely to be associated with clusters harboring non-cool cores gives weight to that hypothesis. But, the simplest relation to investigate is if T_{HBR} is preferentially higher in merger systems. Thus, we now discuss clusters with the highest significant values of T_{HBR} and attempt to establish, via literature based results, the dynamic state of these systems.

The subsample of clusters on which we focus have a $T_{HBR} > 1.1$ at 90% confidence for both their $R_{2500-\mathrm{CORE}}$ and $R_{5000-\mathrm{CORE}}$ apertures. These clusters are listed in Table A.2 and are sorted by the lower limit of T_{HBR}. Shown in Figure 2.8 is a plot

of T_{HBR} versus $T_{0.7-7.0}$ for all the clusters in our sample. The clusters discussed in this section are shown as green triangles and black stars. The clusters with only a $R_{5000-\mathrm{CORE}}$ analysis are listed separately at the bottom of the table. All 33 clusters listed have a core classification of $\psi > 0.9$ (see §2.6.3). The choice of the $T_{HBR} > 1.1$ threshold was arbitrary and intended to limit the number of clusters to which we pay individual attention, but which is still representative of mid- to high-T_{HBR} values. Only two clusters – Abell 697 and MACS J2049.9-3217 – do not have a $T_{HBR} > 1.1$ in one aperture and not the other. In both cases although, this was the result of the lower boundary narrowly missing the cut, but both clusters still have T_{HBR} significantly greater than unity.

For those clusters which have been individually studied, they are listed as mergers based on the conclusions of the literature authors (cited in Table A.2). Many different techniques were used to determine if a system is a merger: bimodal galaxy velocity distributions, morphologies, highly asymmetric temperature distributions, ICM substructure correlated with subclusters, or disagreement of X-ray and lensing masses. From Table A.2 we can see clusters exhibiting the highest significant values of T_{HBR} tend to be ongoing or recent mergers. At the 2σ level, we find increasing values of T_{HBR} favor merger systems with NCCs over relaxed, CC clusters. It appears mergers have left a spectroscopic imprint on the ICM which was predicted by ME01 and which we observe in our sample.

Of the 33 clusters with T_{HBR} significantly > 1.1, only 7 have CCs. Three of those – MKW3S, 3C 28.0, and RX J1720.1+2638 – have their apertures centered on the bright, dense cores in confirmed mergers. Two more clusters – Abell 2384 and RX J1525+0958 – while not confirmed mergers, have morphologies which are consistent with powerful ongoing mergers. Abell 2384 has a long gas tail extending toward a gaseous clump which we assume has recently passed through the cluster. RXJ1525 has a core shaped like a rounded arrowhead and is reminiscent of the bow shock

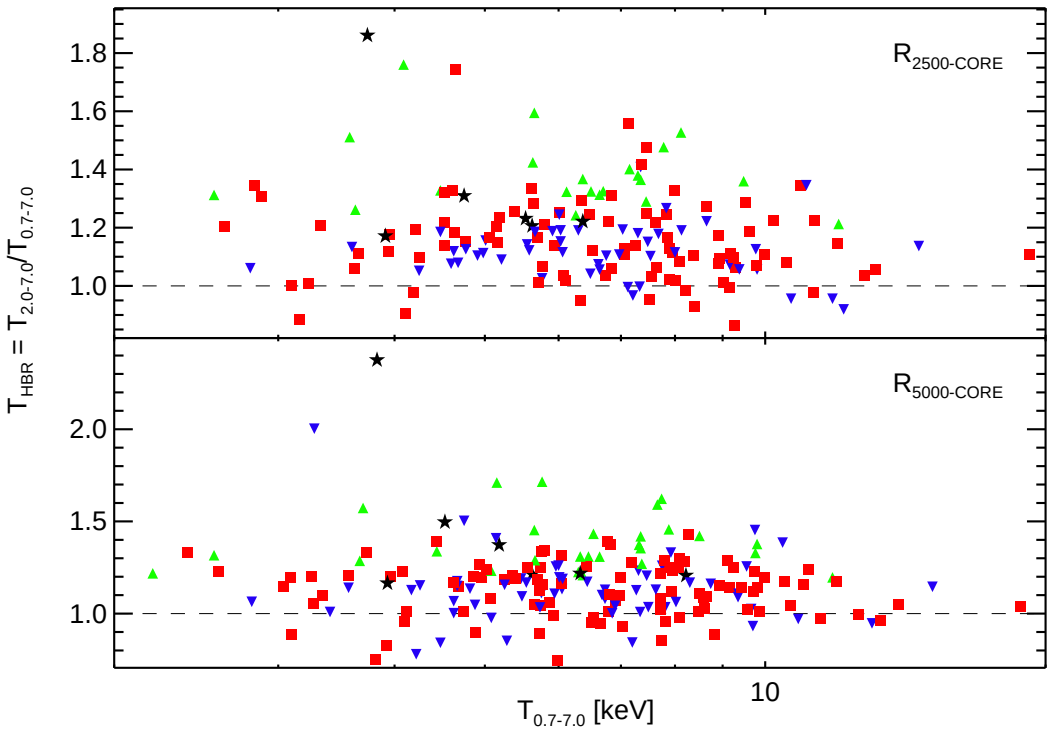

Figure 2.8 T_{HBR} plotted against $T_{0.7-7.0}$ for the $R_{2500-\mathrm{CORE}}$ and $R_{5000-\mathrm{CORE}}$ apertures. Note that the vertical scales for both panels are not the same. The top and bottom panels contain 192 and 166 clusters, respectively. Only two clusters – Abell 697 and MACS J2049.9-3217 – do not have a $T_{HBR} > 1.1$ in one aperture and not the other. In both cases however, it was a result of narrowly missing the cut. The dashed lines are the lines of equivalence. Symbols and color coding are based on two criteria: (1) the presence of a CC and (2) the value of T_{HBR}. Black stars (6 in the top panel; 7 in the bottom) are clusters with a CC and T_{HBR} significantly greater than 1.1. Green upright-triangles (21 in the top; 27 in the bottom) are NCC clusters with T_{HBR} significantly greater than 1.1. Blue down-facing triangles (49 top; 60 bottom) are CC clusters and red squares (90 top; 98 bottom) are NCC clusters. We have found most, if not all, of the clusters with $T_{HBR} \gtrsim 1.1$ are merger systems. Note that the cut at $T_{HBR} > 1.1$ is arbitrary and there are more merger systems in our sample then just those highlighted in this figure. However it is rather suggestive that clusters with the highest values of T_{HBR} appear to be merging systems.

seen in 1E0657-56. Abell 907 has no signs of being a merger system, but the highly compressed surface brightness contours to the west of the core are indicative of a prominent cold front, a tell-tale signature of a subcluster merger event (Markevitch & Vikhlinin, 2007). Abell 2029 presents a very interesting and curious case because of its seemingly high state of relaxation and prominent cool core. There are no complementary indications it has experienced a merger event. Yet its core hosts a wide-angle tail radio source. It has been suggested that such sources might be attributable to cluster merger activity (Sakelliou & Merrifield, 2000). Moreover, the X-ray isophotes to the west of the bright, peaked core are slightly more compressed and may be an indication of past gas sloshing resulting from the merger of a small subcluster. Both of these features have been noted previously, specifically by Clarke et al. (2004, 2005). We suggest the elevated T_{HBR} value for this cluster lends more weight to the argument that A2029 has indeed experienced a merger recently, but how long ago we do not know.

The remaining systems we could not verify as mergers – RX J0439.0+0715, MACS J2243.3-0935, MACS J0547.0-3904, Zwicky 1215, MACS J2311+0338, Abell 267, and NGC 6338 – have NCCs and X-ray morphologies consistent with an ongoing or post-merger scenario. Abell 1204 shows no signs of recent or ongoing merger activity; however, it resides at the bottom of the arbitrary T_{HBR} cut, and as evidenced by Abell 401 and Abell 1689, exceptional spherical symmetry is no guarantee of relaxation. Our analysis here is partially at the mercy of morphological assessment, and only a more stringent study of a carefully selected subsample or analysis of simulated clusters can better determine how closely correlated T_{HBR} is with the timeline of merger events.

2.7 Summary and Conclusions

We have explored the band dependence of the inferred X-ray temperature of the ICM for 166 well-observed ($N_{counts} > 1500$) clusters of galaxies selected from the *Chandra*

Data Archive.

We extracted spectra from the annulus between $R = 70$ kpc and $R = R_{2500}$, R_{5000} for each cluster. We compared the X-ray temperatures inferred for single-component fits to global spectra when the energy range of the fit was 0.7-7.0 keV (broad) and when the energy range was $2.0/(1+z)$-7.0 keV (hard). We found that, on average, the hard-band temperature is significantly higher than the broadband temperature. For the $R_{2500-\mathrm{CORE}}$ aperture we measured a weighted average of $T_{HBR} = 1.16$ with $\sigma = \pm 0.10$ and $\sigma_{mean} = \pm 0.01$ for the $R_{5000-\mathrm{CORE}}$ aperture, and $T_{HBR} = 1.14$ with $\sigma = \pm 0.12$ and $\sigma_{mean} = \pm 0.01$. We also found no systematic trends in the value of T_{HBR}, or the dispersion of T_{HBR}, with S/N, redshift, Galactic absorption, metallicity, observation date, or broadband temperature.

In addition, we simulated an ensemble of 12,765 spectra which contained observation-specific and idealized two-temperature component models, plus a control sample of single-temperature models. From analysis of these simulations we found the statistical fluctuations for a single temperature model are inadequate to explain the significantly different $T_{0.7-7.0}$ and $T_{2.0-7.0}$ we measure in our sample. We also found that the observed scatter, σ_{HBR}, is consistent with the presence of unresolved cool ($T_X < 2.0$ keV) gas contributing a minimum of $> 10\%$ of the total emission. The simulations also show the measured observational scatter in T_{HBR} is greater than the statistical scatter, $\sigma_{control}$. These results are consistent with the process of hierarchical cluster formation.

Upon further exploration, we found that T_{HBR} is enhanced preferentially for clusters which are known merger systems and for clusters without cool cores. Clusters with temperature decrements in their cores (known as cool-core clusters) tend to have best-fit hard-band temperatures that are consistently closer to their best-fit broadband temperatures. The correlation of T_{HBR} with the type of cluster core is insensitive to our choice of classification scheme and is robust against redshift effects.

Our results qualitatively support the finding by ME01 that the temperature ratio, T_{HBR}, might therefore be useful for statistically quantifying the degree of cluster relaxation/virialization.

An additional robust test of the ME01 finding should be made with simulations by tracking T_{HBR} during hierarchical assembly of a cluster. If T_{HBR} is tightly correlated with a cluster's degree of relaxation, then it, along with other methods of substructure measure, may provide a powerful metric for predicting (and therefore reducing) a cluster's deviation from mean mass-scaling relations. The task of reducing scatter in scaling relations will be very important if we are to reliably and accurately measure the mass of clusters.

2.8 Acknowledgments

K. W. C. was supported in this work by the National Aeronautics and Space Administration through *Chandra* X-Ray Observatory Archive grants AR-6016X and AR-4017A, with additional support from a start-up grant for Megan Donahue from Michigan State University. M. D. and Michigan State University acknowledge support from the NASA LTSA program NNG-05GD82G. G. M. V. thanks NASA for support through theory grant NNG-04GI89G. The *Chandra* X-ray Observatory Center is operated by the Smithsonian Astrophysical Observatory for and on behalf of the National Aeronautics Space Administration under contract NAS8-03060. This research has made use of software provided by the *Chandra* X-ray Center (CXC) in the application packages CIAO, ChIPS, and Sherpa. We thank Alexey Vikhlinin for helpful insight and expert advice. K. W. C. also thanks attendees of the "Eight Years of Science with *Chandra* Calibration Workshop" for stimulating discussion regarding *XMM-Chandra* cross-calibration. K. W. C. especially thanks Keith Arnaud for personally providing support and advice for mastering XSPEC. This research has made use of the NASA/IPAC Extragalactic Database (NED), which is operated by the

Jet Propulsion Laboratory, California Institute of Technology, under contract with the National Aeronautics and Space Administration. This research has also made use of NASA's Astrophysics Data System. *ROSAT* data and software were obtained from the High Energy Astrophysics Science Archive Research Center (HEASARC), provided by NASA's Goddard Space Flight Center.

Chapter Three

Cavagnolo, Kenneth W., Donahue, Megan, Voit, G. Mark, Sun, Ming (2008). Intracluster Medium Entropy Profiles For A Chandra Archival Sample of Galaxy Clusters. The Astrophysical Journal Supplement Series. arXiv eprint 0902.1802.

Chapter 3: Intracluster Medium Entropy Profiles For A Chandra Archival Sample of Galaxy Clusters

3.1 Introduction

The general process of galaxy cluster formation through hierarchical merging is well understood, but many details, such as the impact of feedback sources on the cluster environment and radiative cooling in the cluster core, are not. The nature of feedback operating within clusters is of great interest because of the implications regarding the formation of massive galaxies and for the cluster mass-observable scaling relations used in cosmological studies. Early models of structure formation which included only gravitation predicted self-similarity among the galaxy cluster population. These self-similar models made specific predictions for how the physical properties of galaxy clusters, such as temperature and luminosity, should scale with cluster redshift and mass (Kaiser, 1986, 1991; Evrard & Henry, 1991; Navarro et al., 1995, 1997; Evrard et al., 1996; Evrard, 1997; Teyssier et al., 1997; Eke et al., 1998; Bryan & Norman, 1998). However, numerous observational studies have shown clusters do not follow the tight mass-observable scaling relations predicted by simulations (Edge & Stewart, 1991; Allen & Fabian, 1998a; Markevitch, 1998; Arnaud & Evrard, 1999; Horner et al., 1999; Nevalainen et al., 2000; Finoguenov et al., 2001). To reconcile observation with

theory, it was realized non-gravitational effects, such as heating and radiative cooling in cluster cores, could not be neglected if models were to accurately replicate the process of cluster formation (*e.g.* Kaiser, 1991; Evrard & Henry, 1991; Loewenstein, 2000; Voit et al., 2002; Borgani et al., 2002).

As a consequence of radiative cooling, best-fit total cluster temperature decreases while total cluster luminosity increases. In addition, feedback sources such as active galactic nuclei (AGN) and galactic winds can drive cluster cores (where most of the cluster flux originates) away from hydrostatic equilibrium. Thus, at a given mass scale, radiative cooling and feedback conspire to create dispersion in otherwise theoretically tight mass-observable correlations like mass-luminosity and mass-temperature. While considerable progress has been made both observationally and theoretically in the areas of understanding, quantifying, and reducing scatter in cluster scaling relations (Buote & Tsai, 1996; Jeltema et al., 2005; Kravtsov et al., 2006; O'Hara et al., 2006; Nagai et al., 2007; Ventimiglia et al., 2008), it is still important to understand how non-gravitational processes, taken as a whole, affect cluster formation and evolution.

A related issue to the departure of clusters from self-similarity is that of cooling flows in cluster cores. The core cooling time in 50%-66% of clusters is much shorter than both the Hubble time and cluster age (Stewart et al., 1984; Edge et al., 1992; White et al., 1997; Peres et al., 1998; Bauer et al., 2005). For such clusters (and without compensatory heating), radiative cooling will result in the formation of a cooling flow (see Fabian, 1994, for a review). Early estimates put the mass deposition rates from cooling flows in the range of $100 - 1000 \mathrm{M}_{\odot} \mathrm{yr}^{-1}$ (*e.g.* Jones & Forman, 1984; Edge et al., 1994; Peres et al., 1998) However, cooling flow mass deposition rates inferred from soft X-ray spectroscopy were found to be significantly less than predicted, without much gas reaching temperatures lower than $T_{virial}/3$ (Tamura et al., 2001; Peterson et al., 2001, 2003; Kaastra et al., 2004) Irrespective of system

mass, the expected massive torrents of cool gas turned out to be more like cooling trickles.

In addition to the lack of soft X-ray line emission from cooling flows, prior methodical searches for the end products of cooling flows (*i.e.* in the form of molecular gas and emission line nebulae) revealed far less mass is locked-up in cooled by-products than expected (Heckman et al., 1989; McNamara et al., 1990; O'Dea et al., 1994b; Voit & Donahue, 1995). The disconnects between observation and theory have been termed "the cooling flow problem" and raise the question, "Where has all the cool gas gone?" The substantial amount of observational evidence suggests some combination of energetic feedback sources, such as AGN outbursts and supernovae explosions, have heated the ICM to selectively remove gas with a short cooling time and establish quasi-stable thermal balance in the ICM.

Both the breakdown of self-similarity and the cooling flow problem point toward the need for a better understanding of cluster feedback and radiative cooling. Recent revisions to models of how clusters form and evolve by including feedback sources has led to better agreement between observation and theory (Bower et al., 2006; Croton et al., 2006; Saro et al., 2006; Bower et al., 2008). The current paradigm regarding the cluster feedback process holds that AGN are the primary heat delivery mechanism and that an AGN outburst deposits the requisite energy into the ICM to retard, and in some cases, possibly quench cooling (see McNamara & Nulsen, 2007, for a review). How the feedback loop functions is still the topic of much debate, but that AGN are interacting with the hot atmospheres of clusters is no longer in doubt as evidenced by the prevalence of ICM bubbles (*e.g.* Bîrzan et al., 2004; Dunn & Fabian, 2008), the possible presence of sound waves (Fabian et al., 2003; Sanders & Fabian, 2008), and large-scale shocks associated with AGN outbursts (Forman et al., 2005; McNamara et al., 2005; Nulsen et al., 2005).

One robust observable which has proven useful in studying the effect of non-

gravitational processes is ICM entropy. Taken individually, ICM temperature and density do not fully reveal a cluster's thermal history. ICM temperature primarily reflects the depth of a cluster potential well, while the ICM density mostly reflects the capacity of the well to compress the gas. However, at constant pressure the density of a gas is determined by its specific entropy. By rewriting the expression for the adiabatic index – which can be expressed as $K \propto P\rho^{-5/3}$ – using the observables X-ray temperature (T_X) and electron density ($n_{\rm e}$), one can define a new quantity, $K = T_X n_e^{-2/3}$ (Ponman et al., 1999; Lloyd-Davies et al., 2000). The quantity K captures the thermal history of a gas because only gains and losses of heat energy can change K. The expression for K using observable X-ray quantities is commonly referred to as entropy in the X-ray cluster literature, but in actuality the classic thermodynamic specific entropy for a monatomic ideal gas is $s = \ln K^{3/2} + \text{constant}$.

One important property of gas entropy is that convective stability is approached in the ICM when $dK/dr \geq 0$. Thus, gravitational potential wells are giant entropy sorting devices: low entropy gas sinks to the bottom of the potential well, while high entropy gas buoyantly rises to a radius at which the ambient gas has equal entropy. If cluster evolution proceeded under the influence of gravitation only, then the radial entropy distribution of clusters would exhibit power-law behavior for $r > 0.1r_{200}$ with a constant, low entropy core at small radii (Voit et al., 2005). Thus, large-scale departures of the radial entropy distribution from a power-law can be used to measure the effect processes such as AGN heating and radiative cooling have on the ICM. Several studies have previously found that the radial ICM entropy distribution in some clusters flattens at $< 0.1r_{virial}$, or that the core entropy has much larger dispersion than the entropy at larger radii (David et al., 1996; Ponman et al., 1999; Lloyd-Davies et al., 2000; Ponman et al., 2003; Piffaretti et al., 2005; Donahue et al., 2005; Pratt et al., 2006; Donahue et al., 2006; Morandi & Ettori, 2007). However, these previous studies used smaller, focused samples, and to expand the utility of entropy

in understanding cluster thermodynamic history and non-gravitational processes, we have undertaken a much larger study utilizing the *Chandra* Data Archive.

In this chapter we present the data analysis and results from a *Chandra* archival project in which we studied the ICM entropy distribution for 239 galaxy clusters. We have named this project the "Archive of *Chandra* Cluster Entropy Profile Tables" or *ACCEPT* for short. In contrast to the sample of nine classic cooling flow clusters studied in Donahue et al. (2006, hereafter D06), *ACCEPT* covers a broader range of luminosities, temperatures, and morphologies, focusing on more than just cooling flow clusters. One of our primary objectives for this project was to provide the research community with an additional resource to study cluster evolution and confront current and future ICM models with a comprehensive set of entropy profiles.

We have found that the departure of entropy profiles from a power-law at small radii is a feature of most clusters, and given high enough angular resolution, possibly all clusters. We also find that the core entropy distribution of both the full *ACCEPT* collection and the Highest X-Ray Flux Galaxy Cluster Sample (*HIFLUGCS*, Reiprich 2001; Reiprich & Böhringer 2002) are bimodal. In a separate letter (Cavagnolo et al., 2008a), we presented results that show indicators of feedback like radio sources assumed to be associated with AGN and Hα emission are strongly correlated with core entropy.

A key aspect of this project is the dissemination of all data and results to the public. We have created a searchable, interactive web site[1] which hosts all of our results. The *ACCEPT* web site will be continually updated as new *Chandra* cluster and group observations are archived and analyzed. The web site provides all data tables, plots, spectra, reduced *Chandra* data products, reduction scripts, and more. Given the large number of clusters in our sample, we have omitted figures, and tables showing/listing results for individual clusters from this chapter and have made them

[1] http://www.pa.msu.edu/astro/MC2/accept

available at the *ACCEPT* web site.

The structure of this chapter is as follows: In §3.2 we outline initial sample selection criteria and information about the *Chandra* observations selected under these criteria. Data reduction is discussed in §3.3. Spectral extraction and analysis are discussed in §3.3.1, while our method for deriving deprojected electron density profiles is outlined in §3.3.2. A few possible sources of systematics are discussed in §3.4. Results and discussion are presented in §3.5. A brief summary is given in §3.6. For qthis work we have assumed a flat A ΛCDM cosmology with $H_0 = 70$ km s^{-1} Mpc^{-1}, $\Omega_{\rm M} = 0.27$, and $\Omega_\Lambda = 0.73$ is adopted Universe with cosmology $\Omega_{\rm M} = 0.3$, $\Omega_\Lambda = 0.7$, and $H_0 = 70 {\rm kms}^{-1}{\rm Mpc}^{-1}$. All quoted uncertainties are 90% confidence (1.6σ).

3.2 Data Collection

Our sample is collected from observations taken with the *Chandra* X-ray Observatory (Weisskopf et al., 2000) and which are publicly available in the *Chandra* Data Archive (CDA) as of August 2008. All data was taken with the ACIS detectors (Garmire et al., 2003), which have a pixel scale of $\sim 0.492''$ with an on-axis point spread function (PSF) which is smaller than the detectors' pixel size. ACIS has an energy resolution of < 100 eV for $E \lesssim 2$ keV and < 300 eV at all energies. *Chandra*'s unobscured collecting area is $\sim 1145{\rm cm}^2$ with an effective area of $\sim 600{\rm cm}^2$ around the peak emission energies of a typical galaxy cluster. At launch ACIS-I and ACIS-S differed by the better soft-energy sensitivity of ACIS-S, but in-flight degradation of the CCDs has slowly closed the differences between the two chip arrays.

We retrieved all data from the CDA listed under the CDA Science Categories "clusters of galaxies" or "active galaxies." As of submission, we have inspected all CDA clusters of galaxies observations and analyzed 510 of those observations (14.16 Msec). The Coma and Fornax clusters have been intentionally left out of our sample because they are very well studied nearby clusters which require a more intensive

analysis than we undertook in this project.

The data available for some clusters limited our ability to derive an entropy profile. Calculation of ICM entropy requires measurement of the gas temperature and density structure as a function of radius (discussed further in §3.3). To infer temperatures which were reasonably well constrained ($\Delta(kT_X) \approx \pm 1.0$keV) and to measure more than linear temperature gradients, we imposed the requirements that each cluster temperature profile have at least three concentric radial annular bins containing a minimum of 2500 source counts each. A post-analysis check showed our minimum source counts criterion resulted in a mean $\Delta(kT_X) = 0.87$ keV for the final sample.

In section 3.5.4 we cull the flux-limited *HIFLUGCS* primary sample (Reiprich, 2001; Reiprich & Böhringer, 2002) from our full archival collection. The groups M49, NGC 507, NGC 4636, NGC 5044, NGC 5813, and NGC 5846 are part of the *HIFLUGCS* primary sample but were not members of our initial archival sample. In order to take full advantage of the *HIFLUGCS* primary sample, we analyzed observations of these 6 groups. Note, however, that none of these 6 groups are included in the general discussion of *ACCEPT*.

We were unable to analyze some clusters for this study because of complications other than not meeting our minimum requirements for analysis. These clusters were: 2PIGG J0311.8-2655, 3C 129, A168, A514, A753, A1367, A2634, A2670, A2877, A3074, A3128, A3627, AS0463, APMCC 0421, MACS J2243.3-0935, MS J1621.5+2640, RX J1109.7+2145, RX J1206.6+2811, RX J1423.8+2404, SDSS J198.070267-00.984433, Triangulum Australis, and Zw5247.

After applying the temperature profile constraints, adding the 6 *HIFLUGCS* groups, and removing troublesome observations, the final sample presented in this chapter contains 317 observations of 239 clusters with a total exposure time of 9.86 Msec. The sample covers the temperature range $kT_X \sim 1 - 20$ keV, a bolometric luminosity range of $L_{bol} \sim 10^{42-46}$erg s^{-1}, and redshifts of $z \sim 0.05 - 0.89$. Table

A.1 lists the general properties for each observation in *ACCEPT*.

We also report previously unpublished Hα observations taken by M. Donahue. These observations do not enter into the analysis performed in this chapter but are used in Cavagnolo et al. (2008a). Since this chapter represents the data of the full project, we include them here. The new $[N\ II]$/Hα ratios and Hα fluxes are listed in Table B.3. The upper-limits listed in Table B.3 are 3σ significance. The observations were taken with either the 5 m Hale Telescope at the Palomar Observatory, USA, or the Du Pont 2.5 m telescope at the Las Campanas Observatory, Chile. All observations were made with a $2''$ slit centered on the brightest cluster galaxy (BCG) using two position angles: one along the semi-major axis and one along the semi-minor axis of the galaxy. The red light (555-798 nm) setup on the Hale Double Spectrograph used a 316 lines/mm grating with a dispersion of 0.31 nm/pixel and an effective resolution of 0.7-0.8 nm. The Du Pont Modular Spectrograph setup included a 1200 lines/mm grating with a dispersion of 0.12 nm/pixel and an effective resolution of 0.3 nm. The statistical and calibration uncertainties for the observations are both $\sim 10\%$. The statistical uncertainty arises primarily from uncertainty in the continuum subtraction.

3.3 Data Analysis

Measuring ICM entropy profiles first requires measurement of ICM temperature and density profiles. As discussed in Cavagnolo et al. (2008b), the ICM X-ray peak of the point-source cleaned, exposure-corrected cluster image was used as the cluster center, unless the iteratively determined X-ray centroid was more than 70 kpc away from the X-ray peak, in which case the centroid was used as the radial analysis zero point (see Cavagnolo et al. (2008b) for more details on centroiding procedure). The radial temperature structure of each cluster was measured by fitting a single-temperature thermal model to spectra extracted from concentric annuli centered on the cluster X-ray center. To derive the gas density profile, we first deprojected an exposure-corrected,

background-subtracted, point source clean surface brightness profile extracted in the 0.7-2.0keV energy range to attain a volume emission density. This emission density, along with spectroscopic information (count rate and normalization in each annulus), was then used to calculate gas density. The resulting entropy profiles were then fit with two models: a simple model consisting of only a radial power law, and a model which is the sum of a constant core entropy term, K_0, and the radial power law.

In this chapter we cover the basics of deriving gas entropy from X-ray observables, and direct interested readers to D06 for more in-depth discussion of our data reprocessing and reduction, and Cavagnolo et al. (2008b) for details regarding determination of each cluster's center and how the X-ray background was handled. The only difference between the data reduction presented in this chapter and that of D06 and Cavagnolo et al. (2008b), is that we have used newer versions of the *Chandra* X-ray Center (CXC) issued data reduction software (CIAO 3.4.1 and calibration files in the CalDB 3.4.0).

3.3.1 Temperature Profiles

One of the two components needed to derive a gas entropy profile is the temperature as a function of radius. We therefore constructed radial temperature profiles for each cluster in our collection. To reliably constrain a temperature, and allow for the detection of temperature structure beyond linear gradients, we required each temperature profile to have a minimum of three annuli containing 2500 counts each. The annuli for each cluster were generated by first extracting a background-subtracted cumulative counts profile using 1 ACIS detector pixel width annular bins (1 ACIS pixel $\approx 0.492''$) originating from the cluster center and extending to the detector edge. We truncated temperature profiles at the radius bounded by the detector edge, or $0.5r_{180}$, whichever was smaller. Truncation occurred at $0.5r_{180}$ as we are most interested in the radial entropy behavior of cluster core regions ($r \lesssim 100$ kpc)

and $0.5r_{180}$ is the approximate radius where temperature profiles begin to decline at larger radii (Vikhlinin et al., 2005). Additionally, analysis of diffuse gas temperature structure at large radii, which spectroscopically is dominated by background, requires a time consuming, observation-specific analysis of the X-ray background (see Sun et al., 2009, for a detailed discussion on this point).

Cumulative counts profiles were divided into annuli containing at least 2500 counts. For well-resolved clusters, the number of counts per annulus was increased to reduce the resulting uncertainty of kT_X and, for simplicity, to keep the number of annuli less than 50 per cluster. The method we use to derive entropy profiles is most sensitive to the surface brightness radial bin size and not the resolution or uncertainties of the temperature profile. Thus, the loss of resolution in the temperature profile from increasing the number of counts per bin, and thereby reducing the number of annuli, has an insignificant effect on the final entropy profiles and best-fit entropy models.

Background analysis was performed using the blank-sky datasets provided in the CalDB. Backgrounds were reprocessed and reprojected to match each observation. Off-axis chips were used to normalize for variations of the hard-particle background by comparing blank-sky and observation 9.5-12keV count rates. Following the analysis described in Vikhlinin et al. (2005), soft residuals were created and fitted for each observation to account for the spatially-varying soft Galactic background (see also Cavagnolo et al., 2008b). The best-fit spectral model for the residual soft component (scaled for sky area) was included as an additional, fixed background component during fitting of cluster spectra. Errors associated with the additional soft background component were determined by refitting cluster spectra using the $\pm 1\sigma$ temperatures of the soft background component's best fit model and then adding the associated error in quadrature to the final error budget.

For each radial annular region, source and background spectra were extracted from the target cluster and corresponding normalized blank-sky dataset. Following

standard CIAO techniques[2] we created weighted response files (WARF) and redistribution matrices (WRMF) for each cluster using a flux-weighted map (WMAP) across the entire extraction region. These files quantify the effective area, quantum efficiency, and imperfect resolution of the *Chandra* instrumentation as a function of chip position. Each spectrum was binned to contain a minimum of 25 counts per energy bin.

Spectra were fitted with XSPEC 11.3.2ag (Arnaud, 1996) using an absorbed, single-temperature MeKaL model (Mewe et al., 1985, 1986) over the energy range 0.7-7.0 keV. Neutral hydrogen column densities, $N_{\rm H}$, were taken from Dickey & Lockman (1990). A comparison between the $N_{\rm H}$ values of Dickey & Lockman (1990) and the higher-resolution Leiden/Argentine/Bonn (LAB) Survey (Kalberla et al., 2005) revealed that the two surveys agree to within $\pm$20% for 80% of the clusters in our sample. For the other 20% of the sample, using the LAB value, or allowing $N_{\rm H}$ to be free, did not result in best-fit temperatures or metallicities which differ significantly from fits using the Dickey & Lockman (1990) values.

The potentially free parameters of the absorbed thermal model are $N_{\rm H}$, X-ray temperature, metal abundance normalized to solar (heavy-element ratios taken from Anders & Grevesse, 1989), and a normalization (η) which is proportional to the integrated emission measure within the extraction region,

$$\eta = \frac{10^{-14}}{4\pi D_A^2 (1+z)^2} \int n_{\rm e} n_{\rm p} dV, \tag{3.1}$$

where D_A is the angular diameter distance in cm, z is the dimensionless cluster redshift, $n_{\rm e}$ and $n_{\rm p}$ are the electron and proton densities, respectively, in units of cm^{-3}, and V is the volume of the emission region in cm^3. In all spectral fits the metal abundance in each annulus was a free parameter and $N_{\rm H}$ was fixed to the Galactic value. No systematic error was added during fitting and thus all quoted errors are

[2]http://cxc.harvard.edu/ciao/guides/esa.html

statistical only. The statistic used during fitting was χ^2 (XSPEC statistics package CHI). All uncertainties were calculated using 90% confidence.

More than one observation was available in the archive for some clusters. We utilized the combined exposure time for these clusters by first extracting independent spectra, WARFs, WRMFs, normalized background spectra, and soft residuals for each observation. These independent spectra were then read into XSPEC simultaneously and fit with the same spectral model which had all parameters, except normalization, tied among the spectra.

Spectral deprojection of ICM temperature should result in slightly lower temperatures in the central bins of only the clusters with temperature gradients which increase steeply going out from the cluster center. For those clusters, the end result would be a slight lowering of the entropy for the central-most bins. In D06 we studied a sample of nine "classic" cooling flow clusters, all of which have steep temperature gradients ($T(r)_{max}/T(r)_{min} \sim 1.5 - 3.5$). Our analysis in D06 showed that spectral deprojection did not result in significant differences between entropy profiles derived using projected or deprojected temperature profiles. In light of this result, and the fact that deprojection requires about a factor of 5 more computing resources and time, we opted not to deproject our spectra for this phase of the project.

3.3.2 Deprojected Electron Density Profiles

For predominantly free-free emission, emissivity strongly depends on density and only weakly on temperature, $\epsilon \propto \rho^2 T^{1/2}$. Since ICM temperatures generally exceed 2.0 keV, the flux measures in the energy range 0.7-2.0 keV, together with a small correction for any variations in temperature and metallicity, is therefore a good diagnostic of ICM density. To reconstruct the relevant gas density as a function of physical radius, we deprojected the cluster emission from high-resolution surface brightness profiles and converted to electron density using normalizations and count rates taken

from the spectral analysis.

We extracted surface brightness profiles from the 0.7-2.0 keV energy range using concentric annular bins of width $5''$ originating from the cluster center. Surface brightness profiles were corrected with observation-specific, normalized radial exposure profiles to remove the effects of vignetting and exposure time fluctuations. Following the recommendation in the CIAO guide for analyzing extended sources, exposure maps were created using the monoenergetic value associated with the observed count rate peak. The more sophisticated method of creating exposure maps using spectral weights calculated for an incident spectrum with the temperature and metallicity of the observed cluster was also tested for a series of clusters covering a broad temperature range. For the narrow energy band we consider, the chip response is relatively flat and we find no significant differences between the two methods. For all clusters, the monoenergetic value used in creating exposure maps was between $0.8 - 1.7$keV.

The 0.7-2.0 keV spectroscopic count rate and spectral normalization were linearly interpolated from the radial temperature profile grid to match the surface brightness radial grid. Utilizing the deprojection technique of Kriss et al. (1983), the interpolated spectral parameters were used to convert observed surface brightness to deprojected electron density. The conversion from best-fit spectroscopic values to density intrinsically accounts for temperature and metal abundance variations which affect the gas emissivity in our selected energy range. Radial electron density written in terms of relevant quantities is,

$$n_{\rm e}(r) = \sqrt{\frac{(n_{\rm e}/n_{\rm p})\ 4\pi[D_A(1+z)]^2\ C(r)\ \eta(r)}{10^{-14}\ f(r)}} \tag{3.2}$$

where $n_{\rm e}/n_p \approx 1.2$ for a fully ionized solar abundance plasma, $C(r)$ is the radial emission density derived from eq. A1 in Kriss et al. (1983), η is the interpolated spectral normalization from eq. 3.1, D_A is the angular diameter distance, z is cluster

redshift, and $f(r)$ is the interpolated spectroscopic count rate. Cosmic dimming of source surface brightness is accounted for by the $D_A^2(1+z)^2$ term. This method of deprojection takes into account temperature and metallicity fluctuations which affect observed gas emissivity. Errors for the gas density profile were estimated using 5000 Monte Carlo simulations of the original surface brightness profile. The Kriss et al. (1983) deprojection technique assumes spherical symmetry. However, D06 showed such an assumption has little effect on the final entropy profiles (see also Donahue et al., 2003; Bauer et al., 2005, for the low impact of spherical symmetry assumptions for deriving density profiles).

3.3.3 β-model Fits

Noisy surface brightness profiles, or profiles with irregularities such as inversions or extended flat cores, result in unstable, unphysical quantities when using an "onion" deprojection technique like that of Kriss et al. (1983). For cases where deprojection of the binned data was problematic, we resorted to fitting the surface brightness profile with a β-model (Cavaliere & Fusco-Femiano, 1978), which has the positive attribute of having an analytic deprojection solution. It is well known that the β-model does not precisely represent all the features of the ICM for clusters of high central surface brightness (Ettori, 2000; Loken et al., 2002; Hallman et al., 2007). However, for the profiles which required a fit, the β-model was actually a suitable approximation. These clusters have low central surface brightness, unlike the classic cool-core clusters. The single ($N = 1$) and double ($N = 2$) β-models were used in fitting,

$$S_X = \sum_{i=1}^{N} S_i \left[1 + \left(\frac{r}{r_{c,i}}\right)^2\right]^{-3\beta_i+\frac{1}{2}}. \quad (3.3)$$

The models were fitted using Craig Markwardt's robust non-linear least squares minimization IDL routines[3,4]. The data input to the fitting routines were weighted using the inverse square of the observational errors. Using this weighting scheme resulted in reduced χ^2 values near unity for, on average, the inner 80% of the radial range considered. Accuracy of errors output from the fitting routine were checked against a bootstrap Monte Carlo analysis of 1000 surface brightness realizations. Both the single- and double-β models were fit to each profile and using the F-test functionality of Sherpa[5] we determined if the addition of extra model components was justified given the degrees of freedom and χ^2 values of each fit. If the significance was less than 0.05, the extra components were justified and the double-β model was used.

A best-fit β-model was used in place of the data when deriving electron density for the clusters listed in Table B.2. These clusters are also flagged in Table A.1 with the note letter 'a.' The best-fit β-models and background-subtracted, exposure-corrected surface brightness profiles are shown in Figure 3.8. See Appendix 3.3.3 for notes discussing individual clusters. The disagreement between the best-fit β-model and the surface brightness in the central regions for some clusters is also discussed in Appendix 3.3.3. In short, the discrepancy arises from the presence of compact X-ray sources, a topic which is addressed in §3.3.5. All clusters requiring a β-model fit have core entropy > 95keV cm^2 and the mean best-fit parameters are listed in Table B.4.

3.3.4 Entropy Profiles

Radial entropy profiles were calculated using the widely adopted formulation $K(r) = kT_x(r)n_{\rm e}(r)^{-2/3}$. To create the radial entropy profiles, the temperature and density profiles must be on the same radial grid. This was accomplished by interpolating the temperature profile across the higher-resolution radial grid of the deprojected electron

[3]http://rsinc.com/idl/
[4]http://cow.physics.wisc.edu/ craigm/idl/
[5]http://cxc.harvard.edu/ciao3.4/ahelp/ftest.html

density profile using IDL's native linear interpolation routine *interpol*. Because the density profiles have higher radial resolution, the central bin of a cluster temperature profile will span several of the innermost bins of the density profile. Since we are most interested in the behavior of the entropy profiles in the central regions, how the interpolation was performed for the inner regions is important. Thus, temperature interpolation over the region of the density profile where a single central temperature bin encompasses several density profile bins was applied in two ways: (1) as a linear gradient consistent with the slope of the temperature profile at radii larger than the central T_X bin ($\Delta T_{center} \neq 0$; 'extr' in Table B.5), and (2) as a constant ($\Delta T_{center} = 0$; 'flat' in Table B.5). Shown in Figure 3.1 is the ratio of best-fit core entropy, K_0, using the above two methods. The five points lying below the line of equality are clusters which are best-fit by a power-law or have K_0 statistically consistent with zero. It is worth noting that both schemes yield statistically consistent values for K_0 except for the clusters marked by black squares which have a ratio significantly different from unity.

The clusters for which the two methods give K_0 values that significantly differ all have steep temperature gradients with the maximum and minimum radial temperatures differing by a factor of 1.3-5.0. Extrapolation of a steep temperature gradient as $r \rightarrow 0$ results in very low central temperatures (typically $T_X \leq T_{virial}/3$) which are inconsistent with observations, most notably Peterson et al. (2003). Most important however, is that the flattening of entropy we observe in the cores of our sample (discussed in §3.5.1) is ***not*** a result of the method chosen for interpolating the temperature profile. For this chapter, we therefore focus on the entropy results derived assuming a constant temperature for the central density bins covered by a single temperature bin.

Uncertainty in $K(r)$ arising from using a single-component temperature model for each annulus during spectral analysis contributes negligibly to our final fits and

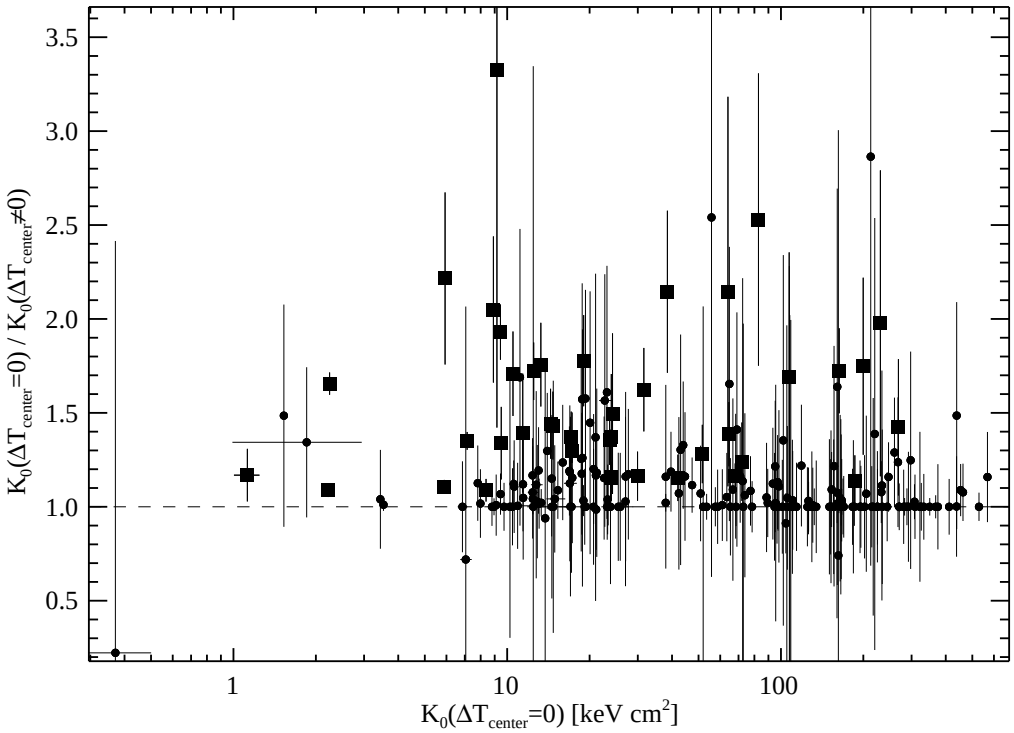

Figure 3.1 Ratio of best-fit K_0 for the two treatments of central temperature interpolation (see §3.3.1): (1) temperature is free to decline across the central density bins ($\Delta T_{center} \neq 0$), and (2) the temperature across the central density bins is isothermal ($\Delta T_{center} = 0$). Filled black squares are clusters for which the K_0 ratio is inconsistent with unity.

is discussed in detail in the Appendix of D06. Briefly summarizing D06: the entropy values we measure at each radius are dominated by the most X-ray luminous component, which is generally the lowest entropy gas at that radius. For the best-fit entropy values to be significantly changed, the volume filling fraction of a higher-entropy component must be non-trivial ($> 50\%$). As discussed in D06, our results are not strongly affected by the presence of multiple, low-luminosity gas phases and are mostly insensitive to X-ray surface brightness decrements, such as X-ray cavities and bubbles, although in extreme cases their influence on an entropy profile can be detected (for an example, see the cluster A2052, also analyzed in D06).

Each entropy profile was fit with two models: a simple model which is a power-law at large radii and approaches a constant value at small radii (eq. 3.4), and a model which is a power-law only (eq. 3.5):

$$K(r) = K_0 + K_{100} \left(\frac{r}{100\mathrm{kpc}}\right)^{\alpha} \quad (3.4)$$

$$K(r) = K_{100} \left(\frac{r}{100\mathrm{kpc}}\right)^{\alpha}. \quad (3.5)$$

In our entropy models, K_0 is what we call core entropy, K_{100} is a normalization for entropy at 100 kpc, and α is the power-law index. Later in this chapter, and in Cavagnolo et al. (2008a), we focus much of our discussion on the parameter K_0 so it is worth clarifying what K_0 does not represent. K_0 is not intended to represent the minimum core entropy or the entropy at $r = 0$. Nor does K_0 capture the gas entropy which would be measured immediately around an AGN or in a compact but extended BCG X-ray corona. Instead, K_0 represents the typical excess of core entropy above the best fitting power-law at larger radii. The intentionally simplistic characterization of cluster core entropy via K_0 was implemented to make comparing a large sample of cluster cores less ambiguous. The entropy models were fitted to the data using Craig Markwardt's IDL routines in the package MPFIT. The output best-fit parameters

and associated errors were checked using a bootstrap Monte Carlo analysis of 5000 entropy profile realizations.

The radial range of fitting was truncated at a maximum radius (determined by eye) to avoid the influence of noisy bins and profile turnover at large radii which result from instability of our deprojection method. All the best-fit parameters for each cluster are listed in Table B.5. The mean best-fit parameters for the full *ACCEPT* sample are given in Table B.4. Also given in Table B.4 are the mean best-fit parameters for clusters below and above $K_0 = 50\text{keV cm}^2$. We show in §3.5.2 that the cut at $K_0 = 50\text{keV cm}^2$ is not completely arbitrary as it approximately demarcates the division between two distinct populations in the K_0 distribution.

Some clusters have a surface brightness profile which is comparable to a double β-model. Our models for the behavior of $K(r)$ are intentionally simplistic and are not intended to fully describe all the features of $K(r)$. Thus, for the small number of clusters with discernible double-β behavior, fitting of the entropy profiles was restricted to the innermost of the two β-like features. These clusters have been flagged in Table A.1 with the note letter 'b.' The best-fit power-law index is typically much steeper for these clusters, but the outer regions, which we do not discuss here, have power-law indices which are typical of the rest of the sample, *i.e.* $\alpha \sim 1.2$.

3.3.5 Exclusion of Central Sources

For many clusters in our sample the ICM X-ray peak, ICM X-ray centroid, BCG optical emission, and BCG infrared emission are coincident or well within 70 kpc of one another. This made identification of the cluster center unambiguous in those cases. However, in some clusters, there is an X-ray point source or compact X-ray source ($r \lesssim 5$ kpc) found very near ($r < 10$ kpc) the cluster center and always associated with a galaxy. We identified 37 clusters with central sources and have flagged them in Table A.1 with the note letter 'd' for AGN and 'e' for compact but

resolved sources. The mean best-fit parameters for these clusters are given in Table B.4 under the sample name 'CSE' for "central source excluded." These clusters cover the redshift range $z = 0.0044 - 0.4641$ with mean $z = 0.1196 \pm 0.1234$, and temperature range $kT_X = 1 - 12$ keV with mean $kT_X = 4.43 \pm 2.53$ keV. For some objects – such as 3C 295, A2052, A426, Cygnus A, Hydra A, or M87 – the source is an AGN and there was no question the source must be removed.

However, determining how to handle the compact X-ray sources was not so straightforward. These compact sources are larger than the PSF, fainter than an AGN, but typically have significantly higher surface brightness than the surrounding ICM such that the compact source's extent was distinguishable from the ICM. These sources are most prominent, and thus the most troublesome, in non-cool core clusters (*i.e.* clusters which are approximately isothermal). They are troublesome because the compact source is typically much cooler and denser than the surrounding ICM and hence has an entropy much lower than the ambient ICM. We believe most of these compact sources to be X-ray coronae associated with the BCG (see Sun et al., 2007, for discussion of BCG coronae).

Without removing the compact sources, we measured radial entropy profiles and found, for all cases, that $K(r)$ abruptly changes at the outer edge of the compact source. Including the compact sources in the measurement of $K(r)$ results in the central cluster region(s) appearing overdense, and at a given temperature the region will have a much lower entropy than if the source were excluded. Such a discontinuity in $K(r)$ results in our simple models of $K(r)$ not being a good description of the profiles. Aside from producing poor fits, a significantly lower entropy influences the value of best-fit parameters because the shape of $K(r)$ is drastically changed. Obviously, two solutions are available: exclude or keep the compact sources during analysis. Deciding what to do with these sources depends upon what cluster properties we are specifically interested in quantifying.

The compact X-ray sources discussed in this section are not representative of the cluster's core entropy; these sources are representative of the entropy within and immediately surrounding peculiar BCGs. Our focus for the *ACCEPT* project was to quantify the entropy structure of the cluster core region and surrounding ICM, not to determine the minimum entropy of cluster cores or to quantify the entropy of peculiar core objects such as BCG coronae. Thus, we opted to exclude these compact sources during our analysis. For a few extraordinary sources, it was simpler to ignore the central bin of the surface brightness profile during analysis because of imperfect exclusion of a compact source's extended emission. These clusters have been flagged in Table A.1 with the note letter 'f.'

It is worth noting that when any source is excluded from the data, the empty pixels where the source once was were not included in the calculation of the surface brightness (counts and pixels are both excluded). Thus, the decrease in surface brightness of a bin where a source has been removed is not a result of the count to area ratio being artificially reduced.

3.4 Systematics

Our models for $K(r)$ were designed so that the best-fit K_0 values are a good measure of the entropy profile flattening at small radii. This flattening could potentially be altered through the effects of systematics such as PSF smearing and binning of the surface brightness profile. To quantify the extent to which our K_0 values are being affected by these systematics, we have analyzed mock *Chandra* observations created using the ray-tracing program MARX[6], and also by analyzing degraded entropy profiles generated from artificially redshifting well-resolved clusters. In the analysis below, we show that the lack of clusters with $K_0 \lesssim 10\mathrm{keV\ cm}^2$ at $z \gtrsim 0.1$ is attributable to resolution effects, but that deviation of an entropy profile from a

[6]http://space.mit.edu/CXC/MARX/

power-law, even if only in the central-most bin, cannot be accounted for by PSF effects. We also discuss the number of profiles which are reasonably well-represented by the power-law only profile, and establish that no more than $\sim 10\%$ of the entropy profiles in *ACCEPT* are consistent with a power-law.

3.4.1 PSF Effects

To assess the effect of PSF smearing on our entropy profiles, we have updated the analysis presented in §4.1 of D06 to use MARX simulations. In the D06 analysis, we assumed the density and temperature structure of the cluster core obeyed power-laws with $n_e \propto r^{-1}$ and $T_X \propto r^{1/3}$. This results in a power-law entropy profile with $K \propto r$. Further assuming the main emission mechanism is thermal bremsstrahlung, *i.e.* $\epsilon_X \propto T_X^{1/2}$, yields a surface brightness profile which has the form $S_X \propto r^{-5/6}$. A source image consistent with these parameters was created in IDL and then input to MARX to create the mock *Chandra* observations.

The MARX simulations were performed using the spectrum of a 4.0 keV, $0.3 \approx Z_{\odot}$ abundance MeKaL model. We have tested using input spectra with $kT_X = 2 - 10$ keV with varying abundances and find the effect of temperature and metallicity on the distribution of photons in MARX to be insignificant for our discussion here. We have neglected the X-ray background in this analysis as it is overwhelmed by cluster emission in the core and is only important at large radii. Observations for both ACIS-S and ACIS-I instruments were simulated using an exposure time of 40 ksec. A surface brightness profile was then extracted from the mock observations using the same $5''$ bins used on the real data.

For $5''$ bins, we find the difference between the central bins of the input surface brightness and the output MARX observations to be less than the statistical uncertainty. One should expect this result, as the on-axis *Chandra* PSF is $\lesssim 1''$ and the surface brightness bins we have used on the data are five times this size. What is

most interesting and important though, is that our analysis using MARX suggests any deviation of the surface brightness – and consequently the entropy profile – from a power-law, even if only in the central bin, is real and cannot be attributed to PSF effects. Even for the most poorly resolved clusters, the deviation away from a power-law we observe in a large majority of our entropy profiles is not a result of our deprojection technique or systematics.

3.4.2 Angular Resolution Effects

Another possible limitation in measuring K_0 is the effect of using discrete, fixed angular size bins when extracting surface brightness profiles. This choice may introduce a redshift-dependence into the best-fit K_0 values because as redshift increases, a fixed angular size encompasses a larger physical volume and the value of K_0 may increase if the bin includes a broad range of gas entropy. Shown in Figure 3.2 is a plot of the best-fit K_0 values for our entire sample versus redshift.

In the full archival sample, we have a few nearby objects ($z < 0.02$) with $K_0 <$ 10keV cm^2 (numbered in Fig. 3.2) and only one at higher redshift – A1991 ($K_0 = 1.53 \pm 0.32$, $z = 0.0587$), which is a very peculiar cluster (Sharma et al., 2004). These low-z, low-K_0 group-scale objects have been included in our archival sample because they are well-known. Ignoring those systems, one can see from Fig. 3.2 that out to $z \approx 0.5$ clusters with $K_0 \geq$ 10keV cm^2 are found at all redshifts. The completeness down to $K_0 \approx$ 10keV cm^2 at most redshifts combined with the low-K_0 nearby systems raises the question: could the lack of clusters with $K_0 \lesssim$ 10keV cm^2 at $z > 0.02$ be plausibly explained by resolution effects?

To investigate this question we tested the effect redshift has on our measurements of K_0 by culling out the subsample of objects with $K_0 \leq$ 10keV cm^2 and $z \leq 0.1$ and degrading their surface brightness profiles to mimic the effect of increasing the cluster redshift. Our test is best illustrated using an example: consider a cluster at

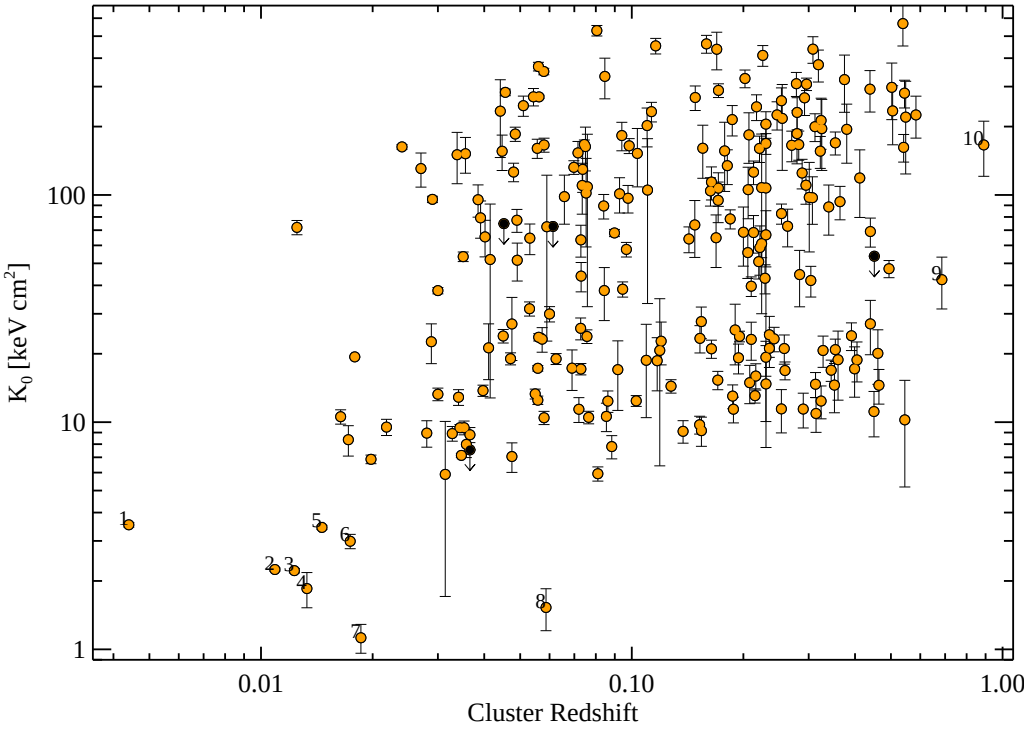

Figure 3.2 Best-fit K_0 vs. redshift. Some clusters have K_0 error bars smaller than the point. The clusters with upper-limits (*black points with downward arrows*) are: A2151, AS0405, MS 0116.3-0115, and RX J1347.5-1145. The numerically labeled clusters are: (1) M87, (2) Centaurus Cluster, (3) RBS 533, (4) HCG 42, (5) HCG 62, (6) SS2B153, (7) A1991, (8) MACS0744.8+3927, and (9) CL J1226.9+3332. For CLJ1226, Maughan et al. (2007) found best-fit $K_0 = 132 \pm 24$keV cm^2 which is not significantly different from our value of $K_0 = 166 \pm 45$keV cm^2. The lack of $K_0 < 10$keV cm^2 clusters at $z > 0.1$ is most likely the result of insufficient angular resolution (see §3.4.2).

$z = 0.1$. For this cluster, $5'' \approx 9$ kpc. Were the cluster at $z = 0.2$, $5''$ would be ≈ 17 kpc. To mimic moving this example cluster from $z = 0.1 \rightarrow 0.2$, we can extract a new surface brightness profile using a bin size of 17 kpc instead of $5''$. This procedure will result in a new surface brightness profile which has the angular resolution for a cluster at a higher redshift, and subsequent analysis of the entropy profile should yield information about how redshift affects the best-fit K_0. The preceding method was used to degrade the profiles of the $K_0 \leq 10$keV cm^2 and $z \leq 0.1$ subsample objects. New surface-brightness bin sizes were calculated for each cluster over an evenly distributed grid of redshifts in the range $z = 0.1 - 0.4$ using step sizes of 0.02.

Our temperature profiles were created using a minimum number of counts per annulus. Hence, clusters with peaked central surface brightness will have higher resolution temperature profiles. Thus, in addition to degrading the surface brightness profiles, the temperature profiles for each cluster were degraded by starting at the innermost temperature profile annulus and combining neighboring annuli moving outward. For each 0.1 step in our redshift grid the number of annuli which were combined was increased. For $z = 0.1$ two neighboring annuli were combined, for $z = 0.2$ three annuli were combined, for $z = 0.3$ four annuli, and five annuli at $z = 0.4$. In concordance with our criterion for creating the original temperature profiles, the number of annuli in the degraded profiles was not allowed to fall below 3. New spectra were extracted for these enlarged regions and analyzed following the same procedure detailed in §3.3.1.

The ensemble of artificially redshifted clusters was analyzed using the procedure outlined in §3.3.4. As artificial redshift increases, the number of radial bins decreases while the size of each bin increases. Fewer radial bins results in a less detailed sampling of an entropy profile's overall curvature, while the larger bins mask the entropy-profile flattening because each bin, particularly the bins nearest the elbow of an entropy profile, encompass a broad range of entropy. Over the redshift range $z = 0.1 - 0.3$,

the increased size of the radial bins (and hence broader range of entropy per bin) dominates, resulting in entropy profiles which have obvious flattened cores, but the entropy measured in each bin has increased. Consequently, best-fit K_0 also increases, on average, as $(K_0' - K_0)/K_0 = 2.12 \pm 1.84$ where K_0 is the original best-fit value and K_0' is the best-fit value of the degraded profiles. But, when $z > 0.3$, the degraded entropy profiles severely under sample both the core flattening and overall profile curvature, resulting in most entropy profiles resembling power-laws with a centralmost bin that deviates only slightly from the power-law at larger radii. This translates into a modest increase of best-fit K_0 which, on average, is $(K_0' - K_0)/K_0 = 0.71 \pm 0.57$. However, there is a caveat to our analysis of the degraded entropy profiles: the size of the region over which the original entropy profiles flatten is not uniform. Hence, for clusters with small flattened cores ($r \lesssim 20$ kpc), degradation of the profiles will more quickly mask out the flattening, and vice versa for the clusters with large cores. It is also worth noting that as redshift increases the best-fit power law indices (α) become shallower (*i.e.* significantly less than 1.1), the errors on K_0 and α increase, and based on χ^2, the power-law only model fits drastically improve – though it is still not a better fit than the model with K_0.

3.4.3 Profile Curvature and Number of Bins

Our analysis of the degraded entropy profiles suggests that K_0 is more sensitive to the value of $K(r)$ in the central bins than it is to the shape of the profile or the number of radial bins. However, for completeness we investigate in this section: (1) if there is a correlation between best-fit K_0 and the curvature of an entropy profile, and (2) if the number of radial bins correlates with best-fit K_0. A systematic correlation of K_0 with these quantities means the estimates of K_0 might be biased by, for example, the curvature of the temperature profile outside the core or by the signal-to-noise of an observation.

To check for a possible correlation between best-fit K_0 and profile curvature we first calculated average profile curvatures, κ_A. For each profile, κ_A was calculated using the standard formulation for the curvature of a function, $\kappa = \|y''\|/(1+y'^2)^{3/2}$, where we set $y = K(r) = K_0 + K_{100}(r/100\mathrm{kpc})^{\alpha}$. This derivation yields,

$$\kappa_A = \frac{\int \frac{\|100^{-\alpha}(\alpha-1)\alpha K_{100} r^{\alpha-2}\|}{[1+(100^{-\alpha}\alpha K_{100} r^{\alpha-1})^2]^{3/2}} dr}{\int dr} \tag{3.6}$$

where α and K_{100} are the best-fit parameters unique to each entropy profile. The integral over all space ensures we evaluate the curvature of each profile in the limit where the profiles have asymptotically approached a constant at small radii and a power law at large radii. We find that at any value of K_0 a large range of curvatures are covered and that there is no systematic trend in K_0 associated with κ_A (top left panel of Fig. 3.3). In addition, plots of best-fit K_0 versus the number of bins fit in each entropy profile do not reveal any trends, only scatter (top right panel of Fig. 3.3).

Our temperature profiles were created using a minimum number of counts per annulus criterion. One can therefore ask if the length of an observation or the number of bins in the temperature profile correlates with best-fit K_0. Shown in the bottom left and right panels of Fig. 3.3 are K_0 versus the total used exposure time for that cluster and K_0 versus number of bins in the temperature profile, respectively. We do not find trends with K_0 in either comparison.

As expected, we do not find any systematic trends with profile shape, number of bins fit in $K(r)$, exposure time, or number of bins in $kT_{\mathrm{X}}(r)$ which would significantly affect our best-fit K_0 values. Thus, we conclude that the K_0 values discussed in this chapter are, as intended, an adequate measure of the core entropy, and that any undetected dependence of K_0 on profile shape or radial resolution affect our results at significance levels much smaller than the measured uncertainties.

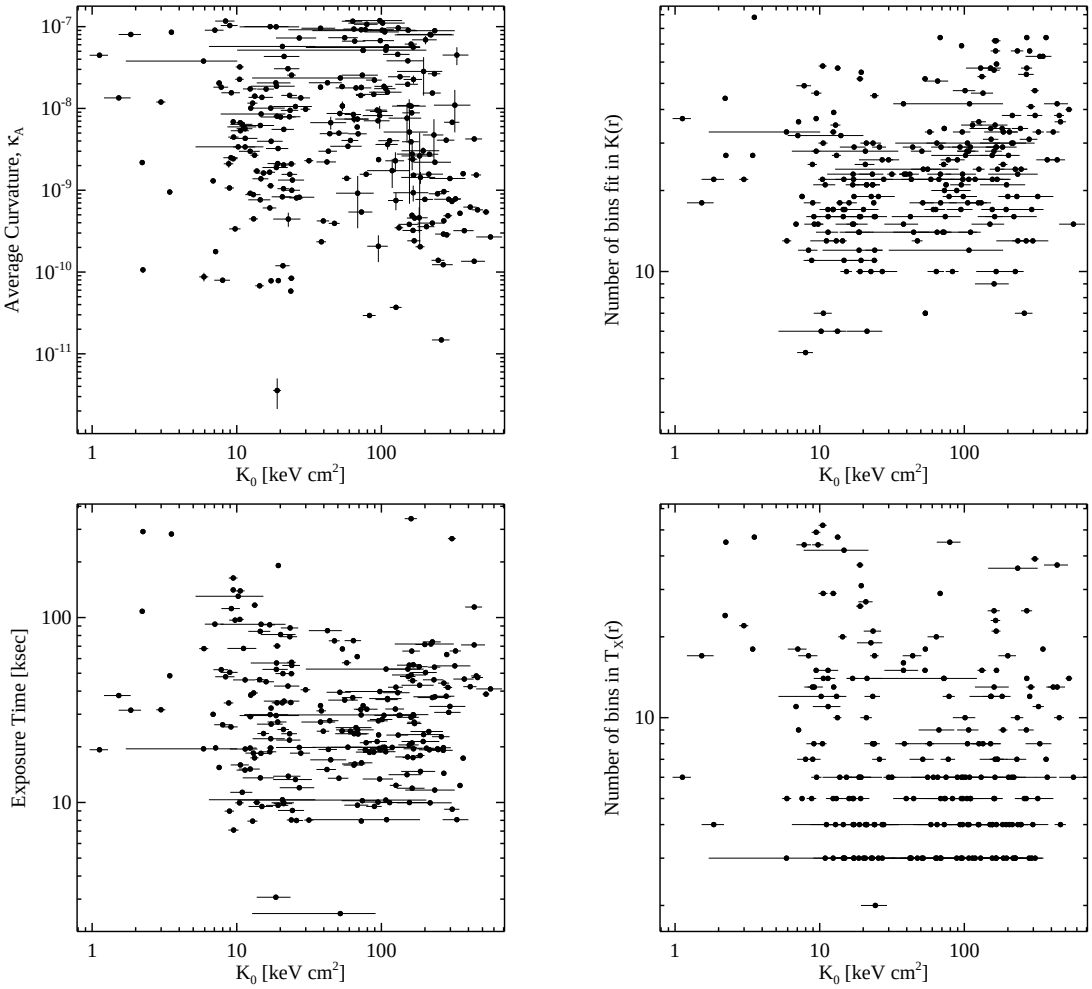

Figure 3.3 Plots of possible systematics versus best-fit K_0. *Top left:* Best-fit K_0 plotted versus average curvature of the corresponding entropy profile (see eq. 3.6) There is no trend between these two quantities suggesting that K_0 is not heavily influenced by the total shape of the entropy profile. *Top right:* Best-fit K_0 plotted versus number of bins in the entropy profile which were used during fitting. Again, no trend is found. *Bottom left:* Best-fit K_0 plotted versus the total used exposure time for each cluster. No trend is found. *Bottom right:* Best-fit K_0 plotted versus the number of bins in the temperature profile for each cluster. As expected, fewer $kT_{\rm X}(r)$ does not correlate with K_0.

3.4.4 Power-law Profiles

Equation 3.4 is a special case of eq. 3.5 with $K_0 = 0$, meaning that the models we fit to $K(r)$ are nested. A comparison between the p-values (shown in Table B.5) of each cluster's best-fit models shows which model exhibits more agreement with the data. In addition, for each fit in Table B.5 we show the deviation in units of sigma, σ_{K_0}, of the best-fit K_0 value from zero. We also show in Table B.4 the number of clusters and the percentage of the sample which have a K_0 statistically consistent with zero at various confidence levels. Table B.4 shows that at the 3σ significance level $\sim 10\%$ of the full *ACCEPT* sample has a best-fit K_0 value which is consistent with zero. Moreover, that there is a systematic trend for a single power-law to be a poor fit mainly at the smallest radii suggests non-zero K_0 is not random.

An important question regarding our entropy profiles is what fraction of the full *ACCEPT* and *HIFLUGCS* samples are well-represented by the power-law only model and/or the power-law plus constant core entropy model? The fitting routine we used to find the best-fit entropy models to our data is a least-squares minimizer which outputs a chi-square value. Assuming chi-square is the statistic describing the probability distribution, the number of degrees of freedom and χ^2 values can be used to calculate a p-value. For the discussion presented below, we have adopted the conventional significance criterion which says if p-value > 0.05, then the null hypothesis cannot be rejected, assuming the null hypothesis is "the" true model. The null hypotheses in the case of our models are that $K(r)$ is best modeled as a power-law only (eqn. 3.5) or a power-law plus constant term (eqn. 3.4).

Note that p-values can only determine if the null hypothesis can be significantly rejected. We stress that p-values do not represent the probability that the null hypothesis is correct, nor do p-values measure the significance of the best-fit model

compared to the null hypothesis. These are both incorrect intepretations. To judge the quality of the best-fit models, specifically in relation to one another, other quantities must be brought to bear such as the significance of K_0 away from zero, the actual values of χ^2, and the typical uncertainty associated with the data.

The fractions provided in Table B.4 represent the number of clusters in the sample which are well-represented by our $K(r)$ models where "well-represented" is defined as any model which has a p-value > 0.05. The fractions are independent of each other, hence they do not sum to unity. It may appear odd that for several sub-groups there are a large fraction of the clusters for which the power-law only model cannot be rejected. But in Table B.5 we show that most clusters have best-fit K_0 values which are several σ_{K_0} greater than zero. The number and percentage of clusters with K_0 statistically consistent with zero at various confidence levels are given in Table B.4. Even at 3σ significance only $\sim 10\%$ of the full *ACCEPT* sample has a best-fit K_0 value which is consistent with zero.

So while it is tempting to think the p-values are implying the power-law model is sufficient to describe $K(r)$ for $\sim 60\%$ of the *ACCEPT* sample, this is not a proper interpretation of the p-values and conflicts with the fact that at least $\sim 90\%$ of the sample have significant non-zero K_0. Equation 3.4 is a special case of eqn. 3.5 with $K_0 = 0$, *e.g.* the models we fit to $K(r)$ are nested. In addition, the added parameter has an acceptable best-fit value, $K_0 = 0$, which lies on the boundary of the parameter space. While under these conditions χ^2, associated p-values, and F-tests are not useful in determining which model is the "best" description of $K(r)$, comparison of the χ^2 values for each fit imply, even if only qualitatively, which model shows more agreement with the data. We have made a comparison of the models using an F-test to determine if the addition of the K_0 parameter made a significant improvement in the best-fit. For all clusters, the addition of a K_0 term was found to be warranted, although it is not obvious that an F-test yields any information given the models are

nested. Moreover, that there is a systematic trend for a single power-law to be a poor fit mainly at the smallest radii suggests non-zero K_0 is not random.

Of the 239 clusters in *ACCEPT*, only four clusters have a K_0 value which is statistically consistent with zero (at 1σ), or are better fit by the power-law only model (based on comparison of reduced χ^2): A2151, AS0405, MS 0116.3-0115, and NGC 507[7]. Two additional clusters, A1991 and A4059, are better fit by the power-law model only when interpolation of the temperature profile in the core is not constant (see §3.3.1). We find that the entropy model which approaches a constant core entropy at small radii appears to be a better descriptor of the radial entropy distribution for most *ACCEPT* clusters. However, we cannot rule out the power-law only model, but do point out that $\sim 90\%$ of clusters have best-fit K_0 values greater than zero at $> 3\sigma$ significance.

3.5 Results and Discussion

Presented in Figure 3.4 is a montage of *ACCEPT* entropy profiles for different temperature ranges. These figures highlight the cornerstone result of *ACCEPT*: a uniformly analyzed collection of entropy profiles covering a broad range of core entropy. Each profile is color-coded to represent the global cluster temperature. Plotted in each panel of Fig. 3.4 are the mean profiles representing $K_0 \leq 50$keV cm^2 clusters (dashed-line) and $K_0 > 50$keV cm^2 clusters (dashed-dotted line), in addition to the pure-cooling model of Voit et al. (2002) (solid black line). The theoretical pure-cooling curve represents the entropy profile of a 5 keV cluster simulated with radiative cooling but no feedback and gives us a useful baseline against which to compare *ACCEPT* profiles.

In the following sections we discuss results gleaned from analysis of our library of entropy profiles. These results include the departure of most entropy profiles from

[7]NGC 507 is part of *HIFLUGCS* analysis only

a simple radial power-law profile, the bimodal distribution of core entropy, and the asymptotic convergence of the entropy profiles to the self-similar $K(r) \propto r^{1.1-1.2}$ power-law at $r \geq 100$kpc.

3.5.1 Non-Zero Core Entropy

Arguably the most striking feature of Figure 3.4 is the departure of most profiles from a simple power-law. Core flattening of surface brightness profiles (and consequently density profiles) is a well known feature of clusters (*e.g.* Jones & Forman 1984, Mohr et al. 1999 and Xue & Wu 2000). What is notable in our work however is that, based on comparison of reduced χ^2 and significance of K_0, very few of the clusters in our sample have an entropy distribution which is best-fit by the power-law only model (eq. 3.5), rather they are sufficiently well-described by the model which flattens in the core (eq. 3.4).

For clusters with central cooling times shorter than the age of the cluster, non-zero core entropy is an expected consequence of episodic heating of the ICM (Voit & Donahue, 2005), with AGN as one possible heating source (Bower, 1997; Loewenstein, 2000; Voit & Bryan, 2001; Soker et al., 2001; Churazov et al., 2002; Brüggen & Kaiser, 2002; Brüggen et al., 2002; Nath & Roychowdhury, 2002; Ruszkowski & Begelman, 2002; Alexander, 2002; Omma et al., 2004; McCarthy et al., 2004; Roychowdhury et al., 2004; Hoeft & Brüggen, 2004; Dalla Vecchia et al., 2004; Soker & Pizzolato, 2005; Pizzolato & Soker, 2005; Brighenti & Mathews, 2006; Mathews et al., 2006). Clusters with cooling times of order the age of the Universe, however, require other mechanisms to generate their core entropy, for example via mergers or extremely energetic AGN outbursts. For the very highest K_0 values, $K_0 > 100$keV cm^2, the mechanism by which the core entropy came to be so large is not well understood as it is difficult to boost the entropy of a gas parcel to > 100keV cm^2 via merger shocks

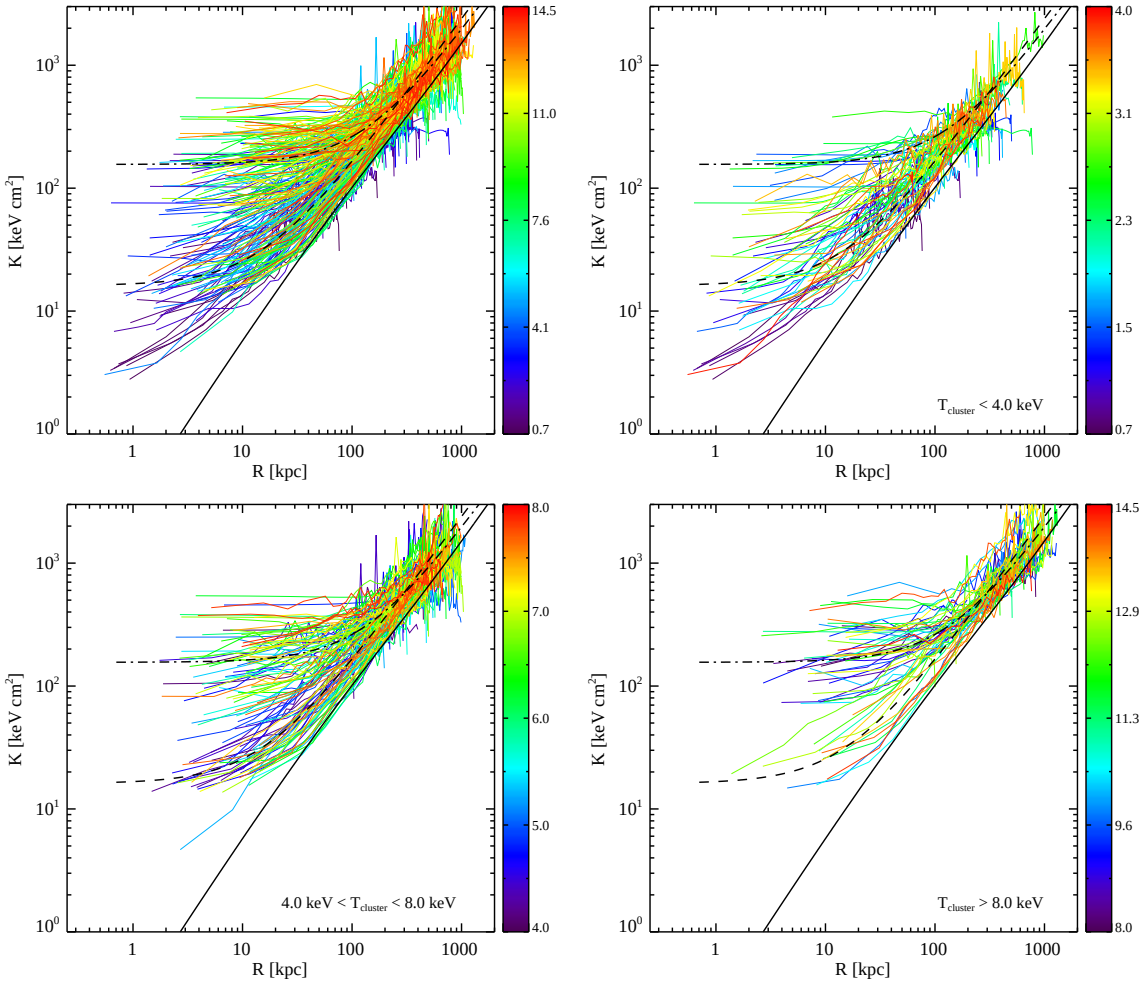

Figure 3.4 Composite plots of entropy profiles for varying cluster temperature ranges. Profiles are color-coded based on average cluster temperature. Units of the color bars are keV. The solid line is the pure-cooling model of Voit et al. (2002), the dashed line is the mean profile for clusters with $K_0 \leq 50$keV cm^2, and the dashed-dotted line is the mean profile for clusters with $K_0 > 50$keV cm^2. *Top left:* This panel contains all the entropy profiles in our study. *Top right:* Clusters with $kT_X < 4$ keV. *Bottom left:* Clusters with 4keV $< kT_X <$ 8keV. *Bottom right:* Clusters with $kT_X > 8$ keV. Note that while the dispersion of core entropy for each temperature range is large, as the kT_X range increases so to does the mean core entropy.

(McCarthy et al., 2008) and would require AGN outburst energies which have never been observed. We are providing the data and results of *ACCEPT* to the public with the hope that the research community finds it a useful new resource to further understand the processes which result in non-zero cluster core entropy.

3.5.2 Bimodality of Core Entropy Distribution

The time required for a gas parcel to radiate away its thermal energy is a function of the gas entropy. Low entropy gas radiates profusely and is thus subject to rapid cooling, and vice versa for high entropy gas. Hence, the distribution of K_0 is of particular interest because it is an approximate indicator of the cooling timescale in the cluster core. The K_0 distribution is also interesting because it may be useful in better understanding the physical processes operating in cluster cores. For example, if processes such as thermal conduction and AGN feedback are important in establishing the entropy state of cluster cores, then models which properly incorporate these processes should approximately reproduce the observed K_0 distribution.

In the top panel of Figure 3.5 is plotted the logarithmically binned distribution of K_0. In the bottom panel of Figure 3.5 is plotted the cumulative distribution of K_0. One can immediately see from these distributions that there are at least two distinct populations separated by a smaller number of clusters with $K_0 \approx 30 - 50\mathrm{keV\ cm}^2$. If the distinct bimodality of the K_0 distribution seen in the binned histogram were an artifact of binning, then the cumulative distribution should be relatively smooth. But, there is clearly a plateau in the cumulative distribution which coincides with the division between the two populations at $K_0 \approx 30 - 50\mathrm{keV\ cm}^2$. We have tested re-binning the K_0 histogram using the optimized binning techniques outlined in Knuth (2006) and Hogg (2008) and find no change in the bimodality or range of the gap in K_0 versus using naive fixed-width bins.

To further test for the presence of a bimodal population, we utilized the KMM test

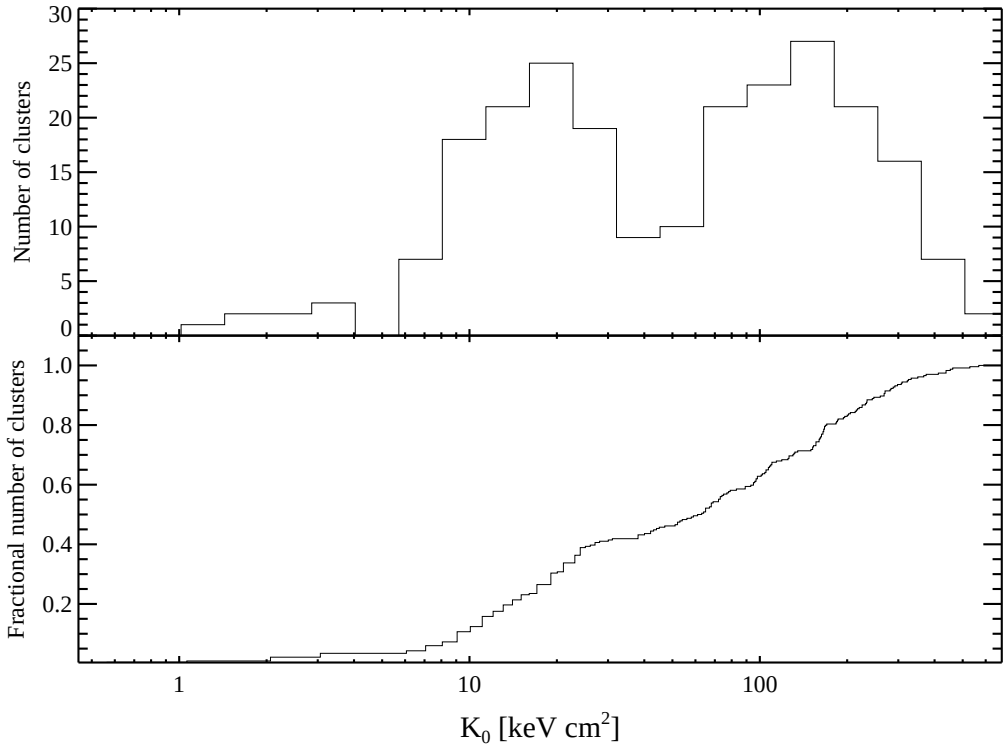

Figure 3.5 *Top panel:* Histogram of best-fit K_0 for all the clusters in *ACCEPT*. Bin widths are 0.15 in log space. *Bottom panel:* Cumulative distribution of K_0 values for the full sample. The distinct bimodality in K_0 is present in both distributions, which would not be seen if it were an artifact of the histogram binning. A KMM test finds the K_0 distribution cannot arise from a simple unimodal Gaussian.

of Ashman et al. (1994). The KMM test estimates the probability that a set of data points is better described by the sum of multiple Gaussians than by a single Gaussian. We tested the unimodal case versus the bimodal case under the assumption that the dispersion of the two Gaussian components are not the same. We have used the updated KMM code of Waters et al. (2009) which incorporates bootstrap resampling to determine uncertainties for all parameters. A post-analysis comparison of fits assuming the populations have the same and different dispersions confirms our initial guess that the dispersions are different is a better model.

The KMM test, as with any statistical test, is very specific. At zeroth order, the KMM test simply determines if a population is unimodal or not, and finds the means of these populations. However, the dispersions of these populations are subject to the quality of sampling and the presence of outliers (*e.g.* KMM must assign all data points to a population). The outputs of the KMM test are the best-fit populations to the data, not necessarily the best-fit populations of the underlying distribution (hence no goodness of fit is output). However, the KMM test does output a p-value, and with the assumption that χ^2 describes the distribution of the likelihood ratio statistic, p is the confidence interval for the null hypothesis.

There are a small number of clusters with $K_0 \leq 4$keV cm^2 that when included in the KMM test significantly change the results. Thus, we conducted tests including and excluding $K_0 \leq 4$keV cm^2 clusters and provide two sets of best-fit parameters. The results of the bimodal KMM test neglecting $K_0 \leq 4$keV cm^2 clusters were two statistically distinct peaks at $K_1 = 17.8 \pm 6.6$keV cm^2 and $K_2 = 154 \pm 52$keV cm^2. 124 clusters were assigned to the first distribution, while 109 were assigned to the second. Including $K_0 \leq 4$keV cm^2 clusters, the bimodal KMM test found populations at $K_1 = 15.0 \pm 5.0$keV cm^2 (89 clusters) and $K_2 = 129 \pm 45$keV cm^2 (136 clusters). The bimodal KMM test neglecting $K_0 \leq 4$keV cm^2 clusters returned $p = 1.16 \times 10^{-7}$, while the test including all clusters returned $p = 1.90 \times 10^{-13}$. These tiny p-values

indicate the unimodal distribution is significantly rejected as the parent distribution of the observed K_0 distribution. We also checked for bimodality as a function of redshift by making cuts in redshift space and running the KMM test using each new distribution. The KMM test indicated that two statistically distinct populations were not present when the redshift range was restricted to clusters with $z > 0.4$. For all other redshift cuts the K_0 distribution was bimodal. There are 20 clusters with $z > 0.4$, and we suspected this was too few clusters to detect two populations. As a test, we randomly selected 20 clusters from our full sample 1000 times and ran the KMM test. A bimodal population was found in 2% of the trials, suggesting the lack of bimodality at $z > 0.4$ is a result of poor statistics.

We pointed out in §3.3.4 that for some clusters in our archival sample, the different interpolation schemes for the centralmost bins of the cluster temperature profiles yielded significantly different K_0 values (see Fig. 3.1). Using the K_0 values derived using temperature profiles which were allowed to decline in the centralmost bins (see §3.3.4), we repeated the above analysis checking for bimodality. We find that bimodality is present using these K_0 values and that the best-fit values from the KMM test are not significantly different for either scheme. Our result of finding bimodality in the K_0 population is robust to the choice of temperature profile interpolation scheme.

One possible explanation for a bimodal core entropy distribution is that it arises from the effects of episodic AGN feedback and electron thermal conduction in the cluster core. Voit & Donahue (2005) outlined a model of AGN feedback whereby outbursts of $\sim 10^{45}$erg s^{-1} occurring every $\sim 10^{8}$yrs can maintain a quasi-steady core entropy of $\approx 10 - 30$keV cm^2. In addition, very energetic and infrequent AGN outbursts of $\geq 10^{61}$erg can increase the core entropy into the $\approx 30-50$keV cm^2 range (Voit & Donahue, 2005). This model of AGN feedback satisfactorily explains the distribution of $K_0 \lesssim 50$keV cm^2, but depletion of the $K_0 = 30 - 50$keV cm^2 region and

populating $K_0 > 50$keV cm^2 requires more physics. Voit et al. (2008) have recently suggested that the dramatic fall-off of clusters beginning at $K_0 \approx 30$keV cm^2 may be the result of electron thermal conduction. After K_0 has exceeded ≈ 30keV cm^2, conduction could severely slow, if not halt, a cluster's core from appreciably cooling and returning to a core entropy state with $K_0 < 30$keV cm^2. Merger shocks can then readily raise K_0 values to $\gtrsim 100$keV cm^2. This model is supported by results presented in Cavagnolo et al. (2008a), Guo et al. (2008), and **?** which find that the formation of thermal instabilities and signatures of ongoing feedback and star formation are extremely sensitive to the core entropy state of a cluster.

We acknowledge that *ACCEPT* is not a complete, uniformly selected sample of clusters. This raises the possibility that our sample is biased towards clusters that have historically drawn the attention of observers, such as cooling flows or mergers. If that were the case, then one reasonable explanation of the K_0 bimodality is that $K_0 = 30 - 50$keV cm^2 clusters have not been the focus of much scientific interest and thus go unobserved. However, as we show in §3.5.4, the complete flux-limited *HIFLUGCS* sample is also bimodal. Nevertheless, flux-limited samples do suffer from some inadequacies and further study of a carefully selected sample of clusters, chosen either from our own archival sample or using representative, rather than complete, samples such as REXCESS (Böhringer et al., 2007), may be warranted.

3.5.3 The *HIFLUGCS* Sub-Sample

ACCEPT is not a flux-limited or volume-limited sample. To ensure our results are not affected by an unknown selection bias, we culled the *HIFLUGCS* sample from *ACCEPT* for separate analysis. *HIFLUGCS* is a flux-limited sample ($f_X \geq 2 \times 10^{-11}$erg s^{-1} cm^{-2}) selected from the *REFLEX* sample (Böhringer et al., 2004) with no consideration of morphology. Thus, at any given luminosity in *HIFLUGCS* there is a good sampling of different morphologies, *i.e.* possible bias toward cool-core clusters

or mergers has been removed. The sample also covers most of the sky with holes near Virgo and the Large and Small Magellanic Clouds, and has no known incompleteness (Chen et al., 2007). There are a total of 106 objects in *HIFLUGCS*: 63 in the primary sample and 43 in the extended sample. Of these 106 objects, no public *Chandra* observations were available for 16 objects (A548e, A548w, A1775, A1800, A3528n, A3530, A3532, A3560, A3695, A3827, A3888, AS0636, HCG 94, IC 1365, NGC 499, RXCJ 2344.2-0422), 6 objects did not meet our minimum analysis requirements and were thus insufficient for study (3C 129, A1367, A2634, A2877, A3627, Triangulum Australis), and as discussed in §3.2, Coma and Fornax were intentionally ignored. This left a total of 82 *HIFLUGCS* objects which we analyzed, 59 from the primary sample ($\sim 94\%$ complete) and 23 from the extended sample ($\sim 50\%$ complete). The primary sample is the more complete of the two, thus we focus our following discussion on the primary sample only.

The clusters missing from the primary *HIFLUGCS* sample are A1367, A2634, Coma, and Fornax. The extent to which these 4 clusters can change our analysis of the K_0 distribution for *HIFLUGCS* is limited. To alter or wash-out bimodality, all 4 clusters would need to fall in the range $K_0 = 30 - 50$keV cm^2, which is certainly not the case for any of these clusters. A1367 has been studied by Donnelly et al. (1998) and Sun & Murray (2002), with both finding that two sub-clusters are merging in the cluster. The merger process, and the potential for associated shock formation, is known to create large increases of gas entropy (McCarthy et al., 2007). Given the combination of low surface brightness, moderate temperatures ($kT_X = 3.5 - 5.0$ keV), lack of a temperature gradient, ongoing merger, and presence of a shock, it is unlikely A1367 has a core entropy $\lesssim 50$keV cm^2. A2634 is a very low surface brightness cluster with the bright radio source 3C 465 at the center of an X-ray coronae (Sun et al., 2007). Clusters with comparable properties to A2634 are not found to have $K_0 \lesssim 50$keV cm^2. Coma and Fornax are known to have core entropy > 50keV cm^2

(?).

Shown in Figure 3.6 are the log-binned (top panel) and cumulative (bottom panel) K_0 distributions of the *HIFLUGCS* primary sample. The bimodality seen in the full *ACCEPT* collection is also present in the *HIFLUGCS* sub-sample. Mean best-fit parameters are given in Table B.4. We again performed two KMM tests: one test with, and another test without, clusters having $K_0 \leq 4$keV cm^2. For the test including $K_0 \leq 4$keV cm^2 clusters we find populations at $K_1 = 9.7 \pm 3.5$keV cm^2 (28 clusters) and $K_2 = 131 \pm 46$keV cm^2 (31 clusters) with $p = 3.34 \times 10^{-3}$. Excluding clusters with $K_0 \leq 4$keV cm^2 we find peaks at $K_1 = 10.5 \pm 3.4$keV cm^2 and $K_2 = 116 \pm 42$keV cm^2, each having 21 and 34 clusters, respectively, and $p = 1.55 \times 10^{-5}$.

Hudson & Reiprich (2007) note a similar core entropy bimodality to the one we find here. Hudson & Reiprich (2007) discuss two distinct groupings of objects in a plot of average cluster temperature versus core entropy, with the dividing point being $K \approx 40$keV cm^2. Our results agree with the findings of Hudson & Reiprich (2007). While the gaps of *ACCEPT* and *HIFLUGCS* do not cover the same K_0 range, it is interesting that both gaps appear to be the deepest around $K_0 \approx 30$keV cm^2. That bimodality is present in both *ACCEPT* and the unbiased *HIFLUGCS* sub-sample suggests bimodality is not the result of simple archival bias.

3.5.4 Distribution of Core Cooling Times

In the X-ray regime, cooling time and entropy are related in that decreasing gas entropy also means shorter cooling time. Thus, if the K_0 distribution is bimodal, the distribution of cooling times should also be bimodal. We have calculated cooling time profiles from the spectral analysis using the relation

$$t_{\rm cool} = \frac{3nkT_X}{2n_{\rm e}n_{\rm H}\Lambda(T,Z)} \tag{3.7}$$

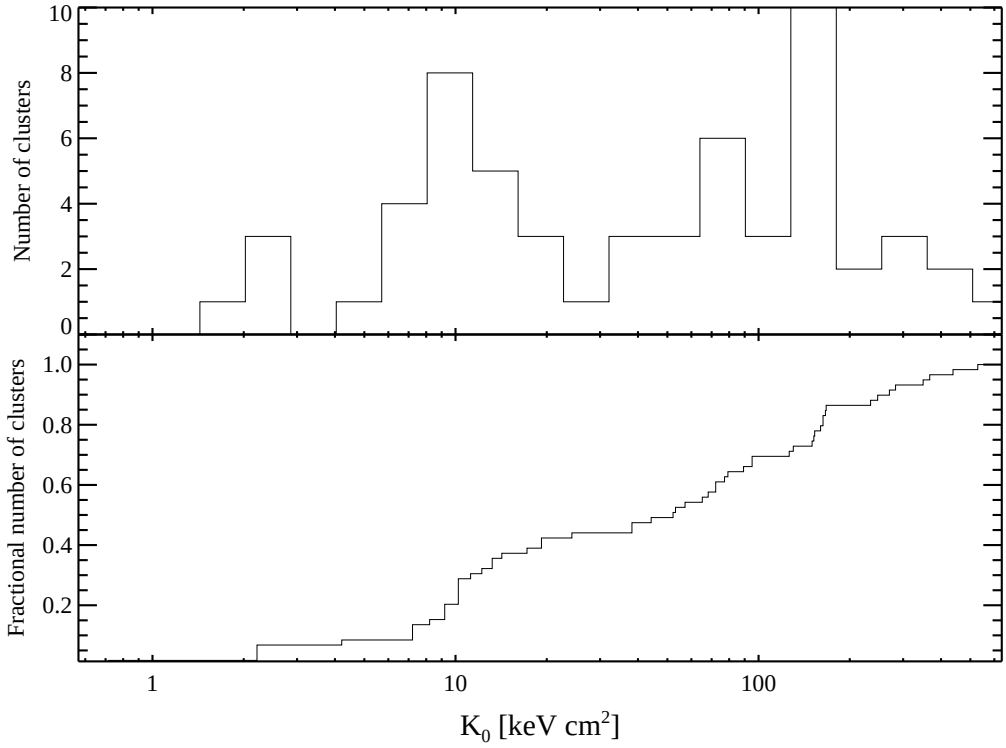

Figure 3.6 *Top panel:* Histogram of best-fit K_0 values for the primary *HIFLUGCS* sample. Bin widths are 0.15 in log space. *Bottom panel:* Cumulative distribution of best-fit K_0 values. The distinct bimodality seen in the full *ACCEPT* sample (Fig. 3.5) is also present in the *HIFLUGCS* subsample and shares the same gap between the low-entropy peak at 10-20 keV cm^2 and the high-entropy peak at 100-200 keV cm^2. That bimodality is present in both samples is strong evidence it is not a result of an unknown archival bias.

where n is the total number density ($\approx 2.3 n_{\rm H}$ for a fully ionized plasma), $n_{\rm e}$ and $n_{\rm H}$ are the electron and proton densities respectively, $\Lambda(T, Z)$ is the cooling function for a given temperature and metal abundance, and 3/2 is a constant associated with isochoric cooling. The values of the cooling function for each temperature profile bin were calculated in XSPEC using the flux of the best-fit spectral model. Following the procedure discussed in §3.3.4, Λ and kT_X were interpolated across the radial grid of the electron density profile. The cooling time profiles were then fit with a simple model analogous to that used for fitting $K(r)$:

$$t_{\rm cool}(r) = t_{c0} + t_{100} \left(\frac{r}{100{\rm kpc}} \right)^{\alpha} \tag{3.8}$$

where t_{c0} is core cooling time and t_{100} is a normalization at 100 kpc.

The K_0 distribution can also be used to explore the distribution of core cooling times. Assuming free-free interactions are the dominant gas cooling mechanism (*i.e.* $\epsilon \propto T^{1/2}$), Donahue et al. (2005) show that entropy is related to cooling time via the formulation:

$$t_{c0}(K_0) \approx 10^8 {\rm yrs} \left(\frac{K_0}{10{\rm keVcm}^2} \right)^{3/2} \left(\frac{kT_X}{5{\rm keV}} \right)^{-1}. \tag{3.9}$$

Shown in Figure 3.7 is the logarithmically binned and cumulative distributions of best-fit core cooling times from eq. 3.8 (top panel) and core cooling times calculated using eq. 3.9 (bottom panel). The bin widths in both histograms are 0.20 in log-space. The pile-up of cluster core cooling times below 1 Gyr is well known, for example in Hu et al. (1985) or more recently in Dunn & Fabian (2008). In addition, the core cooling times we calculate are consistent with the results of other cooling time studies, such as Peres et al. (1998) or **?**. However, what is most important about Fig. 3.7 is that the distinct bimodality of the K_0 distribution is also present in best-fit core cooling time, t_{c0}. A KMM bimodality test using t_{c0} found peaks at $t_{c1} = 0.60 \pm 0.24$Gyr and $t_{c2} = 6.23 \pm 2.19$Gyr with 132 and 101 objects in each respective population. The

probability that the unimodal distribution is a better fit was once again exceedingly small, $p = 8.77 \times 10^{-7}$.

The bimodality we observe in the cooling-time distribution is not as pronounced as what we see in the K_0 distribution, suggesting that the bimodality in entropy might be easier to observe. Since cooling time profiles are more sensitive to the resolution of the temperature profiles than are the entropy profiles, it may be that resolution effects more seriously limit the quantification of the true cooling time of the core. For example, if our temperature interpolation scheme is too coarse, or averaging over many small-scale temperature fluctuations significantly increases t_{c0}, then t_{c0} would not be the best approximation of true core cooling time. In which case, the core cooling times might be shorter and the sharpness and offset of the distribution gaps may not be as distinct.

3.5.5 Slope and Normalization of Power-law Components

Beyond $r \approx 100$kpc the entropy profiles show a striking similarity in the slope of the power-law component which is independent of K_0. For the full sample, the mean value of the power-law normalization at large radii, $\alpha = 1.21 \pm 0.39$. For clusters with $K_0 < 50$keV cm^2, the mean $\alpha = 1.20 \pm 0.38$, and for clusters with $K_0 \geq 50$keV cm^2, the mean $\alpha = 1.23 \pm 0.40$. Our mean slope of $\alpha \approx 1.2$ is not statistically different from the theoretical value of $\alpha = 1.1$ found by Tozzi & Norman (2001) using semi-analytic models and $\alpha = 1.2$ found by Voit et al. (2005) using models with gravitational effects only. For the full sample, the mean value of $K_{100} = 126 \pm 45$keV cm^2. Again distinguishing between clusters below and above $K_0 = 50$keV cm^2, we find $K_{100} = 150 \pm 50$keV cm^2 and $K_{100} = 107 \pm 39$keV cm^2, respectively. Scaling each entropy profile by the cluster virial temperature and virial radius considerably reduces the dispersion in K_{100}, but we reserve detailed discussion of scaling relations for a future paper.

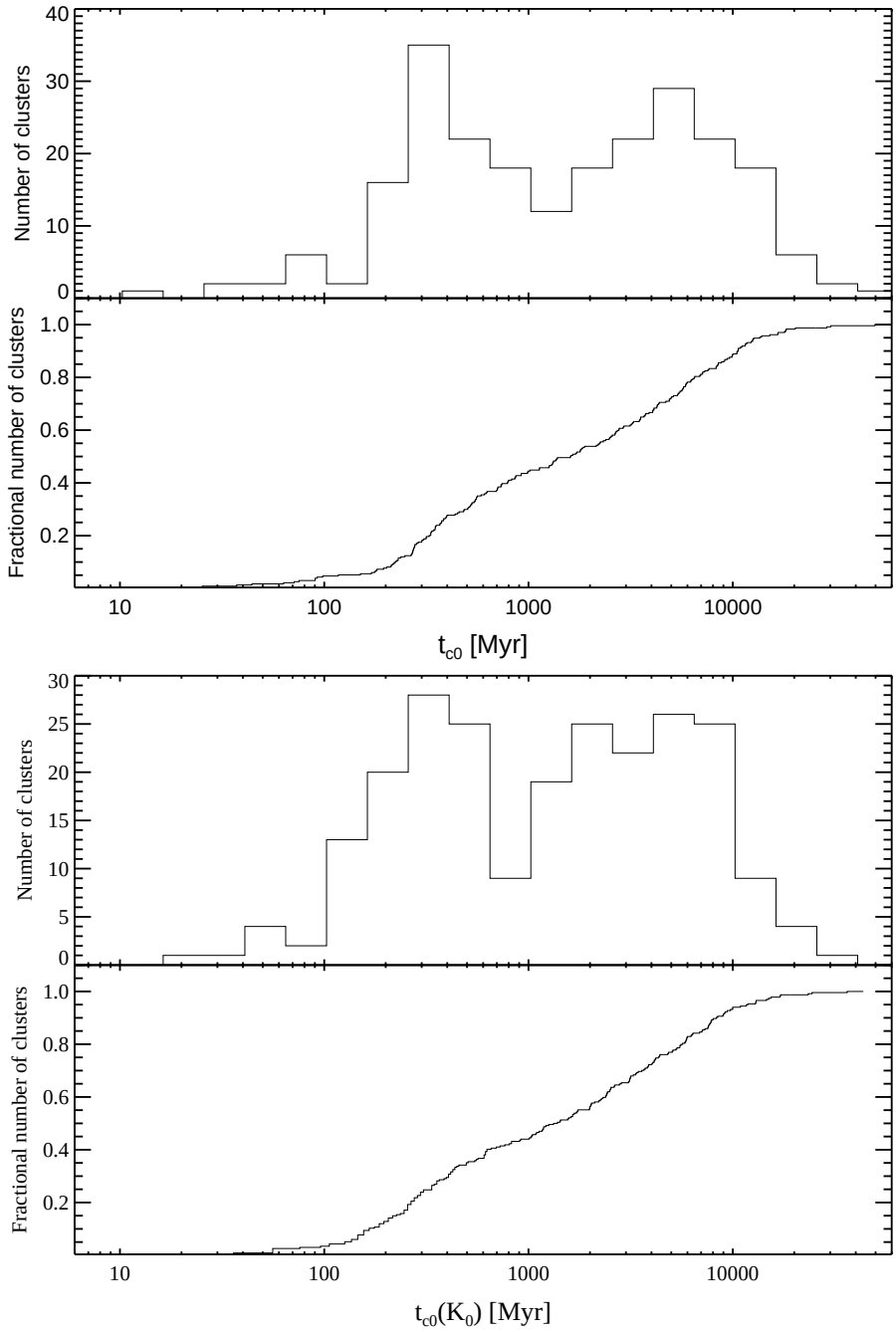

Figure 3.7 *Top panel:* Log-binned histogram and cumulative distribution of best-fit core cooling times, t_{c0} (eqn. 3.8), for all the clusters in *ACCEPT*. Histogram bin widths are 0.2 in log space. *Bottom panel:* Log-binned histogram and cumulative distribution of core cooling times calculated from best-fit K_0 values, $t_{c0}(K_0)$ (eqn. 3.9), for all the clusters in *ACCEPT*. Histogram bin widths are 0.2 in log space. The bimodality we observe in the K_0 distribution is also present in best-fit t_{c0}. However, the gaps between the two populations of t_{c0} and $t_{c0}(K_0)$ differ by ~ 0.3 Gyrs which may be an artifact of the binning.

3.5.6 Comparison of *ACCEPT* with Other Entropy Studies

Studies Using *XMM-Newton*

In §3.4.2 we presented our analysis of the angular resolution effects on entropy profiles. In addition to the analysis shown there, we have also investigated why previous analyses of *XMM-Newton* data have found that the entropy profiles of clusters are adequately fit by simple power laws. For this investigation we have performed the degradation analysis presented in §3.4.2 on all clusters which have a published entropy profile derived using *XMM-Newton* data and have been observed with *Chandra*. These clusters are: 2A 0335+096, A262, A399, A426, A478, A496, A1068, A1413, A1795, A1835, A1991, A2034, A2052, A2204, A2597, A2717, A3112, A4059, Hydra A, MKW3S, PKS 0745-191, and Sersic 159-03. *XMM-Newton* analyses of these clusters were presented in Piffaretti et al. (2005) and Pratt et al. (2006). Below we briefly highlight some of the important analysis methods used in these two studies.

Piffaretti et al. (2005) analyzed *XMM-Newton* data for a sample of 17 cooling flow clusters in the temperature range $kT_X = 1 - 7$ keV taken from Kaastra et al. (2004). The entropy profiles presented in Piffaretti et al. (2005) were derived using the PSF-corrected, deprojected spectral analysis presented in Kaastra et al. (2004). The temperature and density profiles were generated using approximately 8 radial annuli per cluster, in which the spectral analysis was restricted to the energy range 0.2-10.0 keV. The small number of annuli used to derive entropy profiles in the Piffaretti et al. (2005) analysis results in a much coarser angular scale than is presented in *ACCEPT*. Piffaretti et al. (2005) found no evidence for isentropic cores in their sample, that the entropy profiles increased monotonically outward, and that the profiles had a mean power law index of $\alpha = 0.95 \pm 0.02$, which is shallower than the mean α we find in *ACCEPT*. However, the width of the innermost radial bin in the Piffaretti et al. (2005) analysis was never less than $0.01 r_{virial}$, and they found the dispersion of entropy in the innermost bins to be greater than at larger radii, strongly suggesting

that profile flattening in the core was not resolved.

Pratt et al. (2006) used a sample of 10 relaxed systems observed with *XMM-Newton* at $z < 0.2$ with temperatures in the range $kT_X \approx 2.5 - 8$ keV. Entropy profiles were derived using PSF-corrected, deprojected temperature profiles and gas density profiles calculated from an analytical model fit to PSF convolved surface brightness profiles presented in Pointecouteau et al. (2005). The parametric models used in Pointecouteau et al. (2005) to fit the radial surface-brightness data were a double β-model, a β-model modified to allow for more centrally concentrated gas densities, and a triple β-model with all components having a common β value. The temperature profiles had bin sizes of at least $15''$. Like Piffaretti et al. (2005), Pratt et al. (2006) found no isentropic cores and that all the entropy profiles increased monotonically outward. Pratt et al. (2006) did however find $< 20\%$ dispersion in entropy at $r > 0.1r_{200}$ and $> 60\%$ dispersion at $r \sim 0.02r_{200}$ in addition to a mean power law index of $\alpha = 1.08 \pm 0.04$, again suggesting the presence of unresolved flattened cores. However, Pratt et al. (2006) do note that, "the slope of the [entropy] profile becomes shallower towards the centre in some of the clusters." This suggests that had a power-law model with a core term, such as K_0, been used, some central flattening might have been detected. In fact, a few of the Pratt et al. (2006) entropy profiles, for example those of A2204 or A2597, clearly lie below the best-fit power law as they enter the cluster core and then flatten back out in the central bin, suggesting that they might be better fit with a power-law plus a constant.

Utilizing the degradation analysis presented in §3.4.2, we repeated that analysis for the subsample of clusters with published entropy profiles derived from *XMM-Newton* data. We selected the degraded entropy profiles that had bins sizes similar to the bin sizes used in previous *XMM-Newton* analyses. For the degraded profiles, we found that core flattening is harder to detect due to the larger bins. Only clusters with the largest flattened cores (*e.g.* 2A0335, Sersic159, A1413) still had noticeable

entropy-profile curvature, while in contrast, clusters with the smallest cores (*e.g.* A3112, A1991, A4059) were as well fit by the power-law model as a model with non-zero K_0.

General Comparison of Results

There are many published studies of ICM entropy, and in this section we compare the general trends we find with the results of a few other studies. The studies with which we compare our results are:

1. Lloyd-Davies et al. (2000): *ROSAT* and *ASCA* data for 20 bound galaxy systems in the redshift range $z \approx 0.08 - 0.2$ and temperature range $kT_X \approx 0.5 - 14$ keV was used in this study. Lloyd-Davies et al. (2000) clearly show flattened entropy profiles for clusters with $K(r) > 100$keV cm^2 at $r \approx 0.01 r_{virial}$, while below this limit they find the entropy profiles trend downward like power laws. As we showed in §3.4.2 using degraded *XMM-Newton* data, the finding of power-law entropy profile behavior at small radii is most likely the result of not resolving the small flattened entropy cores in cool core clusters.

2. Ponman et al. (2003): This study used a sample of 66 systems, observed with *ROSAT* and *ASCA*, in the redshift range $z = 0.0036 - 0.208$ and temperature range $kT_X = 0.5 - 17$ keV and was the largest sample with which we compared our results. In general, the entropy profiles presented by Ponman et al. (2003) flatten inside $0.1 r_{200}$ irrespective of cluster temperature.

3. Morandi & Ettori (2007): Using *Chandra* data, this study examined 24 galaxy clusters with $kT_X > 6$ keV in the redshift range $z = 0.14 - 0.82$. Morandi & Ettori (2007) found the power law indices for various subsamples to be in the range $\alpha = 1 - 1.18$, and that all of the entropy profiles flatten at $r < 0.5 r_{2500}$. They also found best-fit K_0 values in the range $20 - 300$keV cm^2.

In general, we find good agreement between the properties of our entropy profiles and the profiles presented in the papers cited above, specifically that:

1. Cluster entropy profiles at $r \gtrsim 0.1 r_{virial}$ are well described by an entropy distribution which goes as $K(r) \propto r^{1.1-1.2}$.

2. The core regions ($r \lesssim 0.1 r_{virial}$) of clusters approach isentropic behavior as $r \to 0$, or in the cases where the observations do not resolve the core regions, the dispersion of entropy within the core region is considerably larger than the dispersion of the entropy at larger ($r \gtrsim 0.1 r_{virial}$) radii.

3. The above two properties are seen in the entropy profiles of clusters over a large range of redshifts ($0.05 \lesssim z \lesssim 0.5$), temperatures ($0.5\text{keV} \lesssim kT_X \lesssim 15\text{keV}$), and luminosities ($10^{43-45}$ ergs s^{-1}).

3.6 Summary and Conclusions

We have presented intracluster medium entropy profiles for a sample of 239 galaxy clusters (9.86 Msec) taken from the *Chandra* Data Archive. We have named this project *ACCEPT* for "Archive of Chandra Cluster Entropy Profile Tables." The reduced data products, data tables, figures, cluster images, and results of our analysis for all clusters and observations are freely available at the *ACCEPT* web site: http://www.pa.msu.edu/astro/MC2/accept. We encourage observers and theorists to utilize this library of entropy profiles in their own work.

We created radial temperature profiles using spectra extracted from a minimum of three concentric annuli containing 2500 counts each and extending to either the chip edge or $0.5 r_{180}$, whichever was smaller. We deprojected surface brightness profiles extracted from $5''$ bins over the energy range 0.7-2.0 keV to obtain the electron gas density as a function of radius. Entropy profiles were calculated from the density and temperature profiles as $K(r) = T(r) n(r)^{-2/3}$. Two models for the entropy

distribution were then fit to each profile: a power-law only model (eq. 3.5) and a power-law which approaches a constant value at small radii (eq. 3.4).

We have demonstrated that the entropy profiles for the majority of *ACCEPT* clusters are well-represented by the model which approaches a constant entropy, K_0, in the core. The entropy profiles of *ACCEPT* are also remarkably similar at radii greater than 100 kpc, and asymptotically approach the self-similar pure-cooling curve ($r \propto 1.2$) with a slope of $\alpha = 1.21 \pm 0.39$ (the dispersion here is in the sample, not in the uncertainty of the measurement). We also find that the distribution of K_0 for the full archival sample is bimodal with the two populations separated by a poorly populated region between $K_0 \approx 30-50$keV cm^2. After culling out the primary *HIFLUGCS* sub-sample of Reiprich (2001), we find the K_0 distribution of this complete sub-sample also to be bimodal, indicating that the bimodality we find in our larger sample does not result from archival bias.

When we compared our results with those of a few other entropy studies, specifically Lloyd-Davies et al. (2000), Ponman et al. (2003), Piffaretti et al. (2005), Pratt et al. (2006), and Morandi & Ettori (2007), we found the same general trends, noting however that Piffaretti et al. (2005) and Pratt et al. (2006) did not specifically find isentropic cores. However, those two studies did find large dispersion of entropy in the core region ($r < 0.1 r_{virial}$), suggesting that the broader bins used for analyzing the *XMM-Newton* data resulted in flattened entropy profiles not being resolved like they are using finer radial resolution and *Chandra* data.

Two core cooling times were derived for each cluster: (1) cooling time profiles were calculated using eq. 3.7 and each cooling time profile was then fit with eq. 3.8 returning a best-fit core cooling time, t_{c0}; (2) Using best-fit K_0 values, entropy was converted to a core cooling time, $t_{c0}(K_0)$ using eq. 3.9. We find the distributions of both core cooling times to be bimodal. Comparison of the core cooling times from method (1) and (2) reveals that the gap in the bimodal cooling time distributions

occur over different timescales, $\sim 2-3$ Gyrs for t_{c0}, and $\sim 0.7-1$ for $t_{c0}(K_0)$, but this offset may be the result of resolution limitations.

After analyzing an ensemble of artificially redshifted entropy profiles, we find the lack of $K_0 \lesssim 10\text{keV cm}^2$ clusters at $z > 0.1$ is most likely a result of resolution effects. Investigation of possible systematics affecting best-fit K_0 values, such as profile curvature and number of profile bins, revealed no trends which would significantly affect our results. We came to the conclusion that K_0 is an acceptable measure of average core entropy and is not overly influenced by profile shape or radial resolution. We also find that $\sim 90\%$ of the sample clusters have a best-fit K_0 more than 3σ away from zero.

Our results regarding non-zero core entropy and K_0 bimodality support the sharpening picture of how feedback and radiative cooling in clusters alter global cluster properties and affect massive galaxy formation. Among the many models of AGN feedback, Voit & Donahue (2005) outlined a model which specifically addresses how AGN outbursts generate and sustain non-zero core entropy in the regime of $K_0 \lesssim 30\text{keV cm}^2$ (see also Kaiser & Binney, 2003). In addition, if electron thermal conduction is an important process in clusters, then there exists a critical entropy threshold below which conduction is no longer efficient at wiping out thermal instabilities, the consequences of which should be a bimodal core entropy distribution and a sensitivity of cooling by-product formation (like star formation and AGN activity) to this entropy threshold (Voit et al., 2008; Guo et al., 2008). We show in Cavagnolo et al. (2008a) that indicators of feedback like Hα and radio emission are extremely sensitive to the lower bound of the gap in the bimodal distribution at $K_0 \approx 30\text{keV cm}^2$.

Many details are still missing from the emerging picture of the entropy life cycle in clusters, and there are many open questions regarding the evolution of the ICM and how thermal instabilities form in cluster cores. It is still unclear how clusters

with very high core entropy ($K_0 > 100$keV cm^2) are produced. Is an early episode of preheating necessary? And while resolution has restricted our ability to investigate a possible evolution of K_0 with redshift (which would suggest evolution in the cool-core cluster population), there may be other observational proxies which tightly correlate with K_0 and could then be used to study cluster cores at high-z. It is also becoming clear that the role of ICM magnetic fields can no longer be ignored. More specifically, how magnetohydrodynamic instabilities, such as MTI (Balbus, 2000; Quataert, 2008) and HBI (Parrish & Quataert, 2008), might impact the entropy structure of the ICM and formation of thermal instabilities needs to be investigated more thoroughly. We hope *ACCEPT* will be a useful resource in studying these questions.

3.7 Acknowledgements

KWC was supported in this work through *Chandra* X-ray Observatory Archive grants AR-6016X and AR-4017A. MD and MS acknowledge support from the NASA LTSA program NNG-05GD82G. The *Chandra* X-ray Observatory Center is operated by the Smithsonian Astrophysical Observatory for and on behalf of NASA under contract NAS8-03060. KWC thanks Chris Waters for supplying and supporting his new KMM code, Jim Linnemann for helpful suggestions regarding the error and statistical analysis presented in this chapter, and Brian McNamara for useful discussions. We especially thank Gabriel Pratt for sharing entropy profiles. We also thank the anonymous referee who's comments greatly improved the content of the referred publication. This research has made use of software provided by the Chandra X-ray Center in the application packages CIAO, Chips, and Sherpa. This research has made use of the NASA/IPAC Extragalactic Database which is operated by the Jet Propulsion Laboratory, California Institute of Technology, under contract with NASA. This research has also made use of NASA's Astrophysics Data System. Some software was obtained from the High Energy Astrophysics Science Archive Research Center, provided by

NASA's Goddard Space Flight Center.

3.8 Supplemental Cluster Notes

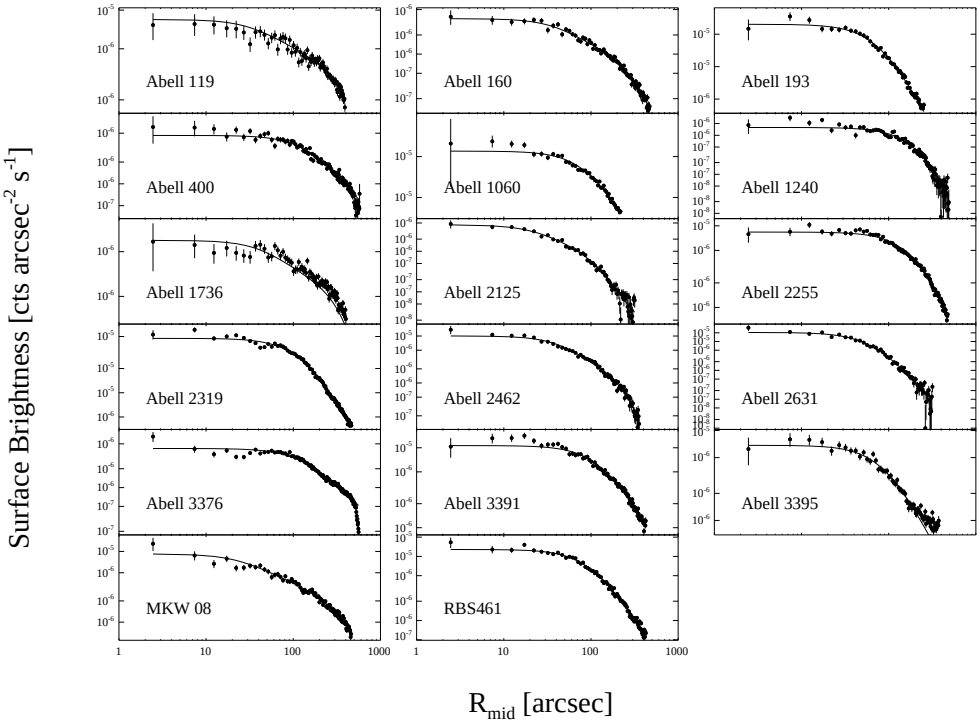

Figure 3.8 Surface brightness profiles for clusters requiring a β-model fit for deprojection (discussed in §3.3.3). The best-fit β-model for each cluster is overplotted as a dashed line. The discrepancy between the data and best-fit model for some clusters results from the presence of a compact X-ray source at the center of the cluster. These cases are discussed belows.

Abell 119 ($z = 0.0442$): This is a highly diffuse cluster without a prominent cool core. The large core region and slowly varying surface brightness made deprojection highly unstable. We have excluded a small source at the very center of the BCG. The exclusion region for the source is $\approx 2.2''$ in radius which at the redshift of the cluster is ~ 2 kpc. This cluster required a double β-model.

Abell 160 ($z = 0.0447$): The highly asymmetric, low surface brightness of this cluster resulted in a noisy surface brightness profile that could not be deprojected.

This cluster required a double β-model. The BCG hosts a compact X-ray source. The exclusion region for the compact source has a radius of $\sim 5''$ or ~ 4.3 kpc. The BCG for this cluster is not coincident with the X-ray centroid and hence is not at the zero-point of our radial analysis.

Abell 193 ($z = 0.0485$): This cluster has an azimuthally symmetric and a very diffuse ICM centered on a BCG which is interacting with a companion galaxy. In Fig. 3.8 one can see that the central three bins of this cluster's surface brightness profile are highly discrepant from the best-fit β-model. This is a result of the BCG being coincident with a bright, compact X-ray source. As we have concluded in 3.3.5, compact X-ray sources are excluded from our analysis as they are not the focus of our study here. Hence we have used the best-fit β-model in deriving $K(r)$ instead of the raw surface brightness.

Abell 400 ($z = 0.0240$): The two ellipticals at the center of this cluster have compact X-ray sources which are excluded during analysis. The core entropy we derive for this cluster is in agreement with that found by Hudson et al. (2006) which supports the accuracy of the β-model we have used.

Abell 1060 ($z = 0.0125$): There is a distinct compact source associated with the BCG in this cluster. The ICM is also very faint and uniform in surface brightness making the compact source that much more obvious. Deprojection was unstable because of imperfect exclusion of the source.

Abell 1240 ($z = 0.1590$): The surface brightness of this cluster is well-modeled by a β-model. There is nothing peculiar worth noting about the BCG or the core of this cluster.

Abell 1736 ($z = 0.0338$): Another "boring" cluster with a very diffuse low surface brightness ICM, no peaky core, and no signs of merger activity in the X-ray.

The noisy surface brightness profile necessitated the use of a double β-model. The BCG is coincident with a very compact X-ray source, but the BCG is offset from the X-ray centroid and thus the central bins are not adversely affected. The radius of the exclusion region for the compact source is $\approx 2.3''$ or 1.5 kpc.

Abell 2125 ($z = 0.2465$): Although the ICM of this cluster is very similar to the other clusters listed here (*i.e.* diffuse, large cores), A2125 is one of the more compact clusters. The presence of several merging sub-clusters (Wang et al., 1997, 2004a) to the NW of the main cluster form a diffuse mass which cannot rightly be excluded. This complication yields inversions of the deprojected surface brightness profile if a double β-model is not used.

Abell 2255 ($z = 0.0805$): This is a very well studied merger cluster (Burns et al., 1995; Feretti et al., 1997a). The core of this cluster is very large ($r > 200$ kpc). Such large extended cores cannot be deprojected using our methods because if too many neighboring bins have approximately the same surface brightness, deprojection results in bins with negative or zero value. The surface brightness for this cluster is well modeled as a β function.

Abell 2319 ($z = 0.0562$): A2319 is another well studied merger cluster (Feretti et al., 1997b; Molendi et al., 1999) with a very large core region ($r > 100$ kpc) and a prominent cold front (O'Hara et al., 2004). Once again, the surface brightness profile is well-fit by a β-model.

Abell 2462 ($z = 0.0737$): This cluster is very similar in appearance to A193: highly symmetric ICM with a bright, compact X-ray source embedded at the center of an extended diffuse ICM. The central compact source has been excluded from our analysis with a region of radius $\approx 1.5''$ or ~ 3 kpc. The central bin of the surface brightness profile is most likely boosted above the best-fit double β-model because of faint extended emission from the compact source which

cannot be discerned from the ambient ICM.

Abell 2631 ($z = 0.2779$): The surface brightness profile for this cluster is rather regular, but because the cluster has a large core it suffers from the same unstable deprojection as A2255 and A2319. The ICM is symmetric about the BCG and is incredibly uniform in the core region. We did not detect or exclude a source at the center of this cluster, but under heavy binning the cluster image appears to have a source coincident with the BCG, and the slightly higher flux in central bin of the surface brightness profile may be a result of an unresolved source.

Abell 3376 ($z = 0.0456$): The large core of this cluster ($r > 120$ kpc) makes deprojection unstable and a β-model must be used.

Abell 3391 ($z = 0.0560$): The BCG is coincident with a compact X-ray source. The source is excluded using a region with radius $\approx 2''$ or ~ 2 kpc. The large uniform core region made deprojection unstable and thus required a β-model fit.

Abell 3395 ($z = 0.0510$): The surface brightness profile for this cluster is noisy resulting in deprojection inversions and requiring a β-model fit. The BCG of this cluster has a compact X-ray source and this source was excluded using a region with radius $\approx 1.9''$ or ~ 2 kpc.

MKW 08 ($z = 0.0270$): MKW 08 is a nearby large group/poor cluster with a pair of interacting elliptical galaxies in the core. The BCG falls directly in the middle of the ACIS-I detector gap. However, despite the lack of proper exposure, CCD dithering reveals that a very bright X-ray source is associated with the BCG. A double β-model was necessary for this cluster because the low surface brightness of the ICM is noisy and deprojection is unstable.

RBS 461 ($z = 0.0290$): This is another nearby large group/poor cluster with an extended, diffuse, axisymmetric, featureless ICM centered on the BCG. The

BCG is coincident with a compact source with size $r \approx 1.7$ kpc. This source was excluded during reduction. The β-model is a good fit to the surface brightness profile.

Chapter Four

Cavagnolo, Kenneth W., Donahue, Megan, Voit, G. Mark, Sun, Ming (2008). An Entropy Threshold for Strong Hα and Radio Emission in the Cores of Galaxy Clusters. The Astrophysical Journal Letters. 683:107-110.

Chapter 4: An Entropy Threshold for Strong Hα and Radio Emission in the Cores of Galaxy Clusters

4.1 Introduction

In recent years the "cooling flow problem" has been the focus of intense scrutiny as the solutions have broad impact on existing theories of galaxy formation (see Peterson & Fabian, 2006, for a review). Current models predict that the most massive galaxies in the Universe – brightest cluster galaxies (BCGs) – should be bluer and more luminous than observations find, unless AGN feedback intervenes to stop late-time star formation (Bower et al., 2006; Croton et al., 2006; Saro et al., 2006). X-ray observations of galaxy clusters have given this hypothesis considerable traction. From the properties of X-ray cavities in the intracluster medium (ICM), Bîrzan et al. (2004) concluded that AGN feedback provides the necessary energy to retard cooling in the cores of clusters (see McNamara & Nulsen, 2007, for a review). This result suggests that, under the right conditions, AGN are capable of quenching star formation by heating the surrounding ICM.

If AGN feedback is indeed responsible for regulating star formation in cluster cores, then the radio and star-forming properties of galaxy clusters should be related to the distribution of ICM specific entropy. In previous observational work (see Donahue

et al., 2005, 2006, and Chapter 3), we have focused on ICM entropy as a means for understanding the cooling and heating processes in clusters because it is a more fundamental property of the ICM than temperature or density alone (Voit et al., 2002; Voit, 2005). ICM temperature mainly reflects the depth and shape of the dark matter potential well, while entropy depends more directly on the history of heating and cooling within the cluster and determines the density distribution of gas within that potential.

We have therefore undertaken a large *Chandra* archival project to study how the entropy structure of clusters correlates with other cluster properties. Chapter 3 presents the radial entropy profiles we have measured for a sample of 239 clusters taken from the *Chandra* Data Archive. We have named this project the Archive of Chandra Cluster Entropy Profile Tables, or *ACCEPT* for short. To characterize the ICM entropy distributions of the clusters, we fit the equation $K(r) = K_0 + K_{100}(r/100\mathrm{kpc})^{\alpha}$ to each entropy profile. In this equation, K_{100} is the normalization of the power-law component at 100 kpc and we refer to K_0 as the central entropy. Bear in mind, however, that K_0 is not necessarily the minimum core entropy or the entropy at $r = 0$, nor is it the gas entropy that would be measured immediately around the AGN or in a BCG X-ray corona. Instead, K_0 represents the typical excess of core entropy above the best-fitting power law found at larger radii. Chapter 3 shows that K_0 is non-zero for almost all clusters in our sample.

In this chapter we present the results of exploring the relationship between the expected by-products of cooling, *e.g.* Hα emission, star formation, and AGN activity, and the K_0 values of clusters in our survey. To determine the activity level of feedback in cluster cores, we selected two readily available observables: Hα and radio emission. We have found that there is a critical entropy level below which Hα and radio emission are often present, while above this threshold these emission sources are much fainter and in most cases undetected. Our results suggest that the formation of thermal

instabilities in the ICM and initiation of processes such as star formation and AGN activity are closely connected to core entropy, and we suspect that the sharp entropy threshold we have found arises from thermal conduction (see Voit et al., 2008, for discussion of this point).

This chapter proceeds in the following manner: In §4.2 we cover the basics of our data analysis. The entropy-Hα relationship is discussed in §4.3, while the entropy-radio relationship is discussed in §4.4. A brief summary is provided in §4.5. For this chapter we have assumed a flat A ΛCDM cosmology with $H_0 = 70$ km s^{-1} Mpc^{-1} , $\Omega_{\rm M} = 0.27$, and $\Omega_\Lambda = 0.73$ is adopted Universe with cosmogony $\Omega_{\rm M} = 0.3$, $\Omega_\Lambda = 0.7$, and $H_0 = 70 {\rm kms}^{-1}{\rm Mpc}^{-1}$. All uncertainties are at the 90% confidence level.

4.2 Data Analysis

This section briefly describes our data reduction and methods for producing entropy profiles. More thorough explanations are given in Donahue et al. (2006), Chapter 2, and Chapter 3.

4.2.1 X-ray

X-ray data were taken from publicly available observations in the *Chandra* Data Archive. Following standard CIAO reduction techniques,[1] data were reprocessed using CIAO version 3.4.1 and CalDB version 3.4.0, resulting in point-source and flare-clean events files at level-2. Entropy profiles were derived from the radial ICM temperature and electron density profiles.

Radial temperature profiles were created by dividing each cluster into concentric annuli with the requirement of at least three annuli containing a minimum of 2500 counts each. Source spectra were extracted from these annuli, while corresponding background spectra were extracted from blank-sky backgrounds tailored to match

[1] http://cxc.harvard.edu/ciao/guides/

each observation. Each blank-sky background was corrected to account for variation of the hard-particle background, while spatial variation of the soft-galactic background was accounted for through the addition of a fixed background component during spectral fitting. Weighted responses that account for spatial variations of the CCD calibration were also created for each observation. Spectra were then fitted over the energy range 0.7-7.0 keV in XSPEC version 11.3.2ag (Arnaud, 1996) using a single-component absorbed thermal model.

Radial electron density profiles were created using surface brightness profiles and spectroscopic information. Exposure-corrected, background-subtracted, point-source-clean surface brightness profiles were extracted from $5''$ concentric annular bins over the energy range 0.7-2.0 keV. In conjunction with the spectroscopic normalization and 0.7-2.0 keV count rate, surface brightness was converted to electron density using the deprojection technique of Kriss et al. (1983). Errors were estimated using 5000 Monte Carlo realizations of the surface brightness profile.

A radial entropy profile for each cluster was then produced from the temperature and electron density profiles. The entropy profiles were fitted with a simple model that is a power-law at large radii and approaches a constant value, K_0, at small radii (see §4.1 for the equation). We define central entropy as K_0 from the best-fit model.

4.2.2 Hα

One goal of our project was to determine if ICM entropy is connected to processes such as star formation. Here we do not directly measure star formation but instead use Hα, which is usually a strong indicator of ongoing star formation in galaxies (Kennicutt, 1983, 1998). It is possible that some of the Hα emission from BCGs is not produced by star formation (Begelman & Fabian, 1990; Sparks et al., 2004; Ruszkowski et al., 2008; Ferland et al., 2008). Nevertheless, Hα emission unambiguously indicates the presence of $\sim 10^4$ K gas in the cluster core and therefore the presence of a multiphase

intracluster medium that could potentially form stars.

Our Hα values have been gathered from several sources, most notably Crawford et al. (1999). Additional sources of data are M. Donahue's observations taken at Las Campanas and Palomar (see Table B.3), Heckman et al. (1989), Donahue et al. (1992), Lawrence et al. (1996), Valluri & Anupama (1996), White et al. (1997), Crawford et al. (2005), and Quillen et al. (2008). We have recalculated the Hα luminosities from these sources using our assumed A ΛCDM cosmology with $H_0 = 70$ km s^{-1} Mpc^{-1}, $\Omega_{\rm M} = 0.27$, and $\Omega_\Lambda = 0.73$ is adopted cosmological model. However, the observations were made with a variety of apertures and in many cases may not reflect the full Hα luminosity of the BCG. The exact levels of $L_{\rm H\alpha}$ are not important for the purposes of this chapter and we use the $L_{\rm H\alpha}$ values here as a binary indicator of multiphase gas: either Hα emission and cool gas are present or they are not.

4.2.3 Radio

Another goal of this work was to explore the relationship between ICM entropy and AGN activity. It has long been known that BCGs are more likely to host radio-loud AGN than other cluster galaxies (Burns et al., 1981; Valentijn & Bijleveld, 1983; Burns, 1990). Thus, we chose to interpret radio emission from the BCG of each *ACCEPT* cluster as a sign of AGN activity.

To make the radio measurements, we have taken advantage of the nearly all-sky flux-limited coverage of the NRAO VLA Sky Survey (NVSS, Condon et al., 1998) and Sydney University Molonglo Sky Survey (SUMSS, Bock et al., 1999; Mauch et al., 2003). NVSS is a continuum survey at 1.4 GHz of the entire sky north of $\delta = -40°$, while SUMSS is a continuum survey at 843 MHz of the entire sky south of $\delta = -30°$. The completeness limit of NVSS is ≈ 2.5 mJy and for SUMSS it is ≈ 10 mJy when $\delta > -50°$ or ≈ 6 mJy when $\delta \leq -50°$. The NVSS positional uncertainty for both right ascension and declination is $\lesssim 1''$ for sources brighter than 15 mJy and $\approx 7''$

at the survey detection limit (Condon et al., 1998). At $z = 0.2$, these uncertainties represent distances on the sky of $\sim 3-20$ kpc. For SUMSS, the positional uncertainty is $\lesssim 2''$ for sources brighter than 20 mJy and is always less than $10''$ (Bock et al., 1999; Mauch et al., 2003). The distance at $z = 0.2$ associated with these uncertainties is $\sim 6 - 30$ kpc. We calculate the radio power for each radio source using the standard relation $\nu L_\nu = 4\pi D_L^2 S_\nu f_0$, where S_ν is the 1.4 GHz or 843 MHz flux from NVSS or SUMSS, D_L is the luminosity distance, and f_0 is the central beam frequency of the observations. Our calculated radio powers are simply an approximation of the bolometric radio luminosity.

Radio sources were found using two methods. The first method was to search for sources within a fixed angular distance of $20''$ around the cluster X-ray peak. The probability of randomly finding a radio source within an aperture of $20''$ is exceedingly low (< 0.004 for NVSS). Thus, in 239 total field searches, we expect to find no more than one spurious source. The second method involved searching for sources within 20 projected kpc of the cluster X-ray peak. At $z \approx 0.051$, $1''$ equals 1 kpc, thus for clusters at $z \gtrsim 0.05$, the 20 kpc aperture is smaller than the $20''$ aperture, and the likelihood of finding a spurious source gets smaller. Both methods produce nearly identical lists of radio sources with the differences arising from the very large, extended lobes of low-redshift radio sources such as Hydra A.

To make a spatial and morphological assessment of the radio emission's origins, *i.e.* determining if the radio emission is associated with the BCG, high angular resolution is necessary. However, NVSS and SUMSS are low-resolution surveys with FWHM of $\approx 45''$. We therefore cannot distinguish between ghost cavities/relics, extended lobes, point sources, or reaccelerated regions or if the emission is coming from a galaxy very near the BCG. We have handled this complication by visually inspecting each radio source in relation to the optical (using DSS I/II)[2] and infrared (using 2MASS)[3]

[2]http://archive.stsci.edu/dss/
[3]http://www.ipac.caltech.edu/2mass/

emission of the BCG. We have used this method to establish that the radio emission is most likely coming from the BCG. When available, high resolution data from VLA FIRST[4] were added to the visual inspection. VLA FIRST is a 10,000 deg^2 high-resolution ($5''$) survey at 20 cm of the north and south Galactic caps (Becker et al., 1995). FIRST is also more sensitive than either NVSS or SUMSS with a detection threshold of 1 mJy.

4.3 Hα Emission and Central Entropy

Of the 239 clusters in *ACCEPT*, we located Hα observations from the literature for 110 clusters. Of those 110, Hα was detected in 46, while the remaining 64 have upper limits. The mean central entropy for clusters with detections is $K_0 = 13.9 \pm 4.9$keV cm^2, and for clusters with only upper-limits $K_0 = 130 \pm 55$keV cm^2.

In Figure 4.1 central entropy is plotted versus Hα luminosity. One can immediately see the dichotomy between clusters with and without Hα emission. If a cluster has a central entropy $\lesssim 30$keV cm^2, then Hα emission is usually "on," while above this threshold the emission is predominantly "off." For brevity we refer to this threshold as $K_{\rm thresh}$ hereafter. The cluster above $K_{\rm thresh}$ that has Hα emission (*blue square with inset orange circle*) is Zw 2701 ($K_0 = 39.7 \pm 3.9$keV cm^2). There are also clusters below $K_{\rm thresh}$ without Hα emission (*blue squares with red stars*): A2029, A2107, EXO 0422-086, and RBS 533. A2151 also lies below $K_{\rm thresh}$ and has no detected Hα emission, but the best-fit K_0 for A2151 is statistically consistent with zero and this cluster is plotted using the 2σ upper-limit of K_0 (Fig. 4.1, *green triangle*). These five clusters are clearly exceptions to the much larger trend. The mean and dispersion of the redshifts for clusters with and without Hα are not significantly different, $z = 0.124 \pm 0.106$ and $z = 0.132 \pm 0.084$ respectively, and applying a redshift cut (*i.e.* $z = 0-0.15$ or $z = 0.15-0.3$) does not change the K_0-Hα dichotomy.

[4]http://sundog.stsci.edu

Most important to note is that changes in the Hα luminosities because of aperture effects will move points up or down in Figure 4.1, while mobility along the K_0 axis is minimal. Qualitatively, the correlation between low central entropy and the presence of Hα emission is very robust.

The clusters with Hα detections are typically between 10 and 30 keV cm^2, have short central cooling times (< 1 Gyr), and under older nomenclature would be classified as "cooling flow" clusters. It has long been known that star formation and associated Hα nebulosity appear only in cluster cores with cooling times less than a Hubble time (Hu et al., 1985; Johnstone et al., 1987; McNamara & O'Connell, 1989; Voit & Donahue, 1997; Cardiel et al., 1998). However, our results suggest that the central cooling time must be at least a factor of 10 smaller than a Hubble time for these manifestations of cooling and star formation to appear. It is also very interesting that the characteristic entropy threshold for strong Hα emission is so sharp. Voit et al. (2008) have recently proposed that electron thermal conduction may be responsible for setting this threshold. This hypothesis has received further support from the theoretical work of Guo et al. (2008) showing that thermal conduction can stabilize non-cool core clusters against the formation of thermal instabilities, and that AGN feedback may be required to limit star formation when conduction is insufficient.

4.4 Radio Sources and Central Entropy

Of the 239 clusters in *ACCEPT*, 100 have radio-source detections with a mean K_0 of 23.3 ± 9.4keV cm^2, while the other 122 clusters with only upper limits have a mean K_0 of 134 ± 52keV cm^2. NVSS and SUMSS are low-resolution surveys with FWHM at $\approx 45''$, which at $z = 0.2$ is $\approx$ 150kpc. This scale is larger than the size of a typical cluster cooling region and makes it difficult to determine absolutely that the radio emission is associated with the BCG. We therefore focus only on clusters at $z < 0.2$. After the redshift cut, 135 clusters remain – 64 with radio detections (mean

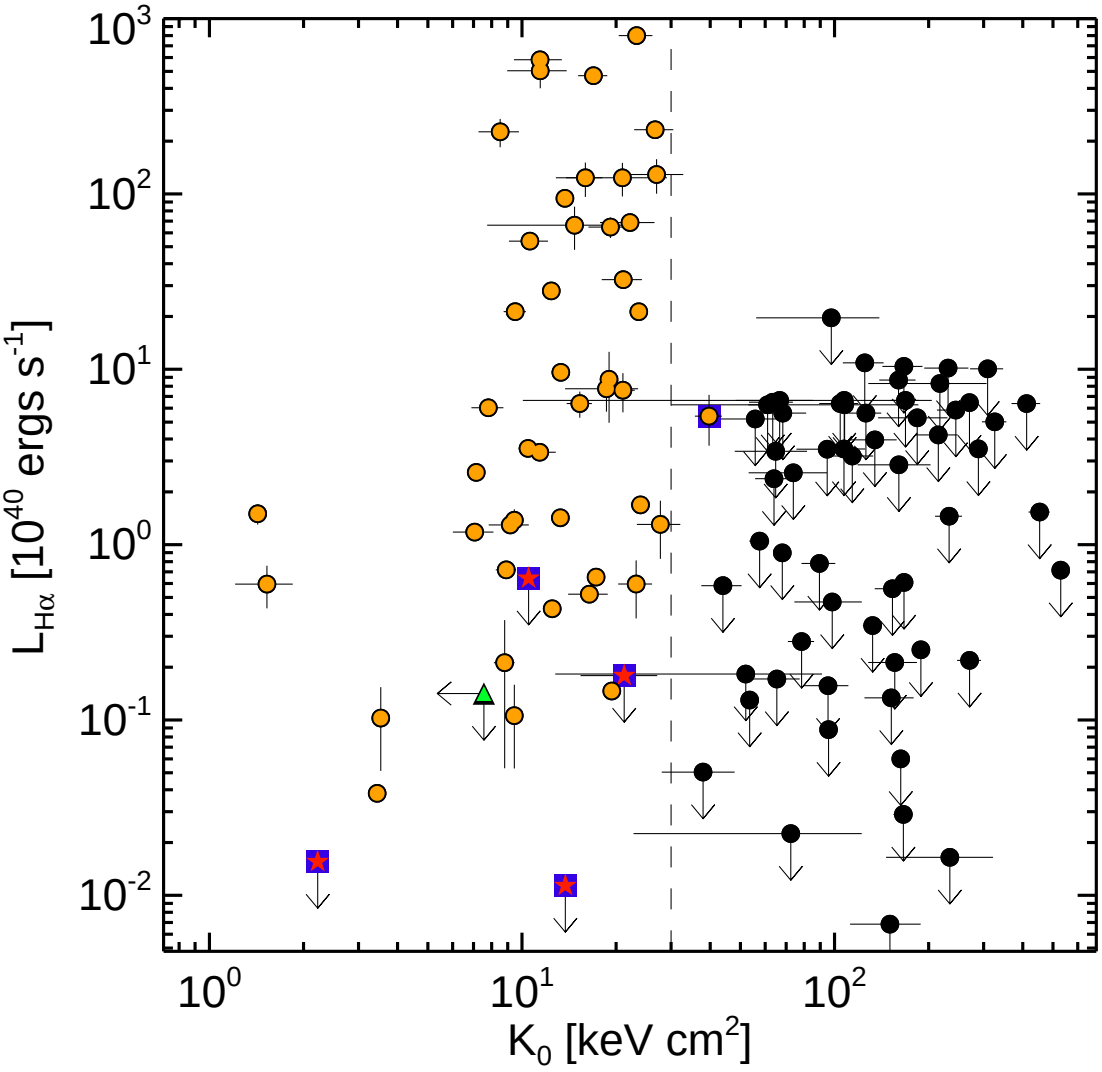

Figure 4.1 Central entropy vs. Hα luminosity. Orange circles represent Hα detections, black circles are non-detection upper limits, and blue squares with inset red stars or orange circles are peculiar clusters that do not adhere to the observed trend (see text). A2151 is plotted using the 2σ upper-limit of the best-fit K_0 and is denoted by a green triangle. The vertical dashed line marks $K_0 = 30$keV cm^2. Note the presence of a sharp Hα detection dichotomy beginning at $K_0 \lesssim 30$keV cm^2.

$K_0 = 18.3 \pm 7.7$keV cm^2) and 71 without (mean $K_0 = 112 \pm 45$keV cm^2).

In Figure 4.2 we have plotted radio power versus K_0. The obvious dichotomy seen in the Hα measures and characterized by $K_{\rm thresh}$is also present in the radio. Clusters with $\nu L_\nu \gtrsim 10^{40}$erg s^{-1} generally have $K_0 \lesssim K_{\rm thresh}$. This trend was first evident in Donahue et al. (2005) and suggests that AGN activity in BCGs, while not exclusively limited to clusters with low core entropy, is much more likely to be found in clusters that have a core entropy less than $K_{\rm thresh}$. That star formation and AGN activity are subject to the same entropy threshold suggests that the mechanism that promotes or initiates one is also involved in the activation of the other. If the entropy of the hot gas in the vicinity of the AGN is correlated with K_0, then the lack of correlation between radio power and K_0 below the 30keV cm^2 threshold suggests that cold-mode accretion (Pizzolato & Soker, 2005; Hardcastle et al., 2007) may be the dominant method of fueling AGN in BCGs.

We have again highlighted exceptions to the general trend seen in Figure 4.2: clusters below $K_{\rm thresh}$ without a radio source (*blue squares with inset red stars*) and clusters above $K_{\rm thresh}$ with a radio source (*blue squares with inset orange circles*). The peculiar clusters below $K_{\rm thresh}$ are A133, A539, A1204, A2107, A2556, AWM7, ESO 5520200, MKW4, MS J0440.5+0204, and MS J1157.3+5531. The peculiar clusters above $K_{\rm thresh}$ are 2PIGG J0011.5-2850, A193, A586, A2063, A2147, A2244, A3558, A4038, and RBS 461. In addition, there are three clusters, A2151, AS405, and MS 0116.3-0115, that have best-fit K_0 statistically consistent with zero and are plotted in Figure 4.2 using the 2σ upper-limit of K_0 (*green triangles*). All three clusters have detected radio sources.

Finding a few clusters in our sample without radio sources where we expect to find them is not surprising given that AGN feedback could be episodic. However, the clusters above $K_{\rm thresh}$ with a central radio source are interesting, and may be special cases of BCGs with embedded coronae. Sun et al. (2007) extensively studied coronae

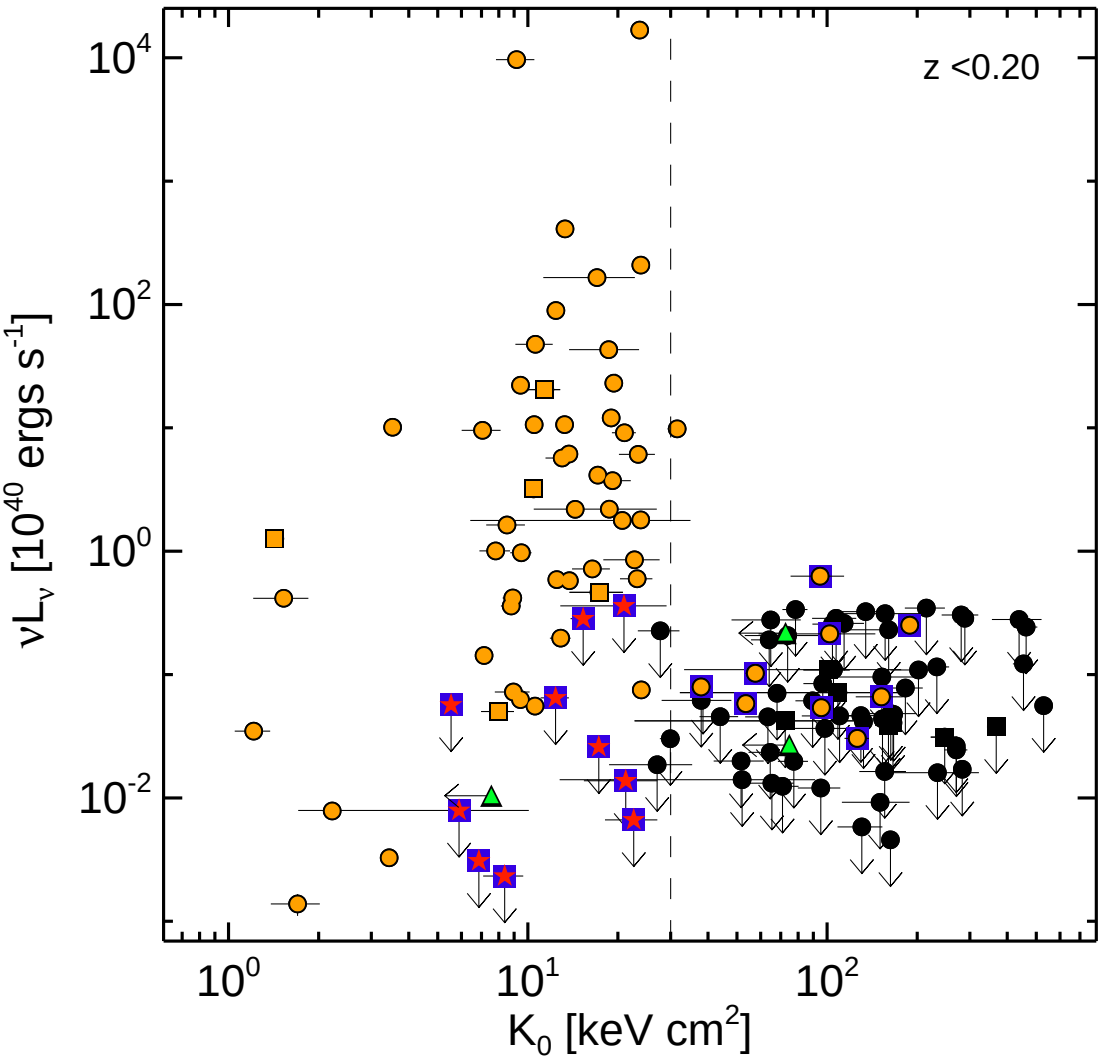

Figure 4.2 BCG radio power vs. K_0 for clusters with $z < 0.2$. Orange symbols represent radio detections and black symbols are non-detection upper-limits. Circles are for NVSS observations and squares are for SUMSS observations. The blue squares with inset red stars or orange circles are peculiar clusters that do not adhere to the observed trend (see text). Green triangles denote clusters plotted using the 2σ upper-limit of the best-fit K_0. The vertical dashed line marks $K_0 = 30$keV cm^2. The radio sources show the same trend as Hα: bright radio emission is preferentially "on" for $K_0 \lesssim 30$keV cm^2.

and found that they are like "mini cooling cores" with low temperatures and high densities. Coronae are a low-entropy environment isolated from the high-entropy ICM and may provide the conditions necessary for gas cooling to proceed. And indeed, 2PIGG 0011, A193, A2151, A2244, A3558, A4038, and RBS 461 show indications that a very compact ($r \lesssim 5$kpc) X-ray source is associated with the BCG (see Section 3.3.5).

4.5 Summary

We have presented a comparison of ICM central entropy values and measures of BCG Hα and radio emission for a *Chandra* archival sample of galaxy clusters. We find that below a characteristic central entropy threshold of $K_0 \approx 30$keV cm^2, Hα and bright radio emission are more likely to be detected, while above this threshold Hα is not detected and radio emission, if detected at all, is significantly fainter. The mean K_0 for clusters with and without Hα detections are $K_0 = 13.9 \pm 4.9$keV cm^2 and $K_0 = 130 \pm 55$keV cm^2, respectively. For clusters at $z < 0.2$ with BCG radio emission the mean $K_0 = 18.3 \pm 7.7$keV cm^2, while for BCGs with only upper limits, the mean $K_0 = 112 \pm 45$keV cm^2. While other mechanisms can produce Hα or radio emission besides star formation and AGN, if one assumes that the Hα and radio emission are coming from these two feedback sources, then our results suggest that the development of multiphase gas in cluster cores (which can fuel both star formation and AGN) is strongly coupled to ICM entropy.

4.6 Acknowledgements

We were supported in this work through Chandra SAO grants AR-4017A, AR-6016X, and G05-6131X and NASA/LTSA grant NNG-05GD82G. The CXC is operated by the SAO for and on behalf of NASA under contract NAS8-03060.

Chapter 5: Summary

5.1 Energy Band Dependence of X-ray Temperatures

Using a sample of 192 galaxy clusters we explored the band dependence of inferred X-ray temperatures for the ICM. Utilizing core-excised global cluster spectra extracted from the regions encircled by R_{2500} and R_{5000}, we inferred X-ray temperatures for a single-component absorbed thermal model in a broadband (0.7-7.0 keV) and a hard-band (2.0-7.0 keV). On average, we found that the hard-band temperatures were greater, with the ratio of the temperatures, T_{HBR}, having a mean value 1.16 ± 0.01 (where the error is of the mean) for the R_{2500} apertures, and 1.14 ± 0.01 for the R_{5000} apertures. No systematic trends were found, in either the values or dispersions, with S/N, redshift, Galactic absorption, metallicity, observation date, or broadband temperature. Analysis of a simulated ensemble of 12,765 observation-specific two-component spectra revealed statistical fluctuations could not account for the skewing measured in T_{HBR}. The simulations also helped establish a lower limit on the flux contribution from a cooler gas component ($T_X < 2.0$ keV) necessary to generate T_{HBR} as large as those found in the data. A second cool gas phase must be contributing $\gtrsim 10\%$ of the total emission. The simulations also reveal the observational scatter is larger than the statistical scatter, a result one should expect if an underlying physical process is responsible for creating dispersion in T_{HBR}.

The *a priori* motivation for studying temperature inhomogeneity comes from the prediction of **?** that T_{HBR} may be related to the process of hierarchical structure formation. After assuming that the establishment and prominence of a cool core in a cluster is an indicator of relaxation, we compared T_{HBR} values with the "strength" of the cool core based on the temperature decrement between the core and the cluster atmosphere. The result was a significant correlation between clusters having higher values of T_{HBR} being less likely to host a cool core. A search of the scientific literature involving the clusters with the highest significant values of T_{HBR} ($T_{HBR} > 1.1$) revealed that most, if not all, of these clusters are undergoing, or have recently undergone, a merger event. With two strong connections between T_{HBR} and cluster dynamical state established, we conclude that temperature inhomogeneity is most likely related to the process of cluster relaxation, and that it may be useful as a metric to further quantify the degree to which a cluster is relaxed, thus addressing point (1) brought up in Section §1.3.1.

5.2 Chandra Archival Sample of Intracluster Entropy Profiles

A library of ICM entropy profiles was created for 239 galaxy clusters taken from the *Chandra* Data Archive to better understand the role of feedback and cooling in shaping global cluster properties. Radial gas density, $n_{\rm e}(r)$, and gas temperature, $kT_x(r)$, profiles were measured for each cluster. Radial entropy was calculated from the relation $K(r) = kT_X(r)n_{\rm e}(r)^{-2/3}$. The uncertainties for each profile were calculated using 5000 Monte Carlo realizations of the observed surface brightness profile. Each profile was then fit with two models: one which is a power-law at all radii (3.5), and another (eqn. 3.5) which is a power-law at large radii but approaches a constant K_0 value at small radii. The K_0 term is defined as the core entropy.

Comparison of p-values, χ^2, and the significance of K_0 above zero for the best-fit models revealed that for 90% of the 239 sample, the model with a constant core entropy is a better description of the data. Systematics such as PSF smearing, angular resolution, profile curvature, and number of radial bins proved not to be important in setting or changing best-fit K_0. The slope of the power-law component was also found to be remarkably similar among the profiles with a mean value of 1.21 ± 0.39 which is not significantly different from the value of ~ 1.1 expected from hierarchical structure formation.

The distribution of K_0 for both the *ACCEPT* and *HIFLUGCS* samples was found to be bimodal. The populations comprising the bimodality are strikingly similar between the two samples with peaks at $K_0 \sim 15$keV cm^2 and $K_0 \sim 150$keV cm^2. The KMM test (Ashman et al., 1994; Waters et al., 2009) was applied and it determined, for both *ACCEPT* and *HIFLUGCS*, that the populations were statistically distinct and that a unimodal distribution was ruled out. The poorly populated region between the populations for both samples occurred at $K_0 \approx 30 - 60$keV cm^2. The measured entropy profile shapes and distribution of K_0 were consistent with existing models of AGN feedback which predict non-zero core entropy. All of the results and data for *ACCEPT* were made available to the public with the intent that theorists and observers might find utility for *ACCEPT* in their own work. The work presented in Chapter 3 directly addressed point (2) of Section §1.3.2.

5.3 An Entropy Threshold for Strong Hα and Radio Emission in the Cores of Galaxy Clusters

To study a suspected connection between low entropy gas in cluster cores and the by-products of cooling, namely AGN activity and formation of thermal instabilities,

the best-fit K_0 values from clusters in *ACCEPT* were compared against radio power and Hα luminosity, both strong indicators of run-away cooling. A search of the research literature turned-up Hα observations for 110 clusters in *ACCEPT*. The NVSS and SUMSS all-sky radio surveys were queried for each cluster to attain νL_ν, either detections or upper-limits. New luminosities were then calculated using the preferred cosmology assumed in this dissertation to place all observations on equal footing.

A comparison of Hα luminosities and best-fit K_0 values showed a strong relation between when Hα emission is detected and when it is not. Below an entropy threshold of $K_0 \lesssim 30\text{keV cm}^2$ Hα emission is predominantly on, while above this threshold it is always off sans the exception of one cluster very near the $K_0 = 30\text{keV cm}^2$ boundary. A very similar correlation was found between νL_ν and K_0 for clusters at $z < 0.2$. A redshift cut was applied because of the low resolution of NVSS and SUMSS. The entropy threshold for νL_ν also occurs at $K_0 \approx 30\text{keV cm}^2$ but with a larger fraction of low power radio sources above $K_0 \approx 30\text{keV cm}^2$ than the fraction which was found in Hα. However, it was found that powerful radio sources ($\nu L_\nu > 10^{40}\text{erg s}^{-1}\text{ cm}^{-2}$) were only found in clusters with $K_0 \lesssim 30\text{keV cm}^2$ adding strength to the argument that entropy sets a scale for development of a multiphase medium in cluster cores. While the discussion is not presented in this dissertation, Voit et al. (2008) propose that it is electron thermal conduction which gives rise to the entropy threshold observed in our study. The work presented in Chapter 4 is an extension of point (2) in §1.3.2.

APPENDICES

Appendix A: Tables cited in Chapter 2

Table A.1 Notes

A (‡) indicates a cluster analyzed within R_{5000} only. Italicized cluster names indicate a cluster which was excluded from our analysis (discussed in §2.5.1). For clusters with multiple observations, the X-ray centers differ by < 0.5 kpc. Col. (1) Cluster name; col. (2) CDA observation identification number; col. (3) R.A. of cluster center; col. (4) Dec. of cluster center; col. (5) nominal exposure time; col. (6) observing mode; col. (7) CCD location of centroid; col. (8) redshift; col. (9) bolometric luminosity.

Table A.2 Notes

Clusters ordered by lower limit of T_{HBR}. Listed T_{HBR} values are for the $R_{2500-\mathrm{CORE}}$ aperture, with the exception of the "$R_{5000-\mathrm{CORE}}$ Only" clusters listed at the end of the table. Excluding the "$R_{5000-\mathrm{CORE}}$ Only" clusters, all clusters listed here had T_{HBR} significantly greater than 1.1 and the same core classification for both the $R_{2500-\mathrm{CORE}}$ and $R_{5000-\mathrm{CORE}}$ apertures. Numbered references given in table: [1] Gioia & Luppino (1994), [2] Kempner et al. (2003), [3] Yuan et al. (2005), [4] Markevitch et al. (1998), [5] Bagchi et al. (2006), [6] Teague et al. (1990), [7] Andersson & Madejski (2004), [8] Burns et al. (1995), [9] Feretti et al. (1997a), [10] Girardi et al. (1997), [11] Dahle et al. (2002), [12] Smith et al. (2005), [13] Gioia et al. (1982), [14] Hallman & Markevitch (2004), [15] Yang et al. (2004), [16] Mercurio et al. (2003), [17] Gómez et al. (2000), [18] Tucker et al. (1998), [19] Krempec-Krygier & Krygier

(1999), [20] Mazzotta et al. (2001), [21] Govoni et al. (2001), [22] Bliton et al. (1998), [23] Gutierrez & Krawczynski (2005), [24] Markevitch et al. (1996), [25] Ohta et al. (2001), [26] Molendi et al. (2000), [27] Clarke et al. (2004), [28] Clarke et al. (2005), [29] this work.

Table A.3 Notes

Note: "77" refers to 0.7-7.0 keV band and "27" refers to 2.0-7.0 keV band. Col. (1) Cluster name; col. (2) size of excluded core region in kpc, (3) R_{2500} in kpc; col. (4) absorbing Galactic neutral hydrogen column density; col. (5,6) best-fit MeKaL temperatures; col. (7) $T_{0.7-7.0}/T_{2.0-7.0}$ also called T_{HBR}; col. (8) best-fit 77 MeKaL abundance; col. (9,10) respective reduced χ^2 statistics, and (11) percent of emission attributable to source. A star ($\star$) indicates a cluster which has multiple observations. Each observation has an independent spectrum extracted along with an associated WARF, WRMF, normalized background spectrum, and soft residual. Each independent spectrum is then fit simultaneously with the same spectral model to produce the final fit.

Table A.4 Notes

Note: "77" refers to 0.7-7.0 keV band and "27" refers to 2.0-7.0 keV band. Col. (1) Cluster name; col. (2) size of excluded core region in kpc, (3) R_{5000} in kpc; col. (4) absorbing Galactic neutral hydrogen column density; col. (5,6) best-fit MeKaL temperatures; col. (7) $T_{0.7-7.0}/T_{2.0-7.0}$ also called T_{HBR}; col. (8) best-fit 77 MeKaL abundance; col. (9,10) respective reduced χ^2 statistics, and (11) percent of emission attributable to source. A star ($\star$) indicates a cluster which has multiple observations. Each observation has an independent spectrum extracted along with an associated WARF, WRMF, normalized background spectrum, and soft residual. Each independent spectrum is then fit simultaneously with the same spectral model to produce the final fit.

Table A.1: Summary of sample for energy band dependance study

Cluster	Obs.ID	R.A. hr:min:sec	Dec. ° :′:″	ExpT ksec	Mode	ACIS	z	$L_{bol.}$ 10^{44} ergs s^{-1}
(1)	(2)	(3)	(4)	(5)	(6)	(7)	(8)	(9)
1E0657 56	3184	06:58:29.622	-55:56:39.79	87.5	VF	I3	0.296	52.48
1E0657 56	5356	06:58:29.619	-55:56:39.78	97.2	VF	I2	0.296	52.48
1E0657 56	5361	06:58:29.620	-55:56:39.80	82.6	VF	I3	0.296	52.48
1RXS J2129.4-0741	3199	21:29:26.274	-07:41:29.38	19.9	VF	I3	0.570	20.58
1RXS J2129.4-0741	3595	21:29:26.281	-07:41:29.36	19.9	VF	I3	0.570	20.58
2PIGG J0011.5-2850	5797	00:11:21.623	-28:51:14.44	19.9	VF	I3	0.075	2.15
2PIGG J0311.8-2655 ‡	5799	03:11:33.904	-26:54:16.48	39.6	VF	I3	0.062	0.25
2PIGG J2227.0-3041	5798	22:27:54.560	-30:34:34.84	22.3	VF	I2	0.073	0.81
3C 220.1	839	09:32:40.218	+79:06:29.46	18.9	F	S3	0.610	3.25
3C 28.0	3233	00:55:50.401	+26:24:36.47	49.7	VF	I3	0.195	4.78
3C 295	2254	14:11:20.280	+52:12:10.55	90.9	VF	I3	0.464	6.92
3C 388	5295	18:44:02.365	+45:33:29.31	30.7	VF	I3	0.092	0.52
4C 55.16	4940	08:34:54.923	+55:34:21.15	96.0	VF	S3	0.242	5.90
ABELL 0013 ‡	4945	00:13:37.883	-19:30:09.10	55.3	VF	S3	0.094	1.41
ABELL 0068	3250	00:37:06.309	+09:09:32.28	10.0	VF	I3	0.255	12.70
ABELL 0119 ‡	4180	00:56:15.150	-01:14:59.70	11.9	VF	I3	0.044	1.39
ABELL 0168	3203	01:14:57.909	+00:24:42.55	40.6	VF	I3	0.045	0.23
ABELL 0168	3204	01:14:57.925	+00:24:42.73	37.6	VF	I3	0.045	0.23
ABELL 0209	3579	01:31:52.585	-13:36:39.29	10.0	VF	I3	0.206	10.96
ABELL 0209	522	01:31:52.595	-13:36:39.25	10.0	VF	I3	0.206	10.96
ABELL 0267	1448	01:52:29.181	+00:57:34.43	7.9	F	I3	0.230	8.62
ABELL 0267	3580	01:52:29.180	+00:57:34.23	19.9	VF	I3	0.230	8.62
ABELL 0370	515	02:39:53.169	-01:34:36.96	88.0	F	S3	0.375	11.95
ABELL 0383	2321	02:48:03.364	-03:31:44.69	19.5	F	S3	0.187	5.32
ABELL 0399	3230	02:57:54.931	+13:01:58.41	48.6	VF	I0	0.072	4.37
ABELL 0401	518	02:58:56.896	+13:34:14.48	18.0	F	I3	0.074	8.39
ABELL 0478	6102	04:13:25.347	+10:27:55.62	10.0	VF	I3	0.088	16.39

Table A.1: Summary of sample for energy band dependance study (continued)

Cluster	Obs.ID	R.A. hr:min:sec	Dec. ° :′:″	ExpT ksec	Mode	ACIS	z	$L_{bol.}$ 10^{44} ergs s^{-1}
(1)	(2)	(3)	(4)	(5)	(6)	(7)	(8)	(9)
ABELL 0514	3578	04:48:19.229	-20:30:28.79	44.5	VF	I3	0.072	0.66
ABELL 0520	4215	04:54:09.711	+02:55:23.69	66.3	VF	I3	0.202	12.97
ABELL 0521	430	04:54:07.004	-10:13:26.72	39.1	VF	S3	0.253	9.77
ABELL 0586	530	07:32:20.339	+31:37:58.59	10.0	VF	I3	0.171	8.54
ABELL 0611	3194	08:00:56.832	+36:03:24.09	36.1	VF	S3	0.288	10.78
ABELL 0644 ‡	2211	08:17:25.225	-07:30:40.03	29.7	VF	I3	0.070	6.95
ABELL 0665	3586	08:30:59.231	+65:50:37.78	29.7	VF	I3	0.181	13.37
ABELL 0697	4217	08:42:57.549	+36:21:57.65	19.5	VF	I3	0.282	26.10
ABELL 0773	5006	09:17:52.566	+51:43:38.18	19.8	VF	I3	0.217	12.87
ABELL 0781	534	09:20:25.431	+30:30:07.56	9.9	VF	I3	0.298	8.24
ABELL 0907	3185	09:58:21.880	-11:03:52.20	48.0	VF	I3	0.153	6.19
ABELL 0963	903	10:17:03.744	+39:02:49.17	36.3	F	S3	0.206	10.65
ABELL 1063S	4966	22:48:44.294	-44:31:48.37	26.7	VF	I3	0.354	71.09
ABELL 1068 ‡	1652	10:40:44.520	+39:57:10.28	26.8	F	S3	0.138	4.19
ABELL 1201 ‡	4216	11:12:54.489	+13:26:08.76	39.7	VF	S3	0.169	3.52
ABELL 1204	2205	11:13:20.419	+17:35:38.45	23.6	VF	I3	0.171	3.92
ABELL 1361 ‡	2200	11:43:39.827	+46:21:21.40	16.7	F	S3	0.117	2.16
ABELL 1423	538	11:57:17.026	+33:36:37.44	9.8	VF	I3	0.213	7.01
ABELL 1651	4185	12:59:22.830	-04:11:45.86	9.6	VF	I3	0.084	6.66
ABELL 1664 ‡	1648	13:03:42.478	-24:14:44.55	9.8	VF	S3	0.128	2.59
ABELL 1682	3244	13:06:50.764	+46:33:19.86	9.8	VF	I3	0.226	7.92
ABELL 1689	1663	13:11:29.612	-01:20:28.69	10.7	F	I3	0.184	24.71
ABELL 1689	5004	13:11:29.606	-01:20:28.61	19.9	VF	I3	0.184	24.71
ABELL 1689	540	13:11:29.595	-01:20:28.47	10.3	F	I3	0.184	24.71
ABELL 1758	2213	13:32:42.978	+50:32:44.83	58.3	VF	S3	0.279	21.01
ABELL 1763	3591	13:35:17.957	+40:59:55.80	19.6	VF	I3	0.187	9.26
ABELL 1795 ‡	5289	13:48:52.829	+26:35:24.01	15.0	VF	I3	0.062	7.59

Table A.1: Summary of sample for energy band dependance study (continued)

Cluster	Obs.ID	R.A. hr:min:sec	Dec. ° :′:″	ExpT ksec	Mode	ACIS	z	$L_{bol.}$ 10^{44} ergs s^{-1}
(1)	(2)	(3)	(4)	(5)	(6)	(7)	(8)	(9)
ABELL 1835	495	14:01:01.951	+02:52:43.18	19.5	F	S3	0.253	39.38
ABELL 1914	3593	14:26:01.399	+37:49:27.83	18.9	VF	I3	0.171	26.25
ABELL 1942	3290	14:38:21.878	+03:40:12.97	57.6	VF	I2	0.224	2.27
ABELL 1995	906	14:52:57.758	+58:02:51.34	0.0	F	S3	0.319	10.19
ABELL 2029 ‡	6101	15:10:56.163	+05:44:40.89	9.9	VF	I3	0.076	13.90
ABELL 2034	2204	15:10:11.003	+33:30:46.46	53.9	VF	I3	0.113	6.45
ABELL 2065 ‡	31821	15:22:29.220	+27:42:46.54	0.0	VF	I3	0.073	2.92
ABELL 2069	4965	15:24:09.181	+29:53:18.05	55.4	VF	I2	0.116	3.82
ABELL 2111	544	15:39:41.432	+34:25:12.26	10.3	F	I3	0.230	7.45
ABELL 2125	2207	15:41:14.154	+66:15:57.20	81.5	VF	I3	0.246	0.77
ABELL 2163	1653	16:15:45.705	-06:09:00.62	71.1	VF	I1	0.170	49.11
ABELL 2204 ‡	499	16:32:45.437	+05:34:21.05	10.1	F	S3	0.152	20.77
ABELL 2204	6104	16:32:45.428	+05:34:20.89	9.6	VF	I3	0.152	22.03
ABELL 2218	1666	16:35:50.831	+66:12:42.31	48.6	VF	I0	0.171	8.39
ABELL 2219 ‡	896	16:40:21.069	+46:42:29.07	42.3	F	S3	0.226	33.15
ABELL 2255	894	17:12:40.385	+64:03:50.63	39.4	F	I3	0.081	3.67
ABELL 2256 ‡	1386	17:03:44.567	+78:38:11.51	12.4	F	I3	0.058	4.65
ABELL 2259	3245	17:20:08.299	+27:40:11.53	10.0	VF	I3	0.164	5.37
ABELL 2261	5007	17:22:27.254	+32:07:58.60	24.3	VF	I3	0.224	17.49
ABELL 2294	3246	17:24:10.149	+85:53:09.77	10.0	VF	I3	0.178	10.35
ABELL 2384	4202	21:52:21.178	-19:32:51.90	31.5	VF	I3	0.095	1.95
ABELL 2390 ‡	4193	21:53:36.825	+17:41:44.38	95.1	VF	S3	0.230	31.02
ABELL 2409	3247	22:00:52.567	+20:58:34.11	10.2	VF	I3	0.148	7.01
ABELL 2537	4962	23:08:22.313	-02:11:29.88	36.2	VF	S3	0.295	10.16
ABELL 2550	2225	23:11:35.806	-21:44:46.70	59.0	VF	S3	0.154	0.58
ABELL 2554 ‡	1696	23:12:19.939	-21:30:09.84	19.9	VF	S3	0.110	1.57
ABELL 2556 ‡	2226	23:13:01.413	-21:38:04.47	19.9	VF	S3	0.086	1.43

Table A.1: Summary of sample for energy band dependance study (continued)

Cluster	Obs.ID	R.A. hr:min:sec	Dec. ° :′:″	ExpT ksec	Mode	ACIS	z	$L_{bol.}$ 10^{44} ergs s^{-1}
(1)	(2)	(3)	(4)	(5)	(6)	(7)	(8)	(9)
ABELL 2631	3248	23:37:38.560	+00:16:28.64	9.2	VF	I3	0.278	12.59
ABELL 2667	2214	23:51:39.395	-26:05:02.75	9.6	VF	S3	0.230	19.91
ABELL 2670	4959	23:54:13.687	-10:25:08.85	39.6	VF	I3	0.076	1.39
ABELL 2717	6974	00:03:11.996	-35:56:08.01	19.8	VF	I3	0.048	0.26
ABELL 2744	2212	00:14:14.396	-30:22:40.04	24.8	VF	S3	0.308	29.00
ABELL 3128 ‡	893	03:29:50.918	-52:34:51.04	19.6	F	I3	0.062	0.35
ABELL 3158 ‡	3201	03:42:54.675	-53:37:24.36	24.8	VF	I3	0.059	3.01
ABELL 3158 ‡	3712	03:42:54.683	-53:37:24.37	30.9	VF	I3	0.059	3.01
ABELL 3164	6955	03:46:16.839	-57:02:11.38	13.5	VF	I3	0.057	0.19
ABELL 3376	3202	06:02:05.122	-39:57:42.82	44.3	VF	I3	0.046	0.75
ABELL 3376	3450	06:02:05.162	-39:57:42.87	19.8	VF	I3	0.046	0.75
ABELL 3391 ‡	4943	06:26:21.511	-53:41:44.81	18.4	VF	I3	0.056	1.44
ABELL 3921	4973	22:49:57.829	-64:25:42.17	29.4	VF	I3	0.093	3.37
AC 114	1562	22:58:48.196	-34:47:56.89	72.5	F	S3	0.312	10.90
CL 0024+17	929	00:26:35.996	+17:09:45.37	39.8	F	S3	0.394	2.88
CL 1221+4918	1662	12:21:26.709	+49:18:21.60	79.1	VF	I3	0.700	8.65
CL J0030+2618	5762	00:30:34.339	+26:18:01.58	17.9	VF	I3	0.500	3.41
CL J0152-1357	913	01:52:42.141	-13:57:59.71	36.5	F	I3	0.831	13.30
CL J0542.8-4100	914	05:42:49.994	-40:59:58.50	50.4	F	I3	0.630	6.18
CL J0848+4456	1708	08:48:48.255	+44:56:17.11	61.4	VF	I1	0.574	3.02
CL J0848+4456	927	08:48:48.252	+44:56:17.13	125.1	VF	I1	0.574	3.02
CL J1113.1-2615	915	11:13:05.167	-26:15:40.43	104.6	F	I3	0.730	2.22
CL J1213+0253	4934	12:13:34.948	+02:53:45.45	18.9	VF	I3	0.409	1.29
CL J1226.9+3332	3180	12:26:58.373	+33:32:47.36	31.7	VF	I3	0.890	30.76
CL J1226.9+3332	5014	12:26:58.372	+33:32:47.38	32.7	VF	I3	0.890	30.76
CL J1641+4001	3575	16:41:53.704	+40:01:44.40	46.5	VF	I3	0.464	1.19
CL J2302.8+0844	918	23:02:48.156	+08:43:52.74	108.6	F	I3	0.730	2.93

Table A.1: Summary of sample for energy band dependance study (continued)

Cluster	Obs.ID	R.A. hr:min:sec	Dec. ° :′:″	ExpT ksec	Mode	ACIS	z	$L_{bol.}$ 10^{44} ergs s^{-1}
(1)	(2)	(3)	(4)	(5)	(6)	(7)	(8)	(9)
DLS J0514-4904	4980	05:14:40.037	-49:03:15.07	19.9	VF	I3	0.091	0.68
EXO 0422-086 ‡	4183	04:25:51.271	-08:33:36.42	10.0	VF	I3	0.040	0.65
HERCULES A ‡	1625	16:51:08.161	+04:59:32.44	14.8	VF	S3	0.154	3.27
IRAS 09104+4109	509	09:13:45.481	+40:56:27.49	9.1	F	S3	0.442	20.15
LYNX E	17081	08:48:58.851	+44:51:51.44	61.4	VF	I2	1.260	2.10
LYNX E	9271	08:48:58.858	+44:51:51.46	125.1	VF	I2	1.260	2.10
MACS J0011.7-1523	3261	00:11:42.965	-15:23:20.79	21.6	VF	I3	0.360	10.75
MACS J0011.7-1523	6105	00:11:42.957	-15:23:20.76	37.3	VF	I3	0.360	10.75
MACS J0025.4-1222	3251	00:25:29.398	-12:22:38.15	19.3	VF	I3	0.584	13.00
MACS J0025.4-1222	5010	00:25:29.399	-12:22:38.10	24.8	VF	I3	0.584	13.00
MACS J0035.4-2015	3262	00:35:26.573	-20:15:46.06	21.4	VF	I3	0.364	19.79
MACS J0111.5+0855	3256	01:11:31.515	+08:55:39.21	19.4	VF	I3	0.263	0.64
MACS J0152.5-2852	3264	01:52:34.479	-28:53:38.01	17.5	VF	I3	0.341	6.33
MACS J0159.0-3412	5818	01:59:00.366	-34:13:00.23	9.4	VF	I3	0.458	18.92
MACS J0159.8-0849	3265	01:59:49.453	-08:50:00.90	17.9	VF	I3	0.405	26.31
MACS J0159.8-0849	6106	01:59:49.452	-08:50:00.92	35.3	VF	I3	0.405	26.31
MACS J0242.5-2132	3266	02:42:35.906	-21:32:26.30	11.9	VF	I3	0.314	12.74
MACS J0257.1-2325	1654	02:57:09.150	-23:26:06.25	19.8	F	I3	0.505	21.72
MACS J0257.1-2325	3581	02:57:09.152	-23:26:06.21	18.5	VF	I3	0.505	21.72
MACS J0257.6-2209	3267	02:57:41.024	-22:09:11.12	20.5	VF	I3	0.322	10.77
MACS J0308.9+2645	3268	03:08:55.927	+26:45:38.34	24.4	VF	I3	0.324	20.42
MACS J0329.6-0211	3257	03:29:41.681	-02:11:47.67	9.9	VF	I3	0.450	12.82
MACS J0329.6-0211	3582	03:29:41.688	-02:11:47.81	19.9	VF	I3	0.450	12.82
MACS J0329.6-0211	6108	03:29:41.681	-02:11:47.57	39.6	VF	I3	0.450	12.82
MACS J0404.6+1109	3269	04:04:32.491	+11:08:02.10	21.8	VF	I3	0.355	3.90
MACS J0417.5-1154	3270	04:17:34.686	-11:54:32.71	12.0	VF	I3	0.440	37.99
MACS J0429.6-0253	3271	04:29:36.088	-02:53:09.02	23.2	VF	I3	0.399	11.58

Table A.1: Summary of sample for energy band dependance study (continued)

Cluster	Obs.ID	R.A. hr:min:sec	Dec. ° :′:″	ExpT ksec	Mode	ACIS	z	$L_{bol.}$ 10^{44} ergs s^{-1}
(1)	(2)	(3)	(4)	(5)	(6)	(7)	(8)	(9)
MACS J0451.9+0006	5815	04:51:54.291	+00:06:20.20	10.2	VF	I3	0.430	8.20
MACS J0455.2+0657	5812	04:55:17.426	+06:57:47.15	9.9	VF	I3	0.425	9.77
MACS J0520.7-1328	3272	05:20:42.052	-13:28:49.38	19.2	VF	I3	0.340	9.63
MACS J0547.0-3904	3273	05:47:01.582	-39:04:28.24	21.7	VF	I3	0.210	1.59
MACS J0553.4-3342	5813	05:53:27.200	-33:42:53.02	9.9	VF	I3	0.407	32.68
MACS J0717.5+3745	1655	07:17:31.654	+37:45:18.52	19.9	F	I3	0.548	46.58
MACS J0717.5+3745	4200	07:17:31.651	+37:45:18.46	59.2	VF	I3	0.548	46.58
MACS J0744.8+3927	3197	07:44:52.802	+39:27:24.43	20.2	VF	I3	0.686	24.67
MACS J0744.8+3927	3585	07:44:52.809	+39:27:24.41	19.9	VF	I3	0.686	24.67
MACS J0744.8+3927	6111	07:44:52.800	+39:27:24.42	49.5	VF	I3	0.686	24.67
MACS J0911.2+1746	3587	09:11:11.325	+17:46:31.02	17.9	VF	I3	0.541	10.52
MACS J0911.2+1746	5012	09:11:11.329	+17:46:30.99	23.8	VF	I3	0.541	10.52
MACS J0949+1708	3274	09:49:51.824	+17:07:05.62	14.3	VF	I3	0.382	19.19
MACS J1006.9+3200	5819	10:06:54.668	+32:01:34.61	10.9	VF	I3	0.359	6.06
MACS J1105.7-1014	5817	11:05:46.462	-10:14:37.20	10.3	VF	I3	0.466	11.29
MACS J1108.8+0906	3252	11:08:55.393	+09:05:51.16	9.9	VF	I3	0.449	8.96
MACS J1108.8+0906	5009	11:08:55.402	+09:05:51.14	24.5	VF	I3	0.449	8.96
MACS J1115.2+5320	3253	11:15:15.632	+53:20:03.71	8.8	VF	I3	0.439	14.29
MACS J1115.2+5320	5008	11:15:15.636	+53:20:03.74	18.0	VF	I3	0.439	14.29
MACS J1115.2+5320	5350	11:15:15.632	+53:20:03.77	6.9	VF	I3	0.439	14.29
MACS J1115.8+0129	3275	11:15:52.048	+01:29:56.56	15.9	VF	I3	0.120	1.47
MACS J1131.8-1955	3276	11:31:56.011	-19:55:55.85	13.9	VF	I3	0.307	17.45
MACS J1149.5+2223	1656	11:49:35.856	+22:23:55.02	18.5	VF	I3	0.544	21.60
MACS J1149.5+2223	3589	11:49:35.858	+22:23:55.05	20.0	VF	I3	0.544	21.60
MACS J1206.2-0847	3277	12:06:12.276	-08:48:02.40	23.5	VF	I3	0.440	37.02
MACS J1226.8+2153	3590	12:26:51.207	+21:49:55.22	19.0	VF	I3	0.370	2.63
MACS J1311.0-0310	3258	13:11:01.685	-03:10:39.70	14.9	VF	I3	0.494	10.03

Table A.1: Summary of sample for energy band dependance study (continued)

Cluster	Obs.ID	R.A. hr:min:sec	Dec. ° :′:″	ExpT ksec	Mode	ACIS	z	$L_{bol.}$ 10^{44} ergs s^{-1}
(1)	(2)	(3)	(4)	(5)	(6)	(7)	(8)	(9)
MACS J1311.0-0310	6110	13:11:01.680	-03:10:39.75	63.2	VF	I3	0.494	10.03
MACS J1319+7003	3278	13:20:08.370	+70:04:33.81	21.6	VF	I3	0.328	7.03
MACS J1427.2+4407	6112	14:27:16.175	+44:07:30.33	9.4	VF	I3	0.477	14.18
MACS J1427.6-2521	3279	14:27:39.389	-25:21:04.66	16.9	VF	I3	0.220	1.55
MACS J1621.3+3810	3254	16:21:25.552	+38:09:43.56	9.8	VF	I3	0.461	11.49
MACS J1621.3+3810	3594	16:21:25.558	+38:09:43.54	19.7	VF	I3	0.461	11.49
MACS J1621.3+3810	6109	16:21:25.555	+38:09:43.54	37.5	VF	I3	0.461	11.49
MACS J1621.3+3810	6172	16:21:25.559	+38:09:43.53	29.8	VF	I3	0.461	11.49
MACS J1731.6+2252	3281	17:31:39.902	+22:52:00.55	20.5	VF	I3	0.366	9.32
MACS J1824.3+4309	3255	18:24:18.444	+43:09:43.39	14.9	VF	I3	0.487	2.48
MACS J1931.8-2634	3282	19:31:49.656	-26:34:33.99	13.6	VF	I3	0.352	23.14
MACS J2046.0-3430	5816	20:46:00.522	-34:30:15.50	10.0	VF	I3	0.413	5.79
MACS J2049.9-3217	3283	20:49:56.245	-32:16:52.30	23.8	VF	I3	0.325	8.71
MACS J2211.7-0349	3284	22:11:45.856	-03:49:37.24	17.7	VF	I3	0.270	22.11
MACS J2214.9-1359	3259	22:14:57.487	-14:00:09.35	19.5	VF	I3	0.503	24.05
MACS J2214.9-1359	5011	22:14:57.481	-14:00:09.39	18.5	VF	I3	0.503	24.05
MACS J2228+2036	3285	22:28:33.241	+20:37:11.42	19.9	VF	I3	0.412	17.92
MACS J2229.7-2755	3286	22:29:45.358	-27:55:38.41	16.4	VF	I3	0.324	9.49
MACS J2243.3-0935	3260	22:43:21.537	-09:35:44.30	20.5	VF	I3	0.101	0.78
MACS J2245.0+2637	3287	22:45:04.547	+26:38:07.88	16.9	VF	I3	0.304	9.36
MACS J2311+0338	3288	23:11:33.213	+03:38:06.51	13.6	VF	I3	0.300	10.98
MKW3S	900	15:21:51.930	+07:42:31.97	57.3	VF	I3	0.045	1.14
MS 0016.9+1609	520	00:18:33.503	+16:26:12.99	67.4	VF	I3	0.541	32.94
MS 0302.7+1658	525	03:05:31.614	+17:10:02.06	10.0	VF	I3	0.424	2.41
MS 0440.5+0204 ‡	4196	04:43:09.952	+02:10:18.70	59.4	VF	S3	0.190	2.17
MS 0451.6-0305	902	04:54:11.004	-03:00:52.19	44.2	F	S3	0.539	33.32
MS 0735.6+7421	4197	07:41:44.245	+74:14:38.23	45.5	VF	S3	0.216	7.57

Table A.1: Summary of sample for energy band dependance study (continued)

Cluster	Obs.ID	R.A. hr:min:sec	Dec. ° :′:″	ExpT ksec	Mode	ACIS	z	$L_{bol.}$ 10^{44} ergs s^{-1}
(1)	(2)	(3)	(4)	(5)	(6)	(7)	(8)	(9)
MS 0839.8+2938	2224	08:42:55.969	+29:27:26.97	29.8	F	S3	0.194	3.10
MS 0906.5+1110	924	09:09:12.753	+10:58:32.00	29.7	VF	I3	0.163	4.64
MS 1006.0+1202	925	10:08:47.194	+11:47:55.99	29.4	VF	I3	0.221	4.75
MS 1008.1-1224	926	10:10:32.312	-12:39:56.80	44.2	VF	I3	0.301	6.44
MS 1054.5-0321	512	10:56:58.499	-03:37:32.76	89.1	F	S3	0.830	27.22
MS 1455.0+2232	4192	14:57:15.088	+22:20:32.49	91.9	VF	I3	0.259	10.25
MS 1621.5+2640	546	16:23:35.522	+26:34:25.67	30.1	F	I3	0.426	6.49
MS 2053.7-0449	1667	20:56:21.295	-04:37:46.81	44.5	VF	I3	0.583	2.96
MS 2053.7-0449	551	20:56:21.297	-04:37:46.80	44.3	F	I3	0.583	2.96
MS 2137.3-2353	4974	21:40:15.178	-23:39:40.71	57.4	VF	S3	0.313	11.28
MS J1157.3+5531 ‡	4964	11:59:52.295	+55:32:05.61	75.1	VF	S3	0.081	0.12
NGC 6338 ‡	4194	17:15:23.036	+57:24:40.29	47.3	VF	I3	0.028	0.13
PKS 0745-191	6103	07:47:31.469	-19:17:40.01	10.3	VF	I3	0.103	18.41
RBS 0797	2202	09:47:12.971	+76:23:13.90	11.7	VF	I3	0.354	26.07
RDCS 1252-29	4198	12:52:54.221	-29:27:21.01	163.4	VF	I3	1.237	2.28
RX J0232.2-4420	4993	02:32:18.771	-44:20:46.68	23.4	VF	I3	0.284	18.17
RX J0340-4542	6954	03:40:44.765	-45:41:18.41	17.9	VF	I3	0.082	0.33
RX J0439+0520	527	04:39:02.218	+05:20:43.11	9.6	VF	I3	0.208	3.57
RX J0439.0+0715	1449	04:39:00.710	+07:16:07.65	6.3	F	I3	0.230	9.44
RX J0439.0+0715	3583	04:39:00.710	+07:16:07.63	19.2	VF	I3	0.230	9.44
RX J0528.9-3927	4994	05:28:53.039	-39:28:15.53	22.5	VF	I3	0.263	12.99
RX J0647.7+7015	3196	06:47:50.029	+70:14:49.66	19.3	VF	I3	0.584	26.48
RX J0647.7+7015	3584	06:47:50.024	+70:14:49.69	20.0	VF	I3	0.584	26.48
RX J0819.6+6336 ‡	2199	08:19:26.007	+63:37:26.53	14.9	F	S3	0.119	0.98
RX J0910+5422	2452	09:10:44.478	+54:22:03.77	65.3	VF	I3	1.100	1.33
RX J1053+5735	4936	10:53:39.844	+57:35:18.42	92.2	F	S3	1.140	1.59
RX J1347.5-1145	3592	13:47:30.593	-11:45:10.25	57.7	VF	I3	0.451	100.36

Table A.1: Summary of sample for energy band dependance study (continued)

Cluster	Obs.ID	R.A. hr:min:sec	Dec. ° :′:″	ExpT ksec	Mode	ACIS	z	$L_{bol.}$ 10^{44} ergs s^{-1}
(1)	(2)	(3)	(4)	(5)	(6)	(7)	(8)	(9)
RX J1347.5-1145	507	13:47:30.598	-11:45:10.27	10.0	F	S3	0.451	100.36
RX J1350+6007	2229	13:50:48.038	+60:07:08.39	58.3	VF	I3	0.804	2.19
RX J1423.8+2404	1657	14:23:47.759	+24:04:40.65	18.5	VF	I3	0.545	15.84
RX J1423.8+2404	4195	14:23:47.763	+24:04:40.63	115.6	VF	S3	0.545	15.84
RX J1504.1-0248	5793	15:04:07.415	-02:48:15.70	39.2	VF	I3	0.215	34.64
RX J1525+0958	1664	15:24:39.729	+09:57:44.42	50.9	VF	I3	0.516	3.29
RX J1532.9+3021	1649	15:32:55.642	+30:18:57.69	9.4	VF	S3	0.345	20.77
RX J1532.9+3021	1665	15:32:55.641	+30:18:57.61	10.0	VF	I3	0.345	20.77
RX J1716.9+6708	548	17:16:49.015	+67:08:25.80	51.7	F	I3	0.810	8.04
RX J1720.1+2638	4361	17:20:09.941	+26:37:29.11	25.7	VF	I3	0.164	11.39
RX J1720.2+3536	3280	17:20:16.953	+35:36:23.63	20.8	VF	I3	0.391	13.02
RX J1720.2+3536	6107	17:20:16.949	+35:36:23.68	33.9	VF	I3	0.391	13.02
RX J1720.2+3536	7225	17:20:16.947	+35:36:23.69	2.0	VF	I3	0.391	13.02
RX J2011.3-5725	4995	20:11:26.889	-57:25:09.08	24.0	VF	I3	0.279	2.77
RX J2129.6+0005	552	21:29:39.944	+00:05:18.83	10.0	VF	I3	0.235	12.56
S0463	6956	04:29:07.040	-53:49:38.02	29.3	VF	I3	0.099	22.19
S0463	7250	04:29:07.063	-53:49:38.11	29.1	VF	I3	0.099	22.19
TRIANG AUSTR ‡	1281	16:38:22.712	-64:21:19.70	11.4	F	I3	0.051	9.41
V 1121.0+2327	1660	11:20:57.195	+23:26:27.60	71.3	VF	I3	0.560	3.28
ZWCL 1215	4184	12:17:40.787	+03:39:39.42	12.1	VF	I3	0.075	3.49
ZWCL 1358+6245	516	13:59:50.526	+62:31:04.57	54.1	F	S3	0.328	12.42
ZWCL 1953	1659	08:50:06.677	+36:04:16.16	24.9	F	I3	0.380	17.11
ZWCL 3146	909	10:23:39.735	+04:11:08.05	46.0	F	I3	0.290	29.59
ZWCL 5247	539	12:34:21.928	+09:47:02.83	9.3	VF	I3	0.229	4.87
ZWCL 7160	543	14:57:15.158	+22:20:33.85	9.9	F	I3	0.258	10.14
ZWICKY 2701	3195	09:52:49.183	+51:53:05.27	26.9	VF	S3	0.210	5.19
ZwCL 1332.8+5043	5772	13:34:20.698	+50:31:04.64	19.5	VF	I3	0.620	4.46

Table A.1: Summary of sample for energy band dependance study (continued)

Cluster	Obs.ID	R.A. hr:min:sec	Dec. $^\circ$:′:″	ExpT ksec	Mode	ACIS	z	$L_{bol.}$ 10^{44} ergs s^{-1}
(1)	(2)	(3)	(4)	(5)	(6)	(7)	(8)	(9)
ZwCl 0848.5+3341	4205	08:51:38.873	+33:31:08.00	11.4	VF	S3	0.371	4.58

Table A.2: Clusters with $T_{HBR} > 1.1$ with 90% confidence.

Name	T_{HBR}	Merger?	Core Class	T_{dec}	X-ray Morphology	Ref.
RX J1525+0958	$1.86^{+0.83}_{-0.51}$	Y	CC	$0.42^{+0.14}_{-0.08}$	Arrowhead shape & no discernible core	[29]
MS 1008.1-1224	$1.59^{+0.37}_{-0.27}$	Y	NCC	$0.93^{+0.19}_{-0.14}$	Wide gas tail extending ≈550 kpc north	[1]
ABELL 2034	$1.40^{+0.14}_{-0.11}$	Y	NCC	$1.07^{+0.11}_{-0.09}$	Prominent cold front & gas tail extending south	[2]
ABELL 401	$1.37^{+0.12}_{-0.10}$	Y	NCC	$1.13^{+0.12}_{-0.10}$	Highly spherical & possible cold front to north	[3]
ABELL 1689	$1.36^{+0.14}_{-0.12}$	Y	NCC	$0.95^{+0.09}_{-0.07}$	Exceptionally spherical & bright central core	[6],[7]
RX J0439.0+0715 ..	$1.42^{+0.24}_{-0.18}$	Unknown	NCC	$0.98^{+0.11}_{-0.09}$	Bright core & possible cold front to north	[29]
ABELL 3376	$1.33^{+0.11}_{-0.10}$	Y	NCC	$0.97^{+0.07}_{-0.07}$	Highly disturbed & broad gas tail to west	[4],[5]
ABELL 2255	$1.32^{+0.12}_{-0.10}$	Y	NCC	$1.48^{+0.32}_{-0.23}$	Spherical & compressed isophotes west of core	[8],[9]
ABELL 2218	$1.36^{+0.19}_{-0.15}$	Y	NCC	$1.39^{+0.23}_{-0.19}$	Spherical, core of cluster elongated NW-SE	[10]
ABELL 1763	$1.48^{+0.39}_{-0.26}$	Y	NCC	$0.83^{+0.17}_{-0.13}$	Elongated ENE-SSW & cold front to west of core	[11],[12]
MACS J2243.3-0935	$1.76^{+0.81}_{-0.55}$	Unknown	NCC	$1.73^{+0.44}_{-0.32}$	No core & highly flattened along WNW-ESE axis	[29]
ABELL 2069	$1.32^{+0.17}_{-0.14}$	Y	NCC	$1.00^{+0.18}_{-0.14}$	No core & highly elongated NNW-SSE	[13]
ABELL 2384	$1.31^{+0.16}_{-0.14}$	Unknown	CC	$0.59^{+0.03}_{-0.03}$	Gas tail extending 1.1 Mpc from core	[29]
ABELL 168	$1.31^{+0.16}_{-0.14}$	Y	NCC	$1.16^{+0.14}_{-0.10}$	Highly disrupted & irregular	[14],[15]
ABELL 209	$1.38^{+0.28}_{-0.22}$	Y	NCC	$1.08^{+0.22}_{-0.17}$	Asymmetric core structure & possible cold front	[16]
ABELL 665	$1.29^{+0.15}_{-0.13}$	Y	NCC	$1.14^{+0.19}_{-0.15}$	Wide, broad gas tail to north & cold front	[17]
1E0657-56	$1.21^{+0.06}_{-0.05}$	Y	NCC	$1.04^{+0.10}_{-0.08}$	The famous "Bullet Cluster"	[18]
MACS J0547.0-3904	$1.51^{+0.50}_{-0.36}$	Unknown	NCC	$0.77^{+0.14}_{-0.18}$	Bright core & gas spur extending NW	[29]
ZWCL 1215	$1.31^{+0.21}_{-0.18}$	Unknown	NCC	$0.95^{+0.15}_{-0.12}$	No core, flattened along NE-SW axis	[29]
ABELL 1204	$1.26^{+0.17}_{-0.14}$	Unknown	NCC	$0.96^{+0.05}_{-0.05}$	Highly spherical & bright centralized core	[29]
MKW3S	$1.17^{+0.05}_{-0.05}$	Y	CC	$0.87^{+0.02}_{-0.02}$	High mass group, egg shaped & bright core	[19]
MACS J2311+0338	$1.53^{+0.69}_{-0.42}$	Unknown	NCC	$0.69^{+0.20}_{-0.15}$	Elongated N-S & disc-like core	[29]
ABELL 267	$1.33^{+0.27}_{-0.21}$	Unknown	NCC	$1.09^{+0.20}_{-0.16}$	Elongated NNE-SSW & cold front to north	[29]
RX J1720.1+2638 ..	$1.22^{+0.12}_{-0.11}$	Y	CC	$0.73^{+0.04}_{-0.04}$	Very spherical, bright peaky core, & cold front	[20]
ABELL 907	$1.21^{+0.10}_{-0.08}$	Unknown	CC	$0.76^{+0.03}_{-0.03}$	NW-SW elongation & western cold front	[29]
ABELL 514	$1.26^{+0.19}_{-0.15}$	Y	NCC	$1.56^{+1.07}_{-0.40}$	Very diffuse & disrupted	[21]
ABELL 1651	$1.24^{+0.16}_{-0.13}$	Y	NCC	$1.07^{+0.10}_{-0.08}$	Spherical & compressed isophotes to SW	[22]

Table A.2: Clusters with $T_{HBR} > 1.1$ with 90% confidence. (continued)

Name	T_{HBR}	Merger?	Core Class	T_{dec}	X-ray Morphology	Ref.
3C 28.0	$1.23^{+0.14}_{-0.12}$	Y	CC	$0.54^{+0.03}_{-0.03}$	Obvious merger & ∼1 Mpc gas tail	[23]
				$R_{5000-\mathrm{CORE}}$ Only		
TRIANG AUSTR ..	$1.42^{+0.14}_{-0.14}$	Y	NCC	$0.90^{+0.06}_{-0.09}$	Highly diffuse & no bright core	[24]
ABELL 3158	$1.23^{+0.05}_{-0.05}$	Y	NCC	$1.15^{+0.05}_{-0.05}$	Large centroid variation	[25]
ABELL 2256	$1.29^{+0.13}_{-0.12}$	Y	NCC	$1.40^{+0.15}_{-0.12}$	Spiral shaped & distinct NW edge	[26]
NGC 6338	$1.22^{+0.12}_{-0.10}$	Unknown	NCC	$0.96^{+0.04}_{-0.03}$	Disrupted group companion to north	[29]
ABELL 2029	$1.21^{+0.12}_{-0.10}$	Y	CC	$0.86^{+0.04}_{-0.04}$	Possible cold front to W & WAT radio source	[27],[28]

Table A.3: Summary of Excised R_{2500} Spectral Fits

Cluster	$R_{\rm CORE}$ kpc	R_{2500} kpc	N_H 10^{20} cm^{-2}	T_{77} keV	T_{27} keV	T_{HBR}	Z_{77} $Z_\odot$	$\chi^2_{red,77}$	$\chi^2_{red,27}$	% Source
(1)	(2)	(3)	(4)	(5)	(6)	(7)	(8)	(9)	(10)	(11)
1E0657 56 ⋆	69	688	6.53	$11.99^{+0.27}_{-0.26}$	$14.54^{+0.67}_{-0.53}$	$1.21^{+0.06}_{-0.05}$	$0.29^{+0.03}_{-0.02}$	1.24	1.11	92
1RXS J2129.4-0741 ⋆	71	526	4.36	$8.22^{+1.18}_{-0.95}$	$8.10^{+1.47}_{-1.10}$	$0.99^{+0.23}_{-0.18}$	$0.43^{+0.18}_{-0.17}$	1.07	1.05	80
2PIGG J0011.5-2850	69	547	2.18	$5.15^{+0.25}_{-0.24}$	$6.20^{+0.79}_{-0.65}$	$1.20^{+0.16}_{-0.14}$	$0.26^{+0.09}_{-0.08}$	1.09	1.00	70
2PIGG J2227.0-3041	69	378	1.11	$2.80^{+0.15}_{-0.14}$	$2.97^{+0.34}_{-0.27}$	$1.06^{+0.13}_{-0.11}$	$0.35^{+0.09}_{-0.08}$	1.16	1.15	69
3C 220.1	71	456	1.91	$9.26^{+14.71}_{-3.98}$	$8.00^{+17.66}_{-4.03}$	$0.86^{+2.35}_{-0.57}$	$0.00^{+0.59}_{-0.00}$	1.20	1.40	30
3C 28.0	70	420	5.71	$5.53^{+0.29}_{-0.27}$	$6.81^{+0.71}_{-0.60}$	$1.23^{+0.14}_{-0.12}$	$0.30^{+0.08}_{-0.07}$	0.98	0.88	87
3C 295	69	465	1.35	$5.16^{+0.42}_{-0.38}$	$5.93^{+0.84}_{-0.69}$	$1.15^{+0.19}_{-0.16}$	$0.38^{+0.12}_{-0.11}$	0.91	0.93	79
3C 388	69	420	6.11	$3.23^{+0.23}_{-0.21}$	$3.26^{+0.49}_{-0.37}$	$1.01^{+0.17}_{-0.13}$	$0.51^{+0.16}_{-0.14}$	0.95	0.95	68
4C 55.16	69	426	4.00	$4.98^{+0.17}_{-0.17}$	$5.54^{+0.40}_{-0.36}$	$1.11^{+0.09}_{-0.08}$	$0.49^{+0.07}_{-0.07}$	0.89	0.80	58
ABELL 0068	70	680	4.60	$9.01^{+1.53}_{-1.14}$	$9.13^{+2.60}_{-1.71}$	$1.01^{+0.34}_{-0.23}$	$0.46^{+0.24}_{-0.22}$	1.15	1.13	79
ABELL 0168 ⋆	70	398	3.27	$2.56^{+0.11}_{-0.08}$	$3.36^{+0.37}_{-0.35}$	$1.31^{+0.16}_{-0.14}$	$0.29^{+0.06}_{-0.04}$	1.07	1.03	40
ABELL 0209 ⋆	70	609	1.68	$7.30^{+0.59}_{-0.51}$	$10.07^{+1.91}_{-1.41}$	$1.38^{+0.28}_{-0.22}$	$0.23^{+0.10}_{-0.09}$	1.12	1.11	82
ABELL 0267 ⋆	70	545	2.74	$6.70^{+0.56}_{-0.47}$	$8.88^{+1.68}_{-1.27}$	$1.33^{+0.27}_{-0.21}$	$0.32^{+0.11}_{-0.11}$	1.18	1.15	82
ABELL 0370	69	516	3.37	$7.35^{+0.72}_{-0.84}$	$10.35^{+1.89}_{-2.27}$	$1.41^{+0.29}_{-0.35}$	$0.45^{+0.06}_{-0.23}$	1.08	1.04	39
ABELL 0383	69	423	4.07	$4.91^{+0.29}_{-0.27}$	$5.42^{+0.74}_{-0.59}$	$1.10^{+0.16}_{-0.13}$	$0.44^{+0.11}_{-0.11}$	0.97	0.90	64
ABELL 0399	69	546	$7.57^{+0.71}_{-0.71}$	$7.95^{+0.35}_{-0.31}$	$8.87^{+0.55}_{-0.50}$	$1.12^{+0.08}_{-0.08}$	$0.30^{+0.05}_{-0.05}$	1.12	0.99	82
ABELL 0401	69	643	12.48	$6.37^{+0.19}_{-0.19}$	$8.71^{+0.72}_{-0.61}$	$1.37^{+0.12}_{-0.10}$	$0.26^{+0.06}_{-0.06}$	1.44	1.05	78
ABELL 0478	69	598	30.90	$7.30^{+0.26}_{-0.24}$	$8.62^{+0.58}_{-0.54}$	$1.18^{+0.09}_{-0.08}$	$0.45^{+0.06}_{-0.05}$	1.05	0.95	91
ABELL 0514	71	516	3.14	$3.33^{+0.16}_{-0.16}$	$4.02^{+0.54}_{-0.46}$	$1.21^{+0.17}_{-0.15}$	$0.25^{+0.08}_{-0.06}$	1.07	0.97	53
ABELL 0520	70	576	$1.06^{+1.06}_{-1.05}$	$9.29^{+0.67}_{-0.60}$	$9.88^{+0.85}_{-0.73}$	$1.06^{+0.12}_{-0.10}$	$0.37^{+0.07}_{-0.07}$	1.11	1.04	87
ABELL 0521	70	558	6.17	$7.03^{+0.59}_{-0.53}$	$8.39^{+1.62}_{-1.22}$	$1.19^{+0.25}_{-0.20}$	$0.39^{+0.13}_{-0.12}$	1.10	1.15	49
ABELL 0586	70	635	4.71	$6.47^{+0.55}_{-0.47}$	$8.06^{+1.46}_{-1.11}$	$1.25^{+0.25}_{-0.19}$	$0.56^{+0.17}_{-0.16}$	0.91	0.81	82
ABELL 0611	70	523	4.99	$7.06^{+0.55}_{-0.48}$	$7.97^{+1.09}_{-0.91}$	$1.13^{+0.18}_{-0.15}$	$0.35^{+0.11}_{-0.10}$	0.97	0.98	54
ABELL 0665	69	617	4.24	$7.45^{+0.38}_{-0.34}$	$9.61^{+1.02}_{-0.85}$	$1.29^{+0.15}_{-0.13}$	$0.31^{+0.06}_{-0.07}$	1.02	0.93	87
ABELL 0697	69	612	3.34	$9.52^{+0.87}_{-0.76}$	$12.24^{+2.05}_{-1.63}$	$1.29^{+0.25}_{-0.20}$	$0.37^{+0.12}_{-0.11}$	1.08	1.02	89

Table A.3: Summary of Excised R_{2500} Spectral Fits (continued)

Cluster	$R_{\rm CORE}$ kpc	R_{2500} kpc	N_H 10^{20} cm^{-2}	T_{77} keV	T_{27} keV	T_{HBR}	Z_{77} $Z_\odot$	$\chi^2_{red,77}$	$\chi^2_{red,27}$	% Source
(1)	(2)	(3)	(4)	(5)	(6)	(7)	(8)	(9)	(10)	(11)
ABELL 0773	69	615	1.46	$7.83^{+0.66}_{-0.57}$	$9.75^{+1.65}_{-1.27}$	$1.25^{+0.24}_{-0.19}$	$0.44^{+0.12}_{-0.12}$	1.06	1.09	84
ABELL 0907	69	488	5.69	$5.62^{+0.18}_{-0.17}$	$6.78^{+0.49}_{-0.43}$	$1.21^{+0.10}_{-0.08}$	$0.42^{+0.06}_{-0.05}$	1.13	1.00	88
ABELL 0963	69	543	1.39	$6.73^{+0.32}_{-0.30}$	$6.98^{+0.66}_{-0.57}$	$1.04^{+0.11}_{-0.10}$	$0.29^{+0.07}_{-0.08}$	1.06	1.02	64
ABELL 1063S	69	648	1.77	$11.96^{+0.88}_{-0.79}$	$13.70^{+1.68}_{-1.38}$	$1.15^{+0.16}_{-0.14}$	$0.38^{+0.09}_{-0.09}$	1.02	0.98	90
ABELL 1204	70	419	1.44	$3.63^{+0.18}_{-0.16}$	$4.58^{+0.57}_{-0.45}$	$1.26^{+0.17}_{-0.14}$	$0.31^{+0.09}_{-0.09}$	1.06	0.90	88
ABELL 1423	70	614	1.60	$6.01^{+0.75}_{-0.64}$	$7.53^{+2.35}_{-1.55}$	$1.25^{+0.42}_{-0.29}$	$0.30^{+0.18}_{-0.17}$	0.87	0.65	78
ABELL 1651	70	596	2.02	$6.26^{+0.30}_{-0.27}$	$7.78^{+0.90}_{-0.76}$	$1.24^{+0.16}_{-0.13}$	$0.42^{+0.09}_{-0.09}$	1.19	1.20	86
ABELL 1689 ⋆	70	679	1.87	$9.48^{+0.38}_{-0.35}$	$12.89^{+1.23}_{-1.01}$	$1.36^{+0.14}_{-0.12}$	$0.36^{+0.06}_{-0.05}$	1.13	1.02	91
ABELL 1758	69	574	1.09	$12.14^{+1.15}_{-0.92}$	$11.16^{+3.08}_{-2.14}$	$0.92^{+0.27}_{-0.19}$	$0.56^{+0.13}_{-0.13}$	1.21	1.09	58
ABELL 1763	69	561	0.82	$7.78^{+0.67}_{-0.60}$	$11.49^{+2.89}_{-1.84}$	$1.48^{+0.39}_{-0.26}$	$0.25^{+0.11}_{-0.10}$	1.12	0.92	84
ABELL 1835	70	570	2.36	$9.77^{+0.57}_{-0.52}$	$11.00^{+1.23}_{-1.03}$	$1.13^{+0.14}_{-0.12}$	$0.31^{+0.08}_{-0.07}$	0.98	1.02	86
ABELL 1914	70	698	0.97	$9.62^{+0.55}_{-0.49}$	$11.42^{+1.26}_{-1.06}$	$1.19^{+0.15}_{-0.13}$	$0.30^{+0.08}_{-0.07}$	1.07	1.03	92
ABELL 1942	69	473	2.75	$4.77^{+0.38}_{-0.35}$	$5.49^{+0.98}_{-0.74}$	$1.15^{+0.22}_{-0.18}$	$0.33^{+0.12}_{-0.14}$	1.06	1.04	70
ABELL 1995	71	381	1.44	$8.37^{+0.70}_{-0.61}$	$9.23^{+1.44}_{-1.13}$	$1.10^{+0.20}_{-0.16}$	$0.39^{+0.12}_{-0.11}$	1.02	0.96	74
ABELL 2034	69	594	1.58	$7.15^{+0.23}_{-0.22}$	$10.02^{+0.92}_{-0.75}$	$1.40^{+0.14}_{-0.11}$	$0.32^{+0.05}_{-0.05}$	1.22	1.00	84
ABELL 2069	70	623	1.97	$6.50^{+0.33}_{-0.29}$	$8.61^{+1.02}_{-0.84}$	$1.32^{+0.17}_{-0.14}$	$0.26^{+0.08}_{-0.07}$	1.04	0.96	71
ABELL 2111	70	592	2.20	$7.13^{+1.29}_{-0.95}$	$11.10^{+4.67}_{-3.05}$	$1.56^{+0.71}_{-0.48}$	$0.13^{+0.19}_{-0.13}$	1.06	0.88	76
ABELL 2125	70	371	2.75	$2.88^{+0.30}_{-0.27}$	$3.76^{+0.98}_{-0.65}$	$1.31^{+0.37}_{-0.26}$	$0.31^{+0.18}_{-0.16}$	1.26	1.30	61
ABELL 2163	69	751	12.04	$19.20^{+0.87}_{-0.80}$	$21.30^{+1.77}_{-1.47}$	$1.11^{+0.11}_{-0.09}$	$0.10^{+0.06}_{-0.06}$	1.37	1.26	90
ABELL 2204	70	575	5.84	$8.65^{+0.58}_{-0.52}$	$10.57^{+1.48}_{-1.23}$	$1.22^{+0.19}_{-0.16}$	$0.37^{+0.10}_{-0.09}$	0.95	1.00	90
ABELL 2218	70	558	3.12	$7.35^{+0.39}_{-0.35}$	$10.03^{+1.26}_{-0.98}$	$1.36^{+0.19}_{-0.15}$	$0.22^{+0.07}_{-0.06}$	1.01	0.90	87
ABELL 2255	71	596	2.53	$6.12^{+0.20}_{-0.19}$	$8.10^{+0.66}_{-0.58}$	$1.32^{+0.12}_{-0.10}$	$0.30^{+0.06}_{-0.06}$	1.13	0.95	76
ABELL 2259	69	480	3.70	$5.18^{+0.46}_{-0.39}$	$6.40^{+1.33}_{-0.95}$	$1.24^{+0.28}_{-0.21}$	$0.41^{+0.14}_{-0.14}$	1.05	1.01	85
ABELL 2261	69	576	3.31	$7.63^{+0.47}_{-0.43}$	$9.30^{+1.21}_{-0.91}$	$1.22^{+0.18}_{-0.14}$	$0.36^{+0.08}_{-0.08}$	0.99	0.95	90
ABELL 2294	69	572	6.10	$9.98^{+1.43}_{-1.12}$	$11.07^{+3.19}_{-2.11}$	$1.11^{+0.36}_{-0.25}$	$0.53^{+0.21}_{-0.21}$	1.07	0.95	82
ABELL 2384	70	436	2.99	$4.75^{+0.22}_{-0.20}$	$6.22^{+0.72}_{-0.60}$	$1.31^{+0.16}_{-0.14}$	$0.23^{+0.07}_{-0.07}$	1.06	0.92	81

Table A.3: Summary of Excised R_{2500} Spectral Fits (continued)

Cluster	$R_{\rm CORE}$ kpc	R_{2500} kpc	N_H 10^{20} cm^{-2}	T_{77} keV	T_{27} keV	T_{HBR}	Z_{77} $Z_\odot$	$\chi^2_{red,77}$	$\chi^2_{red,27}$	% Source
(1)	(2)	(3)	(4)	(5)	(6)	(7)	(8)	(9)	(10)	(11)
ABELL 2409	70	511	6.72	$5.94^{+0.43}_{-0.38}$	$6.77^{+0.99}_{-0.82}$	$1.14^{+0.19}_{-0.16}$	$0.37^{+0.13}_{-0.11}$	1.13	0.96	88
ABELL 2537	69	497	4.26	$8.40^{+0.76}_{-0.68}$	$7.81^{+1.15}_{-0.93}$	$0.93^{+0.16}_{-0.13}$	$0.40^{+0.13}_{-0.13}$	0.91	0.84	46
ABELL 2631	70	631	3.74	$7.06^{+1.06}_{-0.84}$	$7.83^{+2.18}_{-1.45}$	$1.11^{+0.35}_{-0.24}$	$0.34^{+0.19}_{-0.18}$	0.97	0.88	83
ABELL 2667	70	525	1.64	$6.75^{+0.48}_{-0.43}$	$7.45^{+1.06}_{-0.88}$	$1.10^{+0.18}_{-0.15}$	$0.36^{+0.11}_{-0.11}$	1.17	1.08	76
ABELL 2670	69	451	2.88	$3.95^{+0.14}_{-0.12}$	$4.65^{+0.42}_{-0.36}$	$1.18^{+0.11}_{-0.10}$	$0.42^{+0.08}_{-0.06}$	1.13	1.07	70
ABELL 2717	70	298	1.12	$2.63^{+0.17}_{-0.16}$	$3.17^{+0.58}_{-0.43}$	$1.21^{+0.23}_{-0.18}$	$0.48^{+0.13}_{-0.10}$	0.88	0.87	55
ABELL 2744	71	647	1.82	$9.18^{+0.68}_{-0.60}$	$10.20^{+1.38}_{-1.10}$	$1.11^{+0.17}_{-0.14}$	$0.24^{+0.10}_{-0.09}$	0.99	0.90	67
ABELL 3164	70	451	2.55	$2.83^{+0.53}_{-0.26}$	$3.81^{+3.56}_{-1.42}$	$1.35^{+1.28}_{-0.52}$	$0.39^{+0.33}_{-0.21}$	0.88	0.94	29
ABELL 3376 ⋆	70	463	5.21	$4.48^{+0.11}_{-0.12}$	$5.95^{+0.47}_{-0.42}$	$1.33^{+0.11}_{-0.10}$	$0.39^{+0.05}_{-0.08}$	1.16	1.09	63
ABELL 3921	69	535	3.07	$5.70^{+0.24}_{-0.23}$	$6.65^{+0.65}_{-0.54}$	$1.17^{+0.12}_{-0.11}$	$0.31^{+0.08}_{-0.07}$	1.02	0.96	77
AC 114	70	550	1.44	$7.53^{+0.49}_{-0.44}$	$8.30^{+1.03}_{-0.85}$	$1.10^{+0.15}_{-0.13}$	$0.26^{+0.08}_{-0.09}$	1.07	1.06	55
CL 0024+17	71	435	4.36	$6.03^{+1.66}_{-1.10}$	$7.18^{+7.91}_{-3.16}$	$1.19^{+1.35}_{-0.57}$	$0.60^{+0.37}_{-0.33}$	1.00	1.44	37
CL 1221+4918	71	445	1.44	$6.62^{+1.24}_{-0.99}$	$7.11^{+1.73}_{-1.31}$	$1.07^{+0.33}_{-0.25}$	$0.34^{+0.20}_{-0.18}$	0.94	0.93	62
CL J0030+2618	70	786	4.10	$4.63^{+2.72}_{-1.32}$	$5.18^{+8.29}_{-1.96}$	$1.12^{+1.91}_{-0.53}$	$0.26^{+0.75}_{-0.26}$	1.00	1.23	37
CL J0152-1357	70	391	1.45	$7.33^{+2.78}_{-1.77}$	$7.31^{+3.43}_{-2.02}$	$1.00^{+0.60}_{-0.37}$	$0.00^{+0.24}_{-0.00}$	0.89	1.00	36
CL J0542.8-4100	71	446	3.59	$6.07^{+1.47}_{-1.05}$	$6.29^{+2.14}_{-1.41}$	$1.04^{+0.43}_{-0.29}$	$0.16^{+0.23}_{-0.16}$	1.04	0.91	66
CL J0848+4456 ⋆	71	319	2.53	$4.53^{+1.57}_{-1.13}$	$5.52^{+3.28}_{-1.74}$	$1.22^{+0.84}_{-0.49}$	$0.00^{+0.45}_{-0.00}$	0.92	0.93	58
CL J1113.1-2615	70	435	5.51	$4.19^{+1.61}_{-1.02}$	$4.10^{+2.47}_{-1.44}$	$0.98^{+0.70}_{-0.42}$	$0.46^{+0.63}_{-0.44}$	1.01	1.08	23
CL J1226.9+3332 ⋆	69	450	1.37	$11.81^{+2.25}_{-1.70}$	$11.29^{+2.45}_{-1.77}$	$0.96^{+0.28}_{-0.20}$	$0.21^{+0.21}_{-0.21}$	0.81	0.86	86
CL J2302.8+0844	70	514	5.05	$4.25^{+1.17}_{-1.32}$	$4.67^{+2.00}_{-1.80}$	$1.10^{+0.56}_{-0.54}$	$0.13^{+0.33}_{-0.13}$	0.89	0.97	50
DLS J0514-4904	70	507	2.52	$4.62^{+0.53}_{-0.47}$	$6.14^{+2.08}_{-1.34}$	$1.33^{+0.48}_{-0.32}$	$0.37^{+0.24}_{-0.20}$	1.04	1.12	54
MACS J0011.7-1523 ⋆	69	451	2.08	$6.49^{+0.48}_{-0.43}$	$6.76^{+0.81}_{-0.66}$	$1.04^{+0.15}_{-0.12}$	$0.30^{+0.10}_{-0.09}$	0.86	0.90	87
MACS J0025.4-1222 ⋆	70	473	2.72	$6.33^{+0.85}_{-0.70}$	$6.01^{+1.05}_{-0.85}$	$0.95^{+0.21}_{-0.17}$	$0.37^{+0.16}_{-0.15}$	0.90	0.92	80
MACS J0035.4-2015	70	527	1.55	$7.46^{+0.79}_{-0.66}$	$9.31^{+1.75}_{-1.29}$	$1.25^{+0.27}_{-0.21}$	$0.33^{+0.12}_{-0.12}$	0.94	0.93	90
MACS J0111.5+0855	70	435	4.18	$4.11^{+1.61}_{-1.05}$	$3.72^{+3.08}_{-1.29}$	$0.91^{+0.83}_{-0.39}$	$0.11^{+0.59}_{-0.11}$	0.68	0.65	49
MACS J0152.5-2852	70	459	1.46	$5.64^{+0.89}_{-0.70}$	$7.24^{+2.57}_{-1.59}$	$1.28^{+0.50}_{-0.32}$	$0.22^{+0.17}_{-0.17}$	1.10	1.02	84

Table A.3: Summary of Excised R_{2500} Spectral Fits (continued)

Cluster	$R_{\rm CORE}$ kpc	R_{2500} kpc	N_H 10^{20} cm^{-2}	T_{77} keV	T_{27} keV	T_{HBR}	Z_{77} $Z_\odot$	$\chi^2_{red,77}$	$\chi^2_{red,27}$	% Source
(1)	(2)	(3)	(4)	(5)	(6)	(7)	(8)	(9)	(10)	(11)
MACS J0159.0-3412	70	572	1.54	$10.90^{+4.77}_{-2.53}$	$14.65^{+12.31}_{-5.39}$	$1.34^{+1.27}_{-0.58}$	$0.26^{+0.35}_{-0.26}$	0.87	0.92	81
MACS J0159.8-0849 ⋆	69	585	2.01	$9.16^{+0.71}_{-0.63}$	$9.83^{+1.13}_{-0.96}$	$1.07^{+0.15}_{-0.13}$	$0.30^{+0.09}_{-0.09}$	1.08	1.09	90
MACS J0242.5-2132	70	498	2.71	$5.58^{+0.63}_{-0.52}$	$6.26^{+1.38}_{-0.99}$	$1.12^{+0.28}_{-0.21}$	$0.34^{+0.16}_{-0.15}$	1.03	0.83	87
MACS J0257.1-2325 ⋆	70	579	2.09	$9.25^{+1.28}_{-1.01}$	$10.16^{+1.95}_{-1.54}$	$1.10^{+0.26}_{-0.21}$	$0.14^{+0.12}_{-0.12}$	0.99	1.08	84
MACS J0257.6-2209	69	540	2.02	$8.02^{+1.12}_{-0.88}$	$8.17^{+1.92}_{-1.30}$	$1.02^{+0.28}_{-0.20}$	$0.30^{+0.16}_{-0.17}$	1.12	1.26	84
MACS J0308.9+2645	69	539	11.88	$10.54^{+1.28}_{-1.07}$	$11.38^{+2.16}_{-1.66}$	$1.08^{+0.24}_{-0.19}$	$0.28^{+0.13}_{-0.14}$	0.97	1.01	87
MACS J0329.6-0211 ⋆	70	420	6.21	$6.30^{+0.47}_{-0.41}$	$7.50^{+0.83}_{-0.69}$	$1.19^{+0.16}_{-0.13}$	$0.41^{+0.10}_{-0.09}$	1.10	1.17	86
MACS J0404.6+1109	70	494	14.96	$5.77^{+1.14}_{-0.88}$	$6.15^{+2.00}_{-1.30}$	$1.07^{+0.41}_{-0.28}$	$0.24^{+0.22}_{-0.20}$	0.85	0.78	73
MACS J0417.5-1154	70	429	4.00	$11.07^{+1.98}_{-1.49}$	$14.90^{+5.03}_{-3.24}$	$1.35^{+0.51}_{-0.34}$	$0.33^{+0.19}_{-0.19}$	1.07	0.97	94
MACS J0429.6-0253	69	495	5.70	$5.66^{+0.64}_{-0.54}$	$6.71^{+1.26}_{-0.98}$	$1.19^{+0.26}_{-0.21}$	$0.35^{+0.14}_{-0.13}$	1.21	1.12	82
MACS J0451.9+0006	70	459	7.65	$5.80^{+1.46}_{-1.03}$	$7.02^{+3.29}_{-1.80}$	$1.21^{+0.64}_{-0.38}$	$0.51^{+0.33}_{-0.29}$	1.25	1.35	83
MACS J0455.2+0657	71	481	10.45	$7.25^{+2.04}_{-1.33}$	$8.25^{+3.98}_{-2.10}$	$1.14^{+0.64}_{-0.36}$	$0.56^{+0.37}_{-0.33}$	0.83	0.94	82
MACS J0520.7-1328	69	492	8.88	$6.35^{+0.81}_{-0.67}$	$8.22^{+2.18}_{-1.45}$	$1.29^{+0.38}_{-0.27}$	$0.43^{+0.17}_{-0.16}$	1.23	1.38	86
MACS J0547.0-3904	69	364	4.08	$3.58^{+0.44}_{-0.37}$	$5.41^{+1.67}_{-1.18}$	$1.51^{+0.50}_{-0.36}$	$0.09^{+0.15}_{-0.09}$	1.16	1.42	75
MACS J0553.4-3342	70	692	2.88	$13.14^{+3.82}_{-2.50}$	$13.86^{+6.45}_{-3.44}$	$1.05^{+0.58}_{-0.33}$	$0.57^{+0.35}_{-0.33}$	0.80	0.76	87
MACS J0717.5+3745 ⋆	70	563	6.75	$12.77^{+1.16}_{-1.00}$	$13.21^{+1.58}_{-1.29}$	$1.03^{+0.16}_{-0.13}$	$0.30^{+0.10}_{-0.11}$	0.93	0.90	88
MACS J0744.8+3927 ⋆	70	537	4.66	$8.09^{+0.77}_{-0.66}$	$8.77^{+1.04}_{-0.87}$	$1.08^{+0.16}_{-0.14}$	$0.32^{+0.10}_{-0.10}$	1.14	1.18	82
MACS J0911.2+1746 ⋆	70	541	3.55	$7.51^{+1.27}_{-0.99}$	$7.17^{+1.60}_{-1.20}$	$0.95^{+0.27}_{-0.20}$	$0.21^{+0.17}_{-0.16}$	0.93	0.84	78
MACS J0949+1708	70	580	3.17	$9.16^{+1.53}_{-1.18}$	$9.11^{+2.27}_{-1.55}$	$0.99^{+0.30}_{-0.21}$	$0.37^{+0.20}_{-0.20}$	0.89	0.84	89
MACS J1006.9+3200	70	512	1.83	$7.89^{+2.78}_{-1.74}$	$8.05^{+5.70}_{-2.45}$	$1.02^{+0.81}_{-0.38}$	$0.15^{+0.35}_{-0.15}$	1.84	1.15	76
MACS J1105.7-1014	71	502	4.58	$7.54^{+2.29}_{-1.51}$	$7.78^{+3.93}_{-1.97}$	$1.03^{+0.61}_{-0.33}$	$0.22^{+0.29}_{-0.22}$	1.17	1.27	81
MACS J1108.8+0906 ⋆	70	491	2.52	$6.52^{+0.94}_{-0.82}$	$7.31^{+1.89}_{-1.29}$	$1.12^{+0.33}_{-0.24}$	$0.29^{+0.18}_{-0.17}$	0.95	0.80	80
MACS J1115.2+5320 ⋆	70	527	0.98	$8.91^{+1.42}_{-1.12}$	$9.58^{+2.36}_{-1.62}$	$1.08^{+0.32}_{-0.23}$	$0.37^{+0.20}_{-0.18}$	0.93	0.88	75
MACS J1115.8+0129	70	448	4.36	$6.78^{+1.17}_{-0.91}$	$8.27^{+3.27}_{-2.16}$	$1.22^{+0.53}_{-0.36}$	$0.07^{+0.21}_{-0.07}$	1.00	0.97	65
MACS J1131.8-1955	69	576	4.49	$8.64^{+1.23}_{-0.97}$	$11.01^{+3.61}_{-2.10}$	$1.27^{+0.46}_{-0.28}$	$0.42^{+0.17}_{-0.17}$	1.00	1.00	87
MACS J1149.5+2223 ⋆	69	504	2.32	$7.65^{+0.89}_{-0.75}$	$8.13^{+1.36}_{-1.04}$	$1.06^{+0.22}_{-0.17}$	$0.20^{+0.12}_{-0.11}$	1.00	1.09	87

Table A.3: Summary of Excised R_{2500} Spectral Fits (continued)

Cluster	$R_{\rm CORE}$ kpc	R_{2500} kpc	N_H 10^{20} cm^{-2}	T_{77} keV	T_{27} keV	T_{HBR}	Z_{77} $Z_\odot$	$\chi^2_{red,77}$	$\chi^2_{red,27}$	% Source
(1)	(2)	(3)	(4)	(5)	(6)	(7)	(8)	(9)	(10)	(11)
MACS J1206.2-0847	70	522	4.15	$10.21^{+1.19}_{-0.97}$	$12.51^{+2.44}_{-1.87}$	$1.23^{+0.28}_{-0.22}$	$0.33^{+0.13}_{-0.13}$	0.96	1.05	93
MACS J1226.8+2153	71	489	1.82	$4.21^{+1.07}_{-0.80}$	$5.02^{+3.29}_{-1.52}$	$1.19^{+0.84}_{-0.43}$	$0.23^{+0.38}_{-0.23}$	1.02	0.81	67
MACS J1311.0-0310 ⋆	69	425	2.18	$5.76^{+0.48}_{-0.42}$	$5.91^{+0.73}_{-0.62}$	$1.03^{+0.15}_{-0.13}$	$0.39^{+0.13}_{-0.11}$	0.96	0.98	72
MACS J1319+7003	70	496	1.53	$7.99^{+2.08}_{-1.43}$	$10.62^{+7.35}_{-3.22}$	$1.33^{+0.98}_{-0.47}$	$0.30^{+0.29}_{-0.28}$	1.25	1.24	74
MACS J1427.2+4407	71	488	1.41	$9.80^{+3.87}_{-2.53}$	$10.35^{+6.30}_{-3.26}$	$1.06^{+0.77}_{-0.43}$	$0.00^{+0.34}_{-0.00}$	0.67	0.50	84
MACS J1427.6-2521	71	426	6.11	$4.65^{+0.92}_{-0.72}$	$8.11^{+5.04}_{-2.77}$	$1.74^{+1.14}_{-0.65}$	$0.18^{+0.26}_{-0.18}$	1.19	1.40	68
MACS J1621.3+3810 ⋆	69	504	1.07	$7.12^{+0.66}_{-0.55}$	$7.09^{+0.92}_{-0.75}$	$1.00^{+0.16}_{-0.13}$	$0.34^{+0.11}_{-0.11}$	0.93	0.86	73
MACS J1731.6+2252	71	521	6.48	$7.45^{+1.32}_{-0.99}$	$10.99^{+4.67}_{-2.46}$	$1.48^{+0.68}_{-0.38}$	$0.35^{+0.19}_{-0.17}$	1.20	1.07	84
MACS J1931.8-2634	70	535	9.13	$6.97^{+0.72}_{-0.61}$	$7.72^{+1.31}_{-0.99}$	$1.11^{+0.22}_{-0.17}$	$0.27^{+0.11}_{-0.12}$	0.95	0.86	90
MACS J2046.0-3430	71	386	4.98	$4.64^{+1.18}_{-0.82}$	$5.49^{+2.29}_{-1.47}$	$1.18^{+0.58}_{-0.38}$	$0.20^{+0.32}_{-0.20}$	0.89	1.11	82
MACS J2049.9-3217	69	524	5.99	$6.83^{+0.84}_{-0.69}$	$8.94^{+2.08}_{-1.48}$	$1.31^{+0.34}_{-0.25}$	$0.43^{+0.17}_{-0.15}$	0.99	0.92	83
MACS J2211.7-0349	69	663	5.86	$11.30^{+1.46}_{-1.17}$	$13.82^{+3.54}_{-2.41}$	$1.22^{+0.35}_{-0.25}$	$0.15^{+0.13}_{-0.14}$	1.24	1.26	88
MACS J2214.9-1359 ⋆	70	529	3.32	$9.78^{+1.38}_{-1.09}$	$10.45^{+2.19}_{-1.56}$	$1.07^{+0.27}_{-0.20}$	$0.23^{+0.14}_{-0.14}$	0.99	1.06	87
MACS J2228+2036	70	545	4.52	$7.86^{+1.08}_{-0.85}$	$9.17^{+2.05}_{-1.46}$	$1.17^{+0.31}_{-0.22}$	$0.39^{+0.16}_{-0.15}$	0.99	1.00	88
MACS J2229.7-2755	69	465	1.34	$5.01^{+0.50}_{-0.43}$	$5.79^{+1.11}_{-0.86}$	$1.16^{+0.25}_{-0.20}$	$0.55^{+0.19}_{-0.18}$	1.05	1.08	85
MACS J2243.3-0935	71	574	4.31	$4.09^{+0.51}_{-0.45}$	$7.20^{+3.17}_{-2.12}$	$1.76^{+0.81}_{-0.55}$	$0.03^{+0.15}_{-0.03}$	1.17	0.92	51
MACS J2245.0+2637	69	454	5.50	$6.06^{+0.63}_{-0.54}$	$6.76^{+1.24}_{-0.93}$	$1.12^{+0.24}_{-0.18}$	$0.60^{+0.20}_{-0.18}$	0.94	1.09	88
MACS J2311+0338	70	363	5.23	$8.12^{+1.44}_{-1.16}$	$12.40^{+5.12}_{-2.88}$	$1.53^{+0.69}_{-0.42}$	$0.46^{+0.22}_{-0.20}$	1.07	1.15	88
MKW3S	70	339	3.05	$3.91^{+0.06}_{-0.06}$	$4.58^{+0.18}_{-0.18}$	$1.17^{+0.05}_{-0.05}$	$0.34^{+0.03}_{-0.04}$	1.38	0.97	86
MS 0016.9+1609	69	550	4.06	$8.94^{+0.71}_{-0.62}$	$9.78^{+1.09}_{-0.90}$	$1.09^{+0.15}_{-0.13}$	$0.29^{+0.09}_{-0.08}$	0.91	0.88	83
MS 0451.6-0305	70	536	5.68	$8.90^{+0.85}_{-0.72}$	$10.43^{+1.59}_{-1.26}$	$1.17^{+0.21}_{-0.17}$	$0.37^{+0.11}_{-0.11}$	1.00	0.93	60
MS 0735.6+7421	69	491	3.40	$5.55^{+0.24}_{-0.22}$	$6.34^{+0.57}_{-0.50}$	$1.14^{+0.11}_{-0.10}$	$0.35^{+0.07}_{-0.06}$	1.05	1.05	62
MS 0839.8+2938	70	415	3.92	$4.68^{+0.32}_{-0.29}$	$5.05^{+0.82}_{-0.65}$	$1.08^{+0.19}_{-0.15}$	$0.46^{+0.13}_{-0.12}$	0.90	0.87	60
MS 0906.5+1110	70	616	3.60	$5.38^{+0.33}_{-0.29}$	$6.76^{+0.92}_{-0.77}$	$1.26^{+0.19}_{-0.16}$	$0.27^{+0.09}_{-0.09}$	1.21	1.08	75
MS 1006.0+1202	70	556	3.63	$5.61^{+0.51}_{-0.43}$	$7.48^{+1.66}_{-1.22}$	$1.33^{+0.32}_{-0.24}$	$0.24^{+0.11}_{-0.12}$	1.30	1.34	75
MS 1008.1-1224	70	548	6.71	$5.65^{+0.49}_{-0.43}$	$9.01^{+1.95}_{-1.38}$	$1.59^{+0.37}_{-0.27}$	$0.26^{+0.11}_{-0.10}$	1.21	0.98	78

Table A.3: Summary of Excised R_{2500} Spectral Fits (continued)

Cluster	$R_{\rm CORE}$ kpc	R_{2500} kpc	N_H 10^{20} cm^{-2}	T_{77} keV	T_{27} keV	T_{HBR}	Z_{77} $Z_\odot$	$\chi^2_{red,77}$	$\chi^2_{red,27}$	% Source
(1)	(2)	(3)	(4)	(5)	(6)	(7)	(8)	(9)	(10)	(11)
MS 1054.5-0321	70	558	3.69	$9.38^{+1.72}_{-1.34}$	$9.91^{+2.66}_{-1.77}$	$1.06^{+0.34}_{-0.24}$	$0.13^{+0.17}_{-0.13}$	1.02	1.03	41
MS 1455.0+2232	69	436	3.35	$4.77^{+0.13}_{-0.13}$	$5.37^{+0.36}_{-0.22}$	$1.13^{+0.08}_{-0.06}$	$0.44^{+0.05}_{-0.05}$	1.29	1.10	90
MS 1621.5+2640	70	537	3.59	$6.11^{+0.95}_{-0.76}$	$6.22^{+1.56}_{-1.10}$	$1.02^{+0.30}_{-0.22}$	$0.40^{+0.23}_{-0.21}$	1.02	1.21	68
MS 2053.7-0449 ⋆	70	561	5.16	$3.66^{+0.81}_{-0.60}$	$4.07^{+1.23}_{-0.83}$	$1.11^{+0.42}_{-0.29}$	$0.39^{+0.38}_{-0.33}$	0.97	1.07	58
MS 2137.3-2353	70	502	3.40	$6.01^{+0.52}_{-0.46}$	$7.48^{+1.68}_{-1.09}$	$1.24^{+0.30}_{-0.20}$	$0.45^{+0.13}_{-0.14}$	1.12	1.25	55
PKS 0745-191	69	651	40.80	$8.13^{+0.37}_{-0.34}$	$9.68^{+0.83}_{-0.72}$	$1.19^{+0.12}_{-0.10}$	$0.38^{+0.06}_{-0.06}$	1.02	0.98	89
RBS 0797	69	493	2.22	$7.68^{+0.92}_{-0.77}$	$9.05^{+1.80}_{-1.33}$	$1.18^{+0.27}_{-0.21}$	$0.32^{+0.14}_{-0.13}$	1.07	1.06	89
RDCS 1252-29	71	276	6.06	$4.25^{+1.82}_{-1.14}$	$4.47^{+2.16}_{-1.29}$	$1.05^{+0.68}_{-0.41}$	$0.79^{+1.01}_{-0.62}$	1.07	1.17	50
RX J0232.2-4420	69	568	2.53	$7.83^{+0.77}_{-0.68}$	$9.92^{+2.11}_{-1.44}$	$1.27^{+0.30}_{-0.21}$	$0.36^{+0.12}_{-0.13}$	1.13	1.09	85
RX J0340-4542	70	412	1.63	$3.16^{+0.38}_{-0.35}$	$2.80^{+0.94}_{-0.57}$	$0.89^{+0.32}_{-0.21}$	$0.62^{+0.31}_{-0.25}$	1.27	1.22	43
RX J0439+0520	70	474	10.02	$4.60^{+0.64}_{-0.59}$	$4.95^{+1.28}_{-0.88}$	$1.08^{+0.32}_{-0.24}$	$0.44^{+0.29}_{-0.24}$	1.03	1.14	77
RX J0439.0+0715 ⋆	70	532	11.16	$5.63^{+0.36}_{-0.32}$	$8.02^{+1.25}_{-0.93}$	$1.42^{+0.24}_{-0.18}$	$0.32^{+0.10}_{-0.08}$	1.28	1.16	82
RX J0528.9-3927	70	640	2.36	$7.89^{+0.96}_{-0.76}$	$8.91^{+2.30}_{-1.42}$	$1.13^{+0.32}_{-0.21}$	$0.27^{+0.14}_{-0.14}$	0.92	0.93	83
RX J0647.7+7015 ⋆	69	512	5.18	$11.28^{+1.85}_{-1.45}$	$11.01^{+2.17}_{-1.63}$	$0.98^{+0.25}_{-0.19}$	$0.20^{+0.17}_{-0.17}$	1.02	1.00	80
RX J0910+5422 ⋆	71	246	2.07	$4.53^{+3.02}_{-1.70}$	$5.98^{+5.30}_{-2.49}$	$1.32^{+1.46}_{-0.74}$	$0.00^{+0.73}_{-0.00}$	0.90	0.71	31
RX J1347.5-1145 ⋆	70	607	4.89	$14.62^{+0.97}_{-0.79}$	$16.62^{+1.54}_{-1.24}$	$1.14^{+0.13}_{-0.10}$	$0.32^{+0.08}_{-0.07}$	1.12	1.12	93
RX J1350+6007	71	334	1.77	$4.48^{+2.32}_{-1.49}$	$5.31^{+3.02}_{-2.07}$	$1.19^{+0.91}_{-0.61}$	$0.13^{+1.23}_{-0.13}$	0.82	0.72	57
RX J1423.8+2404 ⋆	71	441	2.65	$6.64^{+0.38}_{-0.34}$	$7.01^{+0.59}_{-0.51}$	$1.06^{+0.11}_{-0.09}$	$0.37^{+0.07}_{-0.07}$	1.02	0.98	86
RX J1504.1-0248	70	628	6.27	$8.00^{+0.27}_{-0.24}$	$8.92^{+0.52}_{-0.46}$	$1.11^{+0.08}_{-0.07}$	$0.40^{+0.04}_{-0.05}$	1.29	1.25	91
RX J1525+0958	70	416	2.96	$3.74^{+0.63}_{-0.45}$	$6.96^{+2.88}_{-1.73}$	$1.86^{+0.83}_{-0.51}$	$0.67^{+0.36}_{-0.29}$	1.29	0.93	79
RX J1532.9+3021 ⋆	70	458	2.21	$6.03^{+0.42}_{-0.38}$	$6.95^{+0.88}_{-0.72}$	$1.15^{+0.17}_{-0.14}$	$0.42^{+0.11}_{-0.10}$	0.94	1.05	73
RX J1716.9+6708	71	486	3.71	$5.71^{+1.47}_{-1.06}$	$5.77^{+1.88}_{-1.28}$	$1.01^{+0.42}_{-0.29}$	$0.68^{+0.42}_{-0.35}$	0.79	0.74	55
RX J1720.1+2638	69	510	4.02	$6.37^{+0.28}_{-0.26}$	$7.78^{+0.69}_{-0.61}$	$1.22^{+0.12}_{-0.11}$	$0.35^{+0.07}_{-0.06}$	1.10	1.02	90
RX J1720.2+3536 ⋆	71	455	3.35	$7.21^{+0.53}_{-0.46}$	$6.97^{+0.76}_{-0.59}$	$0.97^{+0.13}_{-0.10}$	$0.41^{+0.10}_{-0.10}$	1.12	1.09	85
RX J2011.3-5725	71	416	4.76	$3.94^{+0.45}_{-0.37}$	$4.40^{+1.20}_{-0.81}$	$1.12^{+0.33}_{-0.23}$	$0.34^{+0.21}_{-0.18}$	0.94	1.09	76
RX J2129.6+0005	70	690	4.30	$5.91^{+0.54}_{-0.47}$	$7.02^{+1.30}_{-0.99}$	$1.19^{+0.25}_{-0.19}$	$0.45^{+0.15}_{-0.15}$	1.21	1.07	80

Table A.3: Summary of Excised R_{2500} Spectral Fits (continued)

Cluster	$R_{\rm CORE}$ kpc	R_{2500} kpc	N_H 10^{20} cm^{-2}	T_{77} keV	T_{27} keV	T_{HBR}	Z_{77} $Z_\odot$	$\chi^2_{red,77}$	$\chi^2_{red,27}$	% Source
(1)	(2)	(3)	(4)	(5)	(6)	(7)	(8)	(9)	(10)	(11)
S0463 ⋆	70	433	1.06	$3.10^{+0.29}_{-0.25}$	$3.10^{+0.66}_{-0.53}$	$1.00^{+0.23}_{-0.19}$	$0.24^{+0.14}_{-0.11}$	1.10	1.07	47
V 1121.0+2327	70	444	1.30	$3.60^{+0.62}_{-0.46}$	$4.08^{+1.09}_{-0.80}$	$1.13^{+0.36}_{-0.27}$	$0.36^{+0.29}_{-0.24}$	1.21	1.19	66
ZWCL 1215	70	392	1.76	$6.64^{+0.40}_{-0.35}$	$8.72^{+1.30}_{-1.07}$	$1.31^{+0.21}_{-0.18}$	$0.29^{+0.09}_{-0.09}$	1.17	1.04	88
ZWCL 1358+6245	70	553	1.94	$10.66^{+1.48}_{-1.13}$	$10.19^{+4.83}_{-2.24}$	$0.96^{+0.47}_{-0.23}$	$0.47^{+0.19}_{-0.19}$	1.08	1.04	55
ZWCL 1953	69	730	3.10	$7.37^{+1.00}_{-0.78}$	$10.44^{+3.25}_{-2.20}$	$1.42^{+0.48}_{-0.33}$	$0.19^{+0.13}_{-0.13}$	0.84	0.78	74
ZWCL 3146	70	723	2.70	$7.48^{+0.32}_{-0.30}$	$8.61^{+0.66}_{-0.58}$	$1.15^{+0.10}_{-0.09}$	$0.31^{+0.05}_{-0.06}$	1.03	0.98	86
ZWCL 5247	70	635	1.70	$5.06^{+0.85}_{-0.64}$	$5.91^{+2.09}_{-1.30}$	$1.17^{+0.46}_{-0.30}$	$0.22^{+0.21}_{-0.19}$	0.83	0.72	74
ZWCL 7160	69	637	3.10	$4.53^{+0.40}_{-0.35}$	$5.16^{+1.01}_{-0.77}$	$1.14^{+0.24}_{-0.19}$	$0.40^{+0.15}_{-0.14}$	0.94	0.92	80
ZWICKY 2701	69	445	0.83	$5.21^{+0.34}_{-0.30}$	$5.68^{+0.85}_{-0.66}$	$1.09^{+0.18}_{-0.14}$	$0.43^{+0.13}_{-0.11}$	0.89	0.94	57
ZwCL 1332.8+5043	70	642	1.10	$3.62^{+3.46}_{-1.20}$	$3.84^{+5.93}_{-1.48}$	$1.06^{+1.93}_{-0.54}$	$0.76^{+12.45}_{-0.76}$	0.24	0.29	48
ZwCl 0848.5+3341	71	518	1.12	$6.83^{+2.18}_{-1.33}$	$7.24^{+5.11}_{-2.26}$	$1.06^{+0.82}_{-0.39}$	$0.56^{+0.54}_{-0.45}$	0.82	0.93	37

Table A.4: Summary of Excised R_{5000} Spectral Fits

Cluster	$R_{\rm CORE}$ kpc	R_{5000} kpc	N_H 10^{20} cm^{-2}	T_{77} keV	T_{27} keV	T_{HBR}	Z_{77} $Z_\odot$	$\chi^2_{red,77}$	$\chi^2_{red,27}$	% Source
(1)	(2)	(3)	(4)	(5)	(6)	(7)	(8)	(9)	(10)	(11)
1E0657 56 ⋆	69	487	6.53	$11.81^{+0.29}_{-0.27}$	$14.13^{+0.58}_{-0.53}$	$1.20^{+0.06}_{-0.05}$	$0.29^{+0.03}_{-0.03}$	1.22	1.10	95
1RXS J2129.4-0741 ⋆	71	373	4.36	$8.47^{+1.31}_{-1.04}$	$8.57^{+1.73}_{-1.27}$	$1.01^{+0.26}_{-0.19}$	$0.51^{+0.20}_{-0.19}$	1.16	1.27	87
2PIGG J0011.5-2850	69	387	2.18	$5.25^{+0.29}_{-0.27}$	$6.21^{+0.83}_{-0.68}$	$1.18^{+0.17}_{-0.14}$	$0.23^{+0.09}_{-0.08}$	1.08	1.01	78
2PIGG J0311.8-2655	69	321	1.46	$3.35^{+0.25}_{-0.22}$	$3.67^{+0.71}_{-0.54}$	$1.10^{+0.23}_{-0.18}$	$0.33^{+0.13}_{-0.11}$	1.03	1.10	51
2PIGG J2227.0-3041	69	267	1.11	$2.81^{+0.16}_{-0.15}$	$2.99^{+0.36}_{-0.28}$	$1.06^{+0.14}_{-0.11}$	$0.35^{+0.11}_{-0.08}$	1.14	1.10	77
3C 220.1	71	322	1.91	$7.81^{+7.50}_{-2.99}$	$7.49^{+11.53}_{-3.51}$	$0.96^{+1.74}_{-0.58}$	$0.00^{+0.55}_{-0.00}$	0.60	0.78	36
3C 28.0	70	297	5.71	$5.18^{+0.28}_{-0.27}$	$7.11^{+1.15}_{-0.90}$	$1.37^{+0.23}_{-0.19}$	$0.30^{+0.09}_{-0.07}$	0.96	0.77	90
3C 295	69	329	1.35	$5.47^{+0.49}_{-0.42}$	$6.51^{+0.92}_{-0.78}$	$1.19^{+0.20}_{-0.17}$	$0.29^{+0.11}_{-0.11}$	1.02	1.04	87
3C 388	69	297	6.11	$3.27^{+0.24}_{-0.21}$	$3.44^{+0.73}_{-0.51}$	$1.05^{+0.24}_{-0.17}$	$0.43^{+0.16}_{-0.13}$	1.09	1.04	76
4C 55.16	69	302	4.00	$4.88^{+0.16}_{-0.16}$	$5.11^{+0.44}_{-0.39}$	$1.05^{+0.10}_{-0.09}$	$0.52^{+0.07}_{-0.07}$	0.93	0.85	71
ABELL 0013	69	404	2.03	$5.39^{+0.28}_{-0.25}$	$6.41^{+0.84}_{-0.72}$	$1.19^{+0.17}_{-0.14}$	$0.37^{+0.09}_{-0.09}$	0.96	0.95	44
ABELL 0068	70	480	4.60	$9.72^{+1.82}_{-1.36}$	$10.89^{+5.21}_{-2.85}$	$1.12^{+0.58}_{-0.33}$	$0.41^{+0.24}_{-0.23}$	1.08	1.03	87
ABELL 0119	69	399	3.30	$5.86^{+0.28}_{-0.27}$	$6.20^{+0.74}_{-0.59}$	$1.06^{+0.14}_{-0.11}$	$0.44^{+0.10}_{-0.10}$	0.98	0.89	75
ABELL 0168 ⋆	70	281	3.27	$2.56^{+0.13}_{-0.10}$	$3.37^{+0.48}_{-0.41}$	$1.32^{+0.20}_{-0.17}$	$0.32^{+0.07}_{-0.05}$	1.03	0.97	44
ABELL 0209 ⋆	70	430	1.68	$7.32^{+0.65}_{-0.56}$	$10.05^{+2.33}_{-1.58}$	$1.37^{+0.34}_{-0.24}$	$0.21^{+0.11}_{-0.10}$	1.07	1.15	88
ABELL 0267 ⋆	70	385	2.74	$6.46^{+0.51}_{-0.45}$	$8.46^{+0.52}_{-0.91}$	$1.31^{+0.13}_{-0.17}$	$0.37^{+0.12}_{-0.11}$	1.18	1.29	88
ABELL 0370	69	365	3.37	$8.74^{+0.98}_{-0.83}$	$10.15^{+2.17}_{-1.52}$	$1.16^{+0.28}_{-0.21}$	$0.37^{+0.14}_{-0.13}$	1.05	1.02	50
ABELL 0383	69	300	4.07	$4.95^{+0.30}_{-0.28}$	$5.92^{+1.05}_{-0.85}$	$1.20^{+0.22}_{-0.18}$	$0.43^{+0.12}_{-0.11}$	1.12	1.10	75
ABELL 0399	69	386	$8.33^{+0.82}_{-0.80}$	$7.93^{+0.38}_{-0.35}$	$8.86^{+0.67}_{-0.59}$	$1.12^{+0.10}_{-0.09}$	$0.32^{+0.06}_{-0.05}$	1.06	0.96	87
ABELL 0401	69	454	12.48	$6.54^{+0.22}_{-0.20}$	$9.37^{+0.91}_{-0.74}$	$1.43^{+0.15}_{-0.12}$	$0.29^{+0.07}_{-0.06}$	1.53	1.10	85
ABELL 0478	69	423	30.90	$7.27^{+0.26}_{-0.25}$	$8.19^{+0.56}_{-0.50}$	$1.13^{+0.09}_{-0.08}$	$0.47^{+0.06}_{-0.06}$	1.02	0.93	95
ABELL 0514	71	365	3.14	$3.57^{+0.24}_{-0.23}$	$4.30^{+0.84}_{-0.66}$	$1.20^{+0.25}_{-0.20}$	$0.25^{+0.11}_{-0.10}$	0.99	1.01	55
ABELL 0520	70	407	$1.14^{+1.14}_{-1.16}$	$9.15^{+0.73}_{-0.63}$	$10.43^{+1.41}_{-1.06}$	$1.14^{+0.18}_{-0.14}$	$0.36^{+0.07}_{-0.07}$	1.12	1.01	91
ABELL 0521	70	394	6.17	$7.31^{+0.79}_{-0.64}$	$9.01^{+3.73}_{-1.87}$	$1.23^{+0.53}_{-0.28}$	$0.48^{+0.17}_{-0.16}$	1.11	0.95	55
ABELL 0586	70	450	4.71	$6.43^{+0.55}_{-0.49}$	$8.06^{+1.51}_{-1.14}$	$1.25^{+0.26}_{-0.20}$	$0.50^{+0.15}_{-0.15}$	0.88	0.81	87

Table A.4: Summary of Excised R_{5000} Spectral Fits (continued)

Cluster	$R_{\rm CORE}$ kpc	R_{5000} kpc	N_H 10^{20} cm^{-2}	T_{77} keV	T_{27} keV	T_{HBR}	Z_{77} $Z_\odot$	$\chi^2_{red,77}$	$\chi^2_{red,27}$	% Source
(1)	(2)	(3)	(4)	(5)	(6)	(7)	(8)	(9)	(10)	(11)
ABELL 0611	70	370	4.99	$6.79^{+0.51}_{-0.46}$	$6.88^{+1.23}_{-0.95}$	$1.01^{+0.20}_{-0.16}$	$0.32^{+0.10}_{-0.10}$	1.04	1.07	67
ABELL 0644	70	412	6.31	$7.81^{+0.20}_{-0.19}$	$8.08^{+0.44}_{-0.39}$	$1.03^{+0.06}_{-0.06}$	$0.42^{+0.05}_{-0.04}$	1.15	1.05	92
ABELL 0665	69	436	4.24	$7.35^{+0.40}_{-0.37}$	$10.43^{+1.76}_{-1.31}$	$1.42^{+0.25}_{-0.19}$	$0.29^{+0.07}_{-0.07}$	1.07	0.94	91
ABELL 0697	69	432	3.34	$9.80^{+0.99}_{-0.86}$	$13.50^{+2.90}_{-2.04}$	$1.38^{+0.33}_{-0.24}$	$0.48^{+0.13}_{-0.13}$	1.06	0.96	93
ABELL 0773	69	434	1.46	$8.09^{+0.75}_{-0.65}$	$10.52^{+1.92}_{-1.53}$	$1.30^{+0.27}_{-0.22}$	$0.37^{+0.12}_{-0.12}$	1.03	1.04	89
ABELL 0907	69	345	5.69	$5.62^{+0.19}_{-0.18}$	$6.82^{+0.27}_{-0.22}$	$1.21^{+0.06}_{-0.06}$	$0.46^{+0.06}_{-0.06}$	1.18	1.05	92
ABELL 0963	69	384	1.39	$6.97^{+0.35}_{-0.32}$	$7.65^{+1.00}_{-0.82}$	$1.10^{+0.15}_{-0.13}$	$0.29^{+0.08}_{-0.07}$	1.13	1.12	74
ABELL 1063S	69	458	1.77	$11.94^{+0.91}_{-0.80}$	$14.04^{+1.83}_{-1.47}$	$1.18^{+0.18}_{-0.15}$	$0.38^{+0.10}_{-0.09}$	1.01	0.98	94
ABELL 1068	69	305	0.71	$4.67^{+0.18}_{-0.18}$	$5.49^{+0.71}_{-0.58}$	$1.18^{+0.16}_{-0.13}$	$0.37^{+0.06}_{-0.07}$	0.92	0.91	77
ABELL 1201	69	401	1.85	$5.74^{+0.44}_{-0.40}$	$5.99^{+1.39}_{-0.95}$	$1.04^{+0.26}_{-0.18}$	$0.35^{+0.13}_{-0.11}$	1.06	1.10	50
ABELL 1204	70	297	1.44	$3.67^{+0.18}_{-0.16}$	$4.72^{+0.75}_{-0.57}$	$1.29^{+0.21}_{-0.17}$	$0.32^{+0.09}_{-0.09}$	1.11	0.92	92
ABELL 1361	71	330	2.18	$5.14^{+1.00}_{-0.74}$	$7.24^{+8.23}_{-2.78}$	$1.41^{+1.62}_{-0.58}$	$0.29^{+0.31}_{-0.27}$	1.10	0.82	61
ABELL 1423	70	435	1.60	$6.04^{+0.82}_{-0.68}$	$7.93^{+4.09}_{-2.20}$	$1.31^{+0.70}_{-0.39}$	$0.33^{+0.20}_{-0.17}$	0.95	0.91	84
ABELL 1651	70	421	2.02	$6.30^{+0.32}_{-0.28}$	$7.72^{+0.71}_{-0.65}$	$1.23^{+0.13}_{-0.12}$	$0.44^{+0.09}_{-0.09}$	1.13	1.19	91
ABELL 1664	69	291	8.47	$4.26^{+0.30}_{-0.26}$	$4.91^{+1.05}_{-0.80}$	$1.15^{+0.26}_{-0.20}$	$0.31^{+0.12}_{-0.11}$	1.07	1.08	70
ABELL 1689 $\star$	70	481	1.87	$9.76^{+0.40}_{-0.38}$	$12.97^{+1.25}_{-1.05}$	$1.33^{+0.14}_{-0.12}$	$0.35^{+0.06}_{-0.05}$	1.14	1.04	94
ABELL 1758	69	404	1.09	$9.66^{+0.75}_{-0.64}$	$9.90^{+1.22}_{-1.89}$	$1.02^{+0.15}_{-0.21}$	$0.48^{+0.11}_{-0.11}$	1.03	0.96	68
ABELL 1763	69	396	0.82	$7.74^{+0.73}_{-0.64}$	$12.56^{+6.70}_{-3.12}$	$1.62^{+0.88}_{-0.42}$	$0.22^{+0.11}_{-0.12}$	1.16	1.02	89
ABELL 1795	69	449	1.22	$6.05^{+0.15}_{-0.15}$	$6.85^{+0.42}_{-0.38}$	$1.13^{+0.07}_{-0.07}$	$0.33^{+0.04}_{-0.05}$	1.19	1.03	93
ABELL 1835	70	404	2.36	$9.55^{+0.55}_{-0.51}$	$11.99^{+1.96}_{-1.44}$	$1.26^{+0.22}_{-0.17}$	$0.35^{+0.07}_{-0.08}$	0.91	0.88	91
ABELL 1914	70	493	0.97	$9.73^{+0.58}_{-0.51}$	$11.97^{+1.90}_{-1.40}$	$1.23^{+0.21}_{-0.16}$	$0.32^{+0.08}_{-0.07}$	1.11	1.03	95
ABELL 1942	69	334	2.75	$4.96^{+0.45}_{-0.39}$	$5.94^{+2.24}_{-0.99}$	$1.20^{+0.46}_{-0.22}$	$0.37^{+0.15}_{-0.14}$	1.04	0.87	77
ABELL 1995	71	271	1.44	$8.50^{+0.83}_{-0.71}$	$9.41^{+1.87}_{-1.32}$	$1.11^{+0.25}_{-0.18}$	$0.33^{+0.12}_{-0.12}$	1.05	1.02	81
ABELL 2029	70	434	3.26	$8.22^{+0.31}_{-0.30}$	$9.92^{+0.91}_{-0.73}$	$1.21^{+0.12}_{-0.10}$	$0.40^{+0.06}_{-0.06}$	1.08	1.04	94
ABELL 2034	69	420	1.58	$7.35^{+0.26}_{-0.24}$	$9.96^{+1.09}_{-0.84}$	$1.36^{+0.16}_{-0.12}$	$0.34^{+0.05}_{-0.05}$	1.17	1.02	90
ABELL 2065	69	370	2.96	$5.75^{+0.19}_{-0.17}$	$6.39^{+0.46}_{-0.41}$	$1.11^{+0.09}_{-0.08}$	$0.28^{+0.05}_{-0.05}$	1.11	1.01	89

Table A.4: Summary of Excised R_{5000} Spectral Fits (continued)

Cluster	$R_{\rm CORE}$ kpc	R_{5000} kpc	N_H 10^{20} cm^{-2}	T_{77} keV	T_{27} keV	T_{HBR}	Z_{77} $Z_\odot$	$\chi^2_{red,77}$	$\chi^2_{red,27}$	% Source
(1)	(2)	(3)	(4)	(5)	(6)	(7)	(8)	(9)	(10)	(11)
ABELL 2069	70	440	1.97	$6.33^{+0.36}_{-0.32}$	$8.29^{+1.36}_{-1.02}$	$1.31^{+0.23}_{-0.17}$	$0.24^{+0.08}_{-0.08}$	1.14	1.15	78
ABELL 2111	70	417	2.20	$5.74^{+1.43}_{-0.97}$	$7.18^{+6.73}_{-2.52}$	$1.25^{+1.21}_{-0.49}$	$0.16^{+0.30}_{-0.16}$	1.06	0.97	74
ABELL 2125	70	262	2.75	$3.09^{+0.37}_{-0.31}$	$3.69^{+1.99}_{-0.81}$	$1.19^{+0.66}_{-0.29}$	$0.36^{+0.25}_{-0.20}$	1.25	1.22	68
ABELL 2163	69	531	12.04	$18.78^{+0.89}_{-0.83}$	$19.49^{+2.03}_{-1.86}$	$1.04^{+0.12}_{-0.11}$	$0.09^{+0.06}_{-0.05}$	1.33	1.25	93
ABELL 2204 ⋆	70	406	5.84	$9.35^{+0.43}_{-0.41}$	$10.18^{+0.95}_{-0.77}$	$1.09^{+0.11}_{-0.10}$	$0.37^{+0.07}_{-0.07}$	0.95	0.97	86
ABELL 2218	70	394	3.12	$7.37^{+0.40}_{-0.37}$	$9.36^{+1.42}_{-1.07}$	$1.27^{+0.20}_{-0.16}$	$0.22^{+0.07}_{-0.06}$	1.00	0.91	91
ABELL 2219	69	463	1.76	$12.60^{+0.65}_{-0.61}$	$12.54^{+1.52}_{-1.21}$	$1.00^{+0.13}_{-0.11}$	$0.31^{+0.07}_{-0.07}$	1.02	0.98	81
ABELL 2255	71	422	2.53	$6.37^{+0.24}_{-0.23}$	$7.70^{+0.79}_{-0.49}$	$1.21^{+0.13}_{-0.09}$	$0.34^{+0.06}_{-0.07}$	0.93	0.84	81
ABELL 2256	70	441	4.05	$5.66^{+0.19}_{-0.17}$	$7.30^{+0.69}_{-0.63}$	$1.29^{+0.13}_{-0.12}$	$0.31^{+0.07}_{-0.07}$	1.61	1.44	79
ABELL 2259	69	340	3.70	$5.07^{+0.46}_{-0.40}$	$5.49^{+1.29}_{-0.91}$	$1.08^{+0.27}_{-0.20}$	$0.40^{+0.16}_{-0.14}$	0.92	0.92	90
ABELL 2261	69	407	3.31	$7.86^{+0.51}_{-0.47}$	$9.84^{+1.94}_{-1.30}$	$1.25^{+0.26}_{-0.18}$	$0.40^{+0.09}_{-0.09}$	0.98	0.95	94
ABELL 2294	69	405	6.10	$10.49^{+1.75}_{-1.30}$	$12.33^{+5.72}_{-3.05}$	$1.18^{+0.58}_{-0.33}$	$0.57^{+0.25}_{-0.24}$	1.16	1.08	88
ABELL 2384	70	308	2.99	$4.53^{+0.22}_{-0.21}$	$6.78^{+1.13}_{-0.89}$	$1.50^{+0.26}_{-0.21}$	$0.15^{+0.07}_{-0.06}$	0.99	0.88	86
ABELL 2390	70	447	6.71	$10.85^{+0.34}_{-0.31}$	$10.53^{+0.62}_{-0.53}$	$0.97^{+0.06}_{-0.06}$	$0.35^{+0.05}_{-0.04}$	1.15	1.03	81
ABELL 2409	70	362	6.72	$5.93^{+0.45}_{-0.39}$	$5.87^{+0.95}_{-0.76}$	$0.99^{+0.18}_{-0.14}$	$0.35^{+0.13}_{-0.11}$	1.05	0.76	92
ABELL 2537	69	351	4.26	$8.83^{+0.87}_{-0.74}$	$7.83^{+1.54}_{-1.16}$	$0.89^{+0.20}_{-0.15}$	$0.39^{+0.14}_{-0.14}$	0.93	0.83	59
ABELL 2554	71	415	2.04	$5.35^{+0.45}_{-0.40}$	$6.46^{+1.93}_{-1.24}$	$1.21^{+0.37}_{-0.25}$	$0.35^{+0.15}_{-0.13}$	0.93	0.79	40
ABELL 2556	70	323	2.02	$3.57^{+0.16}_{-0.15}$	$4.07^{+0.56}_{-0.46}$	$1.14^{+0.16}_{-0.14}$	$0.36^{+0.07}_{-0.07}$	0.99	0.95	58
ABELL 2631	70	445	3.74	$7.18^{+1.18}_{-0.94}$	$9.18^{+3.17}_{-1.96}$	$1.28^{+0.49}_{-0.32}$	$0.34^{+0.20}_{-0.19}$	1.03	0.99	89
ABELL 2667	70	370	1.64	$6.68^{+0.48}_{-0.43}$	$7.35^{+1.27}_{-1.05}$	$1.10^{+0.21}_{-0.17}$	$0.41^{+0.12}_{-0.12}$	1.05	0.95	84
ABELL 2670	69	319	2.88	$3.96^{+0.13}_{-0.13}$	$4.75^{+0.50}_{-0.41}$	$1.20^{+0.13}_{-0.11}$	$0.45^{+0.08}_{-0.07}$	1.16	1.09	80
ABELL 2717	70	211	1.12	$2.59^{+0.17}_{-0.16}$	$3.18^{+0.59}_{-0.44}$	$1.23^{+0.24}_{-0.19}$	$0.53^{+0.14}_{-0.12}$	0.90	0.95	67
ABELL 2744	71	458	1.82	$9.82^{+0.89}_{-0.77}$	$11.21^{+2.76}_{-1.81}$	$1.14^{+0.30}_{-0.20}$	$0.30^{+0.12}_{-0.12}$	0.88	0.73	74
ABELL 3128	70	318	1.59	$3.04^{+0.23}_{-0.21}$	$3.48^{+0.73}_{-0.54}$	$1.14^{+0.26}_{-0.19}$	$0.33^{+0.13}_{-0.10}$	1.05	1.13	64
ABELL 3158 ⋆	70	382	1.60	$5.08^{+0.08}_{-0.08}$	$6.26^{+0.26}_{-0.24}$	$1.23^{+0.05}_{-0.05}$	$0.40^{+0.03}_{-0.03}$	1.15	0.97	89
ABELL 3164	70	319	2.55	$2.40^{+0.65}_{-0.48}$	$3.19^{+5.68}_{-1.41}$	$1.33^{+2.39}_{-0.64}$	$0.23^{+0.32}_{-0.19}$	1.29	1.59	30

Table A.4: Summary of Excised R_{5000} Spectral Fits (continued)

Cluster	$R_{\rm CORE}$ kpc	R_{5000} kpc	N_H 10^{20} cm^{-2}	T_{77} keV	T_{27} keV	T_{HBR}	Z_{77} $Z_\odot$	$\chi^2_{red,77}$	$\chi^2_{red,27}$	% Source
(1)	(2)	(3)	(4)	(5)	(6)	(7)	(8)	(9)	(10)	(11)
ABELL 3376 ⋆	70	327	5.21	$4.44^{+0.14}_{-0.13}$	$5.94^{+0.55}_{-0.47}$	$1.34^{+0.13}_{-0.11}$	$0.36^{+0.06}_{-0.06}$	1.18	1.13	65
ABELL 3391	70	397	5.46	$5.72^{+0.31}_{-0.28}$	$6.44^{+0.80}_{-0.66}$	$1.13^{+0.15}_{-0.13}$	$0.11^{+0.08}_{-0.07}$	1.00	0.97	67
ABELL 3921	69	378	3.07	$5.69^{+0.25}_{-0.24}$	$6.74^{+0.71}_{-0.58}$	$1.18^{+0.14}_{-0.11}$	$0.34^{+0.08}_{-0.07}$	0.93	0.85	84
AC 114	70	389	1.44	$7.75^{+0.56}_{-0.50}$	$9.76^{+2.28}_{-1.55}$	$1.26^{+0.31}_{-0.22}$	$0.36^{+0.11}_{-0.10}$	1.01	0.95	63
CL 0024+17	71	309	4.36	$4.75^{+1.07}_{-0.76}$	$7.14^{+5.42}_{-2.83}$	$1.50^{+1.19}_{-0.64}$	$0.58^{+0.35}_{-0.30}$	1.07	0.97	44
CL 1221+4918	71	313	1.44	$6.73^{+1.29}_{-1.02}$	$7.60^{+4.33}_{-2.01}$	$1.13^{+0.68}_{-0.34}$	$0.32^{+0.20}_{-0.19}$	0.92	0.69	73
CL J0030+2618	70	555	4.10	$4.48^{+2.43}_{-1.40}$	$3.77^{+9.73}_{-1.96}$	$0.84^{+2.22}_{-0.51}$	$0.00^{+0.37}_{-0.00}$	1.01	0.85	51
CL J0152-1357	70	277	1.45	$7.20^{+7.14}_{-2.48}$	$6.07^{+6.16}_{-2.51}$	$0.84^{+1.20}_{-0.45}$	$0.00^{+0.63}_{-0.00}$	2.97	3.26	49
CL J0542.8-4100	71	313	3.59	$5.65^{+1.21}_{-0.90}$	$5.93^{+3.52}_{-1.76}$	$1.05^{+0.66}_{-0.35}$	$0.25^{+0.24}_{-0.22}$	0.67	0.58	72
CL J0848+4456 ⋆	71	224	2.53	$3.73^{+1.47}_{-0.85}$	$4.96^{+2.82}_{-1.81}$	$1.33^{+0.92}_{-0.57}$	$0.17^{+0.98}_{-0.17}$	0.87	0.82	64
CL J1113.1-2615	70	308	5.51	$4.74^{+1.52}_{-0.98}$	$4.79^{+1.15}_{-1.26}$	$1.01^{+0.40}_{-0.34}$	$0.53^{+0.52}_{-0.37}$	1.02	1.01	32
CL J1226.9+3332 ⋆	69	318	1.37	$13.02^{+2.69}_{-2.00}$	$12.33^{+2.78}_{-2.13}$	$0.95^{+0.29}_{-0.22}$	$0.18^{+0.23}_{-0.18}$	0.75	0.80	91
CL J2302.8+0844	70	362	5.05	$5.94^{+1.73}_{-1.86}$	$6.58^{+8.08}_{-2.67}$	$1.11^{+1.40}_{-0.57}$	$0.10^{+0.29}_{-0.10}$	0.94	1.01	56
DLS J0514-4904	70	359	2.52	$4.94^{+0.61}_{-0.55}$	$6.26^{+2.33}_{-1.30}$	$1.27^{+0.50}_{-0.30}$	$0.35^{+0.27}_{-0.23}$	0.86	1.03	63
EXO 0422-086	70	294	6.22	$3.41^{+0.14}_{-0.13}$	$3.44^{+0.37}_{-0.31}$	$1.01^{+0.12}_{-0.10}$	$0.37^{+0.08}_{-0.08}$	0.96	0.93	80
HERCULES A	69	312	$1.49^{+2.01}_{-1.49}$	$5.28^{+0.60}_{-0.50}$	$4.50^{+0.88}_{-0.65}$	$0.85^{+0.19}_{-0.15}$	$0.42^{+0.15}_{-0.14}$	0.98	0.98	70
MACS J0011.7-1523 ⋆	69	319	2.08	$6.73^{+0.55}_{-0.47}$	$7.27^{+0.99}_{-0.74}$	$1.08^{+0.17}_{-0.13}$	$0.27^{+0.10}_{-0.09}$	0.90	0.95	92
MACS J0025.4-1222 ⋆	70	335	2.72	$6.65^{+1.07}_{-0.85}$	$6.31^{+1.38}_{-1.02}$	$0.95^{+0.26}_{-0.20}$	$0.39^{+0.22}_{-0.19}$	0.66	0.75	86
MACS J0035.4-2015	70	372	1.55	$7.72^{+0.88}_{-0.74}$	$9.39^{+1.91}_{-1.35}$	$1.22^{+0.28}_{-0.21}$	$0.39^{+0.14}_{-0.13}$	1.02	1.05	94
MACS J0111.5+0855	70	306	4.18	$4.12^{+1.60}_{-1.04}$	$4.16^{+2.96}_{-1.44}$	$1.01^{+0.82}_{-0.43}$	$0.00^{+0.43}_{-0.00}$	0.79	1.23	62
MACS J0152.5-2852	70	324	1.46	$5.75^{+1.05}_{-0.78}$	$7.70^{+3.21}_{-1.89}$	$1.34^{+0.61}_{-0.38}$	$0.28^{+0.22}_{-0.21}$	0.84	0.58	90
MACS J0159.0-3412	70	404	1.54	$10.99^{+5.87}_{-2.95}$	$12.74^{+12.45}_{-4.72}$	$1.16^{+1.29}_{-0.53}$	$0.50^{+0.52}_{-0.50}$	1.35	1.34	85
MACS J0159.8-0849 ⋆	69	413	2.01	$9.36^{+0.77}_{-0.67}$	$10.37^{+1.29}_{-1.04}$	$1.11^{+0.17}_{-0.14}$	$0.29^{+0.09}_{-0.09}$	1.05	1.01	94
MACS J0242.5-2132	70	352	2.71	$5.48^{+0.62}_{-0.51}$	$5.99^{+2.04}_{-1.19}$	$1.09^{+0.39}_{-0.24}$	$0.32^{+0.16}_{-0.15}$	1.08	1.06	92
MACS J0257.1-2325 ⋆	70	409	2.09	$9.42^{+1.37}_{-1.05}$	$10.76^{+2.05}_{-1.69}$	$1.14^{+0.27}_{-0.22}$	$0.14^{+0.13}_{-0.13}$	1.03	1.13	90
MACS J0257.6-2209	69	382	2.02	$8.09^{+1.10}_{-0.88}$	$7.90^{+1.64}_{-1.20}$	$0.98^{+0.24}_{-0.18}$	$0.41^{+0.19}_{-0.18}$	1.13	1.24	90

Table A.4: Summary of Excised R_{5000} Spectral Fits (continued)

Cluster	$R_{\rm CORE}$ kpc	R_{5000} kpc	N_H 10^{20} cm^{-2}	T_{77} keV	T_{27} keV	T_{HBR}	Z_{77} $Z_\odot$	$\chi^2_{red,77}$	$\chi^2_{red,27}$	% Source
(1)	(2)	(3)	(4)	(5)	(6)	(7)	(8)	(9)	(10)	(11)
MACS J0308.9+2645	69	381	11.88	$10.64^{+1.38}_{-1.14}$	$11.12^{+2.23}_{-1.68}$	$1.05^{+0.25}_{-0.19}$	$0.37^{+0.15}_{-0.15}$	0.96	0.97	92
MACS J0329.6-0211 ⋆	70	297	6.21	$6.44^{+0.50}_{-0.45}$	$7.55^{+0.88}_{-0.73}$	$1.17^{+0.16}_{-0.14}$	$0.40^{+0.10}_{-0.09}$	1.12	1.16	91
MACS J0404.6+1109	70	348	14.96	$6.90^{+2.01}_{-1.29}$	$7.40^{+3.63}_{-1.93}$	$1.07^{+0.61}_{-0.34}$	$0.22^{+0.27}_{-0.22}$	0.96	0.92	80
MACS J0417.5-1154	70	304	4.00	$10.44^{+2.08}_{-1.56}$	$14.46^{+5.92}_{-3.41}$	$1.39^{+0.63}_{-0.39}$	$0.41^{+0.23}_{-0.21}$	1.10	1.17	96
MACS J0429.6-0253	69	348	5.70	$5.96^{+0.72}_{-0.60}$	$7.48^{+2.65}_{-1.64}$	$1.26^{+0.47}_{-0.30}$	$0.34^{+0.15}_{-0.14}$	1.02	0.78	89
MACS J0451.9+0006	70	325	7.65	$5.76^{+1.77}_{-1.11}$	$6.68^{+4.50}_{-1.94}$	$1.16^{+0.86}_{-0.40}$	$0.47^{+0.46}_{-0.38}$	1.03	1.33	89
MACS J0455.2+0657	71	340	10.45	$6.99^{+2.27}_{-1.44}$	$8.35^{+5.66}_{-2.49}$	$1.19^{+0.90}_{-0.43}$	$0.48^{+0.35}_{-0.31}$	1.04	1.24	88
MACS J0520.7-1328	69	348	8.88	$6.77^{+1.01}_{-0.79}$	$9.41^{+3.38}_{-1.91}$	$1.39^{+0.54}_{-0.33}$	$0.33^{+0.16}_{-0.16}$	1.22	1.33	91
MACS J0547.0-3904	69	257	4.08	$3.70^{+0.44}_{-0.37}$	$5.82^{+2.97}_{-1.36}$	$1.57^{+0.82}_{-0.40}$	$0.24^{+0.21}_{-0.17}$	1.14	1.21	83
MACS J0553.4-3342	70	490	2.88	$13.90^{+5.89}_{-3.28}$	$14.59^{+11.16}_{-4.72}$	$1.05^{+0.92}_{-0.42}$	$0.38^{+0.39}_{-0.38}$	1.22	1.10	91
MACS J0717.5+3745 ⋆	70	398	6.75	$13.30^{+1.44}_{-1.21}$	$12.82^{+1.70}_{-1.39}$	$0.96^{+0.17}_{-0.14}$	$0.32^{+0.12}_{-0.13}$	0.91	0.87	91
MACS J0744.8+3927 ⋆	70	381	4.66	$8.58^{+0.85}_{-0.73}$	$9.32^{+1.20}_{-0.96}$	$1.09^{+0.18}_{-0.15}$	$0.30^{+0.11}_{-0.11}$	1.14	1.19	89
MACS J0911.2+1746 ⋆	70	382	3.55	$7.71^{+1.55}_{-1.16}$	$7.88^{+2.11}_{-1.44}$	$1.02^{+0.34}_{-0.24}$	$0.22^{+0.20}_{-0.20}$	0.77	0.77	85
MACS J0949+1708	70	411	3.17	$8.94^{+1.57}_{-1.20}$	$10.29^{+5.60}_{-2.41}$	$1.15^{+0.66}_{-0.31}$	$0.48^{+0.23}_{-0.22}$	0.74	0.58	93
MACS J1006.9+3200	70	363	1.83	$7.03^{+2.66}_{-1.64}$	$6.53^{+4.61}_{-2.11}$	$0.93^{+0.74}_{-0.37}$	$0.18^{+0.45}_{-0.18}$	1.64	1.53	81
MACS J1105.7-1014	71	356	4.58	$7.73^{+2.85}_{-1.73}$	$6.61^{+3.02}_{-1.79}$	$0.86^{+0.50}_{-0.30}$	$0.20^{+0.32}_{-0.20}$	1.27	1.08	87
MACS J1108.8+0906 ⋆	70	345	2.52	$6.80^{+1.21}_{-0.93}$	$7.52^{+2.39}_{-1.53}$	$1.11^{+0.40}_{-0.27}$	$0.24^{+0.20}_{-0.19}$	1.08	1.01	86
MACS J1115.2+5320 ⋆	70	372	0.98	$9.58^{+1.85}_{-1.37}$	$9.80^{+2.74}_{-1.81}$	$1.02^{+0.35}_{-0.24}$	$0.37^{+0.22}_{-0.21}$	0.94	0.91	82
MACS J1115.8+0129	70	316	4.36	$6.82^{+1.15}_{-0.88}$	$9.39^{+4.77}_{-2.84}$	$1.38^{+0.74}_{-0.45}$	$0.07^{+0.19}_{-0.07}$	0.94	0.85	77
MACS J1131.8-1955	69	407	4.49	$8.64^{+1.32}_{-1.03}$	$9.45^{+2.52}_{-1.68}$	$1.09^{+0.34}_{-0.23}$	$0.49^{+0.19}_{-0.19}$	1.07	1.02	91
MACS J1149.5+2223 ⋆	69	358	2.32	$7.72^{+0.94}_{-0.79}$	$8.36^{+1.51}_{-1.14}$	$1.08^{+0.24}_{-0.18}$	$0.25^{+0.12}_{-0.13}$	0.87	0.94	75
MACS J1206.2-0847	70	367	4.15	$9.98^{+1.27}_{-1.01}$	$11.93^{+2.56}_{-1.88}$	$1.20^{+0.30}_{-0.22}$	$0.32^{+0.13}_{-0.14}$	1.02	1.15	95
MACS J1226.8+2153	71	347	1.82	$4.86^{+1.58}_{-1.08}$	$5.84^{+3.45}_{-2.14}$	$1.20^{+0.81}_{-0.51}$	$0.00^{+0.28}_{-0.00}$	1.32	1.36	78
MACS J1311.0-0310 ⋆	69	301	2.18	$5.73^{+0.46}_{-0.40}$	$5.92^{+0.70}_{-0.60}$	$1.03^{+0.15}_{-0.13}$	$0.44^{+0.12}_{-0.12}$	0.93	1.00	83
MACS J1319+7003	70	351	1.53	$8.08^{+2.14}_{-1.56}$	$10.12^{+5.50}_{-2.78}$	$1.25^{+0.76}_{-0.42}$	$0.10^{+0.25}_{-0.10}$	1.00	1.07	82
MACS J1427.2+4407	71	346	1.41	$8.61^{+4.04}_{-2.23}$	$8.83^{+5.55}_{-2.81}$	$1.03^{+0.80}_{-0.42}$	$0.14^{+0.36}_{-0.14}$	0.68	0.58	90

Table A.4: Summary of Excised R_{5000} Spectral Fits (continued)

Cluster	$R_{\rm CORE}$ kpc	R_{5000} kpc	N_H 10^{20} cm^{-2}	T_{77} keV	T_{27} keV	T_{HBR}	Z_{77} $Z_\odot$	$\chi^2_{red,77}$	$\chi^2_{red,27}$	% Source
(1)	(2)	(3)	(4)	(5)	(6)	(7)	(8)	(9)	(10)	(11)
MACS J1427.6-2521	71	302	6.11	$4.44^{+0.86}_{-0.64}$	$6.17^{+3.18}_{-1.71}$	$1.39^{+0.77}_{-0.43}$	$0.21^{+0.26}_{-0.21}$	1.07	1.39	79
MACS J1621.3+3810 ⋆	69	358	1.07	$7.49^{+0.73}_{-0.63}$	$7.75^{+1.12}_{-0.89}$	$1.03^{+0.18}_{-0.15}$	$0.35^{+0.13}_{-0.12}$	0.98	0.92	82
MACS J1731.6+2252	71	368	6.48	$8.19^{+1.88}_{-1.31}$	$10.50^{+4.76}_{-2.46}$	$1.28^{+0.65}_{-0.36}$	$0.49^{+0.27}_{-0.25}$	1.16	0.98	87
MACS J1931.8-2634	70	378	9.13	$6.85^{+0.73}_{-0.61}$	$6.86^{+1.58}_{-1.15}$	$1.00^{+0.25}_{-0.19}$	$0.23^{+0.12}_{-0.11}$	1.02	1.07	94
MACS J2046.0-3430	71	274	4.98	$5.02^{+1.95}_{-1.04}$	$6.23^{+2.57}_{-2.30}$	$1.24^{+0.70}_{-0.53}$	$0.23^{+0.55}_{-0.23}$	1.10	1.14	89
MACS J2049.9-3217	69	370	5.99	$7.88^{+1.22}_{-0.98}$	$11.48^{+4.02}_{-2.42}$	$1.46^{+0.56}_{-0.36}$	$0.37^{+0.18}_{-0.16}$	0.94	0.90	89
MACS J2211.7-0349	69	468	5.86	$11.13^{+1.45}_{-1.15}$	$13.77^{+3.49}_{-2.40}$	$1.24^{+0.35}_{-0.25}$	$0.18^{+0.14}_{-0.14}$	1.33	1.34	93
MACS J2214.9-1359 ⋆	70	374	3.32	$9.87^{+1.54}_{-1.17}$	$9.97^{+2.17}_{-1.50}$	$1.01^{+0.27}_{-0.19}$	$0.31^{+0.17}_{-0.17}$	1.03	1.01	92
MACS J2228+2036	70	385	4.52	$7.79^{+1.14}_{-0.90}$	$10.04^{+3.96}_{-2.25}$	$1.29^{+0.54}_{-0.32}$	$0.41^{+0.18}_{-0.17}$	0.84	0.96	92
MACS J2229.7-2755	69	327	1.34	$5.25^{+0.54}_{-0.46}$	$6.07^{+1.76}_{-1.18}$	$1.16^{+0.36}_{-0.25}$	$0.59^{+0.20}_{-0.19}$	0.98	1.02	91
MACS J2243.3-0935	71	406	4.31	$5.15^{+0.65}_{-0.54}$	$8.81^{+4.31}_{-2.67}$	$1.71^{+0.86}_{-0.55}$	$0.05^{+0.17}_{-0.05}$	1.38	1.27	66
MACS J2245.0+2637	69	320	5.50	$6.05^{+0.66}_{-0.56}$	$7.05^{+1.31}_{-1.08}$	$1.17^{+0.25}_{-0.21}$	$0.64^{+0.21}_{-0.20}$	0.78	0.95	92
MACS J2311+0338	70	257	5.23	$7.66^{+1.63}_{-1.20}$	$12.19^{+6.04}_{-3.14}$	$1.59^{+0.86}_{-0.48}$	$0.44^{+0.24}_{-0.23}$	1.22	1.10	92
MKW3S	70	239	3.05	$3.93^{+0.06}_{-0.06}$	$4.58^{+0.19}_{-0.17}$	$1.17^{+0.05}_{-0.05}$	$0.35^{+0.02}_{-0.03}$	1.28	0.93	88
MS 0016.9+1609	69	389	4.06	$9.11^{+0.79}_{-0.68}$	$11.73^{+2.98}_{-1.84}$	$1.29^{+0.35}_{-0.22}$	$0.32^{+0.10}_{-0.09}$	0.91	0.92	88
MS 0440.5+0204	71	497	9.10	$5.99^{+0.91}_{-0.73}$	$4.45^{+1.61}_{-1.37}$	$0.74^{+0.29}_{-0.25}$	$0.66^{+0.32}_{-0.29}$	0.89	0.74	28
MS 0451.6-0305	70	378	5.68	$9.25^{+0.89}_{-0.77}$	$11.55^{+2.88}_{-1.91}$	$1.25^{+0.33}_{-0.23}$	$0.42^{+0.12}_{-0.11}$	0.95	0.94	71
MS 0735.6+7421	69	348	3.40	$5.54^{+0.24}_{-0.23}$	$6.47^{+0.75}_{-0.65}$	$1.17^{+0.14}_{-0.13}$	$0.35^{+0.07}_{-0.07}$	1.09	1.08	74
MS 0839.8+2938	70	294	3.92	$4.63^{+0.30}_{-0.28}$	$4.64^{+0.94}_{-0.71}$	$1.00^{+0.21}_{-0.16}$	$0.49^{+0.13}_{-0.13}$	0.97	0.91	69
MS 0906.5+1110	70	435	3.60	$5.56^{+0.34}_{-0.31}$	$6.94^{+1.23}_{-0.92}$	$1.25^{+0.23}_{-0.18}$	$0.34^{+0.10}_{-0.10}$	1.20	0.97	82
MS 1006.0+1202	70	393	3.63	$5.79^{+0.54}_{-0.46}$	$7.76^{+2.25}_{-1.56}$	$1.34^{+0.41}_{-0.29}$	$0.28^{+0.12}_{-0.12}$	1.22	1.24	82
MS 1008.1-1224	70	389	6.71	$5.76^{+0.56}_{-0.47}$	$9.88^{+2.54}_{-1.70}$	$1.72^{+0.47}_{-0.33}$	$0.24^{+0.11}_{-0.11}$	1.29	1.08	83
MS 1054.5-0321	70	395	3.69	$9.75^{+1.69}_{-1.28}$	$14.17^{+12.06}_{-4.93}$	$1.45^{+1.26}_{-0.54}$	$0.16^{+0.16}_{-0.16}$	1.05	0.85	51
MS 1455.0+2232	69	309	3.35	$4.82^{+0.14}_{-0.13}$	$5.47^{+0.29}_{-0.27}$	$1.13^{+0.07}_{-0.06}$	$0.46^{+0.05}_{-0.05}$	1.34	1.17	94
MS 1621.5+2640	70	379	3.59	$5.72^{+0.90}_{-0.72}$	$5.10^{+2.04}_{-1.27}$	$0.89^{+0.38}_{-0.25}$	$0.37^{+0.23}_{-0.21}$	1.00	0.98	74
MS 2053.7-0449 ⋆	70	397	5.16	$4.68^{+1.04}_{-0.75}$	$5.37^{+1.73}_{-1.19}$	$1.15^{+0.45}_{-0.31}$	$0.26^{+0.26}_{-0.24}$	0.99	0.94	65

Table A.4: Summary of Excised R_{5000} Spectral Fits (continued)

Cluster	$R_{\rm CORE}$ kpc	R_{5000} kpc	N_H 10^{20} cm^{-2}	T_{77} keV	T_{27} keV	T_{HBR}	Z_{77} $Z_\odot$	$\chi^2_{red,77}$	$\chi^2_{red,27}$	% Source
(1)	(2)	(3)	(4)	(5)	(6)	(7)	(8)	(9)	(10)	(11)
MS 2137.3-2353	70	354	3.40	$6.00^{+0.55}_{-0.47}$	$7.56^{+2.79}_{-1.46}$	$1.26^{+0.48}_{-0.26}$	$0.35^{+0.13}_{-0.12}$	1.08	1.28	69
MS J1157.3+5531	69	272	1.22	$3.28^{+0.36}_{-0.32}$	$6.57^{+6.42}_{-3.33}$	$2.00^{+1.97}_{-1.03}$	$0.76^{+0.30}_{-0.19}$	1.22	1.15	37
NGC 6338	71	265	2.60	$2.20^{+0.07}_{-0.06}$	$2.68^{+0.24}_{-0.20}$	$1.22^{+0.12}_{-0.10}$	$0.22^{+0.03}_{-0.04}$	1.04	1.01	51
PKS 0745-191	69	460	40.80	$8.30^{+0.39}_{-0.36}$	$9.69^{+0.84}_{-0.73}$	$1.17^{+0.12}_{-0.10}$	$0.42^{+0.06}_{-0.07}$	1.01	0.97	93
RBS 0797	69	350	2.22	$7.63^{+0.94}_{-0.77}$	$8.62^{+2.60}_{-1.69}$	$1.13^{+0.37}_{-0.25}$	$0.25^{+0.13}_{-0.13}$	1.06	0.83	93
RDCS 1252-29	71	196	6.06	$4.63^{+2.39}_{-1.41}$	$4.94^{+9.84}_{-2.82}$	$1.07^{+2.20}_{-0.69}$	$1.14^{+2.11}_{-0.83}$	1.36	0.28	60
RX J0232.2-4420	69	402	2.53	$7.92^{+0.85}_{-0.74}$	$10.54^{+2.53}_{-1.74}$	$1.33^{+0.35}_{-0.25}$	$0.38^{+0.13}_{-0.13}$	1.05	0.98	91
RX J0340-4542	70	291	1.63	$3.10^{+0.43}_{-0.38}$	$2.75^{+1.15}_{-0.67}$	$0.89^{+0.39}_{-0.24}$	$0.63^{+0.39}_{-0.28}$	1.22	1.30	48
RX J0439+0520	70	336	10.02	$4.67^{+0.58}_{-0.47}$	$5.37^{+2.03}_{-1.24}$	$1.15^{+0.46}_{-0.29}$	$0.36^{+0.22}_{-0.20}$	0.91	0.81	85
RX J0439.0+0715 ⋆	70	376	11.16	$5.65^{+0.38}_{-0.34}$	$8.21^{+1.29}_{-0.96}$	$1.45^{+0.25}_{-0.19}$	$0.34^{+0.09}_{-0.09}$	1.32	1.14	87
RX J0528.9-3927	70	454	2.36	$7.96^{+1.01}_{-0.81}$	$9.84^{+2.92}_{-1.81}$	$1.24^{+0.40}_{-0.26}$	$0.26^{+0.14}_{-0.15}$	0.96	1.04	88
RX J0647.7+7015 ⋆	69	361	5.18	$11.46^{+2.05}_{-1.58}$	$11.18^{+2.46}_{-1.77}$	$0.98^{+0.28}_{-0.20}$	$0.24^{+0.18}_{-0.20}$	1.00	0.92	88
RX J0819.6+6336	71	322	4.11	$3.92^{+0.46}_{-0.40}$	$3.24^{+1.26}_{-0.66}$	$0.83^{+0.34}_{-0.19}$	$0.16^{+0.17}_{-0.14}$	1.00	1.00	50
RX J0910+5422 ⋆	71	172	2.07	$4.08^{+3.11}_{-1.34}$	$5.00^{+5.09}_{-2.03}$	$1.23^{+1.56}_{-0.64}$	$0.43^{+1.89}_{-0.43}$	0.64	0.56	42
RX J1347.5-1145 ⋆	70	429	4.89	$15.12^{+1.03}_{-0.86}$	$17.32^{+1.73}_{-1.40}$	$1.15^{+0.14}_{-0.11}$	$0.33^{+0.07}_{-0.08}$	1.12	1.11	96
RX J1350+6007	71	236	1.77	$4.22^{+3.13}_{-1.53}$	$3.29^{+10.52}_{-1.93}$	$0.78^{+2.56}_{-0.54}$	$0.63^{+5.75}_{-0.63}$	1.00	0.14	66
RX J1423.8+2404 ⋆	71	314	2.65	$6.90^{+0.39}_{-0.37}$	$7.19^{+0.59}_{-0.52}$	$1.04^{+0.10}_{-0.09}$	$0.38^{+0.07}_{-0.08}$	0.94	0.90	90
RX J1504.1-0248	70	445	6.27	$8.02^{+0.26}_{-0.25}$	$8.52^{+0.58}_{-0.50}$	$1.06^{+0.08}_{-0.07}$	$0.39^{+0.04}_{-0.05}$	1.25	1.17	95
RX J1525+0958	70	296	2.96	$3.83^{+0.84}_{-0.53}$	$9.10^{+7.62}_{-3.25}$	$2.38^{+2.06}_{-0.91}$	$0.69^{+0.47}_{-0.36}$	1.96	0.08	83
RX J1532.9+3021 ⋆	70	322	2.21	$6.06^{+0.43}_{-0.39}$	$7.20^{+0.94}_{-0.77}$	$1.19^{+0.18}_{-0.15}$	$0.46^{+0.10}_{-0.11}$	0.92	1.02	83
RX J1716.9+6708	71	342	3.71	$6.51^{+1.79}_{-1.24}$	$6.21^{+4.03}_{-2.26}$	$0.95^{+0.67}_{-0.39}$	$0.56^{+0.39}_{-0.32}$	0.84	0.92	63
RX J1720.1+2638	69	359	4.02	$6.33^{+0.29}_{-0.25}$	$7.71^{+0.84}_{-0.65}$	$1.22^{+0.14}_{-0.11}$	$0.37^{+0.07}_{-0.07}$	1.04	0.96	94
RX J1720.2+3536 ⋆	71	320	3.35	$7.34^{+0.59}_{-0.50}$	$7.40^{+0.86}_{-0.71}$	$1.01^{+0.14}_{-0.12}$	$0.43^{+0.11}_{-0.11}$	1.03	0.94	91
RX J2011.3-5725	71	295	4.76	$4.10^{+0.47}_{-0.39}$	$3.93^{+0.98}_{-0.70}$	$0.96^{+0.26}_{-0.19}$	$0.41^{+0.24}_{-0.20}$	0.95	1.08	84
RX J2129.6+0005	70	489	4.30	$6.01^{+0.55}_{-0.46}$	$7.19^{+1.68}_{-1.21}$	$1.20^{+0.30}_{-0.22}$	$0.51^{+0.16}_{-0.15}$	1.29	1.34	87
S0463 ⋆	70	307	1.06	$3.26^{+0.33}_{-0.38}$	$3.92^{+1.16}_{-0.94}$	$1.20^{+0.38}_{-0.32}$	$0.23^{+0.18}_{-0.15}$	1.08	1.08	54

Table A.4: Summary of Excised R_{5000} Spectral Fits (continued)

Cluster	$R_{\rm CORE}$ kpc	R_{5000} kpc	N_H 10^{20} cm^{-2}	T_{77} keV	T_{27} keV	T_{HBR}	Z_{77} $Z_\odot$	$\chi^2_{red,77}$	$\chi^2_{red,27}$	% Source
(1)	(2)	(3)	(4)	(5)	(6)	(7)	(8)	(9)	(10)	(11)
TRIANG AUSTR	71	539	13.27	$8.50^{+0.29}_{-0.25}$	$12.08^{+1.13}_{-1.13}$	$1.42^{+0.14}_{-0.14}$	$0.03^{+0.04}_{-0.03}$	0.01	1.93	83
V 1121.0+2327	70	315	1.30	$4.17^{+0.78}_{-0.60}$	$4.70^{+3.00}_{-1.17}$	$1.13^{+0.75}_{-0.32}$	$0.46^{+0.36}_{-0.28}$	1.09	0.87	74
ZWCL 1215	70	277	1.76	$6.64^{+0.46}_{-0.38}$	$8.69^{+0.74}_{-0.80}$	$1.31^{+0.14}_{-0.14}$	$0.37^{+0.11}_{-0.11}$	1.10	1.03	91
ZWCL 1358+6245	70	391	1.94	$9.70^{+1.16}_{-0.94}$	$9.04^{+2.09}_{-1.46}$	$0.93^{+0.24}_{-0.18}$	$0.57^{+0.19}_{-0.19}$	1.03	0.90	65
ZWCL 1953	69	516	3.10	$8.28^{+1.22}_{-0.96}$	$11.83^{+4.01}_{-2.55}$	$1.43^{+0.53}_{-0.35}$	$0.21^{+0.14}_{-0.15}$	0.87	0.77	82
ZWCL 3146	70	512	2.70	$7.46^{+0.32}_{-0.30}$	$8.99^{+0.94}_{-0.78}$	$1.21^{+0.14}_{-0.12}$	$0.31^{+0.06}_{-0.05}$	1.06	0.97	91
ZWCL 5247	70	449	1.70	$4.89^{+0.86}_{-0.65}$	$4.39^{+2.30}_{-1.21}$	$0.90^{+0.50}_{-0.27}$	$0.37^{+0.30}_{-0.25}$	1.09	0.93	78
ZWCL 7160	69	451	3.10	$4.63^{+0.42}_{-0.36}$	$5.41^{+1.06}_{-0.80}$	$1.17^{+0.25}_{-0.20}$	$0.36^{+0.14}_{-0.14}$	0.94	0.95	87
ZWICKY 2701	69	315	0.83	$5.08^{+0.32}_{-0.30}$	$4.96^{+0.87}_{-0.69}$	$0.98^{+0.18}_{-0.15}$	$0.45^{+0.13}_{-0.11}$	0.95	0.76	70
ZwCL 1332.8+5043	70	453	1.10	$3.82^{+3.34}_{-1.42}$	$2.86^{+3.96}_{-1.21}$	$0.75^{+1.23}_{-0.42}$	$0.16^{+4.75}_{-0.16}$	0.71	0.95	60
ZwCl 0848.5+3341	71	365	1.12	$6.54^{+2.04}_{-1.27}$	$6.41^{+3.79}_{-1.88}$	$0.98^{+0.66}_{-0.34}$	$0.59^{+0.59}_{-0.48}$	0.89	1.01	47

Appendix B: Tables cited in Chapter 3

Table B.1 Notes

Col. (1) Cluster name; col. (2) CXC CDA Observation Identification Number; col. (3) R.A. of cluster center; col. (4) Decl. of cluster center; col. (5) exposure time; col. (6) observing mode; col. (7) CCD location of cluster center; col. (8) redshift; col. (9) average cluster temperature; col. (10) core entropy measured in this work; col. (11) cluster bolometric luminosity; and col. (12) notes are as follows: (a) - cluster analyzed using the best-fit β-model for the surface brightness profiles (discussed in §3.3.2); (b) - clusters with complex surface brightness of which only the central regions were used in fitting $K(r)$; (c) - cluster only used during analysis of the *HIFLUGCS* sub-sample (discussed in §3.5.4); (d) - cluster with central AGN removed during analysis (discussed in §3.3.5); (e) - cluster with central compact source removed during analysis (discussed in §3.3.5); and (f) - cluster with central bin ignored during fitting (discussed in §3.3.5).

Table B.2 Notes

Col. (1) Cluster name; col. (2) central surface brightness of first component; col. (3) core radius of first component; col. (4) β parameter of first component; col. (5) central surface brightness of second component; col. (6) core radius of second component; col. (7) β parameter of second component; col. (8) model degrees of freedom; and col. (9) reduced chi-squared statistic for best-fit model.

Table B.4 Notes

Listed here are the mean best-fit parameters of the model $K(r) = K_0 + K_{100}(r/100\text{kpc})^{\alpha}$ for various sub-groups of the full *ACCEPT* sample. The 'CSE' sample are the clusters with a central source excluded (discussed in §3.3.5). The K_{12} values represent the entropy at 12 kpc and are calculated from the best-fit models. Col. (1) Sample being considered; col. (2) number of objects in the sub-group; col. (3) fraction of objects with p > 0.05 for power-law only model (eqn. 3.5); col. (4) fraction of objects with p > 0.05 for power-law with constant core entropy model (eqn. 3.4); col. (5) fraction of objects which do not meet p > 0.05 criterion for either model; col. (6) mean best-fit K_0; col. (7) mean entropy at 12 kpc; col. (8) mean best-fit K_{100}; and col. (9) mean best-fit power-law index; and cols. (10,11,12) number of clusters consistent with $K_0 = 0\text{keV cm}^2$ at 1σ, 2σ, and 3σ significance, respectively. Percentage of the sub-group represented by each is also listed.

Table B.5 Notes

Col. (1) Cluster name; col. (2) CDA observation identification number; col. (3) method of T_X interpolation (discussed in §3.3.4); col. (4) maximum radius for fit; col. (5) number of radial bins included in fit; col. (6) best-fit core entropy; col. (7) number of sigma K_0 is away from zero; col. (9) best-fit entropy at 100 kpc; col. (10) best-fit power-law index; col. (11) degrees of freedom in fit; col. (12) χ^2 statistic of best-fit model; and col. (13) probability of worse fit given χ^2 and degrees of freedom.

Table B.1: Summary of Sample for Entropy Study

Cluster	Obs. ID	R.A. hr:min:sec	Decl. ° ′ ″	Exposure Time ksec	ACIS	z	kT_X keV	Notes
(1)	(2)	(3)	(4)	(5)	(6)	(7)	(8)	(9)
1E0657 56	3184	06:58:29.627	-55:56:39.79	87.5	I3	0.2960	11.64	···
	5356	···	···	97.2	I2	···	···	···
	5361	···	···	82.6	I3	···	···	···
2A 335+096	919	03:38:41.105	+09:58:00.66	19.7	S3	0.0347	2.88	···
2PIGG J0011.5-2850	5797	00:11:21.623	-28:51:14.44	19.9	I3	0.0753	5.15	f
2PIGG J2227.0-3041	5798	22:27:54.560	-30:34:34.84	22.3	I2	0.0729	2.79	···
3C 28.0	3233	00:55:50.401	+26:24:36.47	49.7	I3	0.1952	5.53	···
3C 295	2254	14:11:20.280	+52:12:10.55	90.9	I3	0.4641	5.16	d
3C 388	5295	18:44:02.365	+45:33:29.31	30.7	I3	0.0917	3.23	d
4C 55.16	4940	08:34:54.923	+55:34:21.15	96.0	S3	0.2420	4.98	d
Abell 13	4945	00:13:37.883	-19:30:09.10	55.3	S3	0.0940	6.84	···
Abell 68	3250	00:37:06.475	+09:09:32.28	10.0	I3	0.2546	9.01	···
Abell 85	904	00:41:50.406	-09:18:10.79	38.4	I0	0.0558	6.40	···
Abell 119	4180	00:56:15.150	-01:14:59.70	11.9	I3	0.0442	5.86	a,e
Abell 133	2203	01:02:41.756	-21:52:49.79	35.5	S3	0.0558	4.31	···
Abell 141	9410	01:05:34.385	-24:37:58.78	19.9	I3	0.2300	5.31	···
Abell 160	3219	01:13:00.692	+15:29:15.08	58.5	I3	0.0447	1.88	a,e
Abell 193	6931	01:25:07.660	+08:41:57.08	17.9	S3	0.0485	2.50	a,e
Abell 209	3579	01:31:52.565	-13:36:38.79	10.0	I3	0.2060	8.28	···
	522	···	···	10.0	I3	···	···	···
Abell 222	4967	01:37:34.562	-12:59:34.88	45.1	I3	0.2130	4.60	···
Abell 223	49671	01:37:55.963	-12:49:10.53	45.1	I0	0.2070	5.28	e
Abell 262	2215	01:52:46.299	+36:09:11.80	28.7	S3	0.0164	2.18	···
	7921	···	···	110.7	S3	···	···	···
Abell 267	1448	01:52:42.269	+01:00:45.33	7.9	I3	0.2300	6.79	···
	3580	···	···	19.9	I3	···	···	···
Abell 368	9412	02:37:27.640	-26:30:28.99	18.4	I3	0.2200	6.23	···

Table B.1: Summary of Sample for Entropy Study (continued)

Cluster	Obs. ID	R.A. hr:min:sec	Decl. ° :′:″	Exposure Time ksec	ACIS	z	kT_X keV	Notes
(1)	(2)	(3)	(4)	(5)	(6)	(7)	(8)	(9)
Abell 370	515	02:39:53.169	-01:34:36.96	88.0	S3	0.3747	7.35	···
Abell 383	2321	02:48:03.364	-03:31:44.69	19.5	S3	0.1871	4.91	···
Abell 399	3230	02:57:53.382	+13:01:30.86	48.6	I0	0.0716	7.95	···
Abell 400	4181	02:57:41.603	+06:01:27.61	21.5	I3	0.0240	2.31	a,e
Abell 401	2309	02:58:56.920	+13:34:14.51	11.6	I2	0.0745	8.07	···
	518	···	···	18.0	I3	···	···	···
Abell 426	3209	03:19:48.194	+41:30:40.73	95.8	S3	0.0179	3.55	d
	4289	···	···	95.4	S3	···	···	···
Abell 478	1669	04:13:25.345	+10:27:55.15	42.4	S3	0.0883	7.07	···
	6102	···	···	10.0	I3	···	···	···
Abell 496	3361	04:33:38.038	-13:15:39.65	10.0	S3	0.0328	5.03	···
Abell 520	4215	04:54:10.303	+02:55:36.48	66.3	I3	0.2020	9.29	···
Abell 521	430	04:54:06.337	-10:13:16.88	39.1	S3	0.2533	7.03	···
Abell 539	5808	05:16:37.335	+06:26:25.18	24.3	I3	0.0288	3.24	b,e
	7209	···	···	18.6	I3	···	···	···
Abell 562	6936	06:53:21.524	+69:19:51.19	51.5	S3	0.1100	3.04	e
Abell 576	3289	07:21:30.394	+55:45:41.95	38.6	S3	0.0385	4.43	e
Abell 586	530	07:32:20.339	+31:37:58.59	10.0	I3	0.1710	6.47	···
Abell 611	3194	08:00:56.832	+36:03:24.09	36.1	S3	0.2880	7.06	e
Abell 644	2211	08:17:25.225	-07:30:40.03	29.7	I3	0.0698	7.73	···
Abell 665	3586	08:30:59.226	+65:50:20.06	29.7	I3	0.1810	7.45	···
Abell 697	4217	08:42:57.549	+36:21:57.65	19.5	I3	0.2820	9.52	···
Abell 744	6947	09:07:20.455	+16:39:06.18	39.5	I3	0.0729	2.50	e
Abell 754	577	09:09:18.188	-09:41:09.56	44.2	I3	0.0543	9.94	···
Abell 773	5006	09:17:52.566	+51:43:38.18	19.8	I3	0.2170	7.83	···
Abell 907	3185	09:58:21.946	-11:03:50.73	48.0	I3	0.1527	5.59	···
	3205	···	···	47.1	I3	···	···	···

Table B.1: Summary of Sample for Entropy Study (continued)

Cluster	Obs. ID	R.A. hr:min:sec	Decl. ° :′:″	Exposure Time ksec	ACIS	z	kT_X keV	Notes
(1)	(2)	(3)	(4)	(5)	(6)	(7)	(8)	(9)
	535	···	···	11.0	I3	···	···	···
Abell 963	903	10:17:03.744	+39:02:49.17	36.3	S3	0.2056	6.73	···
Abell 1060	2220	10:36:42.828	-27:31:42.06	31.9	I3	0.0125	3.29	a,e,f
Abell 1063S	4966	22:48:44.294	-44:31:48.37	26.7	I3	0.3540	11.96	···
Abell 1068	1652	10:40:44.520	+39:57:10.28	26.8	S3	0.1375	4.62	···
Abell 1201	4216	11:12:54.489	+13:26:08.76	39.7	S3	0.1688	5.61	···
Abell 1204	2205	11:13:20.419	+17:35:38.45	23.6	I3	0.1706	3.63	···
Abell 1240	4961	11:23:38.357	+43:05:48.33	51.3	I3	0.1590	4.77	a
Abell 1361	2200	11:43:39.637	+46:21:20.41	16.7	S3	0.1171	5.32	···
Abell 1413	5003	11:55:17.893	+23:24:21.84	75.1	I2	0.1426	7.41	···
Abell 1423	538	11:57:17.263	+33:36:37.44	9.8	I3	0.2130	6.01	···
Abell 1446	4975	12:02:03.744	+58:02:17.93	58.4	S3	0.1035	3.96	···
Abell 1569	6100	12:36:26.015	+16:32:17.81	41.2	I3	0.0735	2.51	···
Abell 1576	7938	12:36:58.274	+63:11:13.88	15.0	I3	0.2790	10.10	···
Abell 1644	2206	12:57:11.665	-17:24:32.86	18.7	I3	0.0471	4.60	b
	7922	···	···	51.5	I3	···	···	···
Abell 1650	4178	12:58:41.499	-01:45:44.32	27.3	S3	0.0843	6.17	···
Abell 1651	4185	12:59:22.830	-04:11:45.86	9.6	I3	0.0840	6.26	···
Abell 1664	1648	13:03:42.622	-24:14:41.59	9.8	S3	0.1276	4.39	···
	7901	···	···	36.6	S3	···	···	···
Abell 1689	1663	13:11:29.612	-01:20:28.69	10.7	I3	0.1843	10.10	···
	5004	···	···	19.9	I3	···	···	···
	540	···	···	10.3	I3	···	···	···
Abell 1736	4186	13:26:49.453	-27:09:48.13	14.9	I1	0.0338	3.45	a,e
Abell 1758	2213	13:32:48.398	+50:32:32.53	58.3	S3	0.2792	12.14	···
Abell 1763	3591	13:35:17.957	+40:59:55.80	19.6	I3	0.1866	7.78	···
Abell 1795	493	13:48:52.802	+26:35:23.55	19.6	S3	0.0625	7.80	···

Table B.1: Summary of Sample for Entropy Study (continued)

Cluster	Obs. ID	R.A. hr:min:sec	Decl. ° :′:″	Exposure Time ksec	ACIS	z	kT_X keV	Notes
(1)	(2)	(3)	(4)	(5)	(6)	(7)	(8)	(9)
	5289	···	···	15.0	I3	···	···	···
Abell 1835	495	14:01:01.951	+02:52:43.18	19.5	S3	0.2532	9.77	···
Abell 1914	3593	14:26:03.060	+37:49:27.84	18.9	I3	0.1712	9.62	···
Abell 1942	3290	14:38:21.878	+03:40:12.97	57.6	I2	0.2240	4.77	···
Abell 1991	3193	14:54:31.620	+18:38:41.48	38.3	S3	0.0587	2.67	···
Abell 1995	7021	14:52:57.410	+58:02:56.84	48.5	I3	0.3186	3.40	···
Abell 2029	4977	15:10:56.139	+05:44:40.47	77.9	S3	0.0765	7.38	···
	6101	···	···	9.9	I3	···	···	···
	891	···	···	19.8	S3	···	···	···
Abell 2034	2204	15:10:12.498	+33:30:39.57	53.9	I3	0.1130	7.15	f
Abell 2052	5807	15:16:44.514	+07:01:17.02	127.0	S3	0.0353	2.98	d
	890	···	···	36.8	S3	···	···	···
Abell 2063	4187	15:23:04.851	+08:36:20.16	8.8	I3	0.0351	3.61	···
	6263	···	···	16.8	S3	···	···	···
Abell 2065	31821	15:22:29.517	+27:42:22.93	27.7	I3	0.0730	5.75	···
Abell 2069	4965	15:24:11.376	+29:52:19.02	55.4	I2	0.1160	6.50	···
Abell 2104	895	15:40:08.131	-03:18:15.02	49.2	S3	0.1554	8.53	···
Abell 2107	4960	15:39:39.113	+21:46:57.66	35.6	I3	0.0411	3.82	b
Abell 2111	544	15:39:40.637	+34:25:28.01	10.3	I3	0.2300	7.13	···
Abell 2124	3238	15:44:59.131	+36:06:34.11	19.4	S3	0.0658	4.73	···
Abell 2125	2207	15:41:14.154	+66:15:57.20	81.5	I3	0.2465	2.88	a
Abell 2142	1196	15:58:20.880	+27:13:44.21	11.4	S3	0.0898	8.24	···
	1228	···	···	12.1	S3	···	···	···
	5005	···	···	44.6	I3	···	···	···
Abell 2147	3211	16:02:17.025	+15:58:28.32	17.9	I3	0.0356	4.09	···
Abell 2151	4996	16:04:35.887	+17:43:17.36	21.8	I3	0.0366	2.90	e
Abell 2163	1653	16:15:45.705	-06:09:00.62	71.1	I1	0.1695	19.20	···

Table B.1: Summary of Sample for Entropy Study (continued)

Cluster	Obs. ID	R.A. hr:min:sec	Decl. ° :′:″	Exposure Time ksec	ACIS	z	kT_X keV	Notes
(1)	(2)	(3)	(4)	(5)	(6)	(7)	(8)	(9)
Abell 2199	497	16:28:38.249	+39:33:04.28	19.5	S3	0.0300	4.55	b
Abell 2204	499	16:32:46.920	+05:34:32.86	10.1	S3	0.1524	6.97	···
	6104	···	···	9.6	I3	···	···	···
	7940	···	···	77.1	I3	···	···	···
Abell 2218	1666	16:35:50.831	+66:12:42.31	48.6	I0	0.1713	7.35	···
Abell 2219	896	16:40:20.112	+46:42:42.84	42.3	S3	0.2256	12.75	···
Abell 2244	4179	17:02:42.579	+34:03:37.34	57.0	S3	0.0967	5.68	···
Abell 2255	894	17:12:42.935	+64:04:10.81	39.4	I3	0.0805	6.12	a
Abell 2256	1386	17:03:44.567	+78:38:11.51	12.4	I3	0.0579	6.90	a
Abell 2259	3245	17:20:08.299	+27:40:11.53	10.0	I3	0.1640	5.18	···
Abell 2261	5007	17:22:27.254	+32:07:58.60	24.3	I3	0.2240	7.63	···
Abell 2294	3246	17:24:10.149	+85:53:09.77	10.0	I3	0.1780	9.98	···
Abell 2319	3231	19:21:09.638	+43:57:21.53	14.4	I1	0.0562	10.87	a
Abell 2384	4202	21:52:21.178	-19:32:51.90	31.5	I3	0.0945	4.75	···
Abell 2390	4193	21:53:36.825	+17:41:44.38	95.1	S3	0.2301	11.15	···
Abell 2409	3247	22:00:52.567	+20:58:06.55	10.2	I3	0.1479	5.94	···
Abell 2420	8271	22:10:18.792	-12:10:13.35	8.1	I3	0.0846	6.47	···
Abell 2462	4159	22:39:11.367	-17:20:28.33	39.2	S3	0.0737	2.42	a,e
Abell 2537	4962	23:08:22.313	-02:11:29.88	36.2	S3	0.2950	8.40	···
Abell 2554	1696	23:12:19.622	-21:30:11.32	19.9	S3	0.1103	5.29	···
Abell 2556	2226	23:13:01.413	-21:38:04.47	19.9	S3	0.0862	3.50	···
Abell 2589	3210	23:23:57.315	+16:46:38.43	13.7	S3	0.0415	3.65	···
Abell 2597	922	23:25:19.779	-12:07:27.63	39.4	S3	0.0854	4.02	···
Abell 2626	3192	23:36:30.452	+21:08:47.36	24.8	S3	0.0573	3.29	···
Abell 2631	3248	23:37:38.560	+00:16:05.02	9.2	I3	0.2779	7.06	a
Abell 2657	4941	23:44:57.253	+09:11:30.74	16.1	I3	0.0402	3.77	···
Abell 2667	2214	23:51:39.395	-26:05:02.75	9.6	S3	0.2300	6.75	···

Table B.1: Summary of Sample for Entropy Study (continued)

Cluster	Obs. ID	R.A. hr:min:sec	Decl. ° :′:″	Exposure Time ksec	ACIS	z	kT_X keV	Notes
(1)	(2)	(3)	(4)	(5)	(6)	(7)	(8)	(9)
Abell 2717	6974	00:03:12.968	-35:56:00.13	19.8	I3	0.0475	1.69	e
Abell 2744	2212	00:14:19.529	-30:23:30.24	24.8	S3	0.3080	9.18	···
	7915	···	···	18.6	I3	···	···	···
	8477	···	···	45.9	I3	···	···	···
	8557	···	···	27.8	I3	···	···	···
Abell 2813	9409	00:43:24.881	-20:37:25.08	19.9	I3	0.2924	8.96	···
Abell 3084	9413	03:04:03.920	-36:56:27.17	19.9	I3	0.0977	5.30	···
Abell 3088	9414	03:07:01.734	-28:39:55.47	18.9	I3	0.2534	6.71	···
Abell 3112	2516	03:17:57.681	-44:14:17.16	16.9	S3	0.0720	5.17	d
Abell 3120	6951	03:21:56.464	-51:19:35.40	26.8	I3	0.0690	4.40	···
Abell 3158	3201	03:42:54.675	-53:37:24.36	24.8	I3	0.0580	4.94	···
	3712	···	···	30.9	I3	···	···	···
Abell 3266	899	04:31:13.304	-61:27:12.59	29.8	I1	0.0590	9.07	···
Abell 3364	9419	05:47:37.698	-31:52:23.61	19.8	I3	0.1483	7.88	···
Abell 3376	3202	06:02:11.756	-39:56:59.07	44.3	I3	0.0456	4.08	a
	3450	···	···	19.8	I3	···	···	···
Abell 3391	4943	06:26:21.511	-53:41:44.81	18.4	I3	0.0560	6.07	a,e
Abell 3395	4944	06:26:48.463	-54:32:59.21	21.9	I3	0.0510	5.13	a,e
Abell 3528S	8268	12:54:40.897	-29:13:38.10	8.1	I3	0.0530	5.44	···
Abell 3558	1646	13:27:56.854	-31:29:43.78	14.4	S3	0.0480	6.60	e,f
Abell 3562	4167	13:33:37.800	-31:40:12.04	19.3	I2	0.0490	4.59	···
Abell 3571	4203	13:47:28.434	-32:51:52.45	34.0	S3	0.0391	7.77	···
Abell 3581	1650	14:07:29.777	-27:01:05.88	7.2	S3	0.0218	2.10	d
Abell 3667	5751	20:12:41.231	-56:50:35.70	128.9	I3	0.0556	6.51	···
	5752	···	···	60.4	I3	···	···	···
	5753	···	···	103.6	I3	···	···	···
	889	···	···	50.3	I2	···	···	···

Table B.1: Summary of Sample for Entropy Study (continued)

Cluster	Obs. ID	R.A. hr:min:sec	Decl. ° :′:″	Exposure Time ksec	ACIS	z	kT_X keV	Notes
(1)	(2)	(3)	(4)	(5)	(6)	(7)	(8)	(9)
Abell 3822	8269	21:54:04.203	-57:52:02.71	8.1	I3	0.0759	4.89	e
Abell 3827	7920	22:01:53.200	-59:56:43.04	45.6	S3	0.0984	8.05	···
Abell 3921	4973	22:49:57.829	-64:25:42.17	29.4	I3	0.0927	5.69	···
Abell 4038	4992	23:47:43.180	-28:08:34.81	33.5	I2	0.0300	3.11	···
Abell 4059	5785	23:57:01.065	-34:45:33.28	92.1	S3	0.0475	4.69	···
Abell S0405	8272	03:51:32.815	-82:13:10.19	7.9	I3	0.0613	4.11	···
Abell S0592	9420	06:38:48.610	-53:58:26.32	19.9	I3	0.2216	9.08	···
AC 114	1562	22:58:48.316	-34:48:08.20	72.5	S3	0.3120	7.53	···
AWM7	908	02:54:27.631	+41:34:47.07	47.9	I3	0.0172	3.71	b
Centaurus	4190	12:48:49.267	-41:18:39.54	34.3	S3	0.0109	3.96	b
	4191	···	···	34.0	S3	···	···	···
	4954	···	···	89.1	S3	···	···	···
	4955	···	···	44.7	S3	···	···	···
	504	···	···	31.8	S3	···	···	···
	505	···	···	10.0	S3	···	···	···
	5310	···	···	49.3	S3	···	···	···
CID 72	2018	17:33:03.247	+43:45:37.28	30.7	S3	0.0344	1.91	···
	6949	···	···	38.6	I3	···	···	···
	7321	···	···	37.5	I3	···	···	···
	7322	···	···	37.5	I3	···	···	···
CL J1226.9+3332	3180	12:26:58.373	+33:32:47.36	31.7	I3	0.8900	10.00	···
	5014	···	···	32.7	I3	···	···	···
	932	···	···	9.8	S3	···	···	···
Cygnus A	360	19:59:28.381	+40:44:01.98	34.7	S3	0.0561	7.68	d
ESO 3060170	3188	05:40:06.687	-40:50:12.82	14.0	I3	0.0358	2.79	b
	3189	···	···	14.1	I0	···	···	···
ESO 5520200	3206	04:54:52.318	-18:06:56.52	23.9	I3	0.0314	2.37	···

Table B.1: Summary of Sample for Entropy Study (continued)

Cluster	Obs. ID	R.A. hr:min:sec	Decl. ° :′:″	Exposure Time ksec	ACIS	z	kT_X keV	Notes
(1)	(2)	(3)	(4)	(5)	(6)	(7)	(8)	(9)
EXO 422-086	4183	04:25:51.271	-08:33:36.42	10.0	I3	0.0397	3.40	···
HCG 62	921	12:53:05.741	-09:12:15.64	48.5	S3	0.0146	1.10	···
HCG 42	3215	10:00:14.234	-19:38:10.77	31.7	S3	0.0133	0.70	···
Hercules A	1625	16:51:08.161	+04:59:32.44	14.8	S3	0.1541	5.21	···
	5796	···	···	47.5	S3	···	···	···
	6257	···	···	49.5	S3	···	···	···
Hydra A	4970	09:18:05.985	-12:05:43.94	98.8	S3	0.0549	4.00	d
	576	···	···	19.5	S3	···	···	···
M49	321	12:29:46.841	+08:00:01.98	39.6	S3	0.0033	1.33	c
M87	5826	12:30:49.383	+12:23:28.67	126.8	I3	0.0044	2.50	d
	5827	···	···	156.2	I3	···	···	···
MACS J0011.7-1523	3261	00:11:42.965	-15:23:20.79	21.6	I3	0.3600	5.42	···
	6105	···	···	37.3	I3	···	···	···
MACS J0035.4-2015	3262	00:35:26.573	-20:15:46.06	21.4	I3	0.3644	7.39	···
MACS J0159.8-0849	3265	01:59:49.453	-08:50:00.90	17.9	I3	0.4050	9.59	···
	6106	···	···	35.3	I3	···	···	···
MACS J0242.5-2132	3266	02:42:35.906	-21:32:26.30	11.9	I3	0.3140	5.58	···
MACS J0257.1-2325	1654	02:57:09.130	-23:26:05.85	19.8	I3	0.5053	10.50	···
	3581	···	···	18.5	I3	···	···	···
MACS J0257.6-2209	3267	02:57:41.024	-22:09:11.12	20.5	I3	0.3224	8.02	···
MACS J0308.9+2645	3268	03:08:55.927	+26:45:38.34	24.4	I3	0.3240	10.54	···
MACS J0329.6-0211	3257	03:29:41.681	-02:11:47.67	9.9	I3	0.4500	5.20	···
	3582	···	···	19.9	I3	···	···	···
	6108	···	···	39.6	I3	···	···	···
MACS J0417.5-1154	3270	04:17:34.686	-11:54:32.71	12.0	I3	0.4400	11.07	···
MACS J0429.6-0253	3271	04:29:36.088	-02:53:09.02	23.2	I3	0.3990	5.66	···
MACS J0520.7-1328	3272	05:20:42.052	-13:28:49.38	19.2	I3	0.3398	6.27	···

Table B.1: Summary of Sample for Entropy Study (continued)

Cluster	Obs. ID	R.A. hr:min:sec	Decl. ° :′:″	Exposure Time ksec	ACIS	z	kT_X keV	Notes
(1)	(2)	(3)	(4)	(5)	(6)	(7)	(8)	(9)
MACS J0547.0-3904	3273	05:47:01.582	-39:04:28.24	21.7	I3	0.2100	3.58	e
MACS J0717.5+3745	1655	07:17:31.654	+37:45:18.52	19.9	I3	0.5480	10.50	···
	4200	···	···	59.2	I3	···	···	···
MACS J0744.8+3927	3197	07:44:52.802	+39:27:24.41	20.2	I3	0.6860	11.29	···
	3585	···	···	19.9	I3	···	···	···
	6111	···	···	49.5	I3	···	···	···
MACS J1115.2+5320	3253	11:15:15.632	+53:20:03.31	8.8	I3	0.4390	8.03	···
	5008	···	···	18.0	I3	···	···	···
	5350	···	···	6.9	I3	···	···	···
MACS J1115.8+0129	3275	11:15:52.048	+01:29:56.56	15.9	I3	0.1200	6.78	···
MACS J1131.8-1955	3276	11:31:54.580	-19:55:44.54	13.9	I3	0.3070	8.64	···
MACS J1149.5+2223	1656	11:49:35.856	+22:23:55.02	18.5	I3	0.5440	8.40	···
	3589	···	···	20.0	I3	···	···	···
MACS J1206.2-0847	3277	12:06:12.276	-08:48:02.40	23.5	I3	0.4400	10.21	···
MACS J1311.0-0310	3258	13:11:01.665	-03:10:39.50	14.9	I3	0.4940	5.60	···
	6110	···	···	63.2	I3	···	···	···
MACS J1621.3+3810	3254	16:21:24.801	+38:10:08.65	9.8	I3	0.4610	7.53	···
	3594	···	···	19.7	I3	···	···	···
	6109	···	···	37.5	I3	···	···	···
	6172	···	···	29.8	I3	···	···	···
MACS J1931.8-2634	3282	19:31:49.656	-26:34:33.99	13.6	I3	0.3520	6.97	e
MACS J2049.9-3217	3283	20:49:56.245	-32:16:52.30	23.8	I3	0.3254	6.98	···
MACS J2211.7-0349	3284	22:11:45.856	-03:49:37.24	17.7	I3	0.2700	11.30	···
MACS J2214.9-1359	3259	22:14:57.467	-14:00:09.35	19.5	I3	0.5026	8.80	···
	5011	···	···	18.5	I3	···	···	···
MACS J2228+2036	3285	22:28:33.872	+20:37:18.31	19.9	I3	0.4120	7.86	···
MACS J2229.7-2755	3286	22:29:45.358	-27:55:38.41	16.4	I3	0.3240	5.01	···

Table B.1: Summary of Sample for Entropy Study (continued)

Cluster	Obs. ID	R.A. hr:min:sec	Decl. ° :′:″	Exposure Time ksec	ACIS	z	kT_X keV	Notes
(1)	(2)	(3)	(4)	(5)	(6)	(7)	(8)	(9)
MACS J2245.0+2637	3287	22:45:04.657	+26:38:03.46	16.9	I3	0.3040	6.06	···
MKW3S	900	15:21:51.930	+07:42:31.97	57.3	I3	0.0450	2.18	···
MKW 4	3234	12:04:27.218	+01:53:42.79	30.0	S3	0.0198	2.06	···
MKW 8	4942	14:40:39.633	+03:28:13.61	23.1	I3	0.0270	3.29	a,b
MS J0016.9+1609	520	00:18:33.503	+16:26:12.99	67.4	I3	0.5410	8.94	···
MS J0116.3-0115	4963	01:18:53.944	-01:00:07.54	39.3	S3	0.0452	1.84	···
MS J0440.5+0204	4196	04:43:09.952	+02:10:18.70	59.4	S3	0.1900	5.46	···
MS J0451.6-0305	902	04:54:11.004	-03:00:52.19	44.2	S3	0.5386	8.90	···
MS J0735.6+7421	4197	07:41:44.245	+74:14:38.23	45.5	S3	0.2160	5.55	···
MS J0839.8+2938	2224	08:42:55.969	+29:27:26.97	29.8	S3	0.1940	4.68	···
MS J0906.5+1110	924	09:09:12.753	+10:58:32.00	29.7	I3	0.1630	5.38	···
MS J1006.0+1202	925	10:08:47.462	+11:47:36.31	29.4	I3	0.2210	5.61	···
MS J1008.1-1224	926	10:10:32.312	-12:39:56.80	44.2	I3	0.3010	7.45	···
MS J1455.0+2232	4192	14:57:15.088	+22:20:32.49	91.9	I3	0.2590	4.77	···
MS J2137.3-2353	4974	21:40:15.178	-23:39:40.71	57.4	S3	0.3130	6.01	···
MS J1157.3+5531	4964	11:59:52.295	+55:32:05.61	75.1	S3	0.0810	3.28	b
NGC 507	2882	01:23:39.905	+33:15:21.73	43.6	I3	0.0164	1.40	c
NGC 4636	3926	12:42:49.856	+02:41:15.86	74.7	I3	0.0031	0.66	c
	4415	···	···	74.4	I3	···	···	···
NGC 5044	3225	13:15:23.947	-16:23:07.62	83.1	S3	0.0090	1.22	c
	3664	···	···	61.3	S3	···	···	···
NGC 5813	5907	15:01:11.260	+01:42:07.23	48.4	S3	0.0066	0.76	c
NGC 5846	788	15:06:29.289	+01:36:20.13	29.9	S3	0.0057	0.64	c
Ophiuchus	3200	17:12:27.731	-23:22:06.74	50.5	S3	0.0280	11.12	···
PKS 0745-191	2427	07:47:31.436	-19:17:39.78	17.9	S3	0.1028	8.50	···
	508	···	···	28.0	S3	···	···	···
	6103	···	···	10.3	I3	···	···	···

Table B.1: Summary of Sample for Entropy Study (continued)

Cluster	Obs. ID	R.A. hr:min:sec	Decl. ° :′:″	Exposure Time ksec	ACIS	z	kT_X keV	Notes
(1)	(2)	(3)	(4)	(5)	(6)	(7)	(8)	(9)
RBS 461	4182	03:41:17.490	+15:23:54.66	23.4	I3	0.0290	2.60	a,e
RBS 533	3186	04:19:38.105	+02:24:35.54	10.0	I3	0.0123	1.29	···
	3187	···	···	9.6	I3	···	···	···
	5800	···	···	44.5	S3	···	···	···
	5801	···	···	44.4	S3	···	···	···
RBS 797	2202	09:47:12.693	+76:23:13.40	11.7	I3	0.3540	7.68	d
	7902	···	···	38.3	S3	···	···	···
RCS J2327-0204	7355	23:27:27.524	-02:04:39.01	24.7	S3	0.2000	7.06	···
RX J0220.9-3829	9411	02:20:56.582	-38:28:51.21	19.9	I3	0.2287	5.02	···
RX J0232.2-4420	4993	02:32:18.771	-44:20:46.68	23.4	I3	0.2836	7.83	···
RX J0439+0520	527	04:39:02.218	+05:20:43.11	9.6	I3	0.2080	4.60	···
RX J0439.0+0715	1449	04:39:00.710	+07:16:07.65	6.3	I3	0.2300	6.50	···
	3583	···	···	19.2	I3	···	···	···
RX J0528.9-3927	4994	05:28:53.039	-39:28:15.53	22.5	I3	0.2632	7.89	···
RX J0647.7+7015	3196	06:47:50.029	+70:14:49.66	19.3	I3	0.5840	9.07	···
	3584	···	···	20.0	I3	···	···	···
RX J0819.6+6336	2199	08:19:26.007	+63:37:26.53	14.9	S3	0.1190	3.87	···
RX J1000.4+4409	9421	10:00:32.024	+44:08:39.69	18.5	I3	0.1540	3.42	···
RX J1022.1+3830	6942	10:22:10.034	+38:31:23.54	41.5	S3	0.0491	3.04	f
RX J1130.0+3637	6945	11:30:02.789	+36:38:08.26	49.4	S3	0.0600	2.00	···
RX J1320.2+3308	6941	13:20:14.650	+33:08:33.06	38.6	S3	0.0366	1.01	e
RX J1347.5-1145	3592	13:47:30.593	-11:45:10.05	57.7	I3	0.4510	10.88	···
	507	···	···	10.0	S3	···	···	···
RX J1423.8+2404	1657	14:23:47.759	+24:04:40.45	18.5	I3	0.5450	5.92	···
	4195	···	···	115.6	S3	···	···	···
RX J1504.1-0248	5793	15:04:07.415	-02:48:15.70	39.2	I3	0.2150	8.00	···
RX J1532.9+3021	1649	15:32:53.781	+30:20:58.72	9.4	I3	0.3450	5.44	···

Table B.1: Summary of Sample for Entropy Study (continued)

Cluster	Obs. ID	R.A. hr:min:sec	Decl. ° :′:″	Exposure Time ksec	ACIS	z	kT_X keV	Notes
(1)	(2)	(3)	(4)	(5)	(6)	(7)	(8)	(9)
	1665	···	···	10.0	S3	···	···	···
RX J1539.5-8335	8266	15:39:32.485	-83:35:23.83	8.0	I3	0.0728	4.29	···
RX J1720.1+2638	4361	17:20:09.941	+26:37:29.11	25.7	I3	0.1640	6.37	···
RX J1720.2+3536	3280	17:20:16.953	+35:36:23.63	20.8	I3	0.3913	5.65	···
	6107	···	···	33.9	I3	···	···	···
	7225	···	···	2.0	I3	···	···	···
RX J1852.1+5711	5749	18:52:08.815	+57:11:42.63	29.8	I3	0.1094	3.66	···
RX J2129.6+0005	552	21:29:39.944	+00:05:18.83	10.0	I3	0.2350	5.91	···
RXCJ0331.1-2100	10790	03:31:06.020	-21:00:32.93	10.0	I3	0.1880	4.61	···
	9415	···	···	9.9	I3	···	···	···
SC 1327-312	4165	13:29:47.748	-31:36:23.54	18.4	I3	0.0531	3.53	f
Sersic 159-03	1668	23:13:58.764	-42:43:34.70	9.9	S3	0.0580	2.65	···
SS2B153	3243	10:50:26.125	-12:50:41.76	29.5	S3	0.0186	0.80	···
UGC 3957	8265	07:40:58.335	+55:25:38.30	7.9	I3	0.0341	2.85	···
UGC 12491	7896	23:18:38.311	+42:57:29.06	32.7	S3	0.0174	0.87	···
ZWCL 1215	4184	12:17:41.708	+03:39:15.81	12.1	I3	0.0750	6.62	···
ZWCL 1358+6245	516	13:59:50.526	+62:31:04.57	54.1	S3	0.3280	10.66	···
ZWCL 1742	8267	17:44:14.515	+32:59:29.68	8.0	I3	0.0757	4.40	···
ZWCL 1953	1659	08:50:06.677	+36:04:16.16	24.9	I3	0.3800	7.37	···
ZWCL 3146	909	10:23:39.735	+04:11:08.05	46.0	I3	0.2900	7.48	···
ZWCL 7160	543	14:57:15.158	+22:20:33.85	9.9	I3	0.2578	4.53	···
Zwicky 2701	3195	09:52:49.183	+51:53:05.27	26.9	S3	0.2100	5.21	···
ZwCl 0857.9+2107	7897	09:00:36.835	+20:53:40.36	9.0	I3	0.2350	4.29	e

Table B.2: Summary of β-Model Fits

Cluster	S_{01} 10^{-6} cts s^{-1} arcsec^2	r_{c1} $''$	β_1	S_{02} 10^{-6} cts s^{-1} arcsec^2	r_{c2} $''$	β_2	D.O.F.	$\chi^2_{\rm red}$
(1)	(2)	(3)	(4)	(5)	(6)	(7)	(8)	(9)
Abell 119	4.93 ± 0.73	39.1 ± 15.3	0.34 ± 0.07	3.52 ± 0.96	735.2 ± 479.4	1.27 ± 1.27	52	1.76
Abell 160	2.32 ± 0.27	53.4 ± 11.1	0.57 ± 0.12	1.29 ± 0.22	284.0 ± 52.2	0.74 ± 0.10	90	1.18
Abell 193	24.72 ± 1.62	80.8 ± 2.2	0.43 ± 0.01	···	···	···	38	0.43
Abell 400	4.66 ± 0.09	151.3 ± 6.4	0.42 ± 0.01	···	···	···	96	0.57
Abell 1060	21.95 ± 0.44	93.5 ± 8.1	0.35 ± 0.01	···	···	···	42	1.44
Abell 1240	1.58 ± 0.07	247.9 ± 46.9	1.01 ± 0.22	···	···	···	58	1.58
Abell 1736	3.81 ± 0.56	55.6 ± 16.1	0.42 ± 0.12	2.49 ± 0.47	1470.0 ± 87.2	5.00 ± 0.73	35	1.58
Abell 2125	3.50 ± 0.20	26.0 ± 4.9	0.49 ± 0.05	1.02 ± 0.13	159.9 ± 9.2	1.32 ± 0.16	35	0.33
Abell 2255	8.38 ± 0.15	222.7 ± 9.8	0.62 ± 0.02	···	···	···	94	1.45
Abell 2256	21.69 ± 0.19	407.8 ± 17.9	0.99 ± 0.05	···	···	···	88	0.83
Abell 2319	47.39 ± 0.61	128.8 ± 3.1	0.49 ± 0.01	···	···	···	92	1.67
Abell 2462	8.19 ± 1.43	60.8 ± 9.6	0.64 ± 0.11	1.87 ± 0.25	762.7 ± 39.1	5.00 ± 0.87	67	1.54
Abell 2631	20.55 ± 1.01	66.0 ± 4.0	0.73 ± 0.03	···	···	···	58	1.15
Abell 3376	4.21 ± 0.09	125.5 ± 5.6	0.40 ± 0.01	···	···	···	98	1.42
Abell 3391	10.65 ± 0.31	132.3 ± 7.9	0.48 ± 0.01	···	···	···	84	1.86
Abell 3395	6.85 ± 0.67	90.9 ± 6.7	0.49 ± 0.03	···	···	···	38	0.96
MKW 8	7.71 ± 0.62	25.2 ± 2.5	0.32 ± 0.01	1.51 ± 0.08	1124.0 ± 64.1	5.00 ± 0.40	88	0.65
RBS 461	12.84 ± 0.34	102.2 ± 4.1	0.52 ± 0.01	···	···	···	84	1.56

Table B.3: M. Donahue's Hα Observations.

Cluster	Telescope	z	$[NII]$/Hα	Hα Flux
				10^{-15} erg s^{-1} cm^{-2}
Abell 85	PO	0.0558	2.67	0.581
Abell 119	LC	0.0442	···	<0.036
Abell 133	LC	0.0558	···	0.88
Abell 496	LC	0.0328	2.50	2.90
Abell 1644	LC	0.0471	···	1.00
Abell 1650	LC	0.0843	···	<0.029
Abell 1689	LC	0.1843	···	<0.029
Abell 1736	LC	0.0338	···	<0.026
Abell 2597	PO	0.0854	0.85	29.7
Abell 3112	LC	0.0720	2.22	2.66
Abell 3158	LC	0.0586	···	<0.036
Abell 3266	LC	0.0590	1.62	<0.027
Abell 4059	LC	0.0475	3.60	2.22
Cygnus A	PO	0.0561	1.85	28.4
EXO 0422-086	LC	0.0397	···	<0.031
Hydra A	LC	0.0522	0.85	13.4
PKS 0745-191	LC	0.1028	1.02	10.4

Table B.4: Statistics of Best-Fit Parameters

Sample	N_{obj}	K_0 keV cm^2	K_{12} keV cm^2	K_{100} keV cm^2	α	$N_{K_0=0}$ 1σ	2σ	3σ
(1)	(2)	(3)	(4)	(5)	(6)	(7)	(8)	(9)
All K_0								
ACCEPT	233	72.9 ± 33.7	91.6 ± 35.7	126 ± 45	1.21 ± 0.39	4 (2%)	12 (5%)	24 (11%)
HIFLUGCS	59	62.3 ± 32.7	87.2 ± 34.5	166 ± 65	1.18 ± 0.38	1 (2%)	3 (5%)	4 (7%)
CSE	37	61.9 ± 27.4	81.6 ± 31.3	132 ± 45	1.19 ± 0.39	1 (3%)	2 (5%)	6 (16%)
β Models	17	220 ± 74	230 ± 76.9	67.4 ± 27.0	1.45 ± 0.47	...	...	...
4keV cm^2 < K$_0$ $\leq$ 50keV cm^2								
ACCEPT	99	17.5 ± 5.8	31.2 ± 10.3	148 ± 49	1.21 ± 0.39	3 (3%)	5 (5%)	10 (10%)
HIFLUGCS	25	13.6 ± 4.6	29.4 ± 9.63	174 ± 57	1.15 ± 0.37	0 (0%)	0 (0%)	0 (0%)
CSE	17	16.4 ± 5.4	30.9 ± 10.2	146 ± 48	1.19 ± 0.38	0 (0%)	0 (0%)	2 (12%)
$K_0 \leq$ 50keV cm^2								
ACCEPT	107	16.1 ± 5.7	30.5 ± 10.0	150 ± 50	1.20 ± 0.38	4 (4%)	6 (6%)	11 (10%)
HIFLUGCS	29	11.4 ± 4.2	31.2 ± 10.5	235 ± 89	1.17 ± 0.37	1 (4%)	1 (4%)	1 (4%)
CSE	19	15.6 ± 5.2	30.9 ± 10.2	146 ± 48	1.16 ± 0.38	1 (5%)	1 (5%)	3 (16%)
$K_0 >$ 50keV cm^2								
ACCEPT	126	156 ± 54	175 ± 59	107 ± 39	1.23 ± 0.40	0 (0%)	6 (5%)	13 (11%)
HIFLUGCS	30	151 ± 53	172 ± 58	113 ± 43	1.19 ± 0.39	0 (0%)	2 (7%)	3 (10%)
CSE	18	148 ± 49	165 ± 54	118 ± 42	1.23 ± 0.40	0 (0%)	1 (6%)	3 (17%)

Table B.5: Summary of Entropy Profile Fits

Cluster	Method	N_{bins}	r_{max} Mpc	K_0 keV cm^2	$\sigma_{K_0} > 0$	K_{100} keV cm^2	α	DOF	χ^2	p-value
(1)	(2)	(3)	(4)	(5)	(6)	(7)	(8)	(9)	(10)	(11)
1E0657 56	extr	48	1.00	299.4 ± 19.6	15.3	20.5 ± 7.0	1.84 ± 0.16	45	42.09	5.96e-01
	-	-	-	0.0	-	277.9 ± 14.5	0.60 ± 0.04	46	146.18	2.31e-12
	flat	-	-	307.5 ± 19.3	15.9	18.6 ± 6.5	1.88 ± 0.17	45	42.87	5.63e-01
	-	-	-	0.0	-	283.6 ± 14.6	0.58 ± 0.04	46	157.03	4.77e-14
2A 335+096	extr	37	0.12	5.3 ± 0.2	34.8	137.7 ± 1.9	1.43 ± 0.02	34	173.51	1.26e-20
	-	-	-	0.0	-	117.7 ± 1.5	1.06 ± 0.01	35	1188.38	6.24e-227
	flat	-	-	7.1 ± 0.1	49.3	138.6 ± 1.9	1.52 ± 0.02	34	209.16	4.39e-27
	-	-	-	0.0	-	107.4 ± 1.4	0.97 ± 0.01	35	2097.26	0.00e+00
2PIGG J0011.5-2850	extr	27	0.20	75.3 ± 44.8	1.7	236.9 ± 53.2	0.82 ± 0.27	24	2.01	1.00e+00
	-	-	-	0.0	-	318.5 ± 13.6	0.53 ± 0.06	25	3.19	1.00e+00
	flat	-	-	102.0 ± 42.9	2.4	214.7 ± 51.5	0.84 ± 0.29	24	2.79	1.00e+00
	-	-	-	0.0	-	323.8 ± 13.7	0.45 ± 0.05	25	4.40	1.00e+00
2PIGG J2227.0-3041	extr	23	0.15	12.5 ± 1.0	12.3	119.5 ± 3.6	1.32 ± 0.06	20	13.14	8.71e-01
	-	-	-	0.0	-	118.4 ± 3.3	0.88 ± 0.02	21	132.53	3.43e-18
	flat	-	-	17.1 ± 1.0	17.4	113.9 ± 3.6	1.37 ± 0.06	20	11.50	9.32e-01
	-	-	-	0.0	-	108.6 ± 3.1	0.73 ± 0.02	21	202.76	1.04e-31
3C 28.0	extr	12	0.18	20.7 ± 1.3	15.5	111.7 ± 3.9	1.70 ± 0.09	9	23.42	5.32e-03
	-	-	-	0.0	-	115.3 ± 3.4	0.82 ± 0.03	10	151.06	2.25e-27
	flat	-	-	23.9 ± 1.3	18.6	107.8 ± 3.9	1.79 ± 0.09	9	22.93	6.35e-03
	-	-	-	0.0	-	110.8 ± 3.3	0.74 ± 0.03	10	179.58	2.86e-33
3C 295	extr	17	0.50	12.6 ± 2.6	4.9	84.5 ± 6.4	1.45 ± 0.07	14	7.52	9.13e-01
	-	-	-	0.0	-	108.2 ± 3.8	1.20 ± 0.04	15	27.39	2.57e-02
	flat	-	-	14.5 ± 2.5	5.8	81.9 ± 6.3	1.47 ± 0.07	14	8.36	8.70e-01
	-	-	-	0.0	-	109.3 ± 3.8	1.18 ± 0.04	15	34.84	2.59e-03
3C 388	extr	24	0.20	17.0 ± 5.7	3.0	214.2 ± 8.5	0.76 ± 0.07	21	10.82	9.66e-01
	-	-	-	0.0	-	226.3 ± 7.0	0.60 ± 0.02	22	16.13	8.09e-01
	flat	-	-	17.0 ± 5.8	3.0	214.3 ± 8.5	0.76 ± 0.07	21	10.90	9.65e-01

Table B.5: Summary of Entropy Profile Fits (continued)

Cluster	Method	N_{bins}	r_{max} Mpc	K_0 keV cm^2	$\sigma_{K_0} > 0$	K_{100} keV cm^2	α	DOF	χ^2	p-value
(1)	(2)	(3)	(4)	(5)	(6)	(7)	(8)	(9)	(10)	(11)
	-	-	-	0.0	-	226.4 ± 7.0	0.60 ± 0.02	22	16.14	8.09e-01
4C 55.16	extr	21	0.40	22.4 ± 2.9	7.7	162.9 ± 7.7	1.28 ± 0.06	18	7.52	9.85e-01
	-	-	-	0.0	-	197.1 ± 5.6	0.94 ± 0.03	19	46.97	3.61e-04
	flat	-	-	23.3 ± 2.9	8.1	161.6 ± 7.7	1.29 ± 0.06	18	7.92	9.80e-01
	-	-	-	0.0	-	197.0 ± 5.6	0.93 ± 0.03	19	50.60	1.07e-04
Abell 13	extr	35	0.30	182.6 ± 26.2	7.0	182.0 ± 36.8	1.37 ± 0.22	32	11.58	1.00e+00
	-	-	-	0.0	-	401.9 ± 14.1	0.59 ± 0.05	33	32.03	5.15e-01
	flat	-	-	182.6 ± 26.2	7.0	182.0 ± 36.8	1.37 ± 0.22	32	11.58	1.00e+00
	-	-	-	0.0	-	401.9 ± 14.1	0.59 ± 0.05	33	32.03	5.15e-01
Abell 68	extr	31	0.60	217.3 ± 89.0	2.4	142.3 ± 98.3	0.89 ± 0.39	28	1.72	1.00e+00
	-	-	-	0.0	-	393.4 ± 36.9	0.40 ± 0.08	29	3.45	1.00e+00
	flat	-	-	217.3 ± 89.0	2.4	142.3 ± 98.3	0.89 ± 0.39	28	1.72	1.00e+00
	-	-	-	0.0	-	393.4 ± 36.9	0.40 ± 0.08	29	3.45	1.00e+00
Abell 85	extr	39	0.20	7.3 ± 0.6	12.8	165.5 ± 1.9	1.05 ± 0.02	36	52.57	3.67e-02
	-	-	-	0.0	-	170.2 ± 1.8	0.90 ± 0.01	37	201.42	1.67e-24
	flat	-	-	12.5 ± 0.5	23.7	158.8 ± 1.9	1.12 ± 0.02	36	59.03	9.10e-03
	-	-	-	0.0	-	165.5 ± 1.8	0.83 ± 0.01	37	492.25	6.48e-81
Abell 119	extr	23	0.20	210.1 ± 84.5	2.5	207.1 ± 100.1	0.77 ± 0.56	20	0.12	1.00e+00
	-	-	-	0.0	-	418.7 ± 31.2	0.26 ± 0.07	21	1.34	1.00e+00
	flat	-	-	233.9 ± 87.7	2.7	191.3 ± 102.8	0.75 ± 0.61	20	0.10	1.00e+00
	-	-	-	0.0	-	425.5 ± 31.1	0.22 ± 0.06	21	1.19	1.00e+00
Abell 133	extr	20	0.10	13.3 ± 0.5	25.1	170.7 ± 3.9	1.47 ± 0.04	17	44.38	3.01e-04
	-	-	-	0.0	-	142.2 ± 2.7	0.90 ± 0.01	18	504.69	1.08e-95
	flat	-	-	17.3 ± 0.5	35.0	170.1 ± 4.1	1.59 ± 0.04	17	54.26	9.02e-06
	-	-	-	0.0	-	127.5 ± 2.5	0.79 ± 0.01	18	812.02	8.79e-161
Abell 141	extr	33	0.60	144.1 ± 31.3	4.6	68.5 ± 27.5	1.53 ± 0.27	30	136.92	1.32e-15
	-	-	-	0.0	-	221.9 ± 18.4	0.77 ± 0.09	31	447.75	2.25e-75

Table B.5: Summary of Entropy Profile Fits (continued)

Cluster	Method	N_{bins}	r_{max} Mpc	K_0 keV cm^2	$\sigma_{K_0} > 0$	K_{100} keV cm^2	α	DOF	χ^2	p-value
(1)	(2)	(3)	(4)	(5)	(6)	(7)	(8)	(9)	(10)	(11)
	flat	-	-	205.0 ± 27.4	7.5	42.6 ± 20.8	1.78 ± 0.33	30	175.31	1.84e-22
	-	-	-	0.0	-	269.7 ± 17.7	0.57 ± 0.07	31	704.66	2.56e-128
Abell 160	extr	28	0.12	155.8 ± 27.7	5.6	116.3 ± 29.2	0.98 ± 0.57	25	0.33	1.00e+00
	-	-	-	0.0	-	254.7 ± 13.5	0.20 ± 0.04	26	3.66	1.00e+00
	flat	-	-	155.8 ± 27.7	5.6	116.3 ± 29.2	0.98 ± 0.57	25	0.33	1.00e+00
	-	-	-	0.0	-	254.7 ± 13.5	0.20 ± 0.04	26	3.66	1.00e+00
Abell 193	extr	26	0.12	185.5 ± 13.3	13.9	36.0 ± 16.8	2.23 ± 1.89	23	0.02	1.00e+00
	-	-	-	0.0	-	213.8 ± 7.3	0.09 ± 0.04	24	2.92	1.00e+00
	flat	-	-	185.5 ± 13.3	13.9	36.0 ± 16.8	2.23 ± 1.89	23	0.02	1.00e+00
	-	-	-	0.0	-	213.8 ± 7.3	0.09 ± 0.04	24	2.92	1.00e+00
Abell 209	extr	19	0.30	100.7 ± 26.3	3.8	150.5 ± 34.5	0.81 ± 0.21	16	2.48	1.00e+00
	-	-	-	0.0	-	266.2 ± 9.6	0.40 ± 0.04	17	7.88	9.69e-01
	flat	-	-	105.5 ± 26.9	3.9	149.3 ± 35.2	0.80 ± 0.21	16	2.73	1.00e+00
	-	-	-	0.0	-	269.5 ± 9.6	0.38 ± 0.04	17	8.03	9.66e-01
Abell 222	extr	37	0.60	122.2 ± 15.2	8.0	84.8 ± 19.2	0.99 ± 0.15	34	4.82	1.00e+00
	-	-	-	0.0	-	231.9 ± 7.3	0.40 ± 0.03	35	26.22	8.58e-01
	flat	-	-	126.0 ± 15.0	8.4	82.2 ± 19.0	1.00 ± 0.15	34	4.94	1.00e+00
	-	-	-	0.0	-	233.9 ± 7.3	0.39 ± 0.03	35	27.16	8.26e-01
Abell 223	extr	30	0.50	183.9 ± 46.1	4.0	160.7 ± 59.2	1.24 ± 0.31	27	1.35	1.00e+00
	-	-	-	0.0	-	386.1 ± 23.5	0.57 ± 0.08	28	6.55	1.00e+00
	flat	-	-	183.9 ± 46.1	4.0	160.7 ± 59.2	1.24 ± 0.31	27	1.35	1.00e+00
	-	-	-	0.0	-	386.1 ± 23.5	0.57 ± 0.08	28	6.55	1.00e+00
Abell 262	extr	30	0.05	9.4 ± 0.8	11.8	200.9 ± 7.3	0.95 ± 0.04	27	52.37	2.40e-03
	-	-	-	0.0	-	166.6 ± 3.3	0.66 ± 0.01	28	159.48	2.36e-20
	flat	-	-	10.6 ± 0.8	13.8	205.1 ± 7.9	0.98 ± 0.04	27	60.17	2.50e-04
	-	-	-	0.0	-	164.3 ± 3.3	0.65 ± 0.01	28	199.73	7.70e-28
Abell 267	extr	22	0.40	168.3 ± 17.7	9.5	52.0 ± 21.1	1.82 ± 0.38	19	0.62	1.00e+00

Table B.5: Summary of Entropy Profile Fits (continued)

Cluster	Method	N_{bins}	r_{max} Mpc	K_0 keV cm^2	$\sigma_{K_0} > 0$	K_{100} keV cm^2	α	DOF	χ^2	p-value
(1)	(2)	(3)	(4)	(5)	(6)	(7)	(8)	(9)	(10)	(11)
	-	-	-	0.0	-	263.4 ± 11.7	0.41 ± 0.06	20	22.64	3.07e-01
	flat	-	-	168.6 ± 17.6	9.6	51.8 ± 21.0	1.82 ± 0.38	19	0.62	1.00e+00
	-	-	-	0.0	-	263.5 ± 11.7	0.40 ± 0.06	20	22.71	3.03e-01
Abell 368	extr	28	0.50	47.5 ± 8.3	5.7	146.7 ± 15.4	1.20 ± 0.11	25	6.13	1.00e+00
	-	-	-	0.0	-	216.8 ± 8.0	0.77 ± 0.04	26	24.09	5.71e-01
	flat	-	-	50.9 ± 8.2	6.2	144.1 ± 15.4	1.21 ± 0.11	25	6.18	1.00e+00
	-	-	-	0.0	-	218.7 ± 8.0	0.74 ± 0.04	26	26.03	4.61e-01
Abell 370	extr	20	0.50	321.9 ± 90.8	3.5	78.7 ± 89.3	1.24 ± 0.68	17	2.41	1.00e+00
	-	-	-	0.0	-	422.4 ± 34.9	0.40 ± 0.08	18	6.02	9.96e-01
	flat	-	-	321.9 ± 90.8	3.5	78.7 ± 89.3	1.24 ± 0.68	17	2.41	1.00e+00
	-	-	-	0.0	-	422.4 ± 34.9	0.40 ± 0.08	18	6.02	9.96e-01
Abell 383	extr	13	0.20	10.9 ± 1.6	6.6	114.0 ± 5.2	1.34 ± 0.09	10	4.76	9.07e-01
	-	-	-	0.0	-	121.4 ± 4.9	0.96 ± 0.04	11	40.90	2.50e-05
	flat	-	-	13.0 ± 1.6	8.3	110.9 ± 5.2	1.40 ± 0.09	10	6.30	7.89e-01
	-	-	-	0.0	-	119.2 ± 4.9	0.92 ± 0.03	11	58.48	1.78e-08
Abell 399	extr	31	0.20	140.3 ± 19.1	7.3	215.3 ± 22.7	0.73 ± 0.12	28	4.14	1.00e+00
	-	-	-	0.0	-	360.8 ± 7.0	0.32 ± 0.02	29	21.40	8.44e-01
	flat	-	-	153.2 ± 18.8	8.2	204.3 ± 22.4	0.74 ± 0.12	28	4.19	1.00e+00
	-	-	-	0.0	-	362.5 ± 7.0	0.30 ± 0.02	29	22.24	8.10e-01
Abell 400	extr	73	0.18	162.8 ± 3.9	41.6	35.3 ± 5.7	1.76 ± 0.28	70	0.71	1.00e+00
	-	-	-	0.0	-	205.9 ± 2.1	0.17 ± 0.01	71	57.23	8.82e-01
	flat	-	-	162.8 ± 3.9	41.6	35.3 ± 5.7	1.76 ± 0.28	70	0.71	1.00e+00
	-	-	-	0.0	-	205.9 ± 2.1	0.17 ± 0.01	71	57.23	8.82e-01
Abell 401	extr	60	0.40	162.5 ± 7.9	20.7	86.0 ± 10.7	1.37 ± 0.11	57	8.70	1.00e+00
	-	-	-	0.0	-	290.7 ± 4.7	0.43 ± 0.02	58	134.73	4.81e-08
	flat	-	-	166.9 ± 7.7	21.7	81.8 ± 10.4	1.40 ± 0.11	57	8.36	1.00e+00
	-	-	-	0.0	-	292.0 ± 4.7	0.42 ± 0.02	58	142.56	4.50e-09

Table B.5: Summary of Entropy Profile Fits (continued)

Cluster	Method	N_{bins}	r_{max} Mpc	K_0 keV cm^2	$\sigma_{K_0} > 0$	K_{100} keV cm^2	α	DOF	χ^2	p-value
(1)	(2)	(3)	(4)	(5)	(6)	(7)	(8)	(9)	(10)	(11)
Abell 426	extr	56	0.10	19.4 ± 0.2	124.3	119.9 ± 0.5	1.74 ± 0.01	53	1040.29	3.10e-183
	-	-	-	0.0	-	112.3 ± 0.3	0.92 ± 0.00	54	6430.00	0.00e+00
	flat	-	-	19.4 ± 0.2	124.4	119.9 ± 0.5	1.74 ± 0.01	53	1045.73	2.32e-184
	-	-	-	0.0	-	112.3 ± 0.3	0.92 ± 0.00	54	6447.72	0.00e+00
Abell 478	extr	49	0.40	6.9 ± 0.9	7.5	123.4 ± 2.6	0.96 ± 0.02	46	20.38	1.00e+00
	-	-	-	0.0	-	136.7 ± 1.7	0.84 ± 0.01	47	66.62	3.13e-02
	flat	-	-	7.8 ± 0.9	8.5	122.0 ± 2.6	0.97 ± 0.02	46	22.58	9.99e-01
	-	-	-	0.0	-	137.0 ± 1.7	0.84 ± 0.01	47	81.79	1.25e-03
Abell 496	extr	26	0.08	4.3 ± 0.8	5.7	206.1 ± 9.2	1.13 ± 0.04	23	7.05	9.99e-01
	-	-	-	0.0	-	182.9 ± 6.6	0.94 ± 0.02	24	36.09	5.38e-02
	flat	-	-	8.9 ± 0.7	13.4	216.3 ± 10.5	1.27 ± 0.05	23	6.95	1.00e+00
	-	-	-	0.0	-	161.2 ± 5.8	0.83 ± 0.02	24	132.18	6.24e-17
Abell 520	extr	33	0.55	325.5 ± 29.2	11.1	10.2 ± 11.8	2.09 ± 0.71	30	2.86	1.00e+00
	-	-	-	0.0	-	328.7 ± 18.7	0.29 ± 0.05	31	14.09	9.96e-01
	flat	-	-	325.5 ± 29.2	11.1	10.2 ± 11.8	2.09 ± 0.71	30	2.86	1.00e+00
	-	-	-	0.0	-	328.7 ± 18.7	0.29 ± 0.05	31	14.09	9.96e-01
Abell 521	extr	8	0.15	201.6 ± 36.1	5.6	235.7 ± 61.8	1.92 ± 0.72	5	0.23	9.99e-01
	-	-	-	0.0	-	420.3 ± 37.9	0.44 ± 0.10	6	9.70	1.38e-01
	flat	-	-	259.9 ± 36.2	7.2	245.4 ± 61.8	1.91 ± 0.69	5	0.32	9.97e-01
	-	-	-	0.0	-	481.0 ± 37.3	0.35 ± 0.08	6	11.51	7.39e-02
Abell 539	extr	11	0.03	19.6 ± 4.0	4.9	552.4 ± 198.3	1.14 ± 0.21	8	1.80	9.86e-01
	-	-	-	0.0	-	241.9 ± 31.9	0.58 ± 0.05	9	10.03	3.48e-01
	flat	-	-	22.6 ± 4.5	5.0	493.3 ± 165.6	1.05 ± 0.20	8	2.12	9.77e-01
	-	-	-	0.0	-	234.5 ± 27.5	0.53 ± 0.04	9	10.08	3.44e-01
Abell 562	extr	27	0.27	202.1 ± 39.3	5.1	34.6 ± 45.3	1.09 ± 1.19	24	1.66	1.00e+00
	-	-	-	0.0	-	244.4 ± 9.7	0.13 ± 0.06	25	2.41	1.00e+00
	flat	-	-	202.1 ± 39.3	5.1	34.6 ± 45.3	1.09 ± 1.19	24	1.66	1.00e+00

Table B.5: Summary of Entropy Profile Fits (continued)

Cluster	Method	N_{bins}	r_{max} Mpc	K_0 keV cm^2	$\sigma_{K_0} > 0$	K_{100} keV cm^2	α	DOF	χ^2	p-value
(1)	(2)	(3)	(4)	(5)	(6)	(7)	(8)	(9)	(10)	(11)
	-	-	-	0.0	-	244.4 ± 9.7	0.13 ± 0.06	25	2.41	1.00e+00
Abell 576	extr	21	0.08	78.4 ± 18.7	4.2	230.6 ± 26.6	1.19 ± 0.34	18	3.81	1.00e+00
	-	-	-	0.0	-	259.8 ± 16.1	0.51 ± 0.06	19	10.60	9.37e-01
	flat	-	-	95.3 ± 15.4	6.2	221.2 ± 31.5	1.41 ± 0.41	18	4.71	9.99e-01
	-	-	-	0.0	-	247.8 ± 15.2	0.45 ± 0.06	19	15.49	6.91e-01
Abell 586	extr	17	0.25	94.7 ± 19.2	4.9	92.1 ± 25.5	1.25 ± 0.32	14	3.47	9.98e-01
	-	-	-	0.0	-	201.4 ± 7.2	0.53 ± 0.06	15	10.34	7.98e-01
	flat	-	-	94.7 ± 19.2	4.9	92.1 ± 25.5	1.25 ± 0.32	14	3.47	9.98e-01
	-	-	-	0.0	-	201.4 ± 7.2	0.53 ± 0.06	15	10.34	7.98e-01
Abell 611	extr	19	0.40	124.9 ± 18.6	6.7	164.4 ± 31.5	1.25 ± 0.20	16	1.98	1.00e+00
	-	-	-	0.0	-	326.7 ± 15.2	0.53 ± 0.05	17	14.90	6.02e-01
	flat	-	-	124.9 ± 18.6	6.7	164.4 ± 31.5	1.25 ± 0.20	16	1.98	1.00e+00
	-	-	-	0.0	-	326.7 ± 15.2	0.53 ± 0.05	17	14.90	6.02e-01
Abell 644	extr	53	0.35	132.4 ± 9.1	14.5	85.9 ± 11.7	1.55 ± 0.13	50	15.09	1.00e+00
	-	-	-	0.0	-	244.8 ± 4.3	0.68 ± 0.03	51	90.43	5.59e-04
	flat	-	-	132.4 ± 9.1	14.5	85.9 ± 11.7	1.55 ± 0.13	50	15.09	1.00e+00
	-	-	-	0.0	-	244.8 ± 4.3	0.68 ± 0.03	51	90.43	5.59e-04
Abell 665	extr	46	0.70	134.6 ± 23.5	5.7	106.3 ± 25.1	1.06 ± 0.13	43	3.79	1.00e+00
	-	-	-	0.0	-	254.8 ± 10.1	0.61 ± 0.04	44	19.71	9.99e-01
	flat	-	-	134.6 ± 23.5	5.7	106.3 ± 25.1	1.06 ± 0.13	43	3.79	1.00e+00
	-	-	-	0.0	-	254.8 ± 10.1	0.61 ± 0.04	44	19.71	9.99e-01
Abell 697	extr	30	0.60	161.0 ± 24.7	6.5	111.1 ± 29.5	1.09 ± 0.18	27	4.01	1.00e+00
	-	-	-	0.0	-	310.0 ± 13.4	0.46 ± 0.04	28	19.49	8.82e-01
	flat	-	-	166.7 ± 24.4	6.8	108.2 ± 29.1	1.10 ± 0.18	27	4.28	1.00e+00
	-	-	-	0.0	-	313.9 ± 13.3	0.45 ± 0.04	28	20.28	8.54e-01
Abell 744	extr	18	0.12	60.3 ± 9.4	6.4	227.9 ± 15.4	0.83 ± 0.13	15	1.20	1.00e+00
	-	-	-	0.0	-	251.0 ± 11.7	0.41 ± 0.03	16	13.36	6.46e-01

Table B.5: Summary of Entropy Profile Fits (continued)

Cluster	Method	N_{bins}	r_{max} Mpc	K_0 keV cm^2	$\sigma_{K_0} > 0$	K_{100} keV cm^2	α	DOF	χ^2	p-value
(1)	(2)	(3)	(4)	(5)	(6)	(7)	(8)	(9)	(10)	(11)
	flat	-	-	63.4 ± 10.2	6.2	229.3 ± 15.2	0.79 ± 0.13	15	1.27	1.00e+00
	-	-	-	0.0	-	256.9 ± 11.5	0.39 ± 0.02	16	12.56	7.05e-01
Abell 754	extr	58	0.30	270.4 ± 23.8	11.4	69.7 ± 26.5	1.48 ± 0.34	55	13.35	1.00e+00
	-	-	-	0.0	-	366.4 ± 8.1	0.34 ± 0.03	56	35.36	9.86e-01
	flat	-	-	270.4 ± 23.8	11.4	69.7 ± 26.5	1.48 ± 0.34	55	13.35	1.00e+00
	-	-	-	0.0	-	366.4 ± 8.1	0.34 ± 0.03	56	35.36	9.86e-01
Abell 773	extr	35	0.60	244.3 ± 31.7	7.7	41.1 ± 22.5	1.60 ± 0.33	32	3.28	1.00e+00
	-	-	-	0.0	-	283.2 ± 16.6	0.54 ± 0.06	33	19.39	9.71e-01
	flat	-	-	244.3 ± 31.7	7.7	41.1 ± 22.5	1.60 ± 0.33	32	3.28	1.00e+00
	-	-	-	0.0	-	283.2 ± 16.6	0.54 ± 0.06	33	19.39	9.71e-01
Abell 907	extr	31	0.40	20.4 ± 3.3	6.1	191.5 ± 8.1	1.02 ± 0.05	28	7.33	1.00e+00
	-	-	-	0.0	-	223.9 ± 5.4	0.81 ± 0.02	29	32.96	2.79e-01
	flat	-	-	23.4 ± 3.2	7.3	187.0 ± 8.1	1.05 ± 0.05	28	7.62	1.00e+00
	-	-	-	0.0	-	224.1 ± 5.4	0.79 ± 0.02	29	41.74	5.92e-02
Abell 963	extr	24	0.40	22.0 ± 15.7	1.4	205.5 ± 22.9	0.79 ± 0.09	21	2.75	1.00e+00
	-	-	-	0.0	-	234.8 ± 7.8	0.68 ± 0.04	22	4.30	1.00e+00
	flat	-	-	55.8 ± 12.9	4.3	169.1 ± 20.3	0.90 ± 0.10	21	3.37	1.00e+00
	-	-	-	0.0	-	244.6 ± 7.6	0.61 ± 0.03	22	13.86	9.06e-01
Abell 1060	extr	25	0.03	58.1 ± 8.8	6.6	138.8 ± 40.0	0.80 ± 0.30	22	1.55	1.00e+00
	-	-	-	0.0	-	134.9 ± 7.7	0.21 ± 0.03	23	7.68	9.99e-01
	flat	-	-	72.0 ± 5.2	13.8	178.3 ± 100.9	1.25 ± 0.49	22	2.61	1.00e+00
	-	-	-	0.0	-	121.7 ± 6.6	0.15 ± 0.02	23	13.85	9.31e-01
Abell 1063S	extr	24	0.60	169.6 ± 19.7	8.6	42.2 ± 17.7	1.72 ± 0.27	21	2.98	1.00e+00
	-	-	-	0.0	-	235.3 ± 13.3	0.63 ± 0.06	22	34.40	4.47e-02
	flat	-	-	169.6 ± 19.7	8.6	42.2 ± 17.7	1.72 ± 0.27	21	2.98	1.00e+00
	-	-	-	0.0	-	235.3 ± 13.3	0.63 ± 0.06	22	34.40	4.47e-02
Abell 1068	extr	17	0.20	9.0 ± 1.0	8.7	108.9 ± 3.2	1.31 ± 0.06	14	3.45	9.98e-01

Table B.5: Summary of Entropy Profile Fits (continued)

Cluster	Method	N_{bins}	r_{max} Mpc	K_0 keV cm^2	$\sigma_{K_0} > 0$	K_{100} keV cm^2	α	DOF	χ^2	p-value
(1)	(2)	(3)	(4)	(5)	(6)	(7)	(8)	(9)	(10)	(11)
	-	-	-	0.0	-	116.5 ± 3.0	0.96 ± 0.03	15	53.28	3.46e-06
	flat	-	-	9.1 ± 1.0	8.8	108.8 ± 3.2	1.31 ± 0.06	14	3.44	9.98e-01
	-	-	-	0.0	-	116.5 ± 3.0	0.96 ± 0.03	15	54.19	2.44e-06
Abell 1201	extr	14	0.20	39.2 ± 14.0	2.8	200.4 ± 23.8	1.20 ± 0.21	11	1.60	1.00e+00
	-	-	-	0.0	-	245.2 ± 15.1	0.81 ± 0.08	12	6.57	8.85e-01
	flat	-	-	64.8 ± 16.9	3.8	198.9 ± 25.2	1.03 ± 0.21	11	2.19	9.98e-01
	-	-	-	0.0	-	262.1 ± 15.3	0.56 ± 0.05	12	8.39	7.54e-01
Abell 1204	extr	11	0.15	14.1 ± 1.5	9.5	83.1 ± 3.6	1.35 ± 0.11	8	1.62	9.91e-01
	-	-	-	0.0	-	87.9 ± 3.2	0.75 ± 0.03	9	54.35	1.62e-08
	flat	-	-	15.3 ± 1.4	10.8	81.8 ± 3.6	1.40 ± 0.11	8	1.91	9.84e-01
	-	-	-	0.0	-	86.7 ± 3.2	0.73 ± 0.03	9	65.62	1.09e-10
Abell 1240	extr	37	0.50	429.4 ± 46.9	9.1	16.9 ± 28.8	1.96 ± 1.14	34	0.06	1.00e+00
	-	-	-	0.0	-	482.7 ± 27.4	0.17 ± 0.06	35	4.78	1.00e+00
	flat	-	-	462.4 ± 41.7	11.1	8.3 ± 18.2	2.37 ± 1.48	34	0.03	1.00e+00
	-	-	-	0.0	-	504.2 ± 26.9	0.13 ± 0.05	35	4.76	1.00e+00
Abell 1361	extr	14	0.15	14.8 ± 4.3	3.4	119.2 ± 10.7	1.15 ± 0.19	11	3.47	9.83e-01
	-	-	-	0.0	-	121.7 ± 9.4	0.74 ± 0.06	12	12.04	4.43e-01
	flat	-	-	18.6 ± 4.9	3.8	117.9 ± 10.5	1.06 ± 0.18	11	4.08	9.68e-01
	-	-	-	0.0	-	122.2 ± 8.9	0.63 ± 0.05	12	13.17	3.57e-01
Abell 1413	extr	10	0.12	29.8 ± 13.9	2.1	158.2 ± 14.7	0.82 ± 0.20	7	5.97	5.43e-01
	-	-	-	0.0	-	179.6 ± 10.0	0.54 ± 0.05	8	11.45	1.77e-01
	flat	-	-	64.0 ± 8.3	7.7	123.2 ± 13.0	1.19 ± 0.28	7	6.18	5.19e-01
	-	-	-	0.0	-	164.1 ± 9.2	0.38 ± 0.04	8	25.44	1.31e-03
Abell 1423	extr	23	0.40	58.8 ± 12.6	4.7	124.8 ± 20.9	1.22 ± 0.17	20	1.75	1.00e+00
	-	-	-	0.0	-	205.5 ± 9.7	0.73 ± 0.06	21	15.66	7.88e-01
	flat	-	-	68.3 ± 12.9	5.3	124.2 ± 21.1	1.20 ± 0.17	20	1.67	1.00e+00
	-	-	-	0.0	-	215.6 ± 9.7	0.65 ± 0.05	21	17.39	6.87e-01

Table B.5: Summary of Entropy Profile Fits (continued)

Cluster	Method	N_{bins}	r_{max} Mpc	K_0 keV cm^2	$\sigma_{K_0} > 0$	K_{100} keV cm^2	α	DOF	χ^2	p-value
(1)	(2)	(3)	(4)	(5)	(6)	(7)	(8)	(9)	(10)	(11)
Abell 1446	extr	34	0.32	152.4 ± 43.8	3.5	119.5 ± 49.5	0.67 ± 0.27	31	6.87	1.00e+00
	-	-	-	0.0	-	282.4 ± 8.4	0.26 ± 0.04	32	9.71	1.00e+00
	flat	-	-	152.4 ± 43.8	3.5	119.5 ± 49.5	0.67 ± 0.27	31	6.87	1.00e+00
	-	-	-	0.0	-	282.4 ± 8.4	0.26 ± 0.04	32	9.71	1.00e+00
Abell 1569	extr	29	0.20	110.1 ± 27.8	4.0	149.1 ± 28.9	0.51 ± 0.19	26	7.39	1.00e+00
	-	-	-	0.0	-	253.7 ± 9.5	0.20 ± 0.02	27	9.59	9.99e-01
	flat	-	-	110.1 ± 27.8	4.0	149.1 ± 28.9	0.51 ± 0.19	26	7.39	1.00e+00
	-	-	-	0.0	-	253.7 ± 9.5	0.20 ± 0.02	27	9.59	9.99e-01
Abell 1576	extr	33	0.70	174.1 ± 49.7	3.5	102.3 ± 48.5	1.36 ± 0.29	30	41.88	7.32e-02
	-	-	-	0.0	-	286.9 ± 27.0	0.77 ± 0.09	31	250.93	2.94e-36
	flat	-	-	186.2 ± 49.1	3.8	98.3 ± 47.6	1.38 ± 0.29	30	41.62	7.71e-02
	-	-	-	0.0	-	297.3 ± 26.9	0.74 ± 0.09	31	272.38	2.10e-40
Abell 1644	extr	11	0.05	10.7 ± 1.3	8.2	511.4 ± 61.2	1.54 ± 0.10	8	0.50	1.00e+00
	-	-	-	0.0	-	293.9 ± 22.4	1.02 ± 0.04	9	43.93	1.45e-06
	flat	-	-	19.0 ± 1.2	16.4	585.7 ± 81.8	1.76 ± 0.11	8	1.25	9.96e-01
	-	-	-	0.0	-	177.6 ± 12.5	0.71 ± 0.03	9	108.10	3.58e-19
Abell 1650	extr	15	0.12	32.7 ± 10.8	3.0	164.9 ± 12.3	0.80 ± 0.16	12	1.85	1.00e+00
	-	-	-	0.0	-	185.9 ± 9.1	0.49 ± 0.04	13	6.09	9.43e-01
	flat	-	-	38.0 ± 10.0	3.8	159.9 ± 12.1	0.84 ± 0.17	12	2.00	9.99e-01
	-	-	-	0.0	-	183.7 ± 9.0	0.47 ± 0.04	13	7.85	8.53e-01
Abell 1651	extr	27	0.20	87.7 ± 11.2	7.8	117.3 ± 15.3	0.96 ± 0.18	24	13.05	9.65e-01
	-	-	-	0.0	-	207.6 ± 6.7	0.34 ± 0.03	25	28.85	2.70e-01
	flat	-	-	89.5 ± 11.1	8.1	115.5 ± 15.2	0.97 ± 0.19	24	13.26	9.62e-01
	-	-	-	0.0	-	207.6 ± 6.7	0.34 ± 0.03	25	29.42	2.47e-01
Abell 1664	extr	13	0.15	10.0 ± 1.1	9.1	142.7 ± 5.9	1.50 ± 0.08	10	27.58	2.11e-03
	-	-	-	0.0	-	127.9 ± 4.9	0.97 ± 0.03	11	82.78	4.27e-13
	flat	-	-	14.4 ± 1.0	14.8	141.8 ± 6.1	1.70 ± 0.09	10	16.24	9.31e-02

Table B.5: Summary of Entropy Profile Fits (continued)

Cluster	Method	N_{bins}	r_{max} Mpc	K_0 keV cm^2	$\sigma_{K_0} > 0$	K_{100} keV cm^2	α	DOF	χ^2	p-value
(1)	(2)	(3)	(4)	(5)	(6)	(7)	(8)	(9)	(10)	(11)
	-	-	-	0.0	-	117.2 ± 4.6	0.85 ± 0.03	11	127.13	6.63e-22
Abell 1689	extr	20	0.30	78.4 ± 7.6	10.4	111.8 ± 13.8	1.35 ± 0.14	17	7.34	9.79e-01
	-	-	-	0.0	-	218.8 ± 6.3	0.62 ± 0.03	18	52.72	2.90e-05
	flat	-	-	78.4 ± 7.6	10.4	111.8 ± 13.8	1.35 ± 0.14	17	7.34	9.79e-01
	-	-	-	0.0	-	218.8 ± 6.3	0.62 ± 0.03	18	52.72	2.90e-05
Abell 1736	extr	15	0.10	150.4 ± 38.3	3.9	127.3 ± 37.9	0.99 ± 0.83	12	0.10	1.00e+00
	-	-	-	0.0	-	251.9 ± 19.2	0.20 ± 0.06	13	1.58	1.00e+00
	flat	-	-	150.4 ± 38.3	3.9	127.3 ± 37.9	0.99 ± 0.83	12	0.10	1.00e+00
	-	-	-	0.0	-	251.9 ± 19.2	0.20 ± 0.06	13	1.58	1.00e+00
Abell 1758	extr	20	0.40	116.8 ± 44.3	2.6	218.0 ± 58.6	1.03 ± 0.24	17	0.61	1.00e+00
	-	-	-	0.0	-	361.7 ± 20.8	0.62 ± 0.08	18	4.61	9.99e-01
	flat	-	-	230.8 ± 37.2	6.2	144.0 ± 50.2	1.21 ± 0.32	17	1.98	1.00e+00
	-	-	-	0.0	-	417.8 ± 20.2	0.36 ± 0.06	18	9.94	9.34e-01
Abell 1763	extr	39	0.60	214.7 ± 32.8	6.5	70.8 ± 29.1	1.37 ± 0.25	36	2.87	1.00e+00
	-	-	-	0.0	-	288.8 ± 13.8	0.60 ± 0.05	37	18.21	9.96e-01
	flat	-	-	214.7 ± 32.8	6.5	70.8 ± 29.1	1.37 ± 0.25	36	2.87	1.00e+00
	-	-	-	0.0	-	288.8 ± 13.8	0.60 ± 0.05	37	18.21	9.96e-01
Abell 1795	extr	53	0.30	18.4 ± 1.1	17.4	131.4 ± 2.8	1.17 ± 0.03	50	33.33	9.66e-01
	-	-	-	0.0	-	158.9 ± 2.0	0.86 ± 0.01	51	271.73	7.10e-32
	flat	-	-	19.0 ± 1.1	18.1	130.4 ± 2.8	1.18 ± 0.03	50	35.74	9.36e-01
	-	-	-	0.0	-	158.8 ± 2.0	0.86 ± 0.01	51	292.75	1.18e-35
Abell 1835	extr	16	0.30	10.9 ± 2.5	4.4	112.6 ± 7.9	1.25 ± 0.09	13	8.46	8.12e-01
	-	-	-	0.0	-	134.2 ± 5.2	0.99 ± 0.03	14	26.28	2.38e-02
	flat	-	-	11.4 ± 2.5	4.6	111.7 ± 7.9	1.26 ± 0.09	13	8.76	7.91e-01
	-	-	-	0.0	-	134.3 ± 5.3	0.98 ± 0.03	14	28.26	1.32e-02
Abell 1914	extr	29	0.40	63.3 ± 22.3	2.8	175.5 ± 32.3	0.88 ± 0.14	26	3.91	1.00e+00
	-	-	-	0.0	-	256.7 ± 10.4	0.61 ± 0.04	27	9.94	9.99e-01

Table B.5: Summary of Entropy Profile Fits (continued)

Cluster	Method	N_{bins}	r_{max} Mpc	K_0 keV cm^2	$\sigma_{K_0} > 0$	K_{100} keV cm^2	α	DOF	χ^2	p-value
(1)	(2)	(3)	(4)	(5)	(6)	(7)	(8)	(9)	(10)	(11)
	flat	-	-	107.2 ± 18.0	5.9	131.1 ± 28.3	1.05 ± 0.18	26	4.42	1.00e+00
	-	-	-	0.0	-	269.8 ± 10.3	0.52 ± 0.04	27	21.84	7.45e-01
Abell 1942	extr	12	0.22	107.7 ± 77.7	1.4	194.1 ± 88.7	0.66 ± 0.41	9	1.21	9.99e-01
	-	-	-	0.0	-	307.8 ± 17.3	0.35 ± 0.07	10	1.81	9.98e-01
	flat	-	-	107.7 ± 77.7	1.4	194.1 ± 88.7	0.66 ± 0.41	9	1.21	9.99e-01
	-	-	-	0.0	-	307.8 ± 17.3	0.35 ± 0.07	10	1.81	9.98e-01
Abell 1991	extr	19	0.10	1.0 ± 0.3	3.0	151.4 ± 4.1	1.04 ± 0.03	16	31.46	1.18e-02
	-	-	-	0.0	-	151.3 ± 3.6	1.04 ± 0.01	17	31.47	1.75e-02
	flat	-	-	1.5 ± 0.3	4.8	152.2 ± 4.2	1.09 ± 0.03	16	43.79	2.12e-04
	-	-	-	0.0	-	143.7 ± 3.4	0.99 ± 0.01	17	64.00	2.26e-07
Abell 1995	extr	26	0.60	374.3 ± 60.1	6.2	26.8 ± 32.9	2.08 ± 0.81	23	0.99	1.00e+00
	-	-	-	0.0	-	421.2 ± 36.4	0.35 ± 0.11	24	9.74	9.96e-01
	flat	-	-	374.3 ± 60.1	6.2	26.8 ± 32.9	2.08 ± 0.81	23	0.99	1.00e+00
	-	-	-	0.0	-	421.2 ± 36.4	0.35 ± 0.11	24	9.74	9.96e-01
Abell 2029	extr	58	0.40	6.1 ± 0.7	8.7	169.9 ± 2.1	0.92 ± 0.01	55	82.78	9.09e-03
	-	-	-	0.0	-	181.2 ± 1.6	0.82 ± 0.01	56	146.10	5.63e-10
	flat	-	-	10.5 ± 0.7	15.8	163.6 ± 2.1	0.95 ± 0.02	55	58.95	3.33e-01
	-	-	-	0.0	-	182.6 ± 1.6	0.78 ± 0.01	56	235.51	7.10e-24
Abell 2034	extr	67	0.50	215.8 ± 25.1	8.6	99.1 ± 25.3	1.05 ± 0.16	64	11.63	1.00e+00
	-	-	-	0.0	-	333.4 ± 9.0	0.42 ± 0.03	65	31.58	1.00e+00
	flat	-	-	232.6 ± 23.0	10.1	85.1 ± 22.6	1.14 ± 0.17	64	10.87	1.00e+00
	-	-	-	0.0	-	338.1 ± 8.9	0.41 ± 0.03	65	35.48	9.99e-01
Abell 2052	extr	29	0.10	8.9 ± 0.7	13.2	164.8 ± 2.6	1.23 ± 0.03	26	374.86	1.67e-63
	-	-	-	0.0	-	162.4 ± 2.3	0.99 ± 0.01	27	541.69	3.71e-97
	flat	-	-	9.5 ± 0.7	14.3	164.7 ± 2.6	1.25 ± 0.03	26	387.05	5.51e-66
	-	-	-	0.0	-	162.1 ± 2.3	0.99 ± 0.01	27	580.67	3.03e-105
Abell 2063	extr	52	0.18	53.5 ± 2.6	20.6	129.0 ± 3.9	1.07 ± 0.05	49	37.82	8.77e-01

Table B.5: Summary of Entropy Profile Fits (continued)

Cluster	Method	N_{bins}	r_{max} Mpc	K_0 keV cm^2	$\sigma_{K_0} > 0$	K_{100} keV cm^2	α	DOF	χ^2	p-value
(1)	(2)	(3)	(4)	(5)	(6)	(7)	(8)	(9)	(10)	(11)
	-	-	-	0.0	-	180.6 ± 2.4	0.51 ± 0.01	50	224.14	6.72e-24
	flat	-	-	53.5 ± 2.6	20.6	129.0 ± 3.9	1.07 ± 0.05	49	37.82	8.77e-01
	-	-	-	0.0	-	180.6 ± 2.4	0.51 ± 0.01	50	224.14	6.72e-24
Abell 2065	extr	29	0.20	33.1 ± 6.9	4.8	206.9 ± 10.8	0.97 ± 0.09	26	7.99	1.00e+00
	-	-	-	0.0	-	239.0 ± 7.5	0.67 ± 0.03	27	21.36	7.69e-01
	flat	-	-	43.9 ± 6.5	6.8	195.3 ± 10.6	1.02 ± 0.10	26	7.97	1.00e+00
	-	-	-	0.0	-	236.5 ± 7.5	0.60 ± 0.03	27	29.46	3.39e-01
Abell 2069	extr	39	0.40	416.2 ± 41.8	10.0	82.4 ± 46.0	1.22 ± 0.41	36	5.75	1.00e+00
	-	-	-	0.0	-	544.7 ± 16.4	0.20 ± 0.03	37	15.09	1.00e+00
	flat	-	-	453.2 ± 35.6	12.7	54.6 ± 36.3	1.47 ± 0.51	36	5.71	1.00e+00
	-	-	-	0.0	-	557.2 ± 16.2	0.17 ± 0.03	37	16.52	9.99e-01
Abell 2104	extr	9	0.12	98.0 ± 57.6	1.7	276.2 ± 59.7	0.94 ± 0.55	6	0.64	9.96e-01
	-	-	-	0.0	-	350.0 ± 36.1	0.46 ± 0.10	7	2.22	9.47e-01
	flat	-	-	160.6 ± 42.2	3.8	210.1 ± 53.9	1.20 ± 0.77	6	0.74	9.94e-01
	-	-	-	0.0	-	331.9 ± 33.4	0.30 ± 0.08	7	3.39	8.47e-01
Abell 2107	extr	6	0.03	18.0 ± 4.7	3.8	473.9 ± 117.3	1.03 ± 0.16	3	13.10	4.42e-03
	-	-	-	0.0	-	290.4 ± 26.6	0.64 ± 0.04	4	40.08	4.17e-08
	flat	-	-	21.2 ± 5.8	3.6	396.1 ± 92.5	0.91 ± 0.16	3	15.79	1.25e-03
	-	-	-	0.0	-	263.6 ± 21.3	0.55 ± 0.03	4	43.05	1.01e-08
Abell 2111	extr	22	0.40	107.4 ± 97.3	1.1	194.0 ± 118.7	0.65 ± 0.38	19	1.06	1.00e+00
	-	-	-	0.0	-	317.5 ± 23.7	0.39 ± 0.08	20	1.54	1.00e+00
	flat	-	-	107.4 ± 97.3	1.1	194.0 ± 118.7	0.65 ± 0.38	19	1.06	1.00e+00
	-	-	-	0.0	-	317.5 ± 23.7	0.39 ± 0.08	20	1.54	1.00e+00
Abell 2124	extr	19	0.12	88.7 ± 24.2	3.7	272.5 ± 30.8	0.89 ± 0.27	16	2.86	1.00e+00
	-	-	-	0.0	-	325.0 ± 21.8	0.41 ± 0.05	17	7.20	9.81e-01
	flat	-	-	98.3 ± 23.9	4.1	260.8 ± 30.8	0.90 ± 0.28	16	3.24	1.00e+00
	-	-	-	0.0	-	320.8 ± 21.3	0.37 ± 0.05	17	7.78	9.71e-01

Table B.5: Summary of Entropy Profile Fits (continued)

Cluster	Method	N_{bins}	r_{max} Mpc	K_0 keV cm^2	$\sigma_{K_0} > 0$	K_{100} keV cm^2	α	DOF	χ^2	p-value
(1)	(2)	(3)	(4)	(5)	(6)	(7)	(8)	(9)	(10)	(11)
Abell 2125	extr	10	0.20	225.2 ± 32.0	7.0	32.9 ± 41.2	1.35 ± 1.73	7	0.06	1.00e+00
	-	-	-	0.0	-	264.5 ± 11.5	0.10 ± 0.05	8	1.06	9.98e-01
	flat	-	-	225.2 ± 32.0	7.0	32.9 ± 41.2	1.35 ± 1.73	7	0.06	1.00e+00
	-	-	-	0.0	-	264.5 ± 11.5	0.10 ± 0.05	8	1.06	9.98e-01
Abell 2142	extr	75	0.30	58.5 ± 2.7	21.7	132.5 ± 4.5	1.13 ± 0.04	72	17.26	1.00e+00
	-	-	-	0.0	-	205.9 ± 2.1	0.62 ± 0.01	73	240.81	8.51e-20
	flat	-	-	68.1 ± 2.5	27.5	120.6 ± 4.4	1.22 ± 0.04	72	17.98	1.00e+00
	-	-	-	0.0	-	206.1 ± 2.2	0.58 ± 0.01	73	335.00	3.31e-35
Abell 2147	extr	57	0.20	151.9 ± 27.2	5.6	136.2 ± 30.5	0.55 ± 0.19	54	31.13	9.95e-01
	-	-	-	0.0	-	291.4 ± 6.4	0.18 ± 0.02	55	35.26	9.82e-01
	flat	-	-	151.9 ± 27.2	5.6	136.2 ± 30.5	0.55 ± 0.19	54	31.13	9.95e-01
	-	-	-	0.0	-	291.4 ± 6.4	0.18 ± 0.02	55	35.26	9.82e-01
Abell 2151	extr	20	0.07	1.7 ± 3.0	0.6	137.9 ± 6.0	0.61 ± 0.06	17	36.84	3.54e-03
	-	-	-	0.0	-	136.6 ± 5.2	0.58 ± 0.02	18	37.11	5.07e-03
	flat	-	-	0.4 ± 3.6	0.1	135.2 ± 5.4	0.56 ± 0.06	17	36.91	3.46e-03
	-	-	-	0.0	-	135.0 ± 5.0	0.55 ± 0.02	18	36.92	5.37e-03
Abell 2163	extr	42	0.60	437.3 ± 82.7	5.3	72.5 ± 50.8	1.86 ± 0.43	39	7.08	1.00e+00
	-	-	-	0.0	-	449.2 ± 42.9	0.82 ± 0.09	40	20.09	9.96e-01
	flat	-	-	438.0 ± 82.6	5.3	72.2 ± 50.6	1.87 ± 0.43	39	7.08	1.00e+00
	-	-	-	0.0	-	449.3 ± 42.9	0.82 ± 0.09	40	20.17	9.96e-01
Abell 2199	extr	7	0.02	7.6 ± 0.8	9.1	423.7 ± 95.3	1.38 ± 0.12	4	3.72	4.45e-01
	-	-	-	0.0	-	143.3 ± 11.8	0.72 ± 0.03	5	35.07	1.46e-06
	flat	-	-	13.3 ± 0.8	15.6	331.5 ± 90.0	1.35 ± 0.15	4	11.09	2.56e-02
	-	-	-	0.0	-	81.8 ± 5.2	0.44 ± 0.02	5	45.17	1.34e-08
Abell 2204	extr	15	0.20	9.7 ± 0.9	11.1	166.2 ± 6.0	1.41 ± 0.05	12	22.73	3.01e-02
	-	-	-	0.0	-	164.6 ± 5.9	1.02 ± 0.02	13	102.32	5.88e-16
	flat	-	-	9.7 ± 0.9	11.1	166.2 ± 6.0	1.41 ± 0.05	12	22.73	3.01e-02

Table B.5: Summary of Entropy Profile Fits (continued)

Cluster	Method	N_{bins}	r_{max} Mpc	K_0 keV cm^2	$\sigma_{K_0} > 0$	K_{100} keV cm^2	α	DOF	χ^2	p-value
(1)	(2)	(3)	(4)	(5)	(6)	(7)	(8)	(9)	(10)	(11)
	-	-	-	0.0	-	164.6 ± 5.9	1.02 ± 0.02	13	102.32	5.88e-16
Abell 2218	extr	42	0.60	288.6 ± 20.0	14.4	10.7 ± 7.1	2.35 ± 0.41	39	4.83	1.00e+00
	-	-	-	0.0	-	294.5 ± 14.7	0.41 ± 0.05	40	39.78	4.80e-01
	flat	-	-	288.6 ± 20.0	14.4	10.7 ± 7.1	2.35 ± 0.41	39	4.83	1.00e+00
	-	-	-	0.0	-	294.5 ± 14.7	0.41 ± 0.05	40	39.78	4.80e-01
Abell 2219	extr	34	0.60	411.6 ± 43.2	9.5	17.0 ± 19.2	1.97 ± 0.66	31	3.70	1.00e+00
	-	-	-	0.0	-	407.6 ± 26.4	0.36 ± 0.06	32	19.62	9.58e-01
	flat	-	-	411.6 ± 43.2	9.5	17.0 ± 19.2	1.97 ± 0.66	31	3.70	1.00e+00
	-	-	-	0.0	-	407.6 ± 26.4	0.36 ± 0.06	32	19.62	9.58e-01
Abell 2244	extr	34	0.30	57.6 ± 4.2	13.6	109.1 ± 6.0	1.00 ± 0.05	31	14.02	9.96e-01
	-	-	-	0.0	-	180.0 ± 2.1	0.56 ± 0.02	32	102.67	2.46e-09
	flat	-	-	57.6 ± 4.2	13.6	109.1 ± 6.0	1.00 ± 0.05	31	14.02	9.96e-01
	-	-	-	0.0	-	180.0 ± 2.1	0.56 ± 0.02	32	102.67	2.46e-09
Abell 2255	extr	40	0.30	529.1 ± 28.2	18.8	5.8 ± 16.6	2.63 ± 2.69	37	0.24	1.00e+00
	-	-	-	0.0	-	553.0 ± 14.0	0.05 ± 0.03	38	2.79	1.00e+00
	flat	-	-	529.1 ± 28.2	18.8	5.8 ± 16.6	2.63 ± 2.69	37	0.24	1.00e+00
	-	-	-	0.0	-	553.0 ± 14.0	0.05 ± 0.03	38	2.79	1.00e+00
Abell 2256	extr	63	0.35	349.6 ± 11.6	30.2	7.0 ± 7.6	2.54 ± 0.93	60	2.24	1.00e+00
	-	-	-	0.0	-	378.4 ± 6.9	0.08 ± 0.02	61	21.60	1.00e+00
	flat	-	-	349.6 ± 11.6	30.2	7.0 ± 7.6	2.54 ± 0.93	60	2.24	1.00e+00
	-	-	-	0.0	-	378.4 ± 6.9	0.08 ± 0.02	61	21.60	1.00e+00
Abell 2259	extr	36	0.50	114.0 ± 18.9	6.0	61.0 ± 20.4	1.36 ± 0.24	33	1.37	1.00e+00
	-	-	-	0.0	-	189.0 ± 8.7	0.63 ± 0.05	34	15.77	9.97e-01
	flat	-	-	114.0 ± 18.9	6.0	61.0 ± 20.4	1.36 ± 0.24	33	1.37	1.00e+00
	-	-	-	0.0	-	189.0 ± 8.7	0.63 ± 0.05	34	15.77	9.97e-01
Abell 2261	extr	18	0.30	60.5 ± 8.2	7.4	106.5 ± 14.1	1.27 ± 0.16	15	3.63	9.99e-01
	-	-	-	0.0	-	189.6 ± 6.6	0.61 ± 0.04	16	28.62	2.67e-02

Table B.5: Summary of Entropy Profile Fits (continued)

Cluster	Method	N_{bins}	r_{max} Mpc	K_0 keV cm^2	$\sigma_{K_0} > 0$	K_{100} keV cm^2	α	DOF	χ^2	p-value
(1)	(2)	(3)	(4)	(5)	(6)	(7)	(8)	(9)	(10)	(11)
	flat	-	-	61.1 ± 8.1	7.5	106.0 ± 14.1	1.27 ± 0.16	15	3.62	9.99e-01
	-	-	-	0.0	-	189.7 ± 6.6	0.61 ± 0.04	16	29.00	2.40e-02
Abell 2294	extr	22	0.32	128.5 ± 52.0	2.5	246.7 ± 75.6	1.04 ± 0.32	19	0.60	1.00e+00
	-	-	-	0.0	-	409.8 ± 28.7	0.57 ± 0.09	20	3.67	1.00e+00
	flat	-	-	156.3 ± 52.7	3.0	235.7 ± 76.3	1.03 ± 0.33	19	0.83	1.00e+00
	-	-	-	0.0	-	428.8 ± 28.6	0.49 ± 0.08	20	4.23	1.00e+00
Abell 2319	extr	74	0.40	270.2 ± 4.8	56.0	39.4 ± 7.1	1.76 ± 0.15	71	9.83	1.00e+00
	-	-	-	0.0	-	363.1 ± 4.3	0.19 ± 0.01	72	212.75	7.89e-16
	flat	-	-	270.2 ± 4.8	56.0	39.4 ± 7.1	1.76 ± 0.15	71	9.83	1.00e+00
	-	-	-	0.0	-	363.1 ± 4.3	0.19 ± 0.01	72	212.75	7.89e-16
Abell 2384	extr	23	0.20	17.9 ± 3.3	5.4	162.9 ± 7.3	1.31 ± 0.09	20	7.54	9.95e-01
	-	-	-	0.0	-	179.6 ± 6.3	0.99 ± 0.04	21	29.61	1.00e-01
	flat	-	-	38.5 ± 3.0	13.0	139.2 ± 7.3	1.49 ± 0.11	20	7.85	9.93e-01
	-	-	-	0.0	-	163.6 ± 6.1	0.70 ± 0.03	21	87.32	4.67e-10
Abell 2390	extr	11	0.20	14.7 ± 7.0	2.1	202.9 ± 15.6	1.07 ± 0.15	8	0.96	9.99e-01
	-	-	-	0.0	-	214.4 ± 13.9	0.84 ± 0.05	9	4.71	8.59e-01
	flat	-	-	14.7 ± 7.0	2.1	202.9 ± 15.6	1.07 ± 0.15	8	0.96	9.99e-01
	-	-	-	0.0	-	214.4 ± 13.9	0.84 ± 0.05	9	4.71	8.59e-01
Abell 2409	extr	16	0.20	69.6 ± 20.9	3.3	124.1 ± 27.4	0.96 ± 0.32	13	8.79	7.88e-01
	-	-	-	0.0	-	198.6 ± 10.2	0.45 ± 0.06	14	15.23	3.62e-01
	flat	-	-	73.8 ± 20.7	3.6	120.8 ± 27.3	0.97 ± 0.33	13	9.06	7.68e-01
	-	-	-	0.0	-	199.4 ± 10.3	0.43 ± 0.06	14	15.83	3.24e-01
Abell 2420	extr	64	0.50	332.6 ± 67.5	4.9	64.3 ± 62.6	1.12 ± 0.58	61	5.54	1.00e+00
	-	-	-	0.0	-	411.0 ± 22.4	0.28 ± 0.06	62	9.20	1.00e+00
	flat	-	-	332.6 ± 67.5	4.9	64.3 ± 62.6	1.12 ± 0.58	61	5.54	1.00e+00
	-	-	-	0.0	-	411.0 ± 22.4	0.28 ± 0.06	62	9.20	1.00e+00
Abell 2462	extr	58	0.40	129.7 ± 27.0	4.8	83.2 ± 31.1	0.77 ± 0.24	55	1.23	1.00e+00

Table B.5: Summary of Entropy Profile Fits (continued)

Cluster	Method	N_{bins}	r_{max} Mpc	K_0 keV cm^2	$\sigma_{K_0} > 0$	K_{100} keV cm^2	α	DOF	χ^2	p-value
(1)	(2)	(3)	(4)	(5)	(6)	(7)	(8)	(9)	(10)	(11)
	-	-	-	0.0	-	224.1 ± 6.2	0.30 ± 0.03	56	7.73	1.00e+00
	flat	-	-	129.7 ± 27.0	4.8	83.2 ± 31.1	0.77 ± 0.24	55	1.23	1.00e+00
	-	-	-	0.0	-	224.1 ± 6.2	0.30 ± 0.03	56	7.73	1.00e+00
Abell 2537	extr	14	0.30	106.7 ± 19.6	5.4	127.9 ± 29.2	1.24 ± 0.26	11	1.05	1.00e+00
	-	-	-	0.0	-	259.9 ± 11.9	0.51 ± 0.06	12	12.70	3.91e-01
	flat	-	-	110.4 ± 19.4	5.7	124.7 ± 29.0	1.26 ± 0.27	11	1.05	1.00e+00
	-	-	-	0.0	-	261.0 ± 11.9	0.50 ± 0.06	12	13.23	3.52e-01
Abell 2554	extr	30	0.30	105.1 ± 71.8	1.5	318.4 ± 86.2	0.66 ± 0.21	27	0.87	1.00e+00
	-	-	-	0.0	-	436.9 ± 18.7	0.45 ± 0.05	28	1.98	1.00e+00
	flat	-	-	105.1 ± 71.8	1.5	318.4 ± 86.2	0.66 ± 0.21	27	0.87	1.00e+00
	-	-	-	0.0	-	436.9 ± 18.7	0.45 ± 0.05	28	1.98	1.00e+00
Abell 2556	extr	17	0.13	10.6 ± 1.4	7.7	117.5 ± 3.9	1.10 ± 0.06	14	4.27	9.94e-01
	-	-	-	0.0	-	116.2 ± 3.5	0.76 ± 0.02	15	44.30	9.85e-05
	flat	-	-	12.4 ± 1.3	9.2	115.8 ± 4.0	1.13 ± 0.07	14	4.50	9.92e-01
	-	-	-	0.0	-	113.8 ± 3.4	0.72 ± 0.02	15	57.13	7.81e-07
Abell 2589	extr	25	0.10	52.0 ± 39.2	1.3	109.6 ± 34.8	0.61 ± 0.51	22	1.06	1.00e+00
	-	-	-	0.0	-	154.1 ± 13.4	0.29 ± 0.07	23	1.60	1.00e+00
	flat	-	-	52.0 ± 39.2	1.3	109.6 ± 34.8	0.61 ± 0.51	22	1.06	1.00e+00
	-	-	-	0.0	-	154.1 ± 13.4	0.29 ± 0.07	23	1.60	1.00e+00
Abell 2597	extr	8	0.06	9.6 ± 1.6	5.9	96.1 ± 14.0	1.19 ± 0.18	5	4.09	5.37e-01
	-	-	-	0.0	-	70.7 ± 5.0	0.62 ± 0.04	6	23.75	5.81e-04
	flat	-	-	10.6 ± 1.5	7.0	98.9 ± 15.2	1.26 ± 0.19	5	4.10	5.35e-01
	-	-	-	0.0	-	68.5 ± 4.8	0.59 ± 0.04	6	28.70	6.94e-05
Abell 2626	extr	22	0.12	23.2 ± 2.9	8.1	144.1 ± 6.3	1.05 ± 0.09	19	11.88	8.91e-01
	-	-	-	0.0	-	147.7 ± 5.2	0.62 ± 0.03	20	46.28	7.38e-04
	flat	-	-	23.2 ± 2.9	8.1	144.1 ± 6.3	1.05 ± 0.09	19	11.88	8.91e-01
	-	-	-	0.0	-	147.7 ± 5.2	0.62 ± 0.03	20	46.28	7.38e-04

Table B.5: Summary of Entropy Profile Fits (continued)

Cluster	Method	N_{bins}	r_{max} Mpc	K_0 keV cm^2	$\sigma_{K_0} > 0$	K_{100} keV cm^2	α	DOF	χ^2	p-value
(1)	(2)	(3)	(4)	(5)	(6)	(7)	(8)	(9)	(10)	(11)
Abell 2631	extr	38	0.80	308.8 ± 37.4	8.3	29.2 ± 23.4	1.44 ± 0.41	35	0.21	1.00e+00
	-	-	-	0.0	-	347.2 ± 21.7	0.33 ± 0.05	36	13.73	1.00e+00
	flat	-	-	308.8 ± 37.4	8.3	29.2 ± 23.4	1.44 ± 0.41	35	0.21	1.00e+00
	-	-	-	0.0	-	347.2 ± 21.7	0.33 ± 0.05	36	13.73	1.00e+00
Abell 2657	extr	51	0.20	65.4 ± 12.0	5.5	153.5 ± 15.1	0.91 ± 0.13	48	7.69	1.00e+00
	-	-	-	0.0	-	222.0 ± 5.9	0.50 ± 0.03	49	21.73	1.00e+00
	flat	-	-	65.4 ± 12.0	5.5	153.5 ± 15.1	0.91 ± 0.13	48	7.69	1.00e+00
	-	-	-	0.0	-	222.0 ± 5.9	0.50 ± 0.03	49	21.73	1.00e+00
Abell 2667	extr	11	0.20	12.3 ± 4.0	3.1	102.2 ± 7.7	1.17 ± 0.15	8	1.61	9.91e-01
	-	-	-	0.0	-	113.7 ± 6.2	0.85 ± 0.05	9	9.48	3.94e-01
	flat	-	-	19.3 ± 3.4	5.7	93.4 ± 7.6	1.31 ± 0.17	8	1.66	9.90e-01
	-	-	-	0.0	-	110.5 ± 6.2	0.75 ± 0.05	9	20.81	1.35e-02
Abell 2717	extr	26	0.12	26.3 ± 8.2	3.2	152.2 ± 10.1	0.76 ± 0.13	23	2.19	1.00e+00
	-	-	-	0.0	-	167.6 ± 7.9	0.50 ± 0.03	24	7.90	9.99e-01
	flat	-	-	27.0 ± 8.4	3.2	151.2 ± 10.2	0.75 ± 0.13	23	2.15	1.00e+00
	-	-	-	0.0	-	167.2 ± 7.8	0.49 ± 0.03	24	7.77	9.99e-01
Abell 2744	extr	27	0.60	295.1 ± 113.4	2.6	152.8 ± 112.7	0.83 ± 0.37	24	8.72	9.98e-01
	-	-	-	0.0	-	460.3 ± 29.9	0.37 ± 0.05	25	10.50	9.95e-01
	flat	-	-	438.4 ± 58.7	7.5	46.4 ± 44.0	1.41 ± 0.55	24	7.87	9.99e-01
	-	-	-	0.0	-	503.6 ± 29.3	0.30 ± 0.05	25	14.15	9.59e-01
Abell 2813	extr	14	0.30	216.3 ± 48.9	4.4	126.0 ± 74.9	1.52 ± 0.64	11	2.29	9.97e-01
	-	-	-	0.0	-	397.4 ± 33.0	0.42 ± 0.10	12	7.83	7.98e-01
	flat	-	-	267.6 ± 43.8	6.1	90.4 ± 67.3	1.76 ± 0.80	11	2.64	9.95e-01
	-	-	-	0.0	-	417.0 ± 33.5	0.31 ± 0.09	12	8.95	7.07e-01
Abell 3084	extr	34	0.30	96.7 ± 13.4	7.2	193.7 ± 22.8	1.08 ± 0.17	31	4.48	1.00e+00
	-	-	-	0.0	-	288.3 ± 14.4	0.43 ± 0.04	32	17.29	9.84e-01
	flat	-	-	96.7 ± 13.4	7.2	193.7 ± 22.8	1.08 ± 0.17	31	4.48	1.00e+00

Table B.5: Summary of Entropy Profile Fits (continued)

Cluster	Method	N_{bins}	r_{max} Mpc	K_0 keV cm^2	$\sigma_{K_0} > 0$	K_{100} keV cm^2	α	DOF	χ^2	p-value
(1)	(2)	(3)	(4)	(5)	(6)	(7)	(8)	(9)	(10)	(11)
	-	-	-	0.0	-	288.3 ± 14.4	0.43 ± 0.04	32	17.29	9.84e-01
Abell 3088	extr	10	0.20	32.7 ± 9.5	3.4	269.7 ± 25.8	1.51 ± 0.20	7	0.21	1.00e+00
	-	-	-	0.0	-	283.9 ± 23.8	1.02 ± 0.09	8	7.68	4.65e-01
	flat	-	-	82.8 ± 8.4	9.8	216.8 ± 25.8	1.71 ± 0.25	7	0.59	9.99e-01
	-	-	-	0.0	-	230.3 ± 18.8	0.49 ± 0.06	8	18.94	1.52e-02
Abell 3112	extr	18	0.12	8.2 ± 1.6	5.3	170.1 ± 6.8	1.09 ± 0.06	15	3.55	9.99e-01
	-	-	-	0.0	-	162.7 ± 6.0	0.86 ± 0.03	16	23.03	1.13e-01
	flat	-	-	11.4 ± 1.4	8.0	169.1 ± 7.0	1.17 ± 0.07	15	5.32	9.89e-01
	-	-	-	0.0	-	157.3 ± 5.8	0.82 ± 0.03	16	45.16	1.31e-04
Abell 3120	extr	29	0.20	15.0 ± 3.3	4.5	209.1 ± 10.9	1.02 ± 0.08	26	6.41	1.00e+00
	-	-	-	0.0	-	206.6 ± 10.1	0.76 ± 0.03	27	20.49	8.10e-01
	flat	-	-	17.3 ± 3.5	4.9	206.2 ± 10.9	0.99 ± 0.08	26	7.14	1.00e+00
	-	-	-	0.0	-	202.9 ± 9.8	0.70 ± 0.03	27	22.57	7.08e-01
Abell 3158	extr	72	0.40	166.0 ± 11.7	14.1	80.9 ± 12.9	0.90 ± 0.10	69	22.54	1.00e+00
	-	-	-	0.0	-	260.6 ± 2.9	0.32 ± 0.01	70	71.32	4.34e-01
	flat	-	-	166.0 ± 11.7	14.1	80.9 ± 12.9	0.90 ± 0.10	69	22.54	1.00e+00
	-	-	-	0.0	-	260.6 ± 2.9	0.32 ± 0.01	70	71.32	4.34e-01
Abell 3266	extr	15	0.08	63.7 ± 41.9	1.5	405.3 ± 51.6	0.71 ± 0.27	12	0.79	1.00e+00
	-	-	-	0.0	-	418.9 ± 37.8	0.44 ± 0.06	13	2.02	1.00e+00
	flat	-	-	72.5 ± 49.7	1.5	376.7 ± 48.0	0.64 ± 0.28	12	1.26	1.00e+00
	-	-	-	0.0	-	404.6 ± 35.2	0.39 ± 0.05	13	2.34	1.00e+00
Abell 3364	extr	55	0.70	268.6 ± 33.2	8.1	34.5 ± 18.0	1.97 ± 0.32	52	3.99	1.00e+00
	-	-	-	0.0	-	298.6 ± 22.7	0.63 ± 0.08	53	30.04	9.95e-01
	flat	-	-	268.6 ± 33.2	8.1	34.5 ± 18.0	1.97 ± 0.32	52	3.99	1.00e+00
	-	-	-	0.0	-	298.6 ± 22.7	0.63 ± 0.08	53	30.04	9.95e-01
Abell 3376	extr	67	0.30	282.9 ± 9.3	30.3	59.0 ± 10.6	1.71 ± 0.18	64	5.46	1.00e+00
	-	-	-	0.0	-	378.5 ± 4.3	0.30 ± 0.02	65	112.42	2.39e-04

Table B.5: Summary of Entropy Profile Fits (continued)

Cluster	Method	N_{bins}	r_{max} Mpc	K_0 keV cm^2	$\sigma_{K_0} > 0$	K_{100} keV cm^2	α	DOF	χ^2	p-value
(1)	(2)	(3)	(4)	(5)	(6)	(7)	(8)	(9)	(10)	(11)
	flat	-	-	282.9 ± 9.3	30.3	59.0 ± 10.6	1.71 ± 0.18	64	5.46	1.00e+00
	-	-	-	0.0	-	378.5 ± 4.3	0.30 ± 0.02	65	112.42	2.39e-04
Abell 3391	extr	75	0.40	367.5 ± 16.0	22.9	23.6 ± 14.8	1.64 ± 0.47	72	3.59	1.00e+00
	-	-	-	0.0	-	420.4 ± 7.5	0.14 ± 0.02	73	24.89	1.00e+00
	flat	-	-	367.5 ± 16.0	22.9	23.6 ± 14.8	1.64 ± 0.47	72	3.59	1.00e+00
	-	-	-	0.0	-	420.4 ± 7.5	0.14 ± 0.02	73	24.89	1.00e+00
Abell 3395	extr	24	0.12	213.3 ± 26.2	8.2	133.5 ± 30.4	1.58 ± 0.79	21	0.00	1.00e+00
	-	-	-	0.0	-	325.5 ± 14.4	0.23 ± 0.05	22	5.73	1.00e+00
	flat	-	-	247.2 ± 25.2	9.8	105.9 ± 29.8	1.65 ± 1.01	21	0.01	1.00e+00
	-	-	-	0.0	-	332.8 ± 14.0	0.16 ± 0.05	22	4.49	1.00e+00
Abell 3528S	extr	24	0.12	19.4 ± 2.3	8.6	288.1 ± 10.2	1.16 ± 0.05	21	32.09	5.73e-02
	-	-	-	0.0	-	271.7 ± 8.8	0.84 ± 0.02	22	84.38	3.04e-09
	flat	-	-	31.6 ± 2.3	14.0	270.0 ± 10.3	1.17 ± 0.06	21	32.23	5.55e-02
	-	-	-	0.0	-	239.2 ± 7.6	0.65 ± 0.02	22	128.53	4.82e-17
Abell 3558	extr	25	0.12	126.2 ± 11.8	10.7	132.5 ± 17.2	2.11 ± 0.58	22	6.87	9.99e-01
	-	-	-	0.0	-	234.0 ± 10.7	0.42 ± 0.06	23	19.89	6.49e-01
	flat	-	-	126.2 ± 11.8	10.7	132.5 ± 17.2	2.11 ± 0.58	22	6.87	9.99e-01
	-	-	-	0.0	-	234.0 ± 10.7	0.42 ± 0.06	23	19.89	6.49e-01
Abell 3562	extr	26	0.12	71.4 ± 9.0	8.0	166.8 ± 10.4	0.80 ± 0.13	23	33.16	7.84e-02
	-	-	-	0.0	-	217.3 ± 6.5	0.33 ± 0.02	24	54.22	3.99e-04
	flat	-	-	77.4 ± 8.9	8.7	159.8 ± 10.4	0.81 ± 0.13	23	35.16	5.01e-02
	-	-	-	0.0	-	215.4 ± 6.4	0.31 ± 0.02	24	56.31	2.08e-04
Abell 3571	extr	31	0.12	79.3 ± 14.8	5.4	191.3 ± 14.8	0.82 ± 0.16	28	375.69	1.65e-62
	-	-	-	0.0	-	256.1 ± 7.9	0.39 ± 0.03	29	657.82	6.19e-120
	flat	-	-	79.3 ± 14.8	5.4	191.3 ± 14.8	0.82 ± 0.16	28	375.69	1.65e-62
	-	-	-	0.0	-	256.1 ± 7.9	0.39 ± 0.03	29	657.82	6.19e-120
Abell 3581	extr	46	0.10	7.1 ± 0.8	8.4	138.1 ± 5.5	1.15 ± 0.05	43	20.49	9.99e-01

Table B.5: Summary of Entropy Profile Fits (continued)

Cluster	Method	N_{bins}	r_{max} Mpc	K_0 keV cm^2	$\sigma_{K_0} > 0$	K_{100} keV cm^2	α	DOF	χ^2	p-value
(1)	(2)	(3)	(4)	(5)	(6)	(7)	(8)	(9)	(10)	(11)
	-	-	-	0.0	-	121.6 ± 4.0	0.85 ± 0.02	44	65.85	1.80e-02
	flat	-	-	9.5 ± 0.8	12.2	138.1 ± 5.7	1.22 ± 0.05	43	21.56	9.97e-01
	-	-	-	0.0	-	114.3 ± 3.8	0.79 ± 0.02	44	103.30	1.13e-06
Abell 3667	extr	56	0.30	149.3 ± 17.2	8.7	121.9 ± 18.6	0.72 ± 0.09	53	21.14	1.00e+00
	-	-	-	0.0	-	278.7 ± 2.3	0.34 ± 0.01	54	44.43	8.20e-01
	flat	-	-	160.4 ± 15.5	10.4	110.6 ± 16.8	0.78 ± 0.10	53	22.84	1.00e+00
	-	-	-	0.0	-	279.5 ± 2.3	0.33 ± 0.01	54	52.83	5.19e-01
Abell 3822	extr	42	0.30	108.7 ± 76.4	1.4	200.3 ± 90.8	0.66 ± 0.33	39	3.24	1.00e+00
	-	-	-	0.0	-	322.5 ± 16.6	0.38 ± 0.07	40	3.95	1.00e+00
	flat	-	-	108.7 ± 76.4	1.4	200.3 ± 90.8	0.66 ± 0.33	39	3.24	1.00e+00
	-	-	-	0.0	-	322.5 ± 16.6	0.38 ± 0.07	40	3.95	1.00e+00
Abell 3827	extr	67	0.60	144.6 ± 13.4	10.8	113.1 ± 15.2	1.23 ± 0.10	64	1651.91	6.60e-303
	-	-	-	0.0	-	287.2 ± 7.4	0.60 ± 0.03	65	4867.53	0.00e+00
	flat	-	-	164.6 ± 12.5	13.2	94.8 ± 13.7	1.34 ± 0.10	64	1368.56	6.59e-244
	-	-	-	0.0	-	293.5 ± 7.3	0.57 ± 0.03	65	5896.48	0.00e+00
Abell 3921	extr	47	0.40	101.2 ± 17.9	5.7	151.5 ± 23.0	0.86 ± 0.11	44	7.55	1.00e+00
	-	-	-	0.0	-	272.4 ± 6.8	0.48 ± 0.03	45	22.08	9.98e-01
	flat	-	-	101.2 ± 17.9	5.7	151.5 ± 23.0	0.86 ± 0.11	44	7.55	1.00e+00
	-	-	-	0.0	-	272.4 ± 6.8	0.48 ± 0.03	45	22.08	9.98e-01
Abell 4038	extr	42	0.12	37.1 ± 1.2	30.2	118.5 ± 2.7	1.10 ± 0.05	39	58.69	2.22e-02
	-	-	-	0.0	-	127.3 ± 2.0	0.42 ± 0.01	40	393.69	1.15e-59
	flat	-	-	37.9 ± 1.2	31.2	117.9 ± 2.7	1.11 ± 0.05	39	60.31	1.58e-02
	-	-	-	0.0	-	126.5 ± 1.9	0.41 ± 0.01	40	410.34	6.07e-63
Abell 4059	extr	33	0.15	0.0 ± 1.0	0.0	210.7 ± 2.2	0.82 ± 0.01	30	44.86	3.98e-02
	-	-	-	0.0	-	210.7 ± 2.2	0.82 ± 0.01	31	44.86	5.13e-02
	flat	-	-	7.1 ± 1.0	6.7	203.2 ± 2.4	0.88 ± 0.02	30	54.25	4.31e-03
	-	-	-	0.0	-	208.3 ± 2.2	0.77 ± 0.01	31	93.59	3.35e-08

Table B.5: Summary of Entropy Profile Fits (continued)

Cluster	Method	N_{bins}	r_{max} Mpc	K_0 keV cm^2	$\sigma_{K_0} > 0$	K_{100} keV cm^2	α	DOF	χ^2	p-value
(1)	(2)	(3)	(4)	(5)	(6)	(7)	(8)	(9)	(10)	(11)
Abell S0405	extr	34	0.20	23.5 ± 21.0	1.1	261.1 ± 22.1	0.52 ± 0.10	31	8.24	1.00e+00
	-	-	-	0.0	-	281.9 ± 11.3	0.43 ± 0.03	32	9.16	1.00e+00
	flat	-	-	16.9 ± 27.9	0.6	274.2 ± 27.3	0.45 ± 0.10	31	9.79	1.00e+00
	-	-	-	0.0	-	289.3 ± 11.2	0.40 ± 0.02	32	10.10	1.00e+00
Abell S0592	extr	23	0.40	52.2 ± 14.4	3.6	199.0 ± 23.6	0.99 ± 0.12	20	9.34	9.79e-01
	-	-	-	0.0	-	271.1 ± 10.0	0.68 ± 0.04	21	16.08	7.65e-01
	flat	-	-	58.7 ± 14.4	4.1	195.5 ± 23.6	0.99 ± 0.13	20	9.70	9.73e-01
	-	-	-	0.0	-	275.6 ± 10.0	0.65 ± 0.04	21	17.46	6.83e-01
AC 114	flat	20	0.45	199.8 ± 28.0	7.1	70.0 ± 32.6	1.50 ± 0.36	17	3.69	1.00e+00
	-	-	-	0.0	-	306.6 ± 14.8	0.46 ± 0.06	18	16.94	5.28e-01
	extr	-	-	199.8 ± 28.0	7.1	70.0 ± 32.6	1.50 ± 0.36	17	3.69	1.00e+00
	-	-	-	0.0	-	306.6 ± 14.8	0.46 ± 0.06	18	16.94	5.28e-01
AWM7	extr	13	0.02	4.8 ± 1.1	4.5	290.2 ± 28.4	0.89 ± 0.06	10	7.30	6.96e-01
	-	-	-	0.0	-	217.6 ± 10.6	0.70 ± 0.02	11	20.91	3.43e-02
	flat	-	-	8.4 ± 1.3	6.5	227.6 ± 23.1	0.80 ± 0.06	10	13.19	2.13e-01
	-	-	-	0.0	-	157.1 ± 6.6	0.54 ± 0.01	11	32.84	5.58e-04
Centaurus	extr	27	0.03	1.4 ± 0.04	32.1	421.2 ± 5.4	1.25 ± 0.01	24	253.13	3.95e-40
	-	-	-	0.0	-	328.8 ± 3.1	1.11 ± 0.00	25	1159.86	6.17e-229
	flat	-	-	2.2 ± 0.04	56.6	474.9 ± 6.3	1.33 ± 0.01	24	483.38	4.67e-87
	-	-	-	0.0	-	307.3 ± 2.9	1.08 ± 0.00	25	3151.59	0.00e+00
CID 72	extr	37	0.12	4.9 ± 0.3	14.6	139.2 ± 2.1	0.95 ± 0.02	34	135.51	4.60e-14
	-	-	-	0.0	-	128.6 ± 1.7	0.77 ± 0.01	35	313.61	1.74e-46
	flat	-	-	9.4 ± 0.3	29.9	133.2 ± 2.2	0.99 ± 0.02	34	129.24	5.04e-13
	-	-	-	0.0	-	111.3 ± 1.5	0.63 ± 0.01	35	634.02	4.82e-111
CL J1226.9+3332	extr	10	0.40	166.0 ± 45.2	3.7	99.0 ± 58.7	1.41 ± 0.50	7	0.75	9.98e-01
	-	-	-	0.0	-	308.7 ± 25.3	0.55 ± 0.10	8	4.81	7.78e-01
	flat	-	-	166.0 ± 45.2	3.7	99.0 ± 58.7	1.41 ± 0.50	7	0.75	9.98e-01

Table B.5: Summary of Entropy Profile Fits (continued)

Cluster	Method	N_{bins}	r_{max} Mpc	K_0 keV cm^2	$\sigma_{K_0} > 0$	K_{100} keV cm^2	α	DOF	χ^2	p-value
(1)	(2)	(3)	(4)	(5)	(6)	(7)	(8)	(9)	(10)	(11)
	-	-	-	0.0	-	308.7 ± 25.3	0.55 ± 0.10	8	4.81	7.78e-01
Cygnus A	extr	19	0.10	21.7 ± 0.9	24.2	208.4 ± 6.7	1.51 ± 0.05	16	28.49	2.76e-02
	-	-	-	0.0	-	154.4 ± 3.7	0.73 ± 0.02	17	294.72	1.38e-52
	flat	-	-	23.6 ± 0.9	27.1	210.1 ± 6.9	1.57 ± 0.05	16	22.48	1.28e-01
	-	-	-	0.0	-	148.5 ± 3.6	0.70 ± 0.02	17	340.49	4.67e-62
ESO 3060170	extr	5	0.02	7.8 ± 1.0	7.8	1370.5 ± 562.2	1.79 ± 0.20	2	0.77	6.80e-01
	-	-	-	0.0	-	255.8 ± 37.1	0.90 ± 0.05	3	25.78	1.06e-05
	flat	-	-	8.0 ± 1.0	8.0	1400.9 ± 578.9	1.80 ± 0.21	2	0.81	6.67e-01
	-	-	-	0.0	-	251.2 ± 36.3	0.89 ± 0.05	3	26.70	6.81e-06
ESO 5520200	extr	17	0.10	6.3 ± 3.5	1.8	113.8 ± 7.0	0.74 ± 0.10	31	0.15	1.00e+00
	-	-	-	0.0	-	112.0 ± 6.0	0.60 ± 0.03	32	5.57	1.00e+00
	flat	-	-	5.9 ± 4.2	1.4	121.8 ± 6.5	0.67 ± 0.09	31	0.52	1.00e+00
	-	-	-	0.0	-	121.1 ± 5.8	0.57 ± 0.03	32	4.15	1.00e+00
EXO 422-086	extr	19	0.07	10.1 ± 0.8	12.5	199.3 ± 11.4	1.21 ± 0.06	16	11.00	8.10e-01
	-	-	-	0.0	-	142.0 ± 5.6	0.75 ± 0.02	17	112.48	4.11e-16
	flat	-	-	13.8 ± 0.8	17.5	193.8 ± 11.8	1.25 ± 0.06	16	11.24	7.95e-01
	-	-	-	0.0	-	120.4 ± 4.6	0.62 ± 0.02	17	157.52	8.19e-25
HCG 62	extr	27	0.04	3.1 ± 0.08	40.8	203.9 ± 10.4	1.23 ± 0.02	24	153.17	8.52e-21
	-	-	-	0.0	-	63.4 ± 1.7	0.63 ± 0.01	25	660.63	2.48e-123
	flat	-	-	3.4 ± 0.07	47.4	219.0 ± 11.4	1.28 ± 0.03	24	138.50	4.39e-18
	-	-	-	0.0	-	57.7 ± 1.5	0.60 ± 0.01	25	751.59	1.92e-142
HCG 42	extr	22	0.03	1.8 ± 0.3	5.5	128.5 ± 12.8	0.88 ± 0.05	19	44.38	8.38e-04
	-	-	-	0.0	-	89.4 ± 4.1	0.67 ± 0.01	20	60.87	5.23e-06
	flat	-	-	1.9 ± 0.3	5.7	126.5 ± 12.6	0.87 ± 0.05	19	45.28	6.25e-04
	-	-	-	0.0	-	87.4 ± 4.0	0.66 ± 0.01	20	62.24	3.19e-06
Hercules A	extr	16	0.20	2.8 ± 1.5	1.8	151.8 ± 3.3	0.99 ± 0.04	13	2.34	1.00e+00
	-	-	-	0.0	-	154.1 ± 3.1	0.94 ± 0.02	14	6.23	9.60e-01

Table B.5: Summary of Entropy Profile Fits (continued)

Cluster	Method	N_{bins}	r_{max} Mpc	K_0 keV cm^2	$\sigma_{K_0} > 0$	K_{100} keV cm^2	α	DOF	χ^2	p-value
(1)	(2)	(3)	(4)	(5)	(6)	(7)	(8)	(9)	(10)	(11)
	flat	-	-	9.2 ± 1.3	6.8	143.9 ± 3.3	1.07 ± 0.04	13	6.24	9.37e-01
	-	-	-	0.0	-	151.0 ± 3.1	0.87 ± 0.02	14	46.89	2.01e-05
Hydra A	extr	57	0.30	13.0 ± 0.7	19.5	115.3 ± 1.4	1.02 ± 0.02	54	71.44	5.62e-02
	-	-	-	0.0	-	134.0 ± 1.0	0.81 ± 0.01	55	364.39	3.36e-47
	flat	-	-	13.3 ± 0.7	20.0	114.9 ± 1.4	1.03 ± 0.02	54	72.66	4.60e-02
	-	-	-	0.0	-	134.0 ± 1.0	0.80 ± 0.01	55	379.86	4.40e-50
M49	extr	54	1.00	0.9 ± 0.05	18.1	486.7 ± 32.2	1.14 ± 0.02	51	74.03	1.92e-02
	-	-	-	0.0	-	231.3 ± 10.1	0.89 ± 0.01	52	327.07	1.58e-41
	flat	-	-	0.9 ± 0.05	18.9	495.3 ± 32.9	1.14 ± 0.02	51	75.65	1.41e-02
	-	-	-	0.0	-	227.4 ± 10.0	0.88 ± 0.01	52	349.43	1.14e-45
M87	extr	88	0.04	3.5 ± 0.08	43.1	146.4 ± 1.0	0.80 ± 0.00	85	749.92	4.94e-107
	-	-	-	0.0	-	123.8 ± 0.5	0.64 ± 0.00	86	2083.55	0.00e+00
	flat	-	-	3.5 ± 0.08	43.7	146.6 ± 1.0	0.80 ± 0.00	85	763.71	1.06e-109
	-	-	-	0.0	-	123.7 ± 0.5	0.64 ± 0.00	86	2130.02	0.00e+00
MACS J0011.7-1523	extr	16	0.40	14.9 ± 6.4	2.3	111.3 ± 11.6	1.03 ± 0.10	13	1.95	1.00e+00
	-	-	-	0.0	-	134.7 ± 5.1	0.86 ± 0.04	14	5.88	9.70e-01
	flat	-	-	18.8 ± 6.3	3.0	109.1 ± 11.5	1.04 ± 0.10	13	2.28	1.00e+00
	-	-	-	0.0	-	138.4 ± 5.0	0.81 ± 0.04	14	7.99	8.90e-01
MACS J0035.4-2015	extr	29	0.70	69.5 ± 17.1	4.1	93.9 ± 23.0	1.15 ± 0.16	26	0.70	1.00e+00
	-	-	-	0.0	-	183.2 ± 11.5	0.74 ± 0.06	27	11.72	9.95e-01
	flat	-	-	93.4 ± 15.7	6.0	76.4 ± 20.8	1.26 ± 0.17	26	1.00	1.00e+00
	-	-	-	0.0	-	198.2 ± 11.1	0.66 ± 0.05	27	20.41	8.13e-01
MACS J0159.8-0849	extr	15	0.40	11.9 ± 4.0	3.0	133.7 ± 10.0	1.25 ± 0.08	12	2.47	9.98e-01
	-	-	-	0.0	-	155.7 ± 5.8	1.06 ± 0.04	13	9.44	7.39e-01
	flat	-	-	18.8 ± 3.7	5.0	123.9 ± 9.9	1.31 ± 0.09	12	3.68	9.89e-01
	-	-	-	0.0	-	158.3 ± 5.9	1.01 ± 0.04	13	21.08	7.13e-02
MACS J0242.5-2132	extr	22	0.50	9.7 ± 1.9	5.0	76.3 ± 5.1	1.27 ± 0.07	19	11.73	8.97e-01

Table B.5: Summary of Entropy Profile Fits (continued)

Cluster	Method	N_{bins}	r_{max} Mpc	K_0 keV cm^2	$\sigma_{K_0} > 0$	K_{100} keV cm^2	α	DOF	χ^2	p-value
(1)	(2)	(3)	(4)	(5)	(6)	(7)	(8)	(9)	(10)	(11)
	-	-	-	0.0	-	94.0 ± 3.2	1.01 ± 0.04	20	29.52	7.81e-02
	flat	-	-	10.9 ± 1.9	5.7	74.6 ± 5.0	1.29 ± 0.07	19	11.84	8.93e-01
	-	-	-	0.0	-	94.4 ± 3.2	0.99 ± 0.03	20	34.37	2.37e-02
MACS J0257.1-2325	extr	13	0.40	234.5 ± 68.2	3.4	195.8 ± 107.3	1.39 ± 0.57	10	0.24	1.00e+00
	-	-	-	0.0	-	489.1 ± 50.9	0.47 ± 0.12	11	3.07	9.90e-01
	flat	-	-	234.5 ± 68.2	3.4	195.8 ± 107.3	1.39 ± 0.57	10	0.24	1.00e+00
	-	-	-	0.0	-	489.1 ± 50.9	0.47 ± 0.12	11	3.07	9.90e-01
MACS J0257.6-2209	extr	17	0.40	155.1 ± 25.1	6.2	82.7 ± 32.5	1.55 ± 0.34	14	1.00	1.00e+00
	-	-	-	0.0	-	277.1 ± 15.3	0.56 ± 0.07	15	18.10	2.57e-01
	flat	-	-	155.9 ± 25.0	6.2	82.1 ± 32.4	1.55 ± 0.34	14	1.01	1.00e+00
	-	-	-	0.0	-	277.6 ± 15.2	0.56 ± 0.07	15	18.25	2.49e-01
MACS J0308.9+2645	extr	30	0.70	212.8 ± 53.9	3.9	70.1 ± 42.2	1.43 ± 0.35	27	0.86	1.00e+00
	-	-	-	0.0	-	290.5 ± 34.0	0.66 ± 0.10	28	7.88	1.00e+00
	flat	-	-	212.8 ± 53.9	3.9	70.1 ± 42.2	1.43 ± 0.35	27	0.86	1.00e+00
	-	-	-	0.0	-	290.5 ± 34.0	0.66 ± 0.10	28	7.88	1.00e+00
MACS J0329.6-0211	extr	14	0.40	6.6 ± 2.7	2.4	102.9 ± 6.5	1.21 ± 0.07	11	9.63	5.64e-01
	-	-	-	0.0	-	115.4 ± 3.6	1.08 ± 0.03	12	14.83	2.51e-01
	flat	-	-	11.1 ± 2.5	4.4	96.7 ± 6.4	1.26 ± 0.07	11	11.91	3.71e-01
	-	-	-	0.0	-	117.5 ± 3.6	1.03 ± 0.03	12	26.77	8.33e-03
MACS J0417.5-1154	extr	11	0.30	9.5 ± 6.7	1.4	101.6 ± 14.8	1.52 ± 0.22	8	0.88	9.99e-01
	-	-	-	0.0	-	117.2 ± 9.2	1.29 ± 0.13	9	2.51	9.81e-01
	flat	-	-	27.1 ± 7.3	3.7	99.7 ± 15.1	1.42 ± 0.23	8	1.16	9.97e-01
	-	-	-	0.0	-	136.1 ± 9.4	0.85 ± 0.08	9	7.22	6.14e-01
MACS J0429.6-0253	extr	15	0.40	14.8 ± 4.4	3.4	91.4 ± 9.0	1.21 ± 0.11	12	2.46	9.98e-01
	-	-	-	0.0	-	115.3 ± 4.7	0.95 ± 0.05	13	10.52	6.51e-01
	flat	-	-	17.2 ± 4.3	4.0	88.9 ± 9.0	1.23 ± 0.11	12	2.52	9.98e-01
	-	-	-	0.0	-	116.5 ± 4.7	0.92 ± 0.05	13	13.22	4.31e-01

Table B.5: Summary of Entropy Profile Fits (continued)

Cluster	Method	N_{bins}	r_{max} Mpc	K_0 keV cm^2	$\sigma_{K_0} > 0$	K_{100} keV cm^2	α	DOF	χ^2	p-value
(1)	(2)	(3)	(4)	(5)	(6)	(7)	(8)	(9)	(10)	(11)
MACS J0520.7-1328	extr	21	0.50	88.6 ± 22.0	4.0	84.9 ± 28.2	1.20 ± 0.24	18	0.75	1.00e+00
	-	-	-	0.0	-	194.8 ± 12.0	0.64 ± 0.07	19	8.63	9.79e-01
	flat	-	-	88.6 ± 22.0	4.0	84.9 ± 28.2	1.20 ± 0.24	18	0.75	1.00e+00
	-	-	-	0.0	-	194.8 ± 12.0	0.64 ± 0.07	19	8.63	9.79e-01
MACS J0547.0-3904	extr	24	0.40	22.0 ± 4.4	5.0	122.6 ± 10.2	1.19 ± 0.10	21	7.76	9.96e-01
	-	-	-	0.0	-	153.5 ± 6.9	0.84 ± 0.04	22	23.85	3.55e-01
	flat	-	-	23.1 ± 4.4	5.2	121.6 ± 10.2	1.20 ± 0.10	21	7.65	9.96e-01
	-	-	-	0.0	-	153.7 ± 7.0	0.83 ± 0.04	22	25.01	2.97e-01
MACS J0717.5+3745	extr	16	0.50	158.7 ± 111.6	1.4	202.0 ± 128.8	0.69 ± 0.35	13	1.31	1.00e+00
	-	-	-	0.0	-	378.6 ± 26.0	0.40 ± 0.07	14	2.63	1.00e+00
	flat	-	-	220.1 ± 96.4	2.3	160.1 ± 112.2	0.76 ± 0.40	13	1.03	1.00e+00
	-	-	-	0.0	-	404.8 ± 25.2	0.33 ± 0.06	14	3.02	9.99e-01
MACS J0744.8+3927	extr	17	0.60	39.5 ± 11.0	3.6	113.9 ± 17.4	1.10 ± 0.11	14	3.84	9.96e-01
	-	-	-	0.0	-	170.4 ± 7.6	0.81 ± 0.05	15	11.91	6.86e-01
	flat	-	-	42.4 ± 10.9	3.9	112.0 ± 17.2	1.11 ± 0.12	14	3.88	9.96e-01
	-	-	-	0.0	-	172.6 ± 7.5	0.79 ± 0.04	15	12.98	6.04e-01
MACS J1115.2+5320	extr	18	0.50	292.3 ± 60.5	4.8	27.6 ± 42.3	1.73 ± 1.01	15	3.47	9.99e-01
	-	-	-	0.0	-	334.8 ± 32.1	0.33 ± 0.10	16	6.98	9.74e-01
	flat	-	-	292.3 ± 60.5	4.8	27.6 ± 42.3	1.73 ± 1.01	15	3.47	9.99e-01
	-	-	-	0.0	-	334.8 ± 32.1	0.33 ± 0.10	16	6.98	9.74e-01
MACS J1115.8+0129	extr	20	0.20	14.1 ± 5.1	2.8	265.5 ± 18.4	1.26 ± 0.11	17	5.12	9.97e-01
	-	-	-	0.0	-	278.8 ± 17.7	1.05 ± 0.06	18	13.05	7.89e-01
	flat	-	-	22.7 ± 4.9	4.7	253.8 ± 18.4	1.32 ± 0.12	17	5.50	9.96e-01
	-	-	-	0.0	-	270.5 ± 17.7	0.96 ± 0.05	18	24.02	1.54e-01
MACS J1131.8-1955	extr	23	0.50	62.1 ± 22.3	2.8	160.9 ± 33.8	1.18 ± 0.18	20	0.40	1.00e+00
	-	-	-	0.0	-	246.2 ± 16.5	0.84 ± 0.08	21	6.22	9.99e-01
	flat	-	-	97.3 ± 23.0	4.2	156.3 ± 34.7	1.15 ± 0.19	20	0.69	1.00e+00

Table B.5: Summary of Entropy Profile Fits (continued)

Cluster	Method	N_{bins}	r_{max} Mpc	K_0 keV cm^2	$\sigma_{K_0} > 0$	K_{100} keV cm^2	α	DOF	χ^2	p-value
(1)	(2)	(3)	(4)	(5)	(6)	(7)	(8)	(9)	(10)	(11)
	-	-	-	0.0	-	287.7 ± 15.5	0.64 ± 0.06	21	9.81	9.81e-01
MACS J1149.5+2223	extr	32	1.00	280.7 ± 39.2	7.2	33.1 ± 20.6	1.47 ± 0.30	29	1.62	1.00e+00
	-	-	-	0.0	-	282.3 ± 22.1	0.52 ± 0.06	30	15.32	9.88e-01
	flat	-	-	280.7 ± 39.2	7.2	33.1 ± 20.6	1.47 ± 0.30	29	1.62	1.00e+00
	-	-	-	0.0	-	282.3 ± 22.1	0.52 ± 0.06	30	15.32	9.88e-01
MACS J1206.2-0847	extr	30	0.80	61.0 ± 10.1	6.0	97.1 ± 14.6	1.27 ± 0.11	27	1.38	1.00e+00
	-	-	-	0.0	-	181.0 ± 8.5	0.84 ± 0.05	28	25.36	6.08e-01
	flat	-	-	69.0 ± 10.1	6.8	94.7 ± 14.5	1.28 ± 0.11	27	1.87	1.00e+00
	-	-	-	0.0	-	190.5 ± 8.3	0.78 ± 0.05	28	30.00	3.63e-01
MACS J1311.0-0310	extr	14	0.40	42.5 ± 4.2	10.1	67.1 ± 7.4	1.58 ± 0.12	11	2.47	9.96e-01
	-	-	-	0.0	-	127.7 ± 3.9	0.84 ± 0.04	12	67.11	1.11e-09
	flat	-	-	47.4 ± 4.1	11.5	63.5 ± 7.3	1.62 ± 0.12	11	2.39	9.97e-01
	-	-	-	0.0	-	130.2 ± 3.9	0.77 ± 0.04	12	77.77	1.10e-11
MACS J1621.3+3810	extr	17	0.50	13.9 ± 5.6	2.5	135.0 ± 11.6	1.16 ± 0.08	14	6.71	9.45e-01
	-	-	-	0.0	-	158.9 ± 5.8	1.01 ± 0.04	15	11.72	7.00e-01
	flat	-	-	20.1 ± 5.4	3.7	129.8 ± 11.4	1.18 ± 0.08	14	7.04	9.33e-01
	-	-	-	0.0	-	164.4 ± 5.8	0.96 ± 0.04	15	16.97	3.21e-01
MACS J1931.8-2634	extr	16	0.40	10.3 ± 3.8	2.7	93.7 ± 9.3	1.22 ± 0.10	13	4.58	9.83e-01
	-	-	-	0.0	-	112.9 ± 5.1	1.01 ± 0.05	14	10.52	7.23e-01
	flat	-	-	14.6 ± 3.6	4.1	87.5 ± 9.2	1.27 ± 0.11	13	5.80	9.53e-01
	-	-	-	0.0	-	114.6 ± 5.1	0.97 ± 0.04	14	17.89	2.12e-01
MACS J2049.9-3217	extr	21	0.50	195.8 ± 67.6	2.9	92.7 ± 71.5	1.06 ± 0.48	18	0.87	1.00e+00
	-	-	-	0.0	-	309.0 ± 25.4	0.43 ± 0.08	19	3.69	1.00e+00
	flat	-	-	195.8 ± 67.6	2.9	92.7 ± 71.5	1.06 ± 0.48	18	0.87	1.00e+00
	-	-	-	0.0	-	309.0 ± 25.4	0.43 ± 0.08	19	3.69	1.00e+00
MACS J2211.7-0349	extr	29	0.60	165.5 ± 25.5	6.5	78.3 ± 26.3	1.59 ± 0.24	26	0.89	1.00e+00
	-	-	-	0.0	-	270.5 ± 16.5	0.74 ± 0.07	27	20.58	8.06e-01

Table B.5: Summary of Entropy Profile Fits (continued)

Cluster	Method	N_{bins}	r_{max} Mpc	K_0 keV cm^2	$\sigma_{K_0} > 0$	K_{100} keV cm^2	α	DOF	χ^2	p-value
(1)	(2)	(3)	(4)	(5)	(6)	(7)	(8)	(9)	(10)	(11)
	flat	-	-	165.5 ± 25.5	6.5	78.3 ± 26.3	1.59 ± 0.24	26	0.89	1.00e+00
	-	-	-	0.0	-	270.5 ± 16.5	0.74 ± 0.07	27	20.58	8.06e-01
MACS J2214.9-1359	extr	13	0.40	238.6 ± 88.3	2.7	203.6 ± 152.6	1.38 ± 0.66	10	0.08	1.00e+00
	-	-	-	0.0	-	507.6 ± 70.9	0.52 ± 0.16	11	2.25	9.97e-01
	flat	-	-	297.7 ± 83.2	3.6	172.0 ± 147.7	1.46 ± 0.76	10	0.10	1.00e+00
	-	-	-	0.0	-	534.0 ± 73.0	0.40 ± 0.14	11	2.62	9.95e-01
MACS J2228+2036	extr	22	0.60	118.8 ± 39.2	3.0	107.2 ± 45.9	1.00 ± 0.26	19	0.60	1.00e+00
	-	-	-	0.0	-	246.7 ± 17.6	0.55 ± 0.07	20	4.67	1.00e+00
	flat	-	-	118.8 ± 39.2	3.0	107.2 ± 45.9	1.00 ± 0.26	19	0.60	1.00e+00
	-	-	-	0.0	-	246.7 ± 17.6	0.55 ± 0.07	20	4.67	1.00e+00
MACS J2229.7-2755	extr	17	0.40	10.2 ± 2.1	4.8	78.1 ± 5.2	1.32 ± 0.08	14	12.45	5.70e-01
	-	-	-	0.0	-	95.0 ± 3.4	1.04 ± 0.04	15	30.08	1.16e-02
	flat	-	-	12.4 ± 2.0	6.1	75.0 ± 5.2	1.36 ± 0.08	14	13.61	4.79e-01
	-	-	-	0.0	-	95.4 ± 3.4	1.01 ± 0.04	15	39.96	4.60e-04
MACS J2245.0+2637	extr	23	0.50	39.0 ± 6.6	5.9	108.5 ± 13.1	1.31 ± 0.12	20	0.54	1.00e+00
	-	-	-	0.0	-	166.7 ± 7.2	0.82 ± 0.05	21	23.13	3.37e-01
	flat	-	-	42.0 ± 6.5	6.5	105.9 ± 13.1	1.33 ± 0.13	20	0.53	1.00e+00
	-	-	-	0.0	-	168.1 ± 7.2	0.79 ± 0.05	21	25.90	2.10e-01
MKW3S	extr	46	0.20	20.7 ± 1.7	12.1	134.8 ± 2.6	0.93 ± 0.03	43	26.23	9.80e-01
	-	-	-	0.0	-	154.3 ± 1.8	0.66 ± 0.01	44	121.79	3.16e-09
	flat	-	-	23.9 ± 1.6	14.7	131.1 ± 2.5	0.96 ± 0.03	43	27.65	9.67e-01
	-	-	-	0.0	-	153.5 ± 1.8	0.65 ± 0.01	44	159.12	6.08e-15
MKW 4	extr	16	0.03	5.9 ± 0.3	18.9	368.4 ± 26.7	1.21 ± 0.04	13	17.01	1.99e-01
	-	-	-	0.0	-	164.0 ± 6.7	0.74 ± 0.01	14	233.26	8.23e-42
	flat	-	-	6.9 ± 0.3	23.0	392.7 ± 29.4	1.26 ± 0.04	13	19.05	1.21e-01
	-	-	-	0.0	-	146.6 ± 5.9	0.70 ± 0.01	14	305.78	7.37e-57
MKW 8	extr	19	0.05	130.7 ± 22.4	5.8	228.5 ± 54.2	0.87 ± 0.40	16	0.44	1.00e+00

Table B.5: Summary of Entropy Profile Fits (continued)

Cluster	Method	N_{bins}	r_{max} Mpc	K_0 keV cm^2	$\sigma_{K_0} > 0$	K_{100} keV cm^2	α	DOF	χ^2	p-value
(1)	(2)	(3)	(4)	(5)	(6)	(7)	(8)	(9)	(10)	(11)
	-	-	-	0.0	-	275.3 ± 16.3	0.22 ± 0.03	17	4.86	9.98e-01
	flat	-	-	130.7 ± 22.4	5.8	228.5 ± 54.2	0.87 ± 0.40	16	0.44	1.00e+00
	-	-	-	0.0	-	275.3 ± 16.3	0.22 ± 0.03	17	4.86	9.98e-01
MS J0016.9+1609	extr	16	0.50	160.7 ± 22.6	7.1	65.0 ± 26.7	1.28 ± 0.30	13	3.17	9.97e-01
	-	-	-	0.0	-	258.5 ± 11.8	0.40 ± 0.05	14	15.63	3.37e-01
	flat	-	-	162.1 ± 22.5	7.2	64.2 ± 26.5	1.29 ± 0.30	13	3.17	9.97e-01
	-	-	-	0.0	-	259.3 ± 11.7	0.40 ± 0.05	14	15.74	3.30e-01
MS J0116.3-0115	extr	22	0.10	17.2 ± 32.0	0.5	214.2 ± 24.7	0.62 ± 0.23	19	2.51	1.00e+00
	-	-	-	0.0	-	225.3 ± 14.8	0.52 ± 0.05	20	3.02	1.00e+00
	flat	-	-	12.8 ± 31.0	0.4	220.8 ± 24.1	0.63 ± 0.22	19	2.53	1.00e+00
	-	-	-	0.0	-	228.7 ± 15.1	0.55 ± 0.05	20	2.96	1.00e+00
MS J0440.5+0204	extr	19	0.30	22.8 ± 7.6	3.0	165.5 ± 15.1	1.11 ± 0.13	16	5.73	9.91e-01
	-	-	-	0.0	-	196.6 ± 9.6	0.82 ± 0.06	17	11.13	8.50e-01
	flat	-	-	25.5 ± 7.6	3.4	164.0 ± 15.2	1.11 ± 0.13	16	6.15	9.86e-01
	-	-	-	0.0	-	198.0 ± 9.6	0.79 ± 0.05	17	12.34	7.79e-01
MS J0451.6-0305	extr	16	0.50	568.1 ± 115.6	4.9	15.6 ± 49.9	2.81 ± 2.27	13	0.56	1.00e+00
	-	-	-	0.0	-	643.5 ± 79.7	0.21 ± 0.16	14	3.73	9.97e-01
	flat	-	-	568.1 ± 115.6	4.9	15.6 ± 49.9	2.81 ± 2.27	13	0.56	1.00e+00
	-	-	-	0.0	-	643.5 ± 79.7	0.21 ± 0.16	14	3.73	9.97e-01
MS J0735.6+7421	extr	18	0.30	13.8 ± 2.2	6.3	109.9 ± 4.6	1.12 ± 0.05	15	22.06	1.06e-01
	-	-	-	0.0	-	131.3 ± 2.7	0.89 ± 0.02	16	60.72	3.95e-07
	flat	-	-	16.0 ± 2.1	7.5	106.8 ± 4.6	1.14 ± 0.05	15	25.59	4.26e-02
	-	-	-	0.0	-	131.5 ± 2.7	0.87 ± 0.02	16	77.93	3.92e-10
MS J0839.8+2938	extr	16	0.25	15.5 ± 3.1	5.1	110.7 ± 6.3	1.26 ± 0.11	13	3.12	9.98e-01
	-	-	-	0.0	-	127.3 ± 4.9	0.88 ± 0.04	14	21.16	9.75e-02
	flat	-	-	19.2 ± 2.9	6.7	105.8 ± 6.3	1.33 ± 0.11	13	2.50	9.99e-01
	-	-	-	0.0	-	126.1 ± 4.9	0.84 ± 0.04	14	30.67	6.17e-03

Table B.5: Summary of Entropy Profile Fits (continued)

Cluster	Method	N_{bins}	r_{max} Mpc	K_0 keV cm^2	$\sigma_{K_0} > 0$	K_{100} keV cm^2	α	DOF	χ^2	p-value
(1)	(2)	(3)	(4)	(5)	(6)	(7)	(8)	(9)	(10)	(11)
MS J0906.5+1110	extr	29	0.40	104.2 ± 14.9	7.0	97.3 ± 19.6	1.15 ± 0.17	26	1.25	1.00e+00
	-	-	-	0.0	-	222.7 ± 6.4	0.54 ± 0.04	27	19.62	8.46e-01
	flat	-	-	104.2 ± 14.9	7.0	97.3 ± 19.6	1.15 ± 0.17	26	1.25	1.00e+00
	-	-	-	0.0	-	222.7 ± 6.4	0.54 ± 0.04	27	19.62	8.46e-01
MS J1006.0+1202	extr	29	0.50	175.8 ± 20.1	8.7	71.7 ± 25.0	1.40 ± 0.26	26	7.00	1.00e+00
	-	-	-	0.0	-	285.4 ± 12.1	0.41 ± 0.05	27	29.77	3.25e-01
	flat	-	-	160.3 ± 21.3	7.5	82.8 ± 26.9	1.32 ± 0.24	26	6.68	1.00e+00
	-	-	-	0.0	-	278.4 ± 12.2	0.46 ± 0.05	27	26.32	5.01e-01
MS J1008.1-1224	extr	23	0.50	96.0 ± 40.7	2.4	260.2 ± 56.0	0.77 ± 0.18	20	1.45	1.00e+00
	-	-	-	0.0	-	373.9 ± 18.0	0.49 ± 0.05	21	4.07	1.00e+00
	flat	-	-	97.6 ± 41.5	2.4	262.0 ± 56.8	0.76 ± 0.18	20	1.50	1.00e+00
	-	-	-	0.0	-	377.0 ± 18.1	0.48 ± 0.05	21	4.07	1.00e+00
MS J1455.0+2232	extr	16	0.30	16.9 ± 1.5	11.1	81.5 ± 4.0	1.39 ± 0.07	13	10.09	6.86e-01
	-	-	-	0.0	-	107.3 ± 2.7	0.86 ± 0.03	14	80.05	2.76e-11
	flat	-	-	16.9 ± 1.5	11.1	81.5 ± 4.0	1.39 ± 0.07	13	10.09	6.86e-01
	-	-	-	0.0	-	107.3 ± 2.7	0.86 ± 0.03	14	80.05	2.76e-11
MS J2137.3-2353	extr	22	0.50	12.3 ± 1.9	6.5	93.5 ± 5.3	1.36 ± 0.06	19	5.01	9.99e-01
	-	-	-	0.0	-	116.9 ± 3.4	1.08 ± 0.03	20	36.15	1.47e-02
	flat	-	-	14.7 ± 1.8	7.9	89.9 ± 5.3	1.39 ± 0.06	19	5.76	9.98e-01
	-	-	-	0.0	-	117.6 ± 3.4	1.05 ± 0.03	20	50.37	1.96e-04
MS J1157.3+5531	extr	13	0.10	4.1 ± 0.4	9.7	283.8 ± 17.7	1.44 ± 0.05	10	7.54	6.74e-01
	-	-	-	0.0	-	196.2 ± 9.6	1.09 ± 0.02	11	64.85	1.15e-09
	flat	-	-	5.9 ± 0.4	13.9	277.0 ± 17.7	1.45 ± 0.05	10	7.22	7.04e-01
	-	-	-	0.0	-	160.6 ± 7.7	0.95 ± 0.02	11	96.24	9.86e-16
NGC 507	extr	61	0.05	0.0 ± 2.1	0.0	101.7 ± 2.8	0.67 ± 0.01	58	42.84	9.32e-01
	-	-	-	0.0	-	101.7 ± 2.8	0.67 ± 0.01	59	42.84	9.44e-01
	flat	-	-	0.0 ± 2.1	0.0	99.9 ± 2.7	0.65 ± 0.01	58	46.55	8.60e-01

Table B.5: Summary of Entropy Profile Fits (continued)

Cluster	Method	N_{bins}	r_{max} Mpc	K_0 keV cm^2	$\sigma_{K_0} > 0$	K_{100} keV cm^2	α	DOF	χ^2	p-value
(1)	(2)	(3)	(4)	(5)	(6)	(7)	(8)	(9)	(10)	(11)
	-	-	-	0.0	-	99.9 ± 2.7	0.65 ± 0.01	59	46.55	8.80e-01
NGC 4636	extr	12	0.00	1.4 ± 0.1	13.4	10674.9 ± 7937.9	1.93 ± 0.18	9	8.12	5.22e-01
	-	-	-	0.0	-	108.2 ± 19.2	0.77 ± 0.04	10	56.25	1.84e-08
	flat	-	-	1.4 ± 0.1	13.9	11962.1 ± 8977.0	1.96 ± 0.18	9	8.95	4.42e-01
	-	-	-	0.0	-	104.9 ± 18.6	0.77 ± 0.04	10	60.03	3.58e-09
NGC 5044	extr	66	0.03	1.9 ± 0.3	7.2	79.6 ± 6.7	0.93 ± 0.05	63	49.49	8.93e-01
	-	-	-	0.0	-	55.1 ± 2.4	0.67 ± 0.02	64	77.04	1.27e-01
	flat	-	-	2.3 ± 0.3	8.9	82.2 ± 7.2	0.96 ± 0.05	63	48.05	9.18e-01
	-	-	-	0.0	-	52.3 ± 2.2	0.64 ± 0.02	64	86.52	3.19e-02
NGC 5813	extr	60	0.02	1.4 ± 0.2	8.9	102.5 ± 7.1	0.91 ± 0.03	57	107.52	6.00e-05
	-	-	-	0.0	-	69.3 ± 2.1	0.70 ± 0.01	58	161.30	1.14e-11
	flat	-	-	1.4 ± 0.2	8.9	102.5 ± 7.1	0.91 ± 0.03	57	107.52	6.00e-05
	-	-	-	0.0	-	69.3 ± 2.1	0.70 ± 0.01	58	161.30	1.14e-11
NGC 5846	extr	16	0.00	1.8 ± 0.2	10.7	685.8 ± 344.9	1.44 ± 0.15	13	1.16	1.00e+00
	-	-	-	0.0	-	52.7 ± 7.3	0.63 ± 0.03	14	40.72	1.97e-04
	flat	-	-	1.8 ± 0.2	10.7	685.8 ± 344.9	1.44 ± 0.15	13	1.16	1.00e+00
	-	-	-	0.0	-	52.7 ± 7.3	0.63 ± 0.03	14	40.72	1.97e-04
Ophiuchus	extr	18	0.05	4.0 ± 0.6	6.3	375.1 ± 12.8	1.06 ± 0.03	15	9.75	8.35e-01
	-	-	-	0.0	-	328.4 ± 7.8	0.92 ± 0.01	16	42.24	3.63e-04
	flat	-	-	8.9 ± 1.2	7.5	247.5 ± 7.6	0.73 ± 0.03	15	95.06	1.12e-13
	-	-	-	0.0	-	217.0 ± 3.9	0.58 ± 0.01	16	127.43	2.02e-19
PKS 0745-191	extr	34	0.30	11.9 ± 0.7	17.4	111.7 ± 2.7	1.38 ± 0.04	31	17.17	9.79e-01
	-	-	-	0.0	-	129.2 ± 2.4	0.98 ± 0.02	32	245.68	8.53e-35
	flat	-	-	12.4 ± 0.7	18.3	110.7 ± 2.7	1.39 ± 0.04	31	19.54	9.45e-01
	-	-	-	0.0	-	128.9 ± 2.4	0.97 ± 0.02	32	270.30	1.59e-39
RBS 461	extr	70	0.20	95.7 ± 3.0	31.4	68.8 ± 4.5	1.39 ± 0.10	67	22.14	1.00e+00
	-	-	-	0.0	-	173.2 ± 1.8	0.35 ± 0.01	68	217.68	1.45e-17

Table B.5: Summary of Entropy Profile Fits (continued)

Cluster	Method	N_{bins}	r_{max} Mpc	K_0 keV cm^2	$\sigma_{K_0} > 0$	K_{100} keV cm^2	α	DOF	χ^2	p-value
(1)	(2)	(3)	(4)	(5)	(6)	(7)	(8)	(9)	(10)	(11)
	flat	-	-	95.7 ± 3.0	31.4	68.8 ± 4.5	1.39 ± 0.10	67	22.14	1.00e+00
	-	-	-	0.0	-	173.2 ± 1.8	0.35 ± 0.01	68	217.68	1.45e-17
RBS 533	extr	44	0.06	2.0 ± 0.05	39.5	162.8 ± 2.5	0.99 ± 0.01	41	202.89	2.65e-23
	-	-	-	0.0	-	113.5 ± 1.3	0.76 ± 0.00	42	1282.66	1.75e-241
	flat	-	-	2.2 ± 0.05	43.7	164.3 ± 2.5	1.00 ± 0.01	41	215.65	1.46e-25
	-	-	-	0.0	-	110.0 ± 1.3	0.75 ± 0.00	42	1490.02	3.27e-285
RBS 797	extr	24	0.30	20.0 ± 2.4	8.3	95.2 ± 9.0	1.72 ± 0.14	21	89.64	1.86e-10
	-	-	-	0.0	-	116.2 ± 8.0	0.98 ± 0.06	22	1061.58	1.51e-210
	flat	-	-	20.9 ± 2.4	8.9	93.2 ± 9.1	1.75 ± 0.15	21	104.70	4.22e-13
	-	-	-	0.0	-	114.6 ± 8.0	0.96 ± 0.06	22	1188.56	1.25e-237
RCS J2327-0204	extr	18	0.30	65.5 ± 20.2	3.2	220.6 ± 37.0	1.27 ± 0.25	15	31.21	8.24e-03
	-	-	-	0.0	-	300.3 ± 22.5	0.74 ± 0.09	16	119.10	8.17e-18
	flat	-	-	68.5 ± 19.9	3.4	217.2 ± 36.9	1.28 ± 0.26	15	31.00	8.80e-03
	-	-	-	0.0	-	300.1 ± 22.6	0.73 ± 0.09	16	126.00	3.83e-19
RXCJ0331.1-2100	extr	25	0.20	6.4 ± 1.6	4.1	141.0 ± 5.8	1.23 ± 0.06	22	325.76	7.05e-56
	-	-	-	0.0	-	145.9 ± 5.7	1.05 ± 0.03	23	677.70	2.20e-128
	flat	-	-	11.4 ± 1.5	7.7	134.1 ± 5.8	1.30 ± 0.07	22	356.18	4.25e-62
	-	-	-	0.0	-	140.5 ± 5.7	0.95 ± 0.03	23	1408.70	8.65e-284
RX J0220.9-3829	extr	22	0.40	33.1 ± 6.2	5.3	163.7 ± 14.0	1.25 ± 0.11	19	3.90	1.00e+00
	-	-	-	0.0	-	211.1 ± 9.0	0.84 ± 0.05	20	20.59	4.22e-01
	flat	-	-	43.0 ± 6.3	6.8	159.9 ± 14.0	1.23 ± 0.12	19	4.20	1.00e+00
	-	-	-	0.0	-	216.2 ± 9.2	0.73 ± 0.04	20	25.95	1.68e-01
RX J0232.2-4420	extr	14	0.30	34.2 ± 13.0	2.6	176.3 ± 25.0	1.12 ± 0.18	11	0.85	1.00e+00
	-	-	-	0.0	-	225.4 ± 13.1	0.80 ± 0.06	12	5.16	9.53e-01
	flat	-	-	44.6 ± 12.4	3.6	166.5 ± 24.7	1.16 ± 0.18	11	0.71	1.00e+00
	-	-	-	0.0	-	228.9 ± 13.2	0.74 ± 0.06	12	7.42	8.28e-01
RX J0439+0520	extr	18	0.30	12.8 ± 2.9	4.5	97.1 ± 6.2	1.18 ± 0.10	15	6.80	9.63e-01

Table B.5: Summary of Entropy Profile Fits (continued)

Cluster	Method	N_{bins}	r_{max} Mpc	K_0 keV cm^2	$\sigma_{K_0} > 0$	K_{100} keV cm^2	α	DOF	χ^2	p-value
(1)	(2)	(3)	(4)	(5)	(6)	(7)	(8)	(9)	(10)	(11)
	-	-	-	0.0	-	112.8 ± 4.6	0.86 ± 0.04	16	19.20	2.59e-01
	flat	-	-	14.9 ± 2.9	5.2	95.5 ± 6.2	1.19 ± 0.10	15	6.64	9.67e-01
	-	-	-	0.0	-	113.0 ± 4.6	0.82 ± 0.04	16	21.93	1.45e-01
RX J0439.0+0715	extr	22	0.40	61.2 ± 21.3	2.9	152.0 ± 31.1	0.95 ± 0.18	19	5.54	9.99e-01
	-	-	-	0.0	-	212.0 ± 10.6	0.68 ± 0.06	20	8.75	9.86e-01
	flat	-	-	66.8 ± 18.5	3.6	129.6 ± 28.4	1.06 ± 0.20	19	6.20	9.97e-01
	-	-	-	0.0	-	217.0 ± 10.5	0.63 ± 0.06	20	13.41	8.59e-01
RX J0528.9-3927	extr	21	0.40	69.9 ± 13.9	5.0	102.2 ± 22.6	1.45 ± 0.23	18	1.71	1.00e+00
	-	-	-	0.0	-	201.5 ± 11.3	0.74 ± 0.08	19	15.10	7.16e-01
	flat	-	-	72.9 ± 13.8	5.3	99.8 ± 22.4	1.47 ± 0.23	18	1.67	1.00e+00
	-	-	-	0.0	-	203.1 ± 11.3	0.72 ± 0.07	19	15.94	6.61e-01
RX J0647.7+7015	extr	24	0.80	225.1 ± 47.1	4.8	48.8 ± 31.9	1.70 ± 0.39	21	0.42	1.00e+00
	-	-	-	0.0	-	275.6 ± 32.0	0.71 ± 0.10	22	9.72	9.89e-01
	flat	-	-	225.1 ± 47.1	4.8	48.8 ± 31.9	1.70 ± 0.39	21	0.42	1.00e+00
	-	-	-	0.0	-	275.6 ± 32.0	0.71 ± 0.10	22	9.72	9.89e-01
RX J0819.6+6336	extr	28	0.30	20.7 ± 14.3	1.5	170.6 ± 19.4	0.68 ± 0.12	25	10.13	9.96e-01
	-	-	-	0.0	-	194.0 ± 8.8	0.55 ± 0.04	26	11.55	9.93e-01
	flat	-	-	20.7 ± 14.3	1.5	170.6 ± 19.4	0.68 ± 0.12	25	10.13	9.96e-01
	-	-	-	0.0	-	194.0 ± 8.8	0.55 ± 0.04	26	11.55	9.93e-01
RX J1000.4+4409	extr	23	0.30	23.1 ± 4.3	5.4	151.7 ± 9.9	1.12 ± 0.09	20	1.85	1.00e+00
	-	-	-	0.0	-	182.2 ± 7.1	0.77 ± 0.04	21	18.65	6.07e-01
	flat	-	-	27.7 ± 4.4	6.3	151.1 ± 9.9	1.09 ± 0.09	20	1.94	1.00e+00
	-	-	-	0.0	-	184.9 ± 7.2	0.71 ± 0.03	21	21.59	4.24e-01
RX J1022.1+3830	extr	18	0.09	44.0 ± 10.0	4.4	206.8 ± 18.5	1.03 ± 0.21	15	7.73	9.34e-01
	-	-	-	0.0	-	208.7 ± 11.4	0.54 ± 0.04	16	13.56	6.32e-01
	flat	-	-	51.6 ± 9.8	5.3	194.8 ± 18.7	1.04 ± 0.22	15	8.26	9.13e-01
	-	-	-	0.0	-	201.1 ± 10.7	0.48 ± 0.04	16	14.68	5.48e-01

Table B.5: Summary of Entropy Profile Fits (continued)

Cluster	Method	N_{bins}	r_{max} Mpc	K_0 keV cm^2	$\sigma_{K_0} > 0$	K_{100} keV cm^2	α	DOF	χ^2	p-value
(1)	(2)	(3)	(4)	(5)	(6)	(7)	(8)	(9)	(10)	(11)
RX J1130.0+3637	extr	26	0.15	23.4 ± 2.2	10.7	158.7 ± 9.3	1.19 ± 0.09	23	2.01	1.00e+00
	-	-	-	0.0	-	140.8 ± 6.7	0.60 ± 0.03	24	54.32	3.86e-04
	flat	-	-	29.9 ± 2.3	12.9	149.6 ± 9.2	1.14 ± 0.10	23	2.81	1.00e+00
	-	-	-	0.0	-	133.0 ± 6.0	0.48 ± 0.02	24	58.11	1.18e-04
RX J1320.2+3308	extr	11	0.04	7.6 ± 0.6	12.1	162.6 ± 26.6	1.36 ± 0.12	8	5.25	7.31e-01
	-	-	-	0.0	-	67.6 ± 4.2	0.61 ± 0.03	9	50.82	7.56e-08
	flat	-	-	8.8 ± 0.7	13.1	140.3 ± 23.4	1.28 ± 0.12	8	7.01	5.36e-01
	-	-	-	0.0	-	59.9 ± 3.4	0.53 ± 0.02	9	49.88	1.13e-07
RX J1347.5-1145	extr	8	0.22	12.5 ± 20.7	0.6	179.9 ± 35.3	1.06 ± 0.34	5	4.00	5.49e-01
	-	-	-	0.0	-	196.4 ± 18.3	0.90 ± 0.08	6	4.23	6.46e-01
	flat	-	-	12.5 ± 20.7	0.6	179.9 ± 35.3	1.06 ± 0.34	5	4.00	5.49e-01
	-	-	-	0.0	-	196.4 ± 18.3	0.90 ± 0.08	6	4.23	6.46e-01
RX J1423.8+2404	extr	7	0.22	10.2 ± 5.0	2.0	119.9 ± 10.8	1.27 ± 0.17	4	1.75	7.82e-01
	-	-	-	0.0	-	133.8 ± 7.3	1.02 ± 0.05	5	15.01	1.03e-02
	flat	-	-	10.2 ± 5.0	2.0	119.9 ± 10.8	1.27 ± 0.17	4	1.75	7.82e-01
	-	-	-	0.0	-	133.8 ± 7.3	1.02 ± 0.05	5	15.01	1.03e-02
RX J1504.1-0248	extr	27	0.45	13.1 ± 0.9	13.9	95.6 ± 3.5	1.50 ± 0.04	24	2.89	1.00e+00
	-	-	-	0.0	-	121.2 ± 2.7	1.09 ± 0.02	25	154.86	1.07e-20
	flat	-	-	13.1 ± 0.9	13.9	95.6 ± 3.5	1.50 ± 0.04	24	2.89	1.00e+00
	-	-	-	0.0	-	121.2 ± 2.7	1.09 ± 0.02	25	154.86	1.07e-20
RX J1532.9+3021	extr	21	0.50	14.3 ± 1.9	7.6	80.3 ± 5.0	1.46 ± 0.07	18	2.24	1.00e+00
	-	-	-	0.0	-	105.6 ± 3.3	1.08 ± 0.04	19	48.03	2.54e-04
	flat	-	-	16.9 ± 1.8	9.3	76.3 ± 5.0	1.51 ± 0.07	18	2.38	1.00e+00
	-	-	-	0.0	-	106.1 ± 3.3	1.04 ± 0.04	19	67.16	2.71e-07
RX J1539.5-8335	extr	29	0.20	21.8 ± 3.1	7.1	115.1 ± 5.8	1.32 ± 0.11	26	13.29	9.81e-01
	-	-	-	0.0	-	135.3 ± 4.5	0.83 ± 0.04	27	40.39	4.71e-02
	flat	-	-	25.9 ± 2.9	9.1	110.0 ± 5.8	1.41 ± 0.12	26	13.52	9.79e-01

Table B.5: Summary of Entropy Profile Fits (continued)

Cluster	Method	N_{bins}	r_{max} Mpc	K_0 keV cm^2	$\sigma_{K_0} > 0$	K_{100} keV cm^2	α	DOF	χ^2	p-value
(1)	(2)	(3)	(4)	(5)	(6)	(7)	(8)	(9)	(10)	(11)
	-	-	-	0.0	-	133.7 ± 4.5	0.79 ± 0.04	27	54.08	1.49e-03
RX J1720.1+2638	extr	30	0.40	20.7 ± 1.9	10.7	109.7 ± 5.4	1.38 ± 0.06	27	5.34	1.00e+00
	-	-	-	0.0	-	145.3 ± 3.6	0.98 ± 0.03	28	94.37	4.06e-09
	flat	-	-	21.0 ± 1.9	10.9	109.1 ± 5.4	1.39 ± 0.06	27	5.56	1.00e+00
	-	-	-	0.0	-	145.3 ± 3.6	0.98 ± 0.03	28	97.94	1.09e-09
RX J1720.2+3536	extr	13	0.32	17.5 ± 3.5	4.9	101.8 ± 7.9	1.35 ± 0.10	10	2.47	9.91e-01
	-	-	-	0.0	-	129.4 ± 4.7	1.00 ± 0.04	11	23.76	1.38e-02
	flat	-	-	24.0 ± 3.3	7.2	94.4 ± 7.8	1.42 ± 0.11	10	2.67	9.88e-01
	-	-	-	0.0	-	131.3 ± 4.7	0.92 ± 0.04	11	40.43	3.02e-05
RX J1852.1+5711	extr	12	0.12	13.7 ± 6.3	2.2	184.3 ± 12.8	0.96 ± 0.15	9	2.63	9.77e-01
	-	-	-	0.0	-	182.4 ± 10.9	0.73 ± 0.05	10	5.31	8.70e-01
	flat	-	-	18.7 ± 8.3	2.3	170.4 ± 11.8	0.83 ± 0.16	9	5.06	8.29e-01
	-	-	-	0.0	-	173.3 ± 9.8	0.58 ± 0.04	10	7.26	7.01e-01
RX J2129.6+0005	extr	22	0.40	18.0 ± 3.8	4.7	100.8 ± 8.1	1.24 ± 0.10	19	7.01	9.94e-01
	-	-	-	0.0	-	129.2 ± 4.8	0.91 ± 0.05	20	21.36	3.76e-01
	flat	-	-	21.1 ± 3.7	5.7	97.9 ± 8.0	1.26 ± 0.10	19	7.16	9.93e-01
	-	-	-	0.0	-	130.8 ± 4.8	0.87 ± 0.04	20	26.01	1.66e-01
SC 1327-312	extr	31	0.15	65.5 ± 10.1	6.5	160.4 ± 12.5	0.80 ± 0.14	28	1.08	1.00e+00
	-	-	-	0.0	-	212.5 ± 8.1	0.36 ± 0.03	29	15.85	9.77e-01
	flat	-	-	64.6 ± 9.9	6.5	160.8 ± 12.5	0.81 ± 0.14	28	1.03	1.00e+00
	-	-	-	0.0	-	212.0 ± 8.1	0.37 ± 0.03	29	16.01	9.75e-01
Sersic 159-03	extr	23	0.12	7.5 ± 0.8	9.7	79.7 ± 2.3	1.06 ± 0.05	20	15.95	7.20e-01
	-	-	-	0.0	-	77.9 ± 2.0	0.72 ± 0.02	21	77.11	2.44e-08
	flat	-	-	10.5 ± 0.7	15.0	77.8 ± 2.4	1.17 ± 0.06	20	16.81	6.65e-01
	-	-	-	0.0	-	74.0 ± 1.9	0.65 ± 0.02	21	136.22	7.00e-19
SS2B153	extr	38	0.07	1.1 ± 0.2	6.9	71.4 ± 2.1	0.80 ± 0.02	35	24.19	9.15e-01
	-	-	-	0.0	-	63.4 ± 1.4	0.69 ± 0.01	36	59.46	8.24e-03

Table B.5: Summary of Entropy Profile Fits (continued)

Cluster	Method	N_{bins}	r_{max} Mpc	K_0 keV cm^2	$\sigma_{K_0} > 0$	K_{100} keV cm^2	α	DOF	χ^2	p-value
(1)	(2)	(3)	(4)	(5)	(6)	(7)	(8)	(9)	(10)	(11)
	flat	-	-	1.1 ± 0.2	6.9	71.4 ± 2.1	0.80 ± 0.02	35	24.19	9.15e-01
	-	-	-	0.0	-	63.4 ± 1.4	0.69 ± 0.01	36	59.46	8.24e-03
UGC 3957	extr	36	0.12	11.0 ± 1.0	11.2	180.8 ± 7.3	1.01 ± 0.04	33	6.63	1.00e+00
	-	-	-	0.0	-	151.9 ± 5.1	0.68 ± 0.02	34	84.60	3.37e-06
	flat	-	-	12.9 ± 1.0	12.5	175.1 ± 7.1	0.98 ± 0.04	33	6.95	1.00e+00
	-	-	-	0.0	-	144.2 ± 4.7	0.62 ± 0.02	34	91.61	3.48e-07
UGC 12491	extr	23	0.04	3.0 ± 0.2	13.8	148.5 ± 11.7	1.12 ± 0.04	20	445.44	7.29e-82
	-	-	-	0.0	-	77.4 ± 3.4	0.70 ± 0.02	21	2353.02	0.00e+00
	flat	-	-	3.0 ± 0.2	13.8	148.5 ± 11.7	1.12 ± 0.04	20	445.44	7.29e-82
	-	-	-	0.0	-	77.4 ± 3.4	0.70 ± 0.02	21	2353.02	0.00e+00
ZWCL 1215	extr	36	0.25	163.2 ± 35.6	4.6	131.3 ± 43.6	1.00 ± 0.32	33	2.94	1.00e+00
	-	-	-	0.0	-	314.8 ± 10.9	0.37 ± 0.05	34	7.69	1.00e+00
	flat	-	-	163.2 ± 35.6	4.6	131.3 ± 43.6	1.00 ± 0.32	33	2.94	1.00e+00
	-	-	-	0.0	-	314.8 ± 10.9	0.37 ± 0.05	34	7.69	1.00e+00
ZWCL 1358+6245	extr	26	0.60	13.8 ± 3.3	4.2	102.3 ± 9.5	1.40 ± 0.08	23	5.58	1.00e+00
	-	-	-	0.0	-	130.6 ± 6.1	1.15 ± 0.05	24	19.02	7.51e-01
	flat	-	-	20.7 ± 3.2	6.4	98.0 ± 9.4	1.43 ± 0.09	23	5.65	1.00e+00
	-	-	-	0.0	-	138.5 ± 6.1	1.04 ± 0.05	24	32.17	1.23e-01
ZWCL 1742	extr	17	0.12	13.8 ± 1.5	9.0	147.7 ± 9.4	1.39 ± 0.11	14	14.80	3.92e-01
	-	-	-	0.0	-	122.0 ± 6.1	0.78 ± 0.04	15	55.08	1.73e-06
	flat	-	-	23.8 ± 1.7	14.4	126.5 ± 9.0	1.30 ± 0.12	14	24.08	4.49e-02
	-	-	-	0.0	-	100.7 ± 4.5	0.48 ± 0.03	15	69.54	5.39e-09
ZWCL 1953	extr	17	0.45	194.5 ± 56.6	3.4	62.1 ± 57.0	1.39 ± 0.65	14	0.99	1.00e+00
	-	-	-	0.0	-	283.3 ± 27.3	0.45 ± 0.11	15	4.39	9.96e-01
	flat	-	-	194.5 ± 56.6	3.4	62.1 ± 57.0	1.39 ± 0.65	14	0.99	1.00e+00
	-	-	-	0.0	-	283.3 ± 27.3	0.45 ± 0.11	15	4.39	9.96e-01
ZWCL 3146	extr	15	0.30	11.4 ± 2.0	5.7	105.5 ± 6.4	1.29 ± 0.08	12	5.24	9.49e-01

Table B.5: Summary of Entropy Profile Fits (continued)

Cluster	Method	N_{bins}	r_{max} Mpc	K_0 keV cm^2	$\sigma_{K_0} > 0$	K_{100} keV cm^2	α	DOF	χ^2	p-value
(1)	(2)	(3)	(4)	(5)	(6)	(7)	(8)	(9)	(10)	(11)
	-	-	-	0.0	-	126.3 ± 4.5	0.98 ± 0.03	13	31.82	2.55e-03
	flat	-	-	11.4 ± 2.0	5.7	105.5 ± 6.4	1.29 ± 0.08	12	5.24	9.49e-01
	-	-	-	0.0	-	126.3 ± 4.5	0.98 ± 0.03	13	31.82	2.55e-03
ZWCL 7160	extr	21	0.40	18.8 ± 3.2	5.9	89.3 ± 7.3	1.34 ± 0.10	18	2.43	1.00e+00
	-	-	-	0.0	-	117.0 ± 4.8	0.93 ± 0.05	19	29.31	6.13e-02
	flat	-	-	21.1 ± 3.1	6.8	86.3 ± 7.2	1.37 ± 0.10	18	2.82	1.00e+00
	-	-	-	0.0	-	116.9 ± 4.8	0.90 ± 0.05	19	36.37	9.49e-03
Zwicky 2701	extr	24	0.40	34.0 ± 4.2	8.2	135.1 ± 10.3	1.37 ± 0.10	21	4.79	1.00e+00
	-	-	-	0.0	-	187.1 ± 6.6	0.87 ± 0.04	22	43.01	4.71e-03
	flat	-	-	39.7 ± 3.9	10.1	126.0 ± 10.2	1.45 ± 0.10	21	5.67	1.00e+00
	-	-	-	0.0	-	186.4 ± 6.7	0.82 ± 0.04	22	60.27	2.04e-05
ZwCl 0857.9+2107	extr	16	0.30	23.6 ± 5.0	4.8	89.6 ± 10.4	1.40 ± 0.17	13	0.92	1.00e+00
	-	-	-	0.0	-	116.8 ± 7.3	0.86 ± 0.07	14	14.36	4.24e-01
	flat	-	-	24.2 ± 5.0	4.9	89.3 ± 10.4	1.40 ± 0.18	13	0.88	1.00e+00
	-	-	-	0.0	-	116.9 ± 7.4	0.85 ± 0.07	14	14.76	3.95e-01

Appendix C: Chandra Observations Reduction Pipeline (CORP)

This appendix has been written as a tutorial for the first-time analyzer of *Chandra* data (*e.g.* the "you" role in the text). "When your CIAO-Fu is good, only then will you utilize the stowed backgrounds of the CalDB."

C.1 Copyright

As a formality, I have blanketed CORP with the GNU General Public License. Below is the copyright and license agreement for all scripts in CORP:

C.2 Introduction to CORP

The reduction and analysis of *Chandra* data is given in exquisite detail in the CIAO threads on the CXC's web site[1]. There is very little which is not discussed in the CIAO and HelpDesk threads at the CXC web site. However, to streamline the lengthy reduction and analysis process of extended X-ray sources, such as galaxy clusters and groups, I have written several Perl and IDL scripts which make-up my own *Chandra* Observations Reduction Pipeline (CORP, pronounced "core"). The purpose of this pipeline software is to condense CIAO's tedious prompts and command line intensive steps into an easily executable series of scripts which require minimal interaction and produce science-ready data products. A pipeline also ensures that a large sample of observations are reduced the same way, and a pipeline also eases the pain of analyzing several hundred observations.

There is a critical caveat to the use of CORP and analyzing *Chandra* data in general: **no two *Chandra* observations are the same!** CORP has allowances for many different tool settings and instrument setups, but these options are finite, and no amount of automation can replace human interactivity. It is an absolute ****necessity**** that users of CORP view, scrutinize, and double check the output of every reduction/analysis step. This can be time consuming, but not nearly as time consuming as finding and correcting errors embedded in on-going, or goodness forbid, **published** work.

As of writing this dissertation, all CORP scripts properly interact with CIAO 3.4.1 and CalDB 3.4. The CXC software versions matter because the CXC programmers (whom are great people!) have a tendency to reinvent the wheel every so often. This may result in a change to output filenames, extensions, header keywords, data types, et cetera and can cause a script to err. Errors are not guaranteed however, so it is important to be mindful of how CIAO or the CalDB have changed as

[1] http://cxc.harvard.edu/ciao/threads/index.html

a result of an update (release notes are always provided with an update: read them!). There are some pretty great updates to CIAO included in the final 4.1 version, so I highly recommend CORP users email me to request new scripts when CIAO 4.1 is fully deployed.

Now for a few notes about me, the author and programmer:

1. I use plenty of analysis and X-ray "jargon" in this Appendix. If you come across nomenclature which is unfamiliar, consult the CXC web site, there is absolutely nothing you could want to know about *Chandra* that is not there. CORP is my method for automating most of the logic trees which are in the CXC threads, but this does not mean CORP's operation will always be transparent to a user.

2. I am not a computer programmer. In fact, I only knew pseudo-code when I entered graduate school. Hence, my style of programming is best described as inelegant and brutish. Computer resources are cheap and abundant, so I use lots of inefficient code, but the overhead and time consumption are low, so writing efficient code does nothing to accelerate my work. The scripts of CORP use no command line options besides input, and sometimes output, filenames. Everything the script is being commanded to do is controlled by opening the code and editing the "Options" section near the beginning of the program. Do not worry, it's as simple as editing a Word document.

3. As of now, the scripts are available via a tarball which I will email you. Someday distribution of the code will be handled through a public CVS server. The tarball contains all the scripts, a README file (which is a copy of this appendix), and a folder of example data. Descriptions of what each script does, how it is called, what it takes as input, and what is generated as output are all listed in the header of each program.

4. I am not a debugger. Each script is written to run a very specific set of tasks.

Given the proper input, the scripts return the expected output. However, while I wish the scripts were magic, alas, they are not. If you plan on giving the programs non-standard input and there is some operation you are not sure the script will perform, then find out first by dissecting the code. I may have coded a script to handle your odd data, but I may not. Find out first!

C.3 Initial Reprocessing

C.3.1 Retrieving Data

Getting *Chandra* data from the CDA is not complicated. There are three methods to get data: (1) run the stand-alone *Chaser* program, (2) use the web-based version of *Chaser*, named *WebChaser*[2], or (3) run my script `query_cda.pl`. The first thing to do is determine which ObsIDs need to be downloaded. This is accomplished by searching the CDA via *WebChaser*. The *WebChaser* form is self-explanatory: search via object name, sky coordinates, or using any set of other listed methods and options. After searching the CDA, a list of archived observations will be returned. **VERY IMPORTANT:** Now is the time to make a one column file where each line lists one of the ObsIDs to be downloaded:

```
#Obsid
2419
791
etc.
```

This file is needed to download data and build the reference file used by every script in CORP.

Open the script `query_cda.pl` with an editor (like emacs or xemacs). Within the script are three vital options that need to be set: `$get_nh, $get_z`, and `$get_data`.

[2]http://cda.harvard.edu/chaser/

When set to 'yes', these options tell the script to: (1) find the Galactic absorbing column density ($N_{\rm H}$) using the LAB survey (Kalberla et al., 2005), (2) acquire a redshift from NED[3], and (3) download data from the CDA. The `$get_nh` is trustworthy, so set it to 'yes'. However, the `$get_z` option is not robust. The NED query returns a list of galaxy clusters nearest the aimpoint of the *Chandra* observation, but the proper redshift is not always returned. I typically leave this option set to 'yes' and confirm redshifts by manually querying NED (hey, it's less typing).

The `$get_data` option will cause the script to download data and create a directory for each ObsID and place both into the directory specified by the variable `$dest`. The CDA is large, so a pre-compiled listing of where every ObsID is stored is provided in the file `cdaftp.dat` (this file is part of the CORP tarball). The variable `$ftpdat` needs to point to where this file is stored. The CDA is continually updated, so you will need to update `cdaftp.dat` from time to time. This is accomplished by running:

```
[linux]% perl build_cdaftp.pl <output_filename>
```

Now, run the query script. **WARNING:** If there is an existing `newref.list` in the working directory, it will be overwritten.

```
[linux]% perl query_cda.pl <my_list_of_obsids>
```

The download time is completely dependent on download speed, so if there are many ObsIDs to download, work on something else for a while. The script tells the user what $N_{\rm H}$ and redshift it has found and for what object. The script also informs the user how many of the input ObsIDs were successfully found in the CDA and the total exposure time of observations in the query. You will now have new directories which bear the names of the downloaded ObsIDs (for example, `<hard_drive>/<my_root_datadir>/<obsid>`). There should also be a new file named `newref.list`. Each column within `newref.list` is described below:

[3] http://nedwww.ipac.caltech.edu/

Name: This is the name of the `TARGET` object listed for the observation. This is not necessarily the name you'd like to give the object, so feel free to change it.

ObsID: Obviously this is the ObsID. Most of the file naming convention in CORP involves the ObsID since it is a unique identifier. This may seem clumsy and awkward (especially for the clusters that have multiple ObsIDs) but in the battle of clarity and brevity, clarity wins in my book.

RA: The right ascension of the observation target object. The default output format is decimal degrees, but this can be changed to sexigesimal by changing the `query_cda.pl` variable `$outcrdunit` from `'decimal'` to `'sexigesimal'`.

Dec: The declination of the observation target object in decimal degrees.

Rmax: The maximum observation radius. This is the radius from the cluster center to the nearest detector edge. Rmax needs to be specified by the user for each observation. A script which automatically finds Rmax is forthcoming.

MinCts: The minimum number of counts per temperature annulus. The default is 2500 but this number should be increased for observations with sufficient counts or adjusted depending on scientific goals.

z: The redshift of the target object. Even if the script has automatically queried NED for this value, it is best to double-check. A batch query via NED is simple[4].

Nh20: The galactic absorbing neutral hydrogen column density, $N_{\rm H}$, in $10^{20}{\rm cm}^{-2}$. These values are acquired from the `nh` tool which uses the L.A.B. Survey results (Kalberla et al., 2005).

Tx: The global/virial cluster temperature. There are a number of ways to measure to a cluster temperature, it is best to keep a detailed record of how you made this measurement or where you looked-up the temperature (*e.g.* KEEP CITATIONS you'll want them later). If no temperature can be found in the literature, the script `$find_tx.pl` should be used to determine the cluster temperature. This script iter-

[4]http://nedwww.ipac.caltech.edu/help/batch.html

atively determines temperature in core-excised annuli using a user-specified fraction of the virial radius as the outer radius. When to run the script after removing is specified later.

Fe: The global cluster metallicity. The value listed in the reference file is used only as a starting point for most spectral fits, so the value listed is not all that important. I'd go as far to say this is a deprecated entry. Again, if this value if looked-up in the literature, keep a citation record.

Lbol: The cluster bolometric luminosity. *Chandra* has a small field of view, so if this is a value best taken from the literature, for example from Horner (2001).

Chip: The CCD on which the cluster center is located. The default is to list the array on which the observation is taken (I or S), but specifying which `chip_id` (*i.e.* S3 or I0) is left to the user.

E_obs, Diff, Robs: These are deprecated columns which have been left-in because most scripts were written before they were no longer needed. Forthcoming versions of CORP will not need these columns.

Location: Sometimes data is stored across multiple volumes, hence this column specifies the path to each ObsID. For example if one ObsID is stored on `/mnt/HD1` and another is on `/media/USB1`. This allows a single instance of a script to be run on distributed data.

Great! The data is now out of the archive and into your hands. What are all these different files? The answer to that question is lengthy and of fundamental importance in honing your CIAO-Fu. Read the documentation on data products[5,6].

Included in the CORP tarball is a script named `ds9_viewreg.pl`. The script is very useful for viewing observations quickly and has been invaluable throughout the years. The program performs a multitude of tasks and relies on the functionality of

[5]http://cxc.harvard.edu/ciao/data/basics.html
[6]http://cxc.harvard.edu/ciao/threads/intro_data/

DS9[7]. The script header completely explains all the variables and how to use the program. Before starting the bulk of data reduction I recommend using `ds9_viewreg.pl` to determine the `Chip` and `Rmax` values for each ObsID and then entering them into the `newref.list` file.

C.3.2 Create New Level-2 Events File

Before completing any true analysis, such as finding the cluster center or identifying point sources, the CIAO threads recommend creating a new events file. Removing bad grades, time intervals with flares, bad pixels, et cetera ensures that analysis further downstream is more robust. The initial reprocessing step described here requires running the script `reprocess.pl` with some, but not all, of the internal switches set to "yes". Descriptions for the internal switches of this program are in the code header. The program `reprocess.pl` performs multiple tasks and will be used more than once: In the first pass, `reprocess.pl` will perform the tasks outlined below, later it will be used to exclude point sources. For more detail on any of the steps below, read the CIAO documentation[8,9].

First, edit the script so all the options are "yes" and only `$exclude` is equal to "no". To run the script, simply call it with Perl giving the reference file as input (if you do not want an ObsID analyzed, simply comment it out of the reference file by placing a "#" at the front of the line):

```
[linux]% perl reprocess.pl reference.list
```

There is no specific version of Perl required to run CORP. For each ObsID in the reference file, a new `reprocessed` subdirectory has been created and all new files have been placed in that directory. The output files are listed at the end of the script header. The reduction steps performed by `reprocess.pl` are: remove the ACIS

[7] http://hea-www.harvard.edu/RD/ds9/
[8] http://cxc.harvard.edu/ciao/guides/acis_data.html
[9] http://cxc.harvard.edu/ciao/threads/createL2/

afterglow, create a new bad pixel file, set `ardlib.par`, update time-dependent gain (TGAIN), apply charge transfer inefficiency (CTI) correction (if appropriate), filter on event grade, filter on good time intervals (GTIs), destreak, remove background flares and/or periods of excessively high background, make blank-sky background file, and make off-axis blank-sky background file.

Cleaning for flares is a detailed step and is best understood by reading the CIAO documentation. The main steps in extracting and filtering a light curve are removing bright sources, setting the time bin size specific to front or back illuminated CCDs, setting the energy window for the specific CCD type, analyzing the light curve using the contributed routine `lc_clean.sl`, and filtering out the time periods from the GTIs which contain high background. All of these steps are handled automatically by the script, however `lc_clean.sl` **DOES NOT** always find the proper background count rate mean. This results in the beginning or end of flare not being excluded from the GTIs, while perfectly good intervals are excluded (see Figure C.1 as an example). The solution to this problem is very simple.

After reprocessing you should examine each light curve anyway, so finding these cases will be easy. Run

```
[linux]% perl view_prof.pl reference.list
```

with the internal switches set to view lightcurves. If the lightcurve cleaning failed then there will be no lightcurve to view, in which case run the following script for only those clusters which experienced a failure (logged in `errors.log`) by commenting out all the clusters in `reference.list` (placing a `#` at the beginning of the line in `reference.list`) which did not fail, then running:

```
[linux]% idl
IDL> load_ltcrv, 'reference.list'
```

When you find a case where a flare has been improperly removed, estimate the mean background count rate by finding the peak in the count rate distribution in

the bottom pane of the figure. Now we'll create a new ASCII file which contains information about this OBSID and it's flare. The file should have the format:

```
#Obsid  Mean Rate
2419    1.300
791     0.175
```

Save this file, set the `$flarefile` keyword in `reprocess.pl` to point to this new file, and now re-run `reprocess.pl` with all other options set to "no" except the `$clean_events` option which should be "yes". Examine the new lightcurve and repeat this process if the mean is not exactly where you think it should be.

Making blank-sky backgrounds is easily the most involved step in `reprocess.pl` and to fully understand what is being done, reading Maxim Markevitch's Cookbook[10] in conjunction with the background thread[11] are a must.

After `reprocess.pl` has finished running, it is wise to spend the time examining all of the output files. This entails steps such as viewing the `evt1, evt2, bgevt,` and `clean` files; checking the light curves for missed or improperly excluded flares; verifying the background file have the proper exposure times in the headers. If the data is trustworthy, then move along.

C.3.3 Remove Point Sources and Identify Cluster Center

Determining the cluster center and identifying points sources for exclusion is a crucial step in extended source analysis as these steps significantly affect the final results. Reliably determine the cluster center and finding point sources first requires an exposure map. An exposure map is a replication of the optical system's characteristics (*e.g.* CCD quantum efficiency, CCD non-uniformities, vignetting, bad pixels, etc.) dithered and exposed exactly as the observation. The exposure map is used to re-

[10] http://cxc.harvard.edu/contrib/maxim/acisbg/
[11] http://cxc.harvard.edu/ciao/threads/acisbackground/

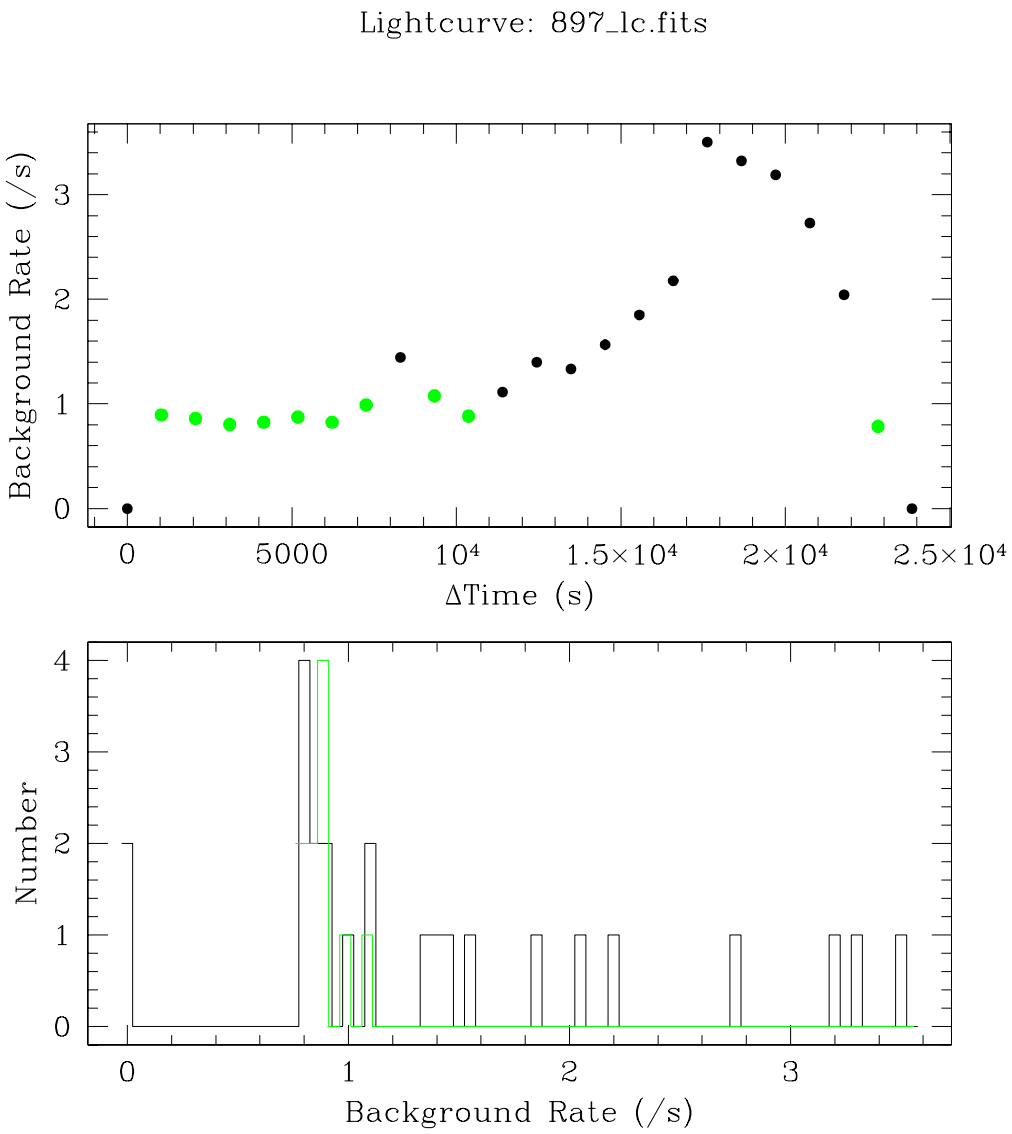

Figure C.1 Shown here is an example light curve output by `lc_clean.sl` which is called when `reprocess.pl` is run. *Top panel:* Plot of background count rate versus time in the observation. Green points mark those time intervals within ±20% of the mean rate. Zero rate bins at the beginning and end of an observation are intentional dead times. The flares can easily be identified in this example. Also note that the automated mean detection did not remove the wings at ∼ 5 ksec and ∼ 9 ksec of the weaker flare. *Bottom panel:* Histogram of the light curve shown in the top panel. The green line is again for the intervals within ±20% of the mean rate.

move instrumental features, like chip gaps, which will be erroneously detected as point sources or skew the calculation of the cluster center.

There are two ways of calculating an exposure map: using a monoenergetic incident spectrum or a more specific spectral model. The script for making exposure maps can do both, and it is up to the user to determine if one or the other is preferred for their analysis. For all of the clusters I have analyzed, the monoenergetic assumption does not give significantly different results from the more elegant spectral model method.

There are many options for making an exposure map and they are explained in the script header. To make an exposure map, run the script `exp_map.pl`:

```
[linux]% perl exp_map.pl reference.list
```

The output will be an instrument map, aspect histogram, exposure map, and a normalized image of the cluster (in flux units). The normalized image is what will be used to find point sources and find the cluster center. By default, the script makes a full resolution (binning=1) exposure map. This has the drawback of being time consuming, but the advantage of more accuracy in spatial analysis. If you are simply experimenting data, then increase the binning factor to four or eight. I do not recommend using such highly binned data for analysis unless the cluster center is especially obvious (*i.e.* in highly peaked clusters) or you plan on remaking point source exclusion regions by hand.

Now that you have an exposure map, edit the options in the script `cent_emi.pl` and run the script.

```
[linux]% perl cent_emi.pl reference.list
```

or

```
[linux]% perl dub_centroid.pl dub_reference.list
```

This program will find the cluster centroid and peak using the CIAO tool `dmstat`. If these two quantities differ by less than 70 kpc, the peak will be returned as the

cluster center. The script also outputs a new reference file with the cluster center in the RA and Dec columns. Now is the moment to be a researcher: view the clusters with the center marked, does this solution look right?

After determining if the cluster center finder worked properly, the next step is to identify and exclude point sources. The script which does this is `find_pt_src.pl` which calls the CIAO tool `wavdetect`. The primary script output is an ASCII file listing the exclusion regions.

```
[linux]% perl find_pt_src.pl reference.list
```

It is very important at this stage to view the observation with the exclusion regions overlaid. The `wavdetect` algorithm is very sophisticated, however it will miss sources (*e.g.* sources very close together), detect spurious sources (*e.g.* chip gaps and edges), detect sources which are bright, diffuse cluster emission (*e.g.* the core of a bright, peaky cluster), and miss sources in regions of high background (*e.g.* point sources in or near bright cluster core).

While viewing the observation and regions with `ds9_viewreg.pl`, it is straight forward to delete, add, and alter regions. After doing so, go to the 'Regions' menu, 'File Format' tab, and click 'Ciao'. Then under the 'Regions' menu click 'Save regions...' and simply overwrite the loaded `<obsid>_exclude.reg` region file. That is all it takes to edit the exclusion regions in a quick, by-eye batch session. Now edit the script `reprocess.pl` so that all options are "no" except for the `$exclude` option which should be "yes". Running `reprocess.pl` will now remove all the regions you just saw/specified in DS9.

```
[linux]% perl reprocess.pl reference.list
```

The output from this final step is the file `<obsid>_exclude.fits` which is the crown jewel of CORP: an up-to-date, flare-clean, point source-clean, events file at level-2. As usual, you should view this file and make sure the point source exclusion functioned as expected. The initial reprocessing steps are now complete, congrats.

C.4 Intermediate Analysis

If at this point you still do not have a temperature for some number of clusters, run the following script to find one:

```
[linux]% perl find_tx.pl reference.list
```

This script can also be used to determine redshifts and metallicities. Read the script header for more detailed instructions on use.

The intermediate analysis steps involve extracting radial profiles and spectra from the observations. These radial profiles form the basis for the final analysis steps of the next section. One script, `make_profile.pl`, extracts both a cumulative counts profile and a surface brightness profile. In the options section of the script you specify the size of the annular bins used to extract the profiles. For the cumulative counts profile I recommend 2 pixel width bins, and either 5 pixel or 10 pixel width bins for the surface brightness profiles. For the surface brightness profiles you also need to specify the energy range for the extraction. There are many other options for this script which are detailed in the program header.

```
[linux]% perl make_profile.pl reference.list
```

or

```
[linux]% perl make_multiprof.pl dub_reference.list
```

Depending on the number of counts in the observation, this step can take a few minutes or a few hours. The script also outputs plots of the two profiles which should be viewed to ensure everything ran correctly.

Now run the script `exp_corr.pl` which extracts a radial profile from the exposure map and will be used for exposure correcting radial profiles later on. As usual, set the options in the header, specifically the bin size of the profile to extract. The bin size needs to match that of the surface brightness profile just extracted. It is possible to extract multiple exposure profiles since the bin size is amended to the output file

name. This step is fast, so extracting profile for bin sizes of 5, 10, or 20 pixels does not take long.

```
[linux]% perl exp_corr.pl reference.list
```

or

```
[linux]% perl multiexp_corr.pl dub_reference.list
```

With the cumulative profile, it is now possible to create annuli for the temperature profile. The script `make_annuli_reg.pro` is used to make the annuli. The cumulative profile is divided up into annular bins containing a minimum number of counts and then these bins are output as region files later used to extract spectra. The entries in the 'Mincts' column of the reference file are used to set the minimum number of counts. I typically run the script with all options set to "no" (meaning only mock regions are produced) and view the output plot to ensure the number and spacing of the bins is appropriate for the cluster in question. What is appropriate? Well, too many closely spaced annuli for a symmetric peaked cluster is redundant, and too few widely spaced annuli for a complex cluster is insufficient, unless of course there are not enough counts to produce more bins. After ensuring the number of annuli produced is agreeable, run the script with the options set to "yes". **WARNING:** by default, the script deletes all annuli and associated spectral files. If you run this script after having extracted spectra, be sure to set `mkbackup` to "yes" AND provide the path to a valid, existing back-up directory, `bkdir`, this will save those existing spectra.

```
[linux]% idl
IDL> make_annuli_reg, 'reference.list'
```

or

```
IDL> make_multiannuli_reg, 'reference.list'
```

A whole ensemble of individual region files with the specified name will be output by this script. With these region files extracting spectra is straightforward, simply

run the script `extract_spectra.pl`. This script has a number of important options which are detailed in the script header.

```
[linux]% perl extract_spectra.pl reference.list
```

If there have been no errors, then you should have radial profiles and spectra for each ObsID in the reference file, congratulations.

C.5 Final Analysis

The final steps in the analysis process are normalizing the background spectra for differences between the blank-sky background and observation background hard-particle count rates, extracting and fitting residual spectra for the local soft background, fitting the cluster spectra, and running the master IDL routine that produces entropy profiles. An explanation of why and how background adjustments are made is presented in Chapter 2.

C.5.1 Spectral Adjustments and Fitting

The hard-particle background is changing as a function of time. Thus, the strength of this background component for the epoch in which the blank-sky backgrounds were taken will be different from when the observations were taken. The first step in accounting for this difference involves running the script `bgd_ratio.pl` which will output the ratio of observation to blank-sky 9.5-12.0 keV count rates.

```
[linux]% perl bgd_ratio.pl reference.list
```

The script outputs a file containing these ratios. Keep this file someplace which is easily accessible as a later script will be querying this list to normalize the spectra.

To account for the spatially varying Galactic soft-component you must extract soft-residuals. Soft-residuals are the leftovers of subtracting a blank-sky spectrum

from an observation spectrum both extracted from the same part of the sky and far from the cluster emission. The first step is to clean-up the off-axis observation chips of all point and diffuse sources. This step can be performed blind because if too many sources are removed it does not matter.

```
[linux]% perl addbg_rm_pt_src.pl reference.list
```

The soft-residual spectra are output from this script.

Prior to fitting any spectra all background spectra need to be normalized. This is done quickly by specifying the names of the spectra to be normalized in the script `adj_backscal.pl` and then running it.

```
[linux]% perl adj_backscal.pl reference.list
```

Normalization is applied by adjusting the header keyword `BACKSCAL` in the spectrum. The `BACKSCAL` keyword is related to the final background subtracted spectrum of an observation by

$$SPEC_{ctr} = \frac{SRC_{cts}}{SRC_{exp}} - \frac{BGD_{cts}}{BGD_{exp}} \cdot \frac{1}{BGD_{scal} \cdot SRC_{scal}} \tag{C.1}$$

where the abbreviations 'SRC' $\rightarrow$ source, 'BGD' $\rightarrow$ background, 'ctr' $\rightarrow$ count rate, 'cts' $\rightarrow$ counts, 'exp' $\rightarrow$ exposure time, and 'scal' $\rightarrow$ `BACKSCAL`. The `BACKSCAL` keyword is defined as the detector area over which the spectrum was extracted, divided by the total detector area. Adjustment of the blank-sky background `BACKSCAL` value follows directly from the above equation by multiplying the existing value of `BACKSCAL` by a correction factor, η, which is related to the ratio of the count rate in the 9.5-12.0 keV range of the observation to the blank-sky background by

$$\eta = (\frac{OBS_{ctr}}{BGD_{ctr}})^{-1}. \tag{C.2}$$

Each background spectrum is copied into a new file before this correction is applied so that reversal at a later date is possible.

Now that the spectra are all adjusted, the fitting can begin. There are a large number of options in spectral fitting and these are detailed in the individual script's header. In addition, interpreting the results of the fitting requires more discussion than is useful here. The order in which fitting is done is important since the master spectral fitting routines need output from the fitting of the soft-residuals.

```
[linux]% perl fit_sofex.pl reference.list <spectral model>
[linux]% perl fit_projected.pl reference.list <spectral model>
or
[linux]% perl fit_simulta.pl dub_reference.list <spectral model>
```

The output of these scripts are data tables with the spectral fits for each annulus associated with each ObsID. With radial profiles in-hand and spectral analysis complete, it is now possible to calculate many more physical properties of a cluster.

C.5.2 Generating Entropy Profiles

So here it is, the end of a long journey. Your CIAO-Fu is good, congratulations. The master program which performs the deprojection, derives electron gas density, pressure, entropy, mass (not to be trusted), and cooling time is `kfitter.pro`. This program has a handler program `run_kfit.pro` which makes batch analysis simpler. These programs have their own `README` files which have not been duplicated here. After running `kfitter.pro` you will have a suite of data tables and plots for each cluster which are publication ready.

C.5.3 Additional Code

I have coded many other tools which are extremely useful in the analysis of galaxy clusters. If you would like to use any of the following tools, simply email me or check

the public CVS repository.

1. Batch query NVSS, SUMSS, or VLA First for radio sources within a region of interest.

2. Calculate the X-ray and Sunyaev-Zel'dovich signatures for a mock cluster based on user input parameters.

3. Generate an image and calculate properties of the Chandra PSF for any location or energy on the ACIS-S or ACIS-I arrays.

4. Generate 2D maps of cluster properties (temperature, density, entropy, abundance, pressure, hardness ratio, *etc.*) and return nice profiles and LaTeX tables for each.

5. Create MySql and/or FITS databases from ASCII tables of cluster data.

6. Calculate gas mass and gravitating mass profiles for a cluster with known temperature and density.

7. Many other tools for simulating data, extracting spectra, making web pages, and on and on.

"Pasta be upon you."

-FSM

BIBLIOGRAPHY

Alexander, P. 2002, MNRAS, 335, 610

Allen, S. W., & Fabian, A. C. 1998a, MNRAS, 297, L57

—. 1998b, MNRAS, 297, L63

Allen, S. W., Fabian, A. C., Johnstone, R. M., White, D. A., Daines, S. J., Edge, A. C., & Stewart, G. C. 1993, MNRAS, 262, 901

Anders, E., & Grevesse, N. 1989, Geochim. Cosmochim. Acta, 53, 197

Andersson, K. E., & Madejski, G. M. 2004, ApJ, 607, 190

Antonucci, R., & Barvainis, R. 1994, AJ, 107, 448

Arnaud, K. A. 1996, in Astronomical Society of the Pacific Conference Series, Vol. 101, Astronomical Data Analysis Software and Systems V, ed. G. H. Jacoby & J. Barnes, 17–+

Arnaud, M., Aghanim, N., & Neumann, D. M. 2002, A&A, 389, 1

Arnaud, M., & Evrard, A. E. 1999, MNRAS, 305, 631

Ashman, K. M., Bird, C. M., & Zepf, S. E. 1994, AJ, 108, 2348

Bagchi, J., Durret, F., Neto, G. B. L., & Paul, S. 2006, Science, 314, 791

Balbus, S. A. 2000, ApJ, 534, 420

Balestra, I., Tozzi, P., Ettori, S., Rosati, P., Borgani, S., Mainieri, V., Norman, C., & Viola, M. 2007, A&A, 462, 429

Bauer, F. E., Fabian, A. C., Sanders, J. S., Allen, S. W., & Johnstone, R. M. 2005, MNRAS, 359, 1481

Becker, R. H., White, R. L., & Helfand, D. J. 1995, ApJ, 450, 559

Begelman, M. C., & Fabian, A. C. 1990, MNRAS, 244, 26P

Bialek, J. J., Evrard, A. E., & Mohr, J. J. 2001, ApJ, 555, 597

Binney, J., & Tabor, G. 1995, MNRAS, 276, 663

Bîrzan, L., Rafferty, D. A., McNamara, B. R., Wise, M. W., & Nulsen, P. E. J. 2004, ApJ, 607, 800

Bliton, M., Rizza, E., Burns, J. O., Owen, F. N., & Ledlow, M. J. 1998, MNRAS, 301, 609

Blumenthal, G. R., Faber, S. M., Primack, J. R., & Rees, M. J. 1984, Nature, 311, 517

Bock, D. C.-J., Large, M. I., & Sadler, E. M. 1999, AJ, 117, 1578

Böhringer, H., et al. 2004, A&A, 425, 367

—. 2007, A&A, 469, 363

Borgani, S., Governato, F., Wadsley, J., Menci, N., Tozzi, P., Quinn, T., Stadel, J., & Lake, G. 2002, MNRAS, 336, 409

Borgani, S., et al. 2001, ApJ, 561, 13

Bower, R. G. 1997, MNRAS, 288, 355

Bower, R. G., Benson, A. J., Lacey, C. G., Baugh, C. M., Cole, S., & Frenk, C. S. 2001, MNRAS, 325, 497

Bower, R. G., Benson, A. J., Malbon, R., Helly, J. C., Frenk, C. S., Baugh, C. M., Cole, S., & Lacey, C. G. 2006, MNRAS, 370, 645

Bower, R. G., McCarthy, I. G., & Benson, A. J. 2008, MNRAS, 390, 1399

Brighenti, F., & Mathews, W. G. 2006, ApJ, 643, 120

Brüggen, M., & Kaiser, C. R. 2002, Nature, 418, 301

Brüggen, M., Kaiser, C. R., Churazov, E., & Enßlin, T. A. 2002, MNRAS, 331, 545

Bryan, G. L., & Norman, M. L. 1998, ApJ, 495, 80

Bucher, S. 2007, Prospects and Issues for a Fifteen Year Chandra Lifetime

—. 2008, Chandra News, 15, 21

Buote, D. A., & Tsai, J. C. 1995, ApJ, 452, 522

—. 1996, ApJ, 458, 27

Burns, J. O. 1990, AJ, 99, 14

Burns, J. O., Hallman, E. J., Gantner, B., Motl, P. M., & Norman, M. L. 2008, ApJ, 675, 1125

Burns, J. O., Roettiger, K., Pinkney, J., Perley, R. A., Owen, F. N., & Voges, W. 1995, ApJ, 446, 583

Burns, J. O., White, R. A., & Hough, D. H. 1981, AJ, 86, 1

Canizares, C. R., Clark, G. W., Jernigan, J. G., & Markert, T. H. 1982, ApJ, 262, 33

Cardiel, N., Gorgas, J., & Aragon-Salamanca, A. 1998, MNRAS, 298, 977

Cash, W. 1979, ApJ, 228, 939

Cavagnolo, K. W., Donahue, M., Voit, G. M., & Sun, M. 2008a, ApJ, 683, L107

—. 2008b, ApJ, 682, 821

Cavaliere, A., & Fusco-Femiano, R. 1978, A&A, 70, 677

Cavaliere, A., Menci, N., & Tozzi, P. 1999, MNRAS, 308, 599

Chen, Y., Reiprich, T. H., Böhringer, H., Ikebe, Y., & Zhang, Y.-Y. 2007, A&A, 466, 805

Churazov, E., Sunyaev, R., Forman, W., & Böhringer, H. 2002, MNRAS, 332, 729

Clarke, T. E., Blanton, E. L., & Sarazin, C. L. 2004, ApJ, 616, 178

Clarke, T. E., Blanton, E. L., & Sarazin, C. L. 2005, in X-Ray and Radio Connections (eds. L.O. Sjouwerman and K.K Dyer) Published electronically by NRAO, http://www.aoc.nrao.edu/events/xraydio Held 3-6 February 2004 in Santa Fe, New Mexico, USA, (E7.08) 7 pages, ed. L. O. Sjouwerman & K. K. Dyer

Clowe, D., Bradač, M., Gonzalez, A. H., Markevitch, M., Randall, S. W., Jones, C., & Zaritsky, D. 2006, ApJ, 648, L109

Condon, J. J., Cotton, W. D., Greisen, E. W., Yin, Q. F., Perley, R. A., Taylor, G. B., & Broderick, J. J. 1998, AJ, 115, 1693

Cowie, L. L., & Binney, J. 1977, ApJ, 215, 723

Cowie, L. L., Songaila, A., Hu, E. M., & Cohen, J. G. 1996, AJ, 112, 839

Crawford, C. S., Allen, S. W., Ebeling, H., Edge, A. C., & Fabian, A. C. 1999, MNRAS, 306, 857

Crawford, C. S., Hatch, N. A., Fabian, A. C., & Sanders, J. S. 2005, MNRAS, 363, 216

Croton, D. J., et al. 2006, MNRAS, 365, 11

Dahle, H., Kaiser, N., Irgens, R. J., Lilje, P. B., & Maddox, S. J. 2002, ApJS, 139, 313

Dalla Vecchia, C., Bower, R. G., Theuns, T., Balogh, M. L., Mazzotta, P., & Frenk, C. S. 2004, MNRAS, 355, 995

David, L. P., Arnaud, K. A., Forman, W., & Jones, C. 1990, ApJ, 356, 32

David, L. P., Jones, C., & Forman, W. 1996, ApJ, 473, 692

David, L. P., & Kempner, J. 2004, ApJ, 613, 831

Dickey, J. M., & Lockman, F. J. 1990, ARA&A, 28, 215

Donahue, M., Gaskin, J. A., Patel, S. K., Joy, M., Clowe, D., & Hughes, J. P. 2003, ApJ, 598, 190

Donahue, M., Horner, D. J., Cavagnolo, K. W., & Voit, G. M. 2006, ApJ, 643, 730

Donahue, M., Mack, J., Voit, G. M., Sparks, W., Elston, R., & Maloney, P. R. 2000, ApJ, 545, 670

Donahue, M., Stocke, J. T., & Gioia, I. M. 1992, ApJ, 385, 49

Donahue, M., & Voit, G. M. 2004, in Clusters of Galaxies: Probes of Cosmological Structure and Galaxy Evolution, ed. J. S. Mulchaey, A. Dressler, & A. Oemler, 143–+

Donahue, M., Voit, G. M., O'Dea, C. P., Baum, S. A., & Sparks, W. B. 2005, ApJ, 630, L13

Donnelly, R. H., Markevitch, M., Forman, W., Jones, C., David, L. P., Churazov, E., & Gilfanov, M. 1998, ApJ, 500, 138

Dunn, R. J. H., & Fabian, A. C. 2008, MNRAS, 385, 757

Ebeling, H., Edge, A. C., Allen, S. W., Crawford, C. S., Fabian, A. C., & Huchra, J. P. 2000, MNRAS, 318, 333

Ebeling, H., Edge, A. C., Böhringer, H., Allen, S. W., Crawford, C. S., Fabian, A. C., Voges, W., & Huchra, J. P. 1998, MNRAS, 301, 881

Ebeling, H., Edge, A. C., & Henry, J. P. 2001, ApJ, 553, 668

Edge, A. C., Fabian, A. C., Allen, S. W., Crawford, C. S., White, D. A., Böhringer, H., & Voges, W. 1994, MNRAS, 270, L1+

Edge, A. C., & Frayer, D. T. 2003, ApJ, 594, L13

Edge, A. C., & Stewart, G. C. 1991, MNRAS, 252, 414

Edge, A. C., Stewart, G. C., & Fabian, A. C. 1992, MNRAS, 258, 177

Edge, A. C., Stewart, G. C., Fabian, A. C., & Arnaud, K. A. 1990, MNRAS, 245, 559

Eisenstein, D. J., et al. 2005, ApJ, 633, 560

Eke, V. R., Navarro, J. F., & Frenk, C. S. 1998, ApJ, 503, 569

Ettori, S. 2000, MNRAS, 311, 313

Evrard, A. E. 1989, ApJ, 341, L71

—. 1990, ApJ, 363, 349

—. 1997, MNRAS, 292, 289

Evrard, A. E., & Henry, J. P. 1991, ApJ, 383, 95

Evrard, A. E., Metzler, C. A., & Navarro, J. F. 1996, ApJ, 469, 494

Fabian, A. C. 1994, ARA&A, 32, 277

Fabian, A. C., Allen, S. W., Crawford, C. S., Johnstone, R. M., Morris, R. G., Sanders, J. S., & Schmidt, R. W. 2002, MNRAS, 332, L50

Fabian, A. C., & Nulsen, P. E. J. 1977, MNRAS, 180, 479

Fabian, A. C., Nulsen, P. E. J., & Canizares, C. R. 1984, Nature, 310, 733

Fabian, A. C., Sanders, J. S., Allen, S. W., Crawford, C. S., Iwasawa, K., Johnstone, R. M., Schmidt, R. W., & Taylor, G. B. 2003, MNRAS, 344, L43

Falcke, H., Rieke, M. J., Rieke, G. H., Simpson, C., & Wilson, A. S. 1998, ApJ, 494, L155+

Feretti, L., Böhringer, H., Giovannini, G., & Neumann, D. 1997a, A&A, 317, 432

Feretti, L., Giovannini, G., & Böhringer, H. 1997b, New Astronomy, 2, 501

Ferland, G. J., Fabian, A. C., Hatch, N. A., Johnstone, R. M., Porter, R. L., van Hoof, P. A. M., & Williams, R. J. R. 2008, MNRAS, 386, L72

Finoguenov, A., Reiprich, T. H., & Böhringer, H. 2001, A&A, 368, 749

Forman, W., et al. 2005, ApJ, 635, 894

Freeman, P. E., Kashyap, V., Rosner, R., & Lamb, D. Q. 2002, ApJS, 138, 185

Frenk, C. S., et al. 1999, ApJ, 525, 554

Fukazawa, Y., Makishima, K., Tamura, T., Ezawa, H., Xu, H., Ikebe, Y., Kikuchi, K., & Ohashi, T. 1998, PASJ, 50, 187

Garmire, G. P., Bautz, M. W., Ford, P. G., Nousek, J. A., & Ricker, Jr., G. R. 2003, in Presented at the Society of Photo-Optical Instrumentation Engineers (SPIE) Conference, Vol. 4851, Society of Photo-Optical Instrumentation Engineers (SPIE) Conference Series, ed. J. E. Truemper & H. D. Tananbaum, 28–44

Gioia, I. M., & Luppino, G. A. 1994, ApJS, 94, 583

Gioia, I. M., Maccacaro, T., Geller, M. J., Huchra, J. P., Stocke, J., & Steiner, J. E. 1982, ApJ, 255, L17

Gioia, I. M., Maccacaro, T., Schild, R. E., Wolter, A., Stocke, J. T., Morris, S. L., & Henry, J. P. 1990, ApJS, 72, 567

Girardi, M., Fadda, D., Escalera, E., Giuricin, G., Mardirossian, F., & Mezzetti, M. 1997, ApJ, 490, 56

Gómez, P. L., Hughes, J. P., & Birkinshaw, M. 2000, ApJ, 540, 726

Govoni, F., Taylor, G. B., Dallacasa, D., Feretti, L., & Giovannini, G. 2001, A&A, 379, 807

Guo, F., Oh, S. P., & Ruszkowski, M. 2008, ApJ, 688, 859

Gursky, H., Kellogg, E., Murray, S., Leong, C., Tananbaum, H., & Giacconi, R. 1971, ApJ, 167, L81+

Gutierrez, K., & Krawczynski, H. 2005, ApJ, 619, 161

Haiman, Z., Mohr, J. J., & Holder, G. P. 2001, ApJ, 553, 545

Hallman, E. J., Burns, J. O., Motl, P. M., & Norman, M. L. 2007, ApJ, 665, 911

Hallman, E. J., & Markevitch, M. 2004, ApJ, 610, L81

Hardcastle, M. J., Evans, D. A., & Croston, J. H. 2007, MNRAS, 376, 1849

Heckman, T. M., Baum, S. A., van Breugel, W. J. M., & McCarthy, P. 1989, ApJ, 338, 48

Henry, J. P., Mullis, C. R., Voges, W., Böhringer, H., Briel, U. G., Gioia, I. M., & Huchra, J. P. 2006, ApJS, 162, 304

Hoeft, M., & Brüggen, M. 2004, ApJ, 617, 896

Hogg, D. W. 2008, arXiv e-prints: 0807.4820

Horner, D. J. 2001, PhD thesis, University of Maryland College Park

Horner, D. J., Mushotzky, R. F., & Scharf, C. A. 1999, ApJ, 520, 78

Hu, E. M., Cowie, L. L., & Wang, Z. 1985, ApJS, 59, 447

Hudson, D. S., & Reiprich, T. H. 2007, in Heating versus Cooling in Galaxies and Clusters of Galaxies, ed. H. Böhringer, G. W. Pratt, A. Finoguenov, & P. Schuecker, 42–+

Hudson, D. S., Reiprich, T. H., Clarke, T. E., & Sarazin, C. L. 2006, A&A, 453, 433

Jaffe, W., & Bremer, M. N. 1997, MNRAS, 284, L1

Jeltema, T. E., Canizares, C. R., Bautz, M. W., & Buote, D. A. 2005, ApJ, 624, 606

Jeltema, T. E., Hallman, E. J., Burns, J. O., & Motl, P. M. 2008, ApJ, 681, 167

Johnstone, R. M., Fabian, A. C., & Nulsen, P. E. J. 1987, MNRAS, 224, 75

Jones, C., & Forman, W. 1984, ApJ, 276, 38

Kaastra, J. S., et al. 2004, A&A, 413, 415

Kaiser, C. R., & Binney, J. 2003, MNRAS, 338, 837

Kaiser, N. 1986, MNRAS, 222, 323

—. 1991, ApJ, 383, 104

Kalberla, P. M. W., Burton, W. B., Hartmann, D., Arnal, E. M., Bajaja, E., Morras, R., & Pöppel, W. G. L. 2005, A&A, 440, 775

Kempner, J. C., Sarazin, C. L., & Markevitch, M. 2003, ApJ, 593, 291

Kennicutt, Jr., R. C. 1983, ApJ, 272, 54

—. 1998, ARA&A, 36, 189

Knuth, K. H. 2006, arXiv e-prints: 0605.197

Kravtsov, A. V., Vikhlinin, A., & Nagai, D. 2006, ApJ, 650, 128

Krempec-Krygier, J., & Krygier, B. 1999, Acta Astronomica, 49, 403

Kriss, G. A., Cioffi, D. F., & Canizares, C. R. 1983, ApJ, 272, 439

Lawrence, C. R., Zucker, J. R., Readhead, A. C. S., Unwin, S. C., Pearson, T. J., & Xu, W. 1996, ApJS, 107, 541

Liedahl, D. A., Osterheld, A. L., & Goldstein, W. H. 1995, ApJ, 438, L115

Lloyd-Davies, E. J., Ponman, T. J., & Cannon, D. B. 2000, MNRAS, 315, 689

Loewenstein, M. 2000, ApJ, 532, 17

Loken, C., Norman, M. L., Nelson, E., Burns, J., Bryan, G. L., & Motl, P. 2002, ApJ, 579, 571

Madau, P., Ferguson, H. C., Dickinson, M. E., Giavalisco, M., Steidel, C. C., & Fruchter, A. 1996, MNRAS, 283, 1388

Markevitch, M. 1998, ApJ, 504, 27

Markevitch, M., Forman, W. R., Sarazin, C. L., & Vikhlinin, A. 1998, ApJ, 503, 77

Markevitch, M., Gonzalez, A. H., David, L., Vikhlinin, A., Murray, S., Forman, W., Jones, C., & Tucker, W. 2002, ApJ, 567, L27

Markevitch, M., & Vikhlinin, A. 2007, Phys. Rep., 443, 1

Markevitch, M., Vikhlinin, A., & Mazzotta, P. 2001, ApJ, 562, L153

Markevitch, M. L., Sarazin, C. L., & Irwin, J. A. 1996, ApJ, 472, L17+

Marshall, H. L., Tennant, A., Grant, C. E., Hitchcock, A. P., O'Dell, S. L., & Plucinsky, P. P. 2004, in Presented at the Society of Photo-Optical Instrumentation Engineers (SPIE) Conference, Vol. 5165, X-Ray and Gamma-Ray Instrumentation for Astronomy XIII. Edited by Flanagan, Kathryn A.; Siegmund, Oswald H. W. Proceedings of the SPIE, Volume 5165, pp. 497-508 (2004)., ed. K. A. Flanagan & O. H. W. Siegmund, 497–508

Martini, P., Kelson, D. D., Mulchaey, J. S., & Athey, A. 2004, in Clusters of Galaxies: Probes of Cosmological Structure and Galaxy Evolution, ed. J. S. Mulchaey, A. Dressler, & A. Oemler

Mathews, W. G., & Bregman, J. N. 1978, ApJ, 224, 308

Mathews, W. G., Faltenbacher, A., & Brighenti, F. 2006, ApJ, 638, 659

Mauch, T., Murphy, T., Buttery, H. J., Curran, J., Hunstead, R. W., Piestrzynski, B., Robertson, J. G., & Sadler, E. M. 2003, MNRAS, 342, 1117

Maughan, B. J. 2007, ApJ, 668, 772

Maughan, B. J., Jones, C., Forman, W., & Van Speybroeck, L. 2008, ApJS, 174, 117

Maughan, B. J., Jones, C., Jones, L. R., & Van Speybroeck, L. 2007, ApJ, 659, 1125

Mazzotta, P., Markevitch, M., Vikhlinin, A., Forman, W. R., David, L. P., & VanSpeybroeck, L. 2001, ApJ, 555, 205

Mazzotta, P., Rasia, E., Moscardini, L., & Tormen, G. 2004, MNRAS, 354, 10

McCarthy, I. G., Babul, A., Bower, R. G., & Balogh, M. L. 2008, MNRAS, 386, 1309

McCarthy, I. G., Balogh, M. L., Babul, A., Poole, G. B., & Horner, D. J. 2004, ApJ, 613, 811

McCarthy, I. G., et al. 2007, MNRAS, 376, 497

McDonough, W., & Braungart, M. 2002, Cradle to Cradle: Remaking the Way We Make Things (New York: North Point Press)

McNamara, B. R., & Jaffe, W. 1994, A&A, 281, 673

McNamara, B. R., & Nulsen, P. E. J. 2007, ARA&A, 45, 117

McNamara, B. R., Nulsen, P. E. J., Wise, M. W., Rafferty, D. A., Carilli, C., Sarazin, C. L., & Blanton, E. L. 2005, Nature, 433, 45

McNamara, B. R., & O'Connell, R. W. 1989, AJ, 98, 2018

McNamara, B. R., O'Connell, R. W., & Bregman, J. N. 1990, ApJ, 360, 20

Mercurio, A., Massarotti, M., Merluzzi, P., Girardi, M., La Barbera, F., & Busarello, G. 2003, A&A, 408, 57

Mewe, R., Gronenschild, E. H. B. M., & van den Oord, G. H. J. 1985, A&AS, 62, 197

Mewe, R., Lemen, J. R., & van den Oord, G. H. J. 1986, A&AS, 65, 511

Mitchell, R. J., Culhane, J. L., Davison, P. J. N., & Ives, J. C. 1976, MNRAS, 175, 29P

Mohr, J. J., & Evrard, A. E. 1997, ApJ, 491, 38

Mohr, J. J., Mathiesen, B., & Evrard, A. E. 1999, ApJ, 517, 627

Molendi, S., De Grandi, S., & Fusco-Femiano, R. 2000, ApJ, 534, L43

Molendi, S., de Grandi, S., Fusco-Femiano, R., Colafrancesco, S., Fiore, F., Nesci, R., & Tamburelli, F. 1999, ApJ, 525, L73

Morandi, A., & Ettori, S. 2007, MNRAS, 380, 1521

Morrison, R., & McCammon, D. 1983, ApJ, 270, 119

Mushotzky, R. F. 1984, Physica Scripta Volume T, 7, 157

Mushotzky, R. F., & Loewenstein, M. 1997, ApJ, 481, L63+

Nagai, D., Kravtsov, A. V., & Vikhlinin, A. 2007, ApJ, 668, 1

Nath, B. B., & Roychowdhury, S. 2002, MNRAS, 333, 145

Navarro, J. F., Frenk, C. S., & White, S. D. M. 1995, MNRAS, 275, 720

—. 1997, ApJ, 490, 493

Nevalainen, J., Markevitch, M., & Forman, W. 2000, ApJ, 536, 73

Nousek, J. A., & Shue, D. R. 1989, ApJ, 342, 1207

Nulsen, P. E. J., McNamara, B. R., Wise, M. W., & David, L. P. 2005, ApJ, 628, 629

O'Dea, C. P., Baum, S. A., & Gallimore, J. F. 1994a, ApJ, 436, 669

O'Dea, C. P., Baum, S. A., Maloney, P. R., Tacconi, L. J., & Sparks, W. B. 1994b, ApJ, 422, 467

O'Hara, T. B., Mohr, J. J., Bialek, J. J., & Evrard, A. E. 2006, ApJ, 639, 64

O'Hara, T. B., Mohr, J. J., & Guerrero, M. A. 2004, ApJ, 604, 604

Ohta, Y., et al. 2001, in Astronomical Society of the Pacific Conference Series, Vol. 251, New Century of X-ray Astronomy, ed. H. Inoue & H. Kunieda, 474–+

Omma, H., Binney, J., Bryan, G., & Slyz, A. 2004, MNRAS, 348, 1105

Ota, N., Kitayama, T., Masai, K., & Mitsuda, K. 2006, ApJ, 640, 673

Parrish, I. J., & Quataert, E. 2008, ApJ, 677, L9

Peres, C. B., Fabian, A. C., Edge, A. C., Allen, S. W., Johnstone, R. M., & White, D. A. 1998, MNRAS, 298, 416

Perlmutter, S., et al. 1999, ApJ, 517, 565

Peterson, J. R., & Fabian, A. C. 2006, Phys. Rep., 427, 1

Peterson, J. R., Kahn, S. M., Paerels, F. B. S., Kaastra, J. S., Tamura, T., Bleeker, J. A. M., Ferrigno, C., & Jernigan, J. G. 2003, ApJ, 590, 207

Peterson, J. R., et al. 2001, A&A, 365, L104

Piffaretti, R., Jetzer, P., Kaastra, J. S., & Tamura, T. 2005, A&A, 433, 101

Pizzolato, F., & Soker, N. 2005, ApJ, 632, 821

Pointecouteau, E., Arnaud, M., & Pratt, G. W. 2005, A&A, 435, 1

Ponman, T. J., Cannon, D. B., & Navarro, J. F. 1999, Nature, 397, 135

Ponman, T. J., Sanderson, A. J. R., & Finoguenov, A. 2003, MNRAS, 343, 331

Poole, G. B., Fardal, M. A., Babul, A., McCarthy, I. G., Quinn, T., & Wadsley, J. 2006, MNRAS, 373, 881

Pratt, G. W., Arnaud, M., & Pointecouteau, E. 2006, A&A, 446, 429

Prestwich, A. H., & Joy, M. 1991, ApJ, 369, L1

Quataert, E. 2008, ApJ, 673, 758

Quillen, A. C., et al. 2008, ApJS, 176, 39

Randall, S. W., Sarazin, C. L., & Ricker, P. M. 2002, ApJ, 577, 579

Reiprich, T. H. 2001, PhD thesis, AA(Max-Planck-Institut für extraterrestrische Physik, P.O. Box 1312, 85741 Garching, Germany)

Reiprich, T. H., & Böhringer, H. 2002, ApJ, 567, 716

Riess, A. G., et al. 1998, AJ, 116, 1009

—. 2007, ApJ, 659, 98

Rosati, P., della Ceca, R., Burg, R., Norman, C., & Giacconi, R. 1995, ApJ, 445, L11

Roychowdhury, S., Ruszkowski, M., Nath, B. B., & Begelman, M. C. 2004, ApJ, 615, 681

Ruszkowski, M., & Begelman, M. C. 2002, ApJ, 581, 223

Ruszkowski, M., Enßlin, T. A., Brüggen, M., Begelman, M. C., & Churazov, E. 2008, MNRAS, 383, 1359

Rybicki, G. B., & Lightman, A. P. 1986, Radiative Processes in Astrophysics (Radiative Processes in Astrophysics, by George B. Rybicki, Alan P. Lightman, pp. 400. ISBN 0-471-82759-2. Wiley-VCH, June 1986.)

Sakelliou, I., & Merrifield, M. R. 2000, MNRAS, 311, 649

Sakelliou, I., & Ponman, T. J. 2004, MNRAS, 351, 1439

Sanders, J. S., & Fabian, A. C. 2008, MNRAS, 390, L93

Sanderson, A. J. R., Ponman, T. J., & O'Sullivan, E. 2006, MNRAS, 372, 1496

Sarazin, C. L. 1986, Reviews of Modern Physics, 58, 1

Sarazin, C. L. 2003, Physics of Plasmas, 10, 1992

Saro, A., Borgani, S., Tornatore, L., Dolag, K., Murante, G., Biviano, A., Calura, F., & Charlot, S. 2006, MNRAS, 373, 397

Serlemitsos, P. J., Smith, B. W., Boldt, E. A., Holt, S. S., & Swank, J. H. 1977, ApJ, 211, L63

Sharma, M., et al. 2004, ApJ, 613, 180

Shaver, P. A., Wall, J. V., Kellermann, K. I., Jackson, C. A., & Hawkins, M. R. S. 1996, Nature, 384, 439

Smith, G. P., Kneib, J.-P., Smail, I., Mazzotta, P., Ebeling, H., & Czoske, O. 2005, MNRAS, 359, 417

Snowden, S. L. 2004, in Astrophysics and Space Science Library, Vol. 309, Soft X-ray Emission from Clusters of Galaxies and Related Phenomena, ed. R. M. J. Lieu, 103–+

Snowden, S. L., Mushotzky, R. F., Kuntz, K. D., & Davis, D. S. 2008, A&A, 478, 615

Soker, N., & Pizzolato, F. 2005, ApJ, 622, 847

Soker, N., White, III, R. E., David, L. P., & McNamara, B. R. 2001, ApJ, 549, 832

Sparks, W. B., Donahue, M., Jordán, A., Ferrarese, L., & Côté, P. 2004, ApJ, 607, 294

Spergel, D. N., et al. 2007, ApJS, 170, 377

Stewart, G. C., Fabian, A. C., Jones, C., & Forman, W. 1984, ApJ, 285, 1

Sun, M., Jones, C., Forman, W., Vikhlinin, A., Donahue, M., & Voit, M. 2007, ApJ, 657, 197

Sun, M., & Murray, S. S. 2002, ApJ, 576, 708

Sun, M., Voit, G. M., Donahue, M., Jones, C., Forman, W., & Vikhlinin, A. 2009, ApJ, 693, 1142

Tamura, T., et al. 2001, A&A, 365, L87

Teague, P. F., Carter, D., & Gray, P. M. 1990, ApJS, 72, 715

Teyssier, R., Chieze, J.-P., & Alimi, J.-M. 1997, ApJ, 480, 36

Townsley, L. K., Broos, P. S., Garmire, G. P., & Nousek, J. A. 2000, ApJ, 534, L139

Tozzi, P., & Norman, C. 2001, ApJ, 546, 63

Tucker, W., et al. 1998, ApJ, 496, L5+

Valentijn, E. A., & Bijleveld, W. 1983, A&A, 125, 223

Valluri, M., & Anupama, G. C. 1996, AJ, 112, 1390

Ventimiglia, D. A., Voit, G. M., Donahue, M., & Ameglio, S. 2008, ApJ, 685, 118

Vikhlinin, A. 2006, ApJ, 640, 710

Vikhlinin, A., Markevitch, M., Murray, S. S., Jones, C., Forman, W., & Van Speybroeck, L. 2005, ApJ, 628, 655

Vikhlinin, A., McNamara, B. R., Forman, W., Jones, C., Quintana, H., & Hornstrup, A. 1998, ApJ, 502, 558

Voit, G. M. 2005, Reviews of Modern Physics, 77, 207

Voit, G. M., & Bryan, G. L. 2001, Nature, 414, 425

Voit, G. M., Bryan, G. L., Balogh, M. L., & Bower, R. G. 2002, ApJ, 576, 601

Voit, G. M., Cavagnolo, K. W., Donahue, M., Rafferty, D. A., McNamara, B. R., & Nulsen, P. E. J. 2008, ApJ, 681, L5

Voit, G. M., & Donahue, M. 1995, ApJ, 452, 164

—. 1997, ApJ, 486, 242

—. 2005, ApJ, 634, 955

Voit, G. M., Kay, S. T., & Bryan, G. L. 2005, MNRAS, 364, 909

Wang, L., & Steinhardt, P. J. 1998, ApJ, 508, 483

Wang, Q. D., Connolly, A., & Brunner, R. 1997, ApJ, 487, L13+

Wang, Q. D., Owen, F., & Ledlow, M. 2004a, ApJ, 611, 821

Wang, S., Khoury, J., Haiman, Z., & May, M. 2004b, Phys. Rev. D, 70, 123008

Wargelin, B. J., Markevitch, M., Juda, M., Kharchenko, V., Edgar, R., & Dalgarno, A. 2004, ApJ, 607, 596

Waters, C. Z., Zepf, S. E., Lauer, T. R., & Baltz, E. A. 2009, ApJ, 693, 463

Weisskopf, M. C., Tananbaum, H. D., Van Speybroeck, L. P., & O'Dell, S. L. 2000, in Presented at the Society of Photo-Optical Instrumentation Engineers (SPIE) Conference, Vol. 4012, Proc. SPIE Vol. 4012, p. 2-16, X-Ray Optics, Instruments, and Missions III, Joachim E. Truemper; Bernd Aschenbach; Eds., ed. J. E. Truemper & B. Aschenbach, 2–16

White, D. A., Jones, C., & Forman, W. 1997, MNRAS, 292, 419

White, S. D. M., Efstathiou, G., & Frenk, C. S. 1993, MNRAS, 262, 1023

White, S. D. M., & Rees, M. J. 1978, MNRAS, 183, 341

Xue, Y.-J., & Wu, X.-P. 2000, MNRAS, 318, 715

Yang, Y., Huo, Z., Zhou, X., Xue, S., Mao, S., Ma, J., & Chen, J. 2004, ApJ, 614, 692

Yuan, Q.-R., Yan, P.-F., Yang, Y.-B., & Zhou, X. 2005, Chinese Journal of Astronomy and Astrophysics, 5, 126